

**Modeling and Processing of Diffusion  
Tensor Magnetic Resonance Images for  
Improved Analysis of Brain Connectivity**

---

**Modellering en Verwerking van  
Diffusietensor Magnetische Resonantie  
Beelden met het Oog op een Verbeterde  
Analyse van de Hersenconnectiviteit**

Proefschrift voorgelegd tot het behalen van de graad van

**Doctor in de Wetenschappen**

Aan de Universiteit Antwerpen, te verdedigen door

**Alexander LEEMANS**

**Promotor**  
Prof. Dr. Jan Sijbers

**Copromotors**  
Prof. Dr. Annemie Van der Linden  
Prof. Dr. Dirk Van Dyck

Antwerpen, 2006







Faculteit Wetenschappen  
Departement Fysica

# Modeling and Processing of Diffusion Tensor Magnetic Resonance Images for Improved Analysis of Brain Connectivity

---

## Modellering en Verwerking van Diffusietensor Magnetische Resonantie Beelden met het Oog op een Verbeterde Analyse van de Hersenconnectiviteit

Proefschrift voorgelegd tot het behalen van de graad van

**Doctor in de Wetenschappen**

aan de Universiteit Antwerpen, te verdedigen door

**Alexander LEEMANS**

### **Promotor**

Prof. Dr. Jan Sijbers

### **Copromotors**

Prof. Dr. Annemie Van der Linden

Prof. Dr. Dirk Van Dyck

Antwerpen, 2006

## **Doctoral committee**

### **Chairman**

Prof. Dr. W. Malfliet

### **Supervisors**

Prof. Dr. J. Sijbers

Prof. Dr. D. Van Dyck

Prof. Dr. A. Van der Linden

### **Unofficial supervisor**

Prof. Dr. P. Parizel

### **External members**

Prof. Dr. D. Jones, Cardiff University Brain and Repair Imaging Centre (CUBRIC), Cardiff, Wales

Prof. Dr. I. Lemahieu, Medical Image and Signal Processing (MEDISIP), Ghent, Belgium

Dr. A. Vilanova i Bartrolí, Biomedical Imaging and Modeling (BIOMIM) – Biomedical Image Analysis, Eindhoven, The Netherlands

## **Contact information**

✉ Alexander Leemans  
Vision Lab, Dept. of Physics  
University of Antwerp (CDE)  
Universiteitsplein 1, Building N1.21  
B-2610 Wilrijk – Antwerpen, Belgium

☎ +32 (0)496 95 28 97

📠 +32 (0)3 820 22 45

✉ alexander.leemans@ua.ac.be

🌐 <http://webhost.ua.ac.be/visielab/leemans>

ISBN 90-5728-054-X

Copyright © 2006 by Alexander Leemans

All rights reserved. No part of the material protected by this copyright notice may be reproduced or utilized in any form or by any means, electronic or mechanical, including photocopying, recording, broadcasting or by any other information storage and retrieval system without written permission from the copyright owner.

### **Cover illustration**

Virtual reconstruction of the human pyramidal white matter fiber tracts in the left hemisphere.

*The research presented in this thesis was performed at the Vision Lab (Dept. of Physics) in close collaboration with the Bio-Imaging Lab (Dept. of Biomedical Sciences) and the Antwerp University Hospital (Dept. of Radiology)*

**Private PhD Defense**

Thursday, April 13, 2006 at 15:00h  
in room U338, Campus Groenenborger,  
University of Antwerp


**Public PhD Defense**

Tuesday, May 23, 2006 at 18:00h  
in auditorium T105, Campus Groenenborger,  
University of Antwerp

# Acknowledgments

First and foremost I would like to thank my supervisor Prof. Dr. Jan Sijbers for his excellent scientific guidance throughout this research in which I learned to share his scientific passion and ideology. I thoroughly enjoyed our brainstorming sessions and those ‘deadline nights’ combined with the requisite shots of caffeine. I could not have imagined having a better advisor and mentor for my PhD research. It was – and still is – a true pleasure working with you!

I am indebted to my cosupervisors Prof. Dr. Dirk Van Dyck and Prof. Dr. Annemie Van der Linden, and my unofficial cosupervisors Dr. Marleen Verhoye and Prof. Dr. Paul Parizel. They provided me with a stimulating research environment, supported my ideas, and were always prepared for work discussions. I feel very fortunate to have learned abundantly from these brilliant scientists. In addition, I would like to thank them for proofreading this thesis.

A special thanks to Dr. teve De Backer for teaching me several cool programming tricks and helping me with the numerous technical obstacles I encountered during this eventful journey. Without this quick-witted jack-of-all-trades, I would still be scripting my first processing tool.

I would like to thank my office mate Dr. Wim D’haes for his contagiously enthusiastic and persevering approach of doing research which really caught on with me. And if I am ever going to build a house, I will know where to find him.

I am grateful to have been part of the Vision Lab, in which I absolutely enjoyed the interactions, both scientifically and amicably, with Prof. Dr. Etienne Cornelis, Jef Driesen, Arno Duijster, Toon Huysmans, Jaber Juntu, Wouter Pintjes, Dirk Poot, Dr. Rudolf Hanel, Alain Smolders, Prof. Dr. Paul Scheunders, Greg Tisson, Dr. Elke Van de Casteele, Dr. Gert Van de Wouwer, Wouter Van den Broek, Wim Van Hecke, Gert Van Gompel, and Dr. Babs Weyn.

Under the exemplary leadership of Mie, the Bio-Imaging Lab provided an ebullient and energetic research environment in which I appreciated the dynamic collabo-



ration and discussions with Tiny Boumans, Geert De Groof, Dr. Ilse Tindemans, Johan Van Audekerke, Dr. Nadja Van Camp, Dr. Vincent van Meir, Greet Vanhoutte, and Ruth Vreys. Their comments and thoughts on biomedical issues were invaluable.

I am very much indebted to the neuroradiology experts Dr. Evert Vandervliet, Dr. Johan Van Goethem, and Prof. Paul Parizel from the Antwerp University Hospital for sharing exciting new ideas and letting me have the disposal of the MR facilities whenever necessary. Furthermore, I would also like to thank Evert for all the MR data acquisitions ... I especially enjoyed the pineapple project – although eating it proved more successful than tracking fibers from it!

I am very much obliged to Dr. David Tuch and Dr. Christian Beaulieu, for allowing me to broaden my scientific horizon. I feel honored to have been able to learn from these talented scientists, distinguished for their high impact contributions within the field of diffusion MR imaging. With regard to my adventure in the Hub, I would also like to thank Margaret Pipes for providing me a temporary surrogate home and for proofreading this thesis. Concerning my Edmontonian collaboration visit, I am also grateful to Dr. Luis Concha and Catherine Lebel for both their scientific and recreational input.

I would like to thank the Institute for the Promotion of Innovation through Science and Technology in Flanders – Belgium (IWT) for financially supporting this research.

I never would have been able to have completed this work were it not for the dedicated support and love of my friends and family. In particular, I would like to express my deepest gratitude to my parents John and Leen for their unconditional love and support ... and for providing me with the requisite amount of white matter fiber tracts to perform this research. From the bottom of my heart, I wish them all the best with ‘Vega De Salas’ in Spain. Furthermore, I am very much obliged to my in-laws Martin and Nelleke, who are also very dear to me. Although chipping antique stones has become a second nature to them, I feel very thankful to them for building up a warm relationship with me. Finally, I would like to express my sincerest appreciation to Dr. Brechje, aka ‘shoeke’. Where do I even start acknowledging her? Let me state that I’ve learned tremendously from her during the last seven years. She raised my spirits when necessary and was always there for me. She truly is – and always will be – my epitome of love. This dissertation is dedicated to her.

# Contents

<b>Acknowledgments</b>	<b>vii</b>
<b>List of Figures</b>	<b>xv</b>
<b>Summary</b>	<b>xvii</b>
Abstract . . . . .	xvii
Motivation and objectives . . . . .	xvii
 <b>I From H<sub>2</sub>O molecules to fiber bundles of the brain</b>	 <b>1</b>
<b>1 Diffusion tensor imaging</b>	<b>3</b>
1.1 Abstract . . . . .	3
1.2 Introduction . . . . .	4
1.3 Theoretical underpinnings of DTI . . . . .	4
1.3.1 Brownian Motion . . . . .	4
1.3.2 Diffusion . . . . .	4
1.3.2.1 Isotropic environment . . . . .	4
1.3.2.2 Anisotropic environment . . . . .	5
1.3.2.3 Diffusion in the central nervous system . . . . .	5
1.3.2.4 Diffusion NMR . . . . .	6
1.3.3 Diffusion-weighted MRI . . . . .	8
1.3.3.1 Acquisition framework . . . . .	8
1.3.3.2 Initial observations and important applications . . . . .	11
1.3.4 The diffusion tensor model . . . . .	11
1.3.4.1 Acquisition and computation of the diffusion tensor . . . . .	12
1.3.4.2 Geometrical interpretation . . . . .	13
1.3.4.3 Scalar invariance measures . . . . .	16
1.4 Visualization of diffusion tensor fields . . . . .	21
1.4.1 Scalar maps . . . . .	21
1.4.2 Color-encoded maps . . . . .	21

1.4.3	Glyphs . . . . .	23
1.5	DTI Artifacts . . . . .	23
1.5.1	Subject motion . . . . .	23
1.5.2	Eddy current distortions . . . . .	24
1.5.3	Image noise . . . . .	24
1.5.4	Susceptibility artifacts . . . . .	26
1.6	Limitations . . . . .	26
1.7	Applications . . . . .	27
1.7.1	Animal studies . . . . .	27
1.7.2	Human studies . . . . .	27
	Bibliography . . . . .	29
<b>2</b>	<b>MR fiber tractography</b>	<b>47</b>
2.1	Abstract . . . . .	47
2.2	Introduction . . . . .	47
2.3	Principals of MR fiber tractography . . . . .	48
2.3.1	Basic concept . . . . .	48
2.3.2	Regularized and continuous DTI data . . . . .	50
2.4	Fiber connectivity reconstruction methods . . . . .	50
2.4.1	Streamline DTT . . . . .	50
2.4.1.1	Euler's method . . . . .	51
2.4.1.2	Runge-Kutta integration . . . . .	52
2.4.1.3	Tensor deflection . . . . .	53
2.4.1.4	Tractography termination thresholds . . . . .	55
2.4.1.5	Limitations . . . . .	56
2.4.2	Front evolution approaches . . . . .	56
2.4.2.1	Fast marching tractography . . . . .	56
2.4.2.2	Further developments . . . . .	58
2.4.3	Probabilistic approaches . . . . .	59
2.5	FT visualization techniques . . . . .	60
2.5.1	Streamlines, streamtubes and hyperstreamlines . . . . .	60
2.5.2	Streamsurfaces and volume rendering . . . . .	62
2.5.3	Fiber clustering . . . . .	64
2.6	Applications . . . . .	64
	Bibliography . . . . .	67
<b>II</b>	<b>Diffusion Tensor Image Processing</b>	<b>77</b>
<b>3</b>	<b>Simulated diffusion tensor phantom</b>	<b>79</b>
3.1	Abstract . . . . .	79

3.2	Introduction . . . . .	80
3.3	Theory . . . . .	81
3.3.1	Backbone of the fiber bundle . . . . .	82
3.3.2	Physical thickness of the fiber bundle . . . . .	82
3.3.2.1	Solid model . . . . .	83
3.3.2.2	Gaussian model . . . . .	83
3.3.2.3	Saturated model . . . . .	84
3.3.3	Principal diffusion direction and eigenvalue fields . . . . .	84
3.3.4	Total diffusion tensor field . . . . .	86
3.4	Methods . . . . .	86
3.5	Results . . . . .	87
3.5.1	Theoretical model . . . . .	87
3.5.1.1	Single WM fiber bundles . . . . .	87
3.5.1.2	Complex WM configurations . . . . .	87
3.5.2	Experimental evaluation of the mathematical framework . . . . .	91
3.5.3	Example of a simulated phantom from experimental data . . . . .	92
3.5.4	Application to WM FT . . . . .	92
3.5.4.1	Synthetic data . . . . .	92
3.5.4.2	Fiber similarity . . . . .	94
3.5.4.3	Optimal curvature threshold . . . . .	94
3.5.4.4	Sensitivity to noise . . . . .	94
3.6	Discussion . . . . .	94
3.7	Conclusions . . . . .	97
	Bibliography . . . . .	97
<b>4</b>	<b>Voxel based DTI coregistration</b>	<b>99</b>
4.1	Abstract . . . . .	99
4.2	Introduction . . . . .	99
4.3	Theory . . . . .	101
4.3.1	Spatial normalization . . . . .	101
4.3.2	Diffusion tensor reorientation . . . . .	102
4.4	Methods . . . . .	102
4.4.1	Simulated DTI data . . . . .	102
4.4.2	Experimental DTI data . . . . .	103
4.5	Results . . . . .	103
4.5.1	Coregistration of simulated DTI data sets . . . . .	103
4.5.2	Coregistration of experimental DTI data sets . . . . .	105
4.6	Conclusions . . . . .	105
	Bibliography . . . . .	105

<b>5</b>	<b>Feature based DTI coregistration</b>	<b>109</b>
5.1	Abstract . . . . .	109
5.2	Introduction . . . . .	110
5.3	Theory . . . . .	111
5.3.1	Curvature and torsion of space curves . . . . .	111
5.3.1.1	Definitions . . . . .	111
5.3.1.2	Invariance properties . . . . .	113
5.3.2	Space curve coregistration . . . . .	113
5.3.2.1	Curve index correspondence . . . . .	114
5.3.2.2	Local space curve transformation . . . . .	115
5.3.2.3	Global space curve transformation . . . . .	116
5.3.2.4	Multiscale coregistration . . . . .	117
5.3.2.5	Computational complexity . . . . .	118
5.4	Methods . . . . .	118
5.4.1	Simulated DTI data . . . . .	118
5.4.2	Brain DTI data . . . . .	119
5.4.3	Fiber tractography . . . . .	119
5.5	Results . . . . .	121
5.5.1	Quantitative analysis of the white matter fiber coregistration technique . . . . .	121
5.5.1.1	Noise sensitivity . . . . .	121
5.5.1.2	Multiscale coregistration . . . . .	121
5.5.1.3	Global transformation estimation . . . . .	121
5.5.1.4	ROI based coregistration . . . . .	123
5.5.1.5	Space curve sampling and time complexity . . . . .	123
5.5.2	Coregistration of brain DTI data sets . . . . .	123
5.6	Discussion . . . . .	127
5.7	Conclusions . . . . .	128
	Bibliography . . . . .	128
<b>6</b>	<b>Conclusions</b>	<b>131</b>
6.1	Overview . . . . .	131
6.2	Future work . . . . .	132
	<b>Appendices</b>	<b>133</b>
	Appendix A . . . . .	133
	Appendix B . . . . .	134
	<b>List of abbreviations</b>	<b>137</b>
	<b>‘ExploreDTI’: toolbox for exploratory DTI and FT</b>	<b>141</b>

---

<b>Curriculum vitae</b>	<b>143</b>
<b>List of publications</b>	<b>145</b>
Journal articles . . . . .	145
Conference proceedings . . . . .	146
Awards . . . . .	149
<b>Nederlandse samenvatting</b>	<b>151</b>
Overzicht . . . . .	151
Motivatie en doelstellingen . . . . .	151



# List of Figures

1.1	The anatomical architecture of brain WM . . . . .	7
1.2	Schematic illustration of the diffusion-weighted imaging sequence . .	10
1.3	Example of diffusion-weighted and diffusion tensor images . . . . .	14
1.4	Ellipsoidal representation of the diffusion tensor field . . . . .	15
1.5	Principal diffusivity vectors with directional color-encoding . . . . .	17
1.6	Scalar measures derived from the diffusion tensor . . . . .	18
1.7	Color-encoded maps and glyphs for visualizing DTI data . . . . .	22
1.8	Correction of eddy current artifacts . . . . .	25
1.9	Visualization of WM structures in the starling brain . . . . .	28
1.10	Callosal agenesis compared with the normal human brain . . . . .	30
2.1	Example of in vivo FT . . . . .	49
2.2	Comparison between raw and regularized DTI data . . . . .	51
2.3	The effect of the step size for streamline FT . . . . .	52
2.4	Comparison between tensor deflection and ‘regular’ streamline FT .	54
2.5	Example of front-evolution based FT . . . . .	57
2.6	Pseudo-probabilistic FT of pyramidal fiber tracts . . . . .	59
2.7	Streamlines and streamtubes with color-encoding according to the PDV and the geometrical shape . . . . .	61
2.8	Streamlines and streamtubes with color-encoding according to the FA and the tract length . . . . .	62
2.9	Hyperstreamlines, transparency rendering, and iso-surface rendering of WM fiber tracts . . . . .	63
2.10	Clustering of fiber tracts . . . . .	65
2.11	Callosal agenesis compared with normal brain using FT . . . . .	66
2.12	WM fiber structures of the human brain reconstructed with FT . . .	67
3.1	Different models for defining the cross-sectional dependency . . . . .	84
3.2	Illustration of the asymptotic behavior of the saturated model . . . .	85
3.3	Example of a fiber tract with different models . . . . .	88



3.4	Elliptical representations of a WM fiber bundle . . . . .	89
3.5	Ellipsoidal diffusion tensor field representation of fiber crossing . . .	90
3.6	Experimental example: the starling brain . . . . .	91
3.7	3D representation of the starling cerebellum . . . . .	93
3.8	3D representation of a simulated WM fiber system . . . . .	95
4.1	Two different data acquisitions of the same human brain . . . . .	103
4.2	Ellipsoidal representations of synthetic DTI data . . . . .	104
4.3	Human brain DTI images . . . . .	106
5.1	Curvature and torsion for space curves . . . . .	112
5.2	Illustration of PCA-based transformation . . . . .	116
5.3	Representations of simulated and brain DTI data . . . . .	120
5.4	Quantitative results of the simulation analysis . . . . .	122
5.5	Qualitative evaluation of the brain DTI coregistration . . . . .	124
5.6	Quantitative analysis of the brain DTI coregistration . . . . .	125
A.1	Different models for defining the cross-sectional dependency . . . . .	134

# Summary

## Abstract

This dissertation deals with modeling and processing of Diffusion Tensor (DT) Magnetic Resonance (MR) data. The development of new DT image processing techniques for improved analysis of brain connectivity (i.e., the complex network of connections by which brain cells communicate) is hereby emphasized. This thesis is divided into two parts. Part I elaborately reviews the requisite background on DT MR Imaging (DTI) (chapter 1) and Fiber Tractography (FT) (chapter 2). Part II provides the main original contributions, i.e. the development of a mathematical framework for simulating DTI data (chapter 3) and the development of two new DTI coregistration techniques (chapter 4 and 5).

## Motivation and objectives

The brain is undoubtedly the most complex biological system, since it performs an abundance of intricate tasks, such as observation, interpretation of information, reaction, planning, and display of behavior. DTI allows one to investigate the connections in this complex system (i.e., the brain connectivity) in vivo and non-invasively. Chapter 1 expounds the physical and mathematical underpinnings of this unique MR technique, in which the concept of diffusion is introduced in MR Imaging (MRI). The principals and importance of Diffusion-Weighted MRI are discussed and subsequently extended to DTI. Furthermore, this chapter considers several DT visualization techniques and presents an overview of the most important scalar measures that are related to the DT model. In addition, the most common artifacts in DT are described and the limitations of DTI are elucidated. This chapter finally mentions several applications, emphasizing the importance of DTI within a medical and biomedical context.

One of the most important applications of DTI is FT and constitutes the subject of chapter 2. FT allows one to virtually reconstruct the brain White Matter

(WM) fiber bundles in vivo and non-invasively using diffusion MR data. After a short description of its basic principles, several FT approaches are elucidated and their potential strengths and weaknesses are discussed. This chapter additionally presents the commonly used FT visualization methods, again underlining the significance of a clear data representation. Several important applications are reported.

For fundamental research in DT image processing, simulations and tests on synthetic data are indispensable. With these tests, the accuracy, precision, reproducibility, and noise sensitivity of the developed DT image processing techniques can be studied quantitatively. An accurate and realistic representation of such a synthetic phantom plays an important role in the performance of a reliable analysis with an eye to applications with experimental DTI data. Chapter 3 presents the development of a mathematical framework for constructing these simulated DTI phantoms. In particular, the synthetic DTI data are modeled using an approximated representation of WM fiber bundles incorporating several physical properties of these fiber bundles. On the one hand, the developed synthetic phantoms serve a reliable ground-truth for testing and evaluating DT processing techniques, such as coregistration, noise filtering, and the correction of motion artifacts. On the other hand, these simulated DTI data are essential for optimizing the numerous user-defined parameters that characterize a FT algorithm. Several examples of how this mathematical framework can be applied to compare FT algorithms are presented in detail.

Coregistration is an important technique within the field of image processing which allows one to map images, or stated more generally, ‘digital object representations’, into a common reference frame. Only then, comparative quantitative studies can be realized objectively, such as the indication of a statistically significant difference between normal and ‘abnormal’ WM fiber structures. Due to the rapid development and the growing diversity of imaging modalities during the last decades, it is impossible to design a universal coregistration method. For here, the quality, nature of information, size, and field of application are important aspects that typify the coregistration technique. Within this context, chapter 4 describes the development of an affine (rotation, translation, scale, and skew) voxel based coregistration technique for DTI data. The voxels of DTI data do not represent scalar values, but second-rank tensors that define the three-dimensional Gaussian distributed diffusion, making conventional coregistration techniques inadequate. Furthermore in this chapter, an efficient reorientation strategy is developed, which is necessary for preserving the important orientational information of the diffusion tensor. As a similarity measure, i.e. the criterium that determines how correspondence between the images is defined, mutual information is utilized. The affine DT coregistra-

tion technique is first evaluated using the synthetic DT phantoms and afterwards applied to brain DTI data.

Chapter 5 presents the development of another coregistration method, in which the reconstructed WM fiber tracts are utilized instead of the voxel based data. In this approach, only the relevant information (i.e., the WM fiber tracts) is used for the computation process, making the coregistration procedure more efficient. Indeed, a large number of voxels in DTI data does not represent a relevant signal and therefore does not significantly contribute to the optimization procedure of voxel based DT coregistration techniques. Furthermore, the coregistration technique is fully automatic and is based on the local invariance properties of the WM fiber pathways, which are represented in a hierarchical way. First, simulations are performed using the developed synthetic DTI data to investigate the accuracy, reproducibility, and the effect of image noise. Second, several user-defined parameters that characterize this coregistration are optimized. Finally, this new coregistration approach is compared with the method from chapter 4 and both advantages and disadvantages are discussed.



## Part I

# From H<sub>2</sub>O molecules to fiber bundles of the brain



# Chapter 1

## Diffusion tensor imaging

Parts of the work in this chapter have been published in

*G. De Groof, M. Verhoye, V. Van Meir, I. Tindemans, A. Leemans, and A. Van der Linden, “In vivo diffusion tensor imaging (DTI) of brain subdivisions and vocal pathways in songbirds”, NeuroImage, Vol. 29, Nr. 3, p. 754–763, 2006.*

### 1.1 Abstract

Diffusion Tensor Magnetic Resonance Imaging (DT-MRI), also referred to as Diffusion Tensor Imaging (DTI), is an advanced imaging technique within the field of Magnetic Resonance Imaging (MRI). In order to comprehend the principles of DTI, an understanding of the Nuclear Magnetic Resonance (NMR) phenomenon and the fundamental concepts of MRI is required first. Although the principles of NMR and MRI are extremely interesting, especially from a physicist’s point of view, a general description expounding these principles is considered beyond the scope of this dissertation and is therefore omitted. An excellent and complete description of the principles of MRI can be found in the work of Slichter and Callaghan [1, 2]. For the novice with little technical background, it might be interesting to read the clear presentation of the basics of MRI, as described in the work of Hashemi and colleagues [3]. In this chapter, the physical principles and the mathematical framework of DTI are introduced. Several DTI visualization approaches are described and DTI artifacts are discussed. Finally, the limitations of DTI are presented and several applications are reviewed to point out the importance of DTI in a clinical and biomedical setting.



## 1.2 Introduction

DTI allows one to obtain quantitative information about the three-dimensional (3D) anisotropic diffusion of water molecules in biological tissue [4–10]. This diffusion anisotropy reflects the presence of spatially oriented microstructures (e.g., neural fibers in the central nervous system), where the mobility of the diffusing particles is mainly determined by the fiber pathway [11]. On the basis of this intrinsic property, which assumes that the orientation of the diffusion tensor field matches the orientation of the corresponding underlying fiber system, DTI has been applied in several studies to infer microstructural characteristics and obtain valuable diagnostic information regarding various neuropathological conditions (e.g., Refs. [12, 13]).

## 1.3 Theoretical underpinnings of DTI

### 1.3.1 Brownian Motion

Although water appears to be static to the naked eye, individual water molecules are constantly in motion, colliding with each other at a high speed. This phenomenon, referred to as ‘Brownian motion’, was first described by the Scottish naturalist Robert Brown in 1828, who observed a random motion of grains of pollen suspended in water [14]. The phenomenon ‘diffusion’ can be considered as the macroscopic observable effect due to the microscopic Brownian motion of particles (e.g., think of a drop of wine in a glass of water that slowly spreads apart<sup>1</sup>). Note that the diffusion of water molecules within its own environment (also known as self-diffusion) is conceptually equivalent to the diffusion of a substance in another host substance.

### 1.3.2 Diffusion

In 1905, Einstein developed a theory that could explain the observations of Brown, providing a time-distance relationship for a particle undergoing a Brownian motion.

#### 1.3.2.1 Isotropic environment

Consider a particle in an isotropic environment (e.g., a water molecule in water) at position  $\mathbf{r}_0$  at time  $t = 0$ . If its subsequent position at time  $t = \tau$  is denoted by  $\mathbf{r}$ , the diffusion coefficient  $D$  can be given by Einstein’s relation [15]:

$$D = \frac{1}{6\tau} \langle \mathbf{R}^T \cdot \mathbf{R} \rangle , \quad (1.1)$$

---

<sup>1</sup>This analogy should of course never be made in France ... for it is a downright shame!

where  $\mathbf{R} = \mathbf{r} - \mathbf{r}_o$  represents the net displacement vector of the particle, ‘ $T$ ’ denotes the transpose, and  $\langle \dots \rangle$  describes the average over the particle ensemble. It is important to note that  $D$  is a scalar which relates time to the *square* displacement and therefore should not be considered as a diffusion velocity. The diffusion coefficient is directionally independent, or stated equivalently, the diffusion is isotropic. For water at 37.5°C the diffusion coefficient  $D$  is approximately  $2.5 \times 10^{-3} \text{ mm}^2/\text{s}$  [16].

### 1.3.2.2 Anisotropic environment

If particles undergoing a Brownian motion are restricted to a bounded medium, like strongly aligned microstructures in fibrous biological tissue (cell membranes, polymers, axonal fibers, etc.), a higher displacement will appear parallel to the direction of these boundaries than in the perpendicular direction. Therefore, it can be stated that the underlying structure of an anisotropic environment is reflected by the corresponding Brownian motion. Taking the covariance of the net displacement vector into account, Einstein’s relation, as described in Eq. (1.1), can be generalized to allow for this directional dependency:

$$\mathbf{D} = \frac{1}{6\tau} \langle \mathbf{R} \cdot \mathbf{R}^T \rangle \equiv \begin{bmatrix} D_{xx} & D_{xy} & D_{xz} \\ D_{yx} & D_{yy} & D_{yz} \\ D_{zx} & D_{zy} & D_{zz} \end{bmatrix}, \quad (1.2)$$

where  $\mathbf{D}$  is called the diffusion tensor. It can be shown that this second-rank tensor is symmetric ( $\mathbf{D}^T = \mathbf{D}$ ) and positive definite [17, 18]. The diffusion is directionally dependent, or stated equivalently, the diffusion is anisotropic.

### 1.3.2.3 Diffusion in the central nervous system

In general, the diffusion tensor additionally depends on the particle mass and the temperature [19]. However, since the particle mass of water molecules in the Central Nervous System (CNS) is fixed and the temperature at which the experimental measurements are conducted can be assumed constant, it is correct to state that the spatial differences of the diffusion tensor can be solely interpreted in terms of the architectural environment. On the other hand, it is important to note that for long acquisition times (e.g., in animal studies using sedatives), a close monitoring of the physiological parameters is required, for here, the temperature-related variations of the diffusion coefficient can be significant (the resulting sensitivity of diffusion to temperature is approximately 2.4% per °C). To understand this diffusion behavior of water molecules in the CNS more clearly, a brief anatomical description of its architectural environment is given next (Fig. 1.1).

**Neurons** The human CNS is made up of more than  $10^{10}$  neurons that transmit information in the form of nerve impulses from one part of the body to another. These physical structures are basically composed of the cell body (neurofibrils, neurotubuli, etc.), the axon, and dendrites [20]. Dendrites are attached to the soma of the neuron, and receive impulses from other neurons at the synapses. A sketch of the neuronal network is shown in Fig. 1.1 (a).

**Axons** The axon is the long cylindrical part of the neuron that transmits impulses away from the dendrites and the cell body [20]. It consists of microtubuli, neurofilaments, and the axonal membrane [Fig. 1.1 (b)]. Most axons are wrapped by sheets of fatty myelinated Schwann cells (also called myeline sheets). The thin layer of connective tissue that surrounds the myelinated axon is known as the endoneurium [Fig. 1.1 (b,c)].

**Fasciculi and fiber bundles** A fasciculus or tract can be described as a group of axons that are bundled together and wrapped in a connective tissue called the perineurium [Fig. 1.1 (c,d)] [20]. A group of fasciculi combined with blood vessels finally build up a nerve fiber, which is surrounded by the epineurium to provide a certain toughness and resistance to tearing [Fig. 1.1 (d,e)].

**White matter (WM)** The portion of the fasciculi in the human brain that contain white fatty myelinated Schwann cells form the WM of the brain. In Fig. 1.1 (e), a brain dissection (histology) shows the spaghetti-like WM structure of the Internal Capsule (IC) and the Corona Radiate (CR), using the preservation method of Klinger from the Iowa Virtual Hospital [21]. From the relatively narrow, but thick, basis pedunculi, the fiber bundles are fanning out to the outer areas of the cerebral cortex.

#### 1.3.2.4 Diffusion NMR

The mobility of water to diffuse across tract boundaries is restricted, causing water to diffuse anisotropically, i.e. there is more diffusion in directions parallel to fiber tracts than in perpendicular directions. This directional dependence of diffusion can be measured with NMR and was mainly pioneered by Purcell, Torrey, Stejskal, and Tanner [22–25].

The diffusion coefficient measured by NMR is best known in the biological NMR literature as the Apparent Diffusion Coefficient (ADC) [26]. This measure is not a true measure of the intrinsic diffusion, but rather depends on the interactions of the diffusing water molecules with the cellular structures over a given diffusion time. The interactions sample the local environment and therefore can infer microstructural characteristics of the tissue from the measured diffusion properties

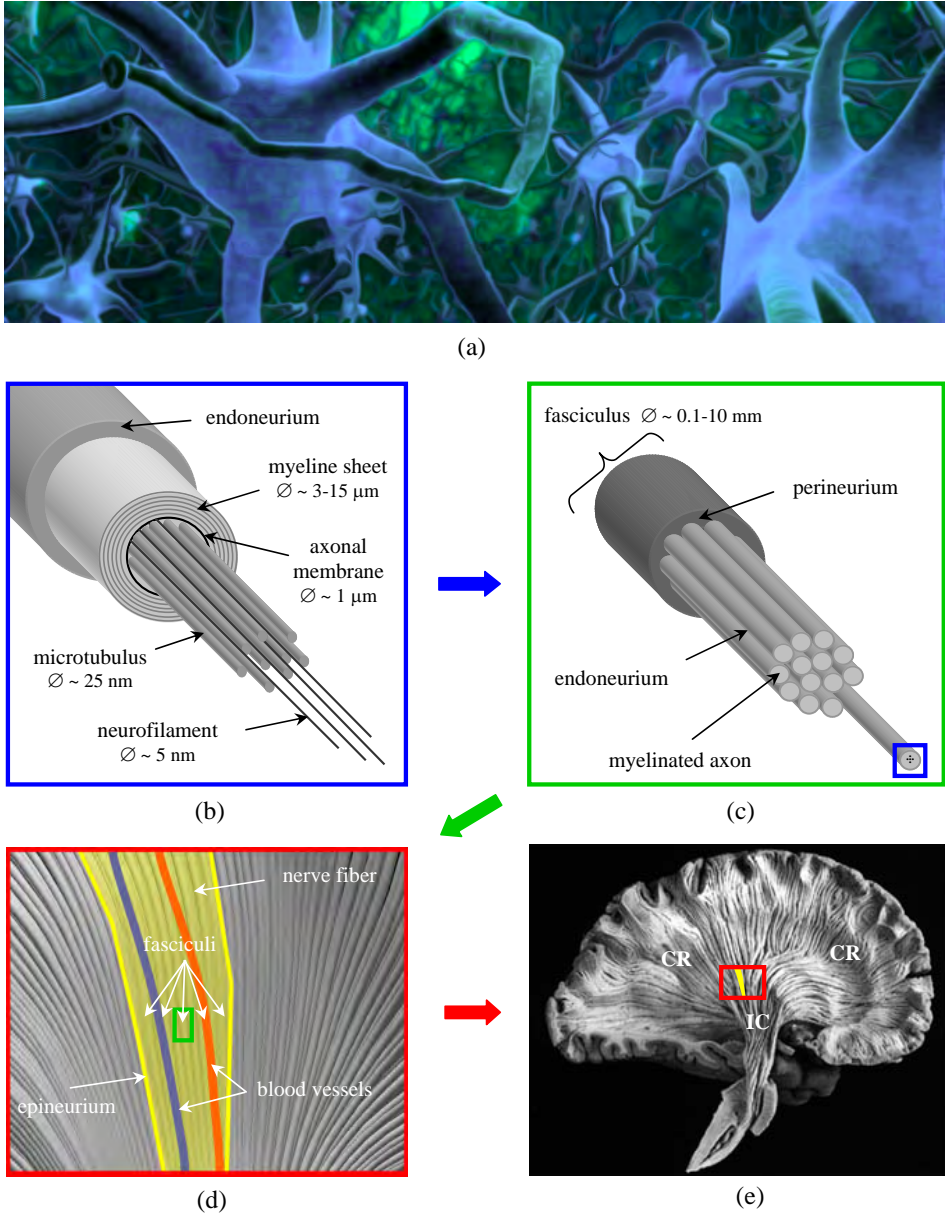


**Figure 1.1.** An illustration of the anatomical configuration of (a) the neuronal network, (b) the axon, (c) the fasciculus, (d) the nerve fiber, and (e) the white matter fiber bundles of the brain [21].

[27]. Note that the ADC could potentially be influenced by active processes within the tissue.

In a recent review by Beaulieu, an excellent description is given about the basis of anisotropic diffusion in the nervous system [11]. There, the relationship of diffusion NMR and its anisotropy with the underlying microstructure of neural fibers is presented in more detail.

### 1.3.3 Diffusion-weighted MRI

Diffusion-Weighted (DW) MRI (DWI) is the imaging technique which is based on the physical principles of diffusion NMR. DWI allows one to measure the amount of water diffusion at different positions in the biological tissue. The acquisition framework of DWI is described next.

#### 1.3.3.1 Acquisition framework

DW images can be measured using a MRI sequence in which two diffusion-encoding gradient pulses are symmetrically positioned around the  $180^\circ$  refocusing Radio Frequency (RF) pulse [23]. Consider two rectangularly shaped diffusion gradient pulses  $\mathbf{g}(t)$  along the  $z$ -direction ( $\|\mathbf{g}(t)\| = g_z(t) = g_z$ ) with duration time  $\delta$  and with time  $\Delta$  between these gradient pulse onsets. The first gradient pulse induces a phase shift  $\phi_1 = \phi_1(z)$  of the spin transverse magnetization, i.e.

$$\phi_1 = \gamma \int_0^\delta g_z(t) z(t) dt = \gamma \delta g_z z_1 , \quad (1.3)$$

where  $\gamma$  is the gyromagnetic ratio for hydrogen nuclei (42MHz/Tesla) and the spin position  $z(t) = z_1$  is assumed to be constant during the short pulse duration  $\delta$  [3]. This gradient pulse causes the spins to dephase and is therefore referred to as the dephasing gradient pulse. Similarly, the second gradient pulse induces a phase shift  $\phi_2 = \phi_2(z)$ , i.e.

$$\phi_2 = -\gamma \int_\Delta^{\Delta+\delta} g_z(t) z(t) dt = -\gamma \delta g_z z_2 , \quad (1.4)$$

where the change of sign in Eq. (1.4) considers the application of the  $180^\circ$  RF pulse. Consequently, this second gradient pulse inverts the phase shift, refocusing the spins. Hence, this gradient pulse is called the rephasing gradient pulse.

For static spins, i.e. spins not undergoing any diffusion ( $z_1 = z_2$ ), the net induced phase shift  $\phi$  will be completely refocused, i.e.

$$\phi = \phi_1 + \phi_2 = \gamma \delta g_z (z_1 - z_2) = 0 . \quad (1.5)$$

On the other hand, spins having completed a change in  $z$ -location due to Brownian motion during the time period  $\Delta$  (i.e., spins undergoing diffusion) will experience a net phase shift

$$\phi = \gamma \delta g_z (z_1 - z_2) \neq 0 . \quad (1.6)$$

These diffusing spins are not completely refocused, resulting in a signal loss [28–30]. In general, the amplitude of the spin-echo signal  $S(\mathbf{r})$ , which describes the signal loss at position  $\mathbf{r}$  due to the application of these diffusion gradients, is given by [3]

$$S(\mathbf{r}) = S_0(\mathbf{r}) \langle e^{i\phi} \rangle \leq S_0(\mathbf{r}) , \quad (1.7)$$

where  $S_0(\mathbf{r})$  is the signal intensity in the absence of a diffusion sensitizing gradient field, i.e.  $\|\mathbf{g}\| = 0$ , and  $\langle \dots \rangle$  represents the ensemble average of the diffusion spin population which causes the aforementioned signal attenuation. This ensemble factor can be calculated explicitly if the statistical spin displacement distribution is known. More specifically, if  $p(\mathbf{r}|\mathbf{r}_0, \tau)$  denotes the conditional probability density function for finding a diffusing spin at position  $\mathbf{r}$  after a time  $\tau$ , given its initial position  $\mathbf{r}_0 = \mathbf{r}(t = 0)$ , Eq. (1.7) can be rewritten as [30]

$$S(\mathbf{r}) = S_0(\mathbf{r}) \int p(\mathbf{r}|\mathbf{r}_0, \tau) e^{i\phi(\mathbf{r}_0 - \mathbf{r})} d\mathbf{r} . \quad (1.8)$$

In Eq. (1.8), the phase  $\phi$  is written for a general gradient direction  $\mathbf{g}$ , analogously to Eq. (1.6), i.e.

$$\phi \equiv \phi(\mathbf{r}_0 - \mathbf{r}) = \gamma \delta \mathbf{g}^T \cdot [\mathbf{r}(t = 0) - \mathbf{r}(t = \Delta)] , \quad (1.9)$$

where the rectangular diffusion gradient  $\mathbf{g}$  can be defined as [23]

$$\mathbf{g} \equiv \mathbf{g}(t) = \|\mathbf{g}\| [H(t - \delta) - H(t) + H(t - \Delta) - H(t - \delta - \Delta)] , \quad (1.10)$$

with  $H(t)$  representing the Heaviside step function. Furthermore, for isotropic media, the conditional probability density function  $p(\mathbf{r}|\mathbf{r}_0, \tau)$  is defined as

$$p(\mathbf{r}|\mathbf{r}_0, \tau) = \frac{1}{\sqrt{[4\pi\tau D(\mathbf{r})]^3}} e^{-\frac{\|\mathbf{r} - \mathbf{r}_0\|^2}{4\tau D(\mathbf{r})}} , \quad (1.11)$$

where  $D(\mathbf{r})$  denotes the diffusion coefficient (or ADC value). Combining Eqs. (1.8) to (1.11), the famous Stejskal-Tanner relation can be obtained, which describes the relationship between the loss of phase coherence in the acquired signal  $S(\mathbf{r})$  and the gradient pulse  $\mathbf{g}$  [23], i.e.

$$S(\mathbf{r}) = S_0(\mathbf{r}) e^{-bD(\mathbf{r})} , \quad (1.12)$$

where the diffusion weighting factor  $b$  in Eq. (1.12), introduced by Le Bihan et al., is defined as [31]:

$$b = \gamma^2 \delta^2 \left( \Delta - \frac{\delta}{3} \right) \|\mathbf{g}\|^2. \quad (1.13)$$

The Stejskal-Tanner equation allows one to relate the measured diffusion signal to the diffusion coefficient of the underlying tissue, assuming that the diffusion is purely Gaussian. In addition, it should be noted that this framework further assumes that  $\delta \ll \Delta$  and that there is no significant effect of additional spatial encoding gradients to the phase of the diffusing spins. A schematic illustration of this elegant acquisition framework is presented in Fig. 1.2.

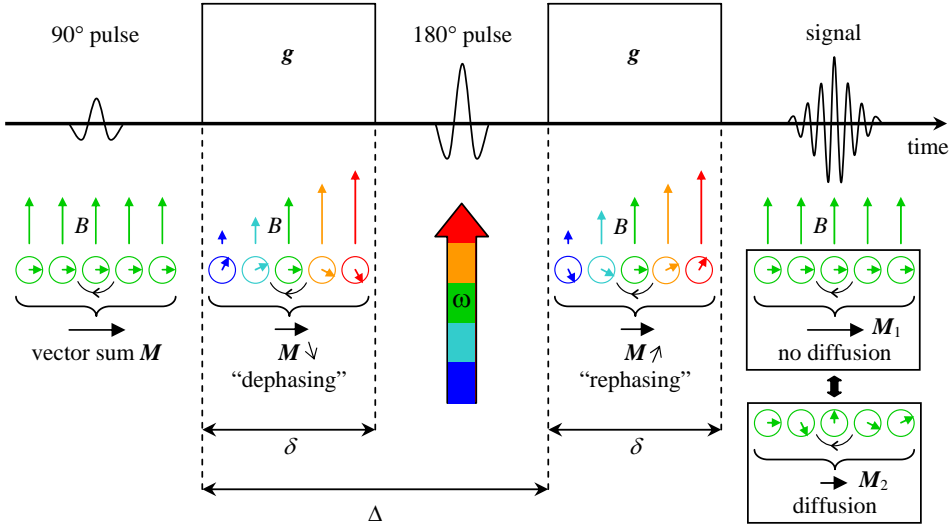


**Figure 1.2.** A schematic illustration of the diffusion-weighted imaging sequence. The length of the colored vertical arrows indicates the strength of the magnetic field  $B$ , which is non-uniform during the application of the gradients  $\mathbf{g}$ . After the first gradient application following the  $90^\circ$  RF pulse, signals lose their uniform phase (called ‘dephasing’, i.e. the vector sum of the magnetic spin moments  $\mathbf{M}$  decreases) because each proton starts to precess at different rates  $\omega$  depending on its position in space (the color-encoding represents the amount of this precession rate). After the second gradient application following the  $180^\circ$  RF pulse, the system restores the uniform phase (called ‘rephasing’, i.e.  $\mathbf{M}$  increases). This rephasing is complete only when spins do not undergo a Brownian motion (i.e., do not diffuse) during the time  $\Delta$  in between the two applications of the gradients ( $\|\mathbf{M}_1\| > \|\mathbf{M}_2\|$ ).

It is important to note that due to the anisotropic environment (e.g., the WM of the brain), the diffusion coefficient  $D(\mathbf{r})$  is dependent on the direction of  $\mathbf{g}$ . In

addition,  $D(\mathbf{r})$  also depends on the gradient strength  $\|\mathbf{g}\|$  and the time sequence parameters  $\delta$  and  $\Delta$ .

In practice, the DW images are often acquired using Echo-Planar Imaging (EPI) sequences [32, 33]. Although these EPI sequences offer improved acquisition times and therefore reduce motion artifacts, they are subject to eddy current distortions introduced by the gradients, especially the large DW imaging gradients.

### 1.3.3.2 Initial observations and important applications

Diffusion anisotropy in biological tissue was initially observed by Cleveland et al. in NMR measurements of the skeletal muscle [34].

The first systematic DWI study of anisotropic water diffusion in the nervous system by Moseley et al. confirmed that water diffusion was anisotropic in normal WM of the cat brain and the spinal cord, whereas diffusion was isotropic in grey matter [35]. At the same time, Chenevert et al. demonstrated anisotropic diffusion within the human WM in vivo [36].

Anisotropy was later also observed in human spinal cord, human sciatic nerve, human tibial nerve, cat optic nerve, peripheral nerves in the rabbit forelimb, and rat trigeminal nerve and corpus callosum in vivo [37–41].

In 1991, it was found by the work of Moseley et al. that the ADC of Cerebrospinal Fluid (CSF) drops drastically in the event of ischemia [42, 43]. Because DWI is one of the few radiological techniques that can detect stroke in its acute phase, the importance of this technique is significant [44]. Some of the first studies also recognized the value of measuring the diffusion anisotropy for following brain maturation or mapping fiber orientation in the brain non-invasively [26, 31, 45–47].

### 1.3.4 The diffusion tensor model

As described in sections 1.3.2 and 1.3.3, diffusion can no longer be characterized by a single scalar for an anisotropic environment. However, the diffusion coefficient  $D(\mathbf{r})$  (or ADC), as obtained by DWI, can be generalized to the diffusion tensor  $\mathbf{D}(\mathbf{r})$  [see Eq. (1.2)] which allows one to describe the molecular mobility along any direction. During typical diffusion times in the order of 50 ms, water molecules in the brain move on average over distances of about  $10\mu\text{m}$ , probing the tissue structure at the microscopic level well beyond the usual image resolution. However, on a statistical basis, the overall effect can be observed within a DW image voxel with size in the order of several  $\text{mm}^3$ . With the advent of this tensor model, introduced by Basser et al., a rigorous formulation of the full 3D Gaussian diffusion process was established providing not only a quantitative measure for the amount diffusion anisotropy, but also the corresponding predominant directions of the water diffusion [6, 7, 9].



### 1.3.4.1 Acquisition and computation of the diffusion tensor

To compute the diffusion tensor  $\mathbf{D}(\mathbf{r})$ , several DW images along different non-collinear gradient directions  $\mathbf{g}_k$  ( $k = 1, \dots, N$ ) should be acquired [9, 48]. Since  $\mathbf{D}(\mathbf{r})$  is characterized by six degrees of freedom, at least six DW measurements  $S_k(\mathbf{r})$  ( $N = 6$ ) are needed, along with a reference image  $S_0(\mathbf{r})$  acquired without diffusion weighting. In general, the symmetric second-rank tensor  $\mathbf{D}(\mathbf{r})$  can be calculated for each voxel at position  $\mathbf{r}$  by solving the equation system

$$S_k(\mathbf{r}) = S_0(\mathbf{r}) e^{-b\hat{\mathbf{g}}_k^T \cdot \mathbf{D}(\mathbf{r}) \cdot \hat{\mathbf{g}}_k} \quad \text{with} \quad \hat{\mathbf{g}}_k = \frac{\mathbf{g}_k}{\|\mathbf{g}_k\|}, \quad (1.14)$$

which can be considered as the generalized anisotropic form of the Stejskal-Tanner relationship [see Eq. (1.12)], where the distribution  $p(\mathbf{r}|\mathbf{r}_0, \tau)$  for isotropic media in Eq. (1.11) has been extended for the general anisotropic case [23], i.e.

$$p(\mathbf{r}|\mathbf{r}_0, \tau) = \frac{1}{\sqrt{(4\pi\tau)^3 |\mathbf{D}|}} e^{-\frac{(\mathbf{r}-\mathbf{r}_0)^T \cdot \mathbf{D}^{-1} \cdot (\mathbf{r}-\mathbf{r}_0)}{4\tau}}, \quad (1.15)$$

where  $|\dots|$  represents the determinant. Note that for different gradient strengths  $\|\mathbf{g}_k\|$ , the  $b$ -value in Eq. (1.14) should also be generalized:

$$b_k = \gamma^2 \delta^2 \left( \Delta - \frac{\delta}{3} \right) \|\mathbf{g}_k\|^2. \quad (1.16)$$

The linear equation system described in Eq. (1.14) can also be represented in matrix form as follows:

$$\underbrace{\begin{bmatrix} (\hat{g}_{1x})^2 & 2\hat{g}_{1x}\hat{g}_{1y} & 2\hat{g}_{1x}\hat{g}_{1z} & (\hat{g}_{1y})^2 & \hat{g}_{1y}\hat{g}_{1z} & (\hat{g}_{1z})^2 \\ (\hat{g}_{2x})^2 & 2\hat{g}_{2x}\hat{g}_{2y} & 2\hat{g}_{2x}\hat{g}_{2z} & (\hat{g}_{2y})^2 & \hat{g}_{2y}\hat{g}_{2z} & (\hat{g}_{2z})^2 \\ \vdots & \vdots & \vdots & \vdots & \vdots & \vdots \\ (\hat{g}_{Nx})^2 & 2\hat{g}_{Nx}\hat{g}_{Ny} & 2\hat{g}_{Nx}\hat{g}_{Nz} & (\hat{g}_{Ny})^2 & \hat{g}_{Ny}\hat{g}_{Nz} & (\hat{g}_{Nz})^2 \end{bmatrix}}_{\mathbf{G}} \underbrace{\begin{bmatrix} D_{xx}(\mathbf{r}) \\ D_{xy}(\mathbf{r}) \\ D_{xz}(\mathbf{r}) \\ D_{yy}(\mathbf{r}) \\ D_{yz}(\mathbf{r}) \\ D_{zz}(\mathbf{r}) \end{bmatrix}}_{\tilde{\mathbf{D}}(\mathbf{r})} = \underbrace{\begin{bmatrix} \frac{1}{b} \ln \left( \frac{S_0(\mathbf{r})}{S_1(\mathbf{r})} \right) \\ \frac{1}{b} \ln \left( \frac{S_0(\mathbf{r})}{S_2(\mathbf{r})} \right) \\ \vdots \\ \frac{1}{b} \ln \left( \frac{S_0(\mathbf{r})}{S_N(\mathbf{r})} \right) \end{bmatrix}}_{\mathbf{B}(\mathbf{r})}. \quad (1.17)$$

For exactly six DW measurements ( $N = 6$ ), the unique diffusion tensor components can easily be calculated as:

$$\tilde{\mathbf{D}}(\mathbf{r}) = \mathbf{G}^{-1} \cdot \mathbf{B}(\mathbf{r}). \quad (1.18)$$

If more than six DW images are acquired, an over-constrained system of equations is obtained which can be solved by using Least Square (LS) methods [49, 50]. For example, applying the linear non-weighted LS approach, the diffusion tensor components can be calculated as:

$$\tilde{\mathbf{D}}(\mathbf{r}) = (\mathbf{G}^T \cdot \mathbf{G})^{-1} \cdot \mathbf{G}^T \cdot \mathbf{B}(\mathbf{r}). \quad (1.19)$$

In the work of Hasan et al., a comparison of different gradient encoding schemes has indicated that six gradient directions are sufficient in determining  $\mathbf{D}$  for practical use [51, 52]. On the other hand, over-determining the solution for  $\tilde{\mathbf{D}}(\mathbf{r})$  has the advantage to reduce the amount of noise propagating from the DW measurements into the calculated diffusion tensor [53, 54]. Moreover, based on Monte Carlo simulations, it has been shown that at least 20 unique gradient directions are necessary for a robust estimation of anisotropy, whereas at least 30 unique sampling orientations are required for a robust estimation of the tensor-orientation [55]. Self-evident drawbacks of acquiring more DW measurements are an increased acquisition and processing time.

In Fig. 1.3 (a), six axial DW measurements  $S_k(\mathbf{r})$  and one non-DW image  $S_0(\mathbf{r})$  are shown, along with the corresponding magnetic field gradients  $\mathbf{g}_k$  ( $k = 1, \dots, 6$ ). In general, measurements are made in the reference frame  $(x, y, z)$  of the MRI scanner gradients. Unfortunately, this frame does not coincide with the diffusion frame of the tissue. Therefore, one must also consider the coupling of the non-diagonal diffusion tensor elements (i.e.,  $\mathbf{D}_{ij}$  with  $i \neq j$  for  $i, j = x, y, z$ ) which reflect the correlation between the molecular displacements in perpendicular directions [Fig. 1.3 (b)]. Hence, it is important to note that by using diffusion-encoding gradient pulses along one direction, signal attenuation not only depends on the diffusion effects along this direction but may also include contributions from other directions.

### 1.3.4.2 Geometrical interpretation

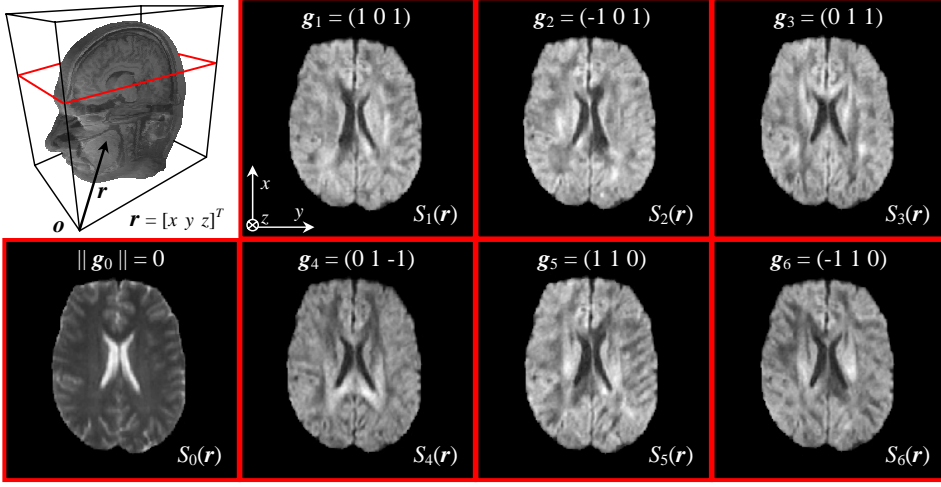
Let us reconsider the physical meaning of the diffusion tensor field  $\mathbf{D} = \mathbf{D}(\mathbf{r}, \tau)$  with diffusion time  $\tau$ . In DTI, it is assumed that the molecular diffusion can be characterized by the macroscopical Gaussian conditional probability density function  $p(\mathbf{r}|\mathbf{r}_0, \tau)$ , given by Eq. (1.15). From this equation, it is clear that the diffusion tensor field  $\mathbf{D}$  is in fact a covariance matrix describing the translational displacement of the diffusing molecules. Therefore, an ellipsoidal shape can be associated with  $\mathbf{D}$ , which represents the probabilistic iso-surface of this molecular diffusion. Since  $\mathbf{D}$  is a symmetric and positive definite second-rank tensor, a real eigenvalue decomposition can be derived:

$$\mathbf{D} = \mathbf{E} \cdot \mathbf{\Lambda} \cdot \mathbf{E}^{-1} , \quad (1.20)$$

with

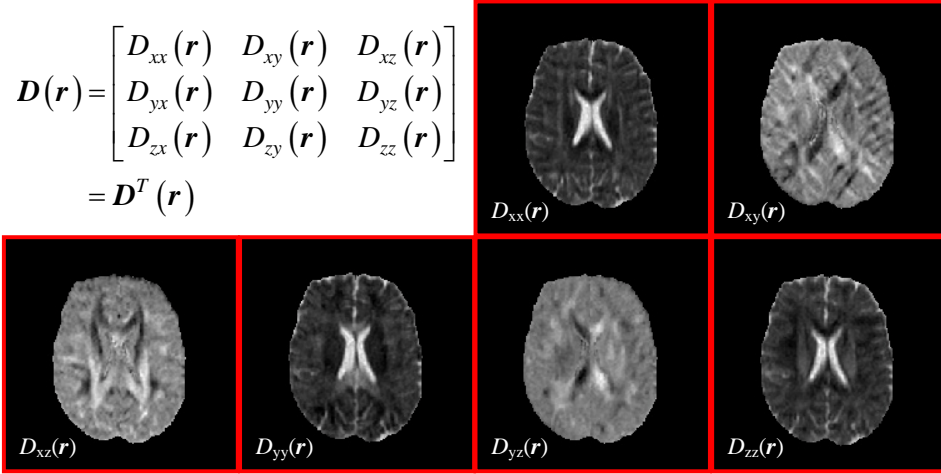
$$\mathbf{E} = [\mathbf{e}_1 \quad \mathbf{e}_2 \quad \mathbf{e}_3] \quad \text{and} \quad \mathbf{\Lambda} = \begin{bmatrix} \lambda_1 & 0 & 0 \\ 0 & \lambda_2 & 0 \\ 0 & 0 & \lambda_3 \end{bmatrix} \quad (1.21)$$

defining the matrix of orthonormal eigenvectors  $\mathbf{e}_i$  and the diagonal matrix of eigenvalues  $\lambda_i$  (with  $i = 1, 2, 3$ ), respectively [56]. Consequently, the principal axes



(a)

$$\begin{aligned}
 \mathbf{D}(\mathbf{r}) &= \begin{bmatrix} D_{xx}(\mathbf{r}) & D_{xy}(\mathbf{r}) & D_{xz}(\mathbf{r}) \\ D_{yx}(\mathbf{r}) & D_{yy}(\mathbf{r}) & D_{yz}(\mathbf{r}) \\ D_{zx}(\mathbf{r}) & D_{zy}(\mathbf{r}) & D_{zz}(\mathbf{r}) \end{bmatrix} \\
 &= \mathbf{D}^T(\mathbf{r})
 \end{aligned}$$



(b)

**Figure 1.3.** (a) Axial DW images  $S_k(\mathbf{r})$  of the human brain. Note the difference in intensity values for different gradient directions  $\mathbf{g}_k$ . (b) The corresponding six unique diffusion tensor components, as derived from Eq. (1.18).

of the ellipsoid and their corresponding principal diffusion coefficients are given by the eigenvectors  $\mathbf{e}_i$  and the eigenvalues  $\lambda_i$  of  $\mathbf{D}$ , respectively (Fig. 1.4).

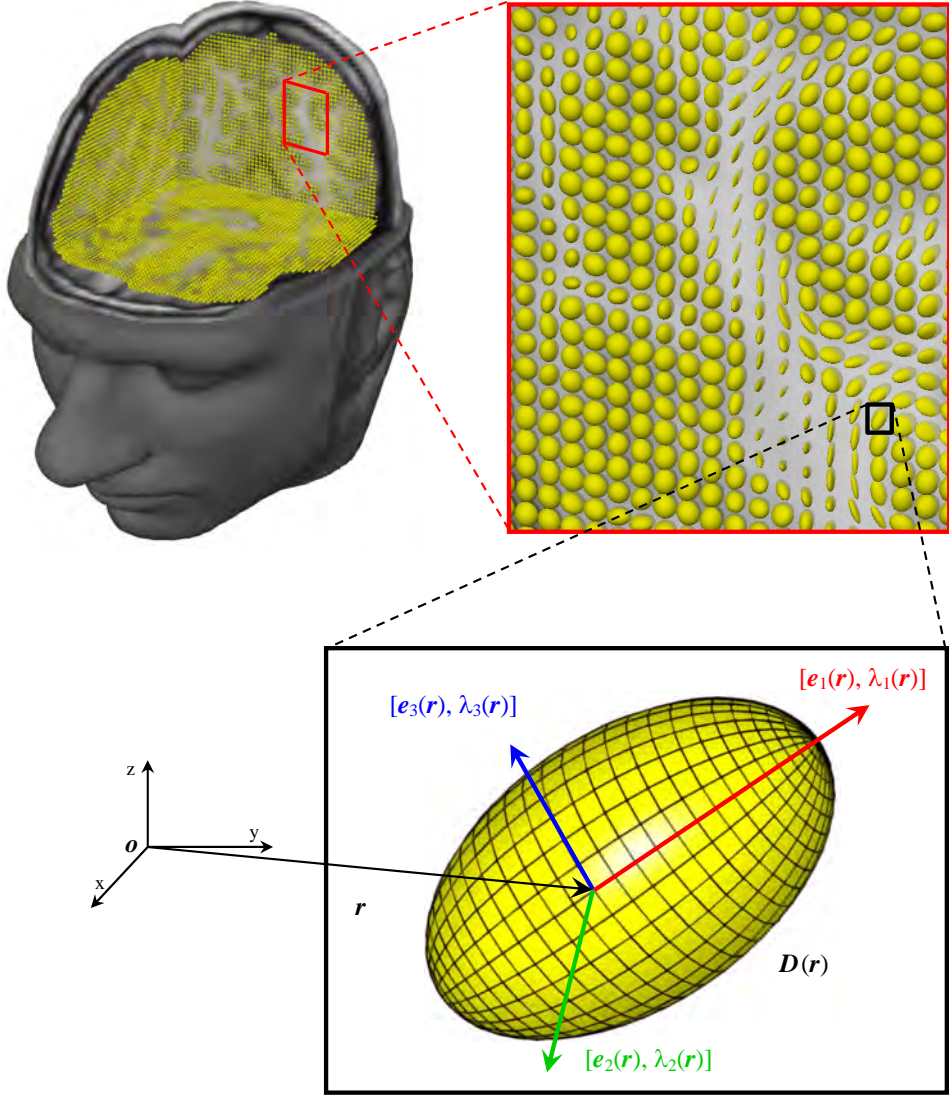


**Figure 1.4.** Ellipsoidal representation of the diffusion tensor field with a  $T_1$ -weighted background image. Note that every voxel (position  $\mathbf{r}$ ) of the data set is uniquely defined by the eigenvectors  $\mathbf{e}_i(\mathbf{r})$  and eigenvalues  $\lambda_i(\mathbf{r})$  of the diffusion tensor  $\mathbf{D}(\mathbf{r})$ .

In general, the eigenvalues and corresponding eigenvectors are sorted with the convention taken as follows:  $\lambda_1 > \lambda_2 > \lambda_3$  [57]. Consequently, the first eigenvector

$\mathbf{e}_1$  (i.e., corresponding with  $\lambda_1$ ) describes the predominant diffusion direction and is therefore also called the Principal Diffusion Vector (PDV) or Principal Diffusivity (PD). Recall that this PDV is assumed to be tangential to the orientation of the corresponding underlying fiber system. As shown in Fig. 1.5, this assumption appears to be valid, especially for large WM fiber structures (i.e.,  $\geq 2$ -3 voxel units in width). In addition, Fig. 1.5 elucidates the convenient color-encoding that can be provided by the components of the PDV [58]. In this way, the predominant diffusion direction can be directly related to a ‘Green’ (G), ‘Red’ (R), and ‘Blue’ (B) digital color triple. In literature, the convention in which the G, R, and, B color components represent the directions perpendicular to the coronal, sagittal, and axial 2D planes, respectively, is often applied, i.e.

$$[\|\mathbf{e}_{1x}\|, \|\mathbf{e}_{1y}\|, \|\mathbf{e}_{1z}\|] = [\text{G}, \text{R}, \text{B}] = [\perp \text{ coronal}, \perp \text{ sagittal}, \perp \text{ axial}] . \quad (1.22)$$

This color-encoding further improves the visibility of different WM fiber bundles.

#### 1.3.4.3 Scalar invariance measures

In addition to the directional information, as described in the previous section, several scalar measures can be extracted from the diffusion tensor which can provide supplementary information on the tissue microstructure, invariant to the applied coordinate system of the acquisition framework.

**Diffusion size** A first measure is the Mean Diffusivity (MD), which characterizes the overall mean-squared displacement of the water molecules. The MD can be calculated as:

$$MD(\mathbf{r}) \equiv MD = \frac{\text{Tr}[\mathbf{D}]}{3} = \frac{D_{xx} + D_{yy} + D_{zz}}{3} = \frac{\lambda_1 + \lambda_2 + \lambda_3}{3} = \langle \lambda \rangle , \quad (1.23)$$

where ‘Tr’ denotes the trace of the diffusion tensor [Fig. 1.6 (a)]. Note that the MD is an invariant, i.e. a quantity that is independent of the orientation of the applied reference frame [6, 7]. Geometrically, the MD can be considered as the average ellipsoid size.

**Diffusion anisotropy** During the last decade, several anisotropy measures have been proposed (e.g., [5, 61–66]). While all these measures attempt to quantify the degree of diffusion anisotropy, i.e. the amount directional diffusion dependence, they differ in their response curves and noise characteristics [67, 68]. Geometrically, the anisotropy can be considered as the eccentricity of the ellipsoid.

Among the most popular anisotropy indices, or at least the most prevalent, are two measures that are based on the normalized variance of the eigenvalues: the

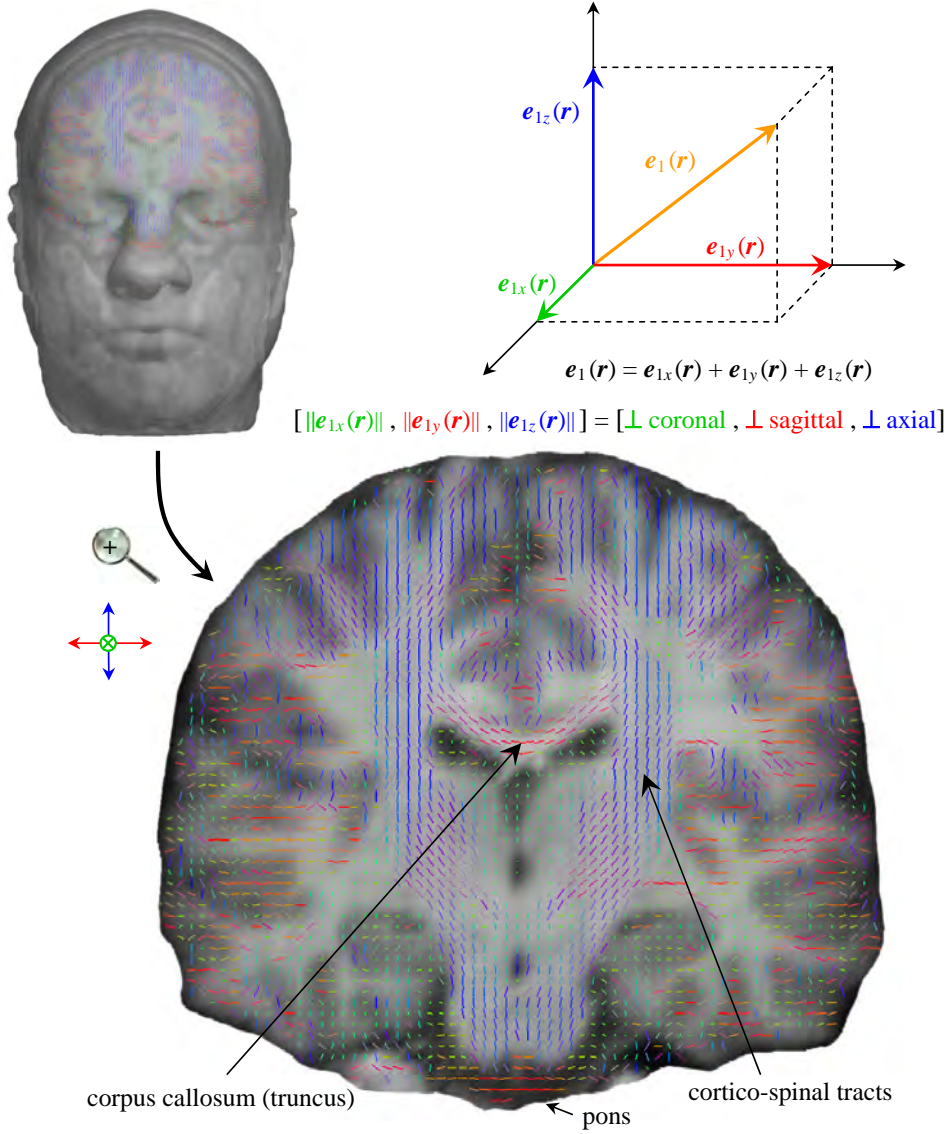


**Figure 1.5.** The principal diffusion vector (PDV) field, as described by the first eigenvector  $e_1(\mathbf{r})$ , with a  $T_1$ -weighted coronal background image. To improve the visibility of this PDV field, a color-encoding is provided reflecting the local direction of the PDV [58]. In addition, this color-encoding facilitates the distinction of different fiber structures. As an example, the ‘truncus of the Corpus Callosum (CC)’, the ‘pons’, and the ‘cortico-spinal tracts’ are indicated on the enlarged coronal slice.



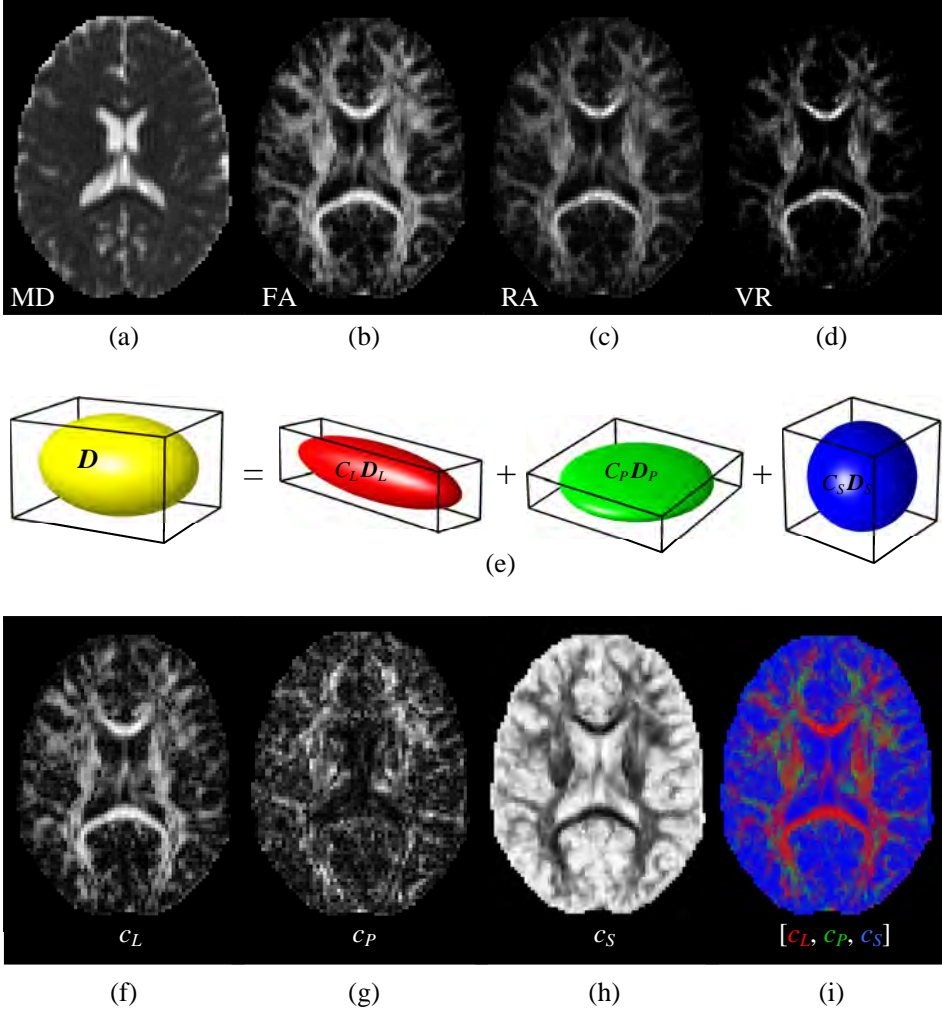


**Figure 1.6.** Scalar measures derived from the diffusion tensor  $D$ . In (a), the MD is shown for an axial slice. (b), (c), and (d) represent the corresponding FA, RA, and VR, respectively. The diffusion tensor decomposition into its geometric components, as developed by Westin et al. [59, 60], is shown in (e). After normalization of the linear (f), planar (g), and spherical (h) coordinates, a clear view of the different diffusion shapes, i.e. ‘cigar’ (red), ‘disc’ (green), and ‘sphere’ (blue), can be obtained (i).

Fractional Anisotropy (FA) and the Relative Anisotropy (RA), which are defined as [4, 9, 69, 70]:

$$FA(\mathbf{r}) \equiv FA = \frac{\sqrt{3[(\lambda_1 - \lambda_2)^2 + (\lambda_2 - \lambda_3)^2 + (\lambda_3 - \lambda_1)^2]}}{\sqrt{2(\lambda_1^2 + \lambda_2^2 + \lambda_3^2)}} \quad (1.24)$$

and

$$RA(\mathbf{r}) \equiv RA = \frac{\sqrt{(\lambda_1 - \lambda_2)^2 + (\lambda_2 - \lambda_3)^2 + (\lambda_3 - \lambda_1)^2}}{\lambda_1 + \lambda_2 + \lambda_3} . \quad (1.25)$$

Note that these measures range from zero (the isotropic case:  $\lambda_1 = \lambda_2 = \lambda_3$ ) to  $\sqrt{2}$  for RA and  $\sqrt{3}$  for FA (infinite anisotropy: e.g.,  $\lambda_1 \neq 0$  and  $\lambda_2 = \lambda_3 = 0$ ) [Fig. 1.6 (b,c)]. In general, these measures, and the measures discussed below, are mostly scaled a posteriori within the unit range  $[0, 1]$ .

Another anisotropy measure is the Volume Ratio (VR) [4, 9]:

$$VR(\mathbf{r}) \equiv VR = \frac{\lambda_1 \lambda_2 \lambda_3}{\langle \lambda \rangle^3} \quad (1.26)$$

and can be considered as the ratio of the tensor ellipsoid volume to the volume of a sphere with the same MD [Fig. 1.6 (d)].

In the work of Westin et al., linear ( $c_l$ ), planar ( $c_p$ ), and spherical ( $c_s$ ) anisotropy coefficients were introduced [59, 60], i.e.

$$c_l = \frac{\lambda_1 - \lambda_2}{3\langle \lambda \rangle} \quad ; \quad c_p = \frac{2(\lambda_2 - \lambda_3)}{3\langle \lambda \rangle} \quad ; \quad c_s = \frac{3\lambda_3}{3\langle \lambda \rangle} . \quad (1.27)$$

Other anisotropy indices introduced in literature are the ‘ultimate anisotropy’ measures [71], the ‘lattice index’ [70], and the Volume Fraction (VF) [70, 72]. Note that several of these anisotropy measures are directly related<sup>2</sup>, for example  $VF = 1 - VR$  and  $FA^2 = 3RA^2/(2RA^2 + 2)$  [67]. A report of diffusion anisotropy values characterizing several structures of the CNS can be found in Refs. [73, 74].

**Geometrical diffusion measures** In the work of Westin et al., a decomposition of the diffusion tensor is presented based on its symmetry properties [59, 60]. This decomposition provides useful quantitative measures describing the geometry of the diffusion ellipsoid and is elucidated next. Using Eq. (1.20), the diffusion tensor  $\mathbf{D}$  can generally be written as:

$$\mathbf{D} = \mathbf{E} \cdot \mathbf{\Lambda} \cdot \mathbf{E}^{-1} = \sum_{i=1}^3 \lambda_i \mathbf{e}_i \cdot \mathbf{e}_i^T . \quad (1.28)$$

<sup>2</sup>It is important to keep in mind that all orientation-independent anisotropy indices are calculated from the same eigenvalues and thus are intrinsically related to each other [71].



Depending on the interrelation of the eigenvalues  $\lambda_i$  of  $\mathbf{D}$ , diffusion can be divided into three different cases, i.e. linear diffusion (the cigar-shaped ellipsoid)

$$\lambda_1 \gg \lambda_2 \approx \lambda_3 \quad \rightarrow \quad \mathbf{D} \approx \lambda_1 \underbrace{\mathbf{e}_1 \cdot \mathbf{e}_1^T}_{\mathbf{D}_L}, \quad (1.29)$$

planar diffusion (the disc-shaped ellipsoid)

$$\lambda_1 \approx \lambda_2 \gg \lambda_3 \quad \rightarrow \quad \mathbf{D} \approx \lambda_1 \underbrace{\sum_{i=1}^2 \mathbf{e}_i \cdot \mathbf{e}_i^T}_{\mathbf{D}_P}, \quad (1.30)$$

and spherical diffusion (the sphere-shaped ellipsoid)

$$\lambda_1 \approx \lambda_2 \approx \lambda_3 \quad \rightarrow \quad \mathbf{D} \approx \lambda_1 \underbrace{\sum_{i=1}^3 \mathbf{e}_i \cdot \mathbf{e}_i^T}_{\mathbf{D}_S}. \quad (1.31)$$

In general, the diffusion tensor  $\mathbf{D}$  can be written as a linear combination of these specific cases, i.e.

$$\mathbf{D} = C_L \mathbf{D}_L + C_P \mathbf{D}_P + C_S \mathbf{D}_S. \quad (1.32)$$

The coefficients  $C_L$ ,  $C_P$ , and  $C_S$  in Eq. (1.32) represent the linear, planar, and spherical components of  $\mathbf{D}$ , respectively, and can be calculated by expanding  $\mathbf{D}$  using the new tensor basis elements  $\{\mathbf{D}_L, \mathbf{D}_P, \mathbf{D}_S\}$  [60]:

$$\begin{aligned} \mathbf{D} &= \sum_{i=1}^3 \lambda_i \mathbf{e}_i \cdot \mathbf{e}_i^T \\ &= \underbrace{[\lambda_1 - \lambda_2]}_{C_L} \underbrace{\mathbf{e}_1 \cdot \mathbf{e}_1^T}_{\mathbf{D}_L} + \underbrace{[\lambda_2 - \lambda_3]}_{C_P} \underbrace{\sum_{i=1}^2 \mathbf{e}_i \cdot \mathbf{e}_i^T}_{\mathbf{D}_P} + \underbrace{\lambda_3}_{C_S} \underbrace{\sum_{i=1}^3 \mathbf{e}_i \cdot \mathbf{e}_i^T}_{\mathbf{D}_S} \\ &= C_L \mathbf{D}_L + C_P \mathbf{D}_P + C_S \mathbf{D}_S. \end{aligned} \quad (1.33)$$

Note that in this new basis,  $\mathbf{D}$  can be classified according to its geometry, for now, the coordinates  $C_L$ ,  $C_P$ , and  $C_S$  describe how close the tensor is to the generic cases of a cigar-, disc-, and sphere-shaped diffusion tensor [Fig. 1.6 (e)]. Since  $C_L$ ,  $C_P$ , and  $C_S$  are calculated from the eigenvalues of the tensor, these geometric shape measures are rotationally invariant.

To obtain quantitative measures that characterize the diffusion shape, the coefficients  $C_L$ ,  $C_P$ , and  $C_S$  should be normalized. By using  $\lambda_1$  as normalization factor, a convenient color-encoding, analogous to Eq. (1.22), can be provided:

$$[c_L, c_P, c_S] = \left[ \frac{C_L}{\lambda_1}, \frac{C_P}{\lambda_1}, \frac{C_S}{\lambda_1} \right] = [\mathbf{R}, \mathbf{G}, \mathbf{B}] = [\text{'cigar'}, \text{'disc'}, \text{'sphere'}], \quad (1.34)$$

which is shown in Fig. 1.6 (f)→(i).

In Ref. [75], parametric and non-parametric statistical methods have been developed to provide additional powerful tools to analyse diffusion tensor data and the corresponding derived scalar measures.

## 1.4 Visualization of diffusion tensor fields

The major difficulty for DTI visualization is the high information content of the diffusion tensor field: in general, three Degrees Of Freedom (DOF) that describe the position in space and six DOF that characterize the diffusion information. Consequently, the big challenge in developing DTI visualization techniques is extracting the maximum amount of information, which may be dependent on the application, while preserving a clear overview.

It should be noted that in the engineering and computer science community, several tensor field visualization techniques have been developed previously for other research fields, such as material sciences and fluid dynamics (e.g., dielectric susceptibility, permittivity, strain and stress, conductivity, wave propagation, etc.), providing useful ‘starter’ tools for DTI visualization [76–78].

During the last decade, several visualization techniques for DTI have been proposed for extracting the relevant information contained in the diffusion tensor. In general, these methods can be divided into scalar maps, color-encoded maps, and glyphs, and are briefly reviewed in the following paragraphs.

### 1.4.1 Scalar maps

For many applications in DTI, it is often sufficient to extract a single scalar measure from the diffusion tensor, like the eigenvalues, the FA, or the MD (see e.g., [79–82]). These measures can simply be represented by a gray-valued or pseudo-color-encoded map. A few examples of these scalar maps are shown in Fig. 1.6 (a)→(d).

### 1.4.2 Color-encoded maps

Color-encoded maps have been developed to provide higher information contents, such as the predominant diffusion directions [45, 58, 83–88] and the geometric shape characteristics [59, 60, 72]. These images are constructed by relating the ‘R’, ‘G’, and ‘B’ color components with the specific characteristics of interest [see Eqs. (1.22)–(1.34) and Figs. 1.6 (i) and 1.7 (a,b)]. Note that the color images in 1.7 (a,b) are scaled with the corresponding FA maps to further facilitate the differentiation

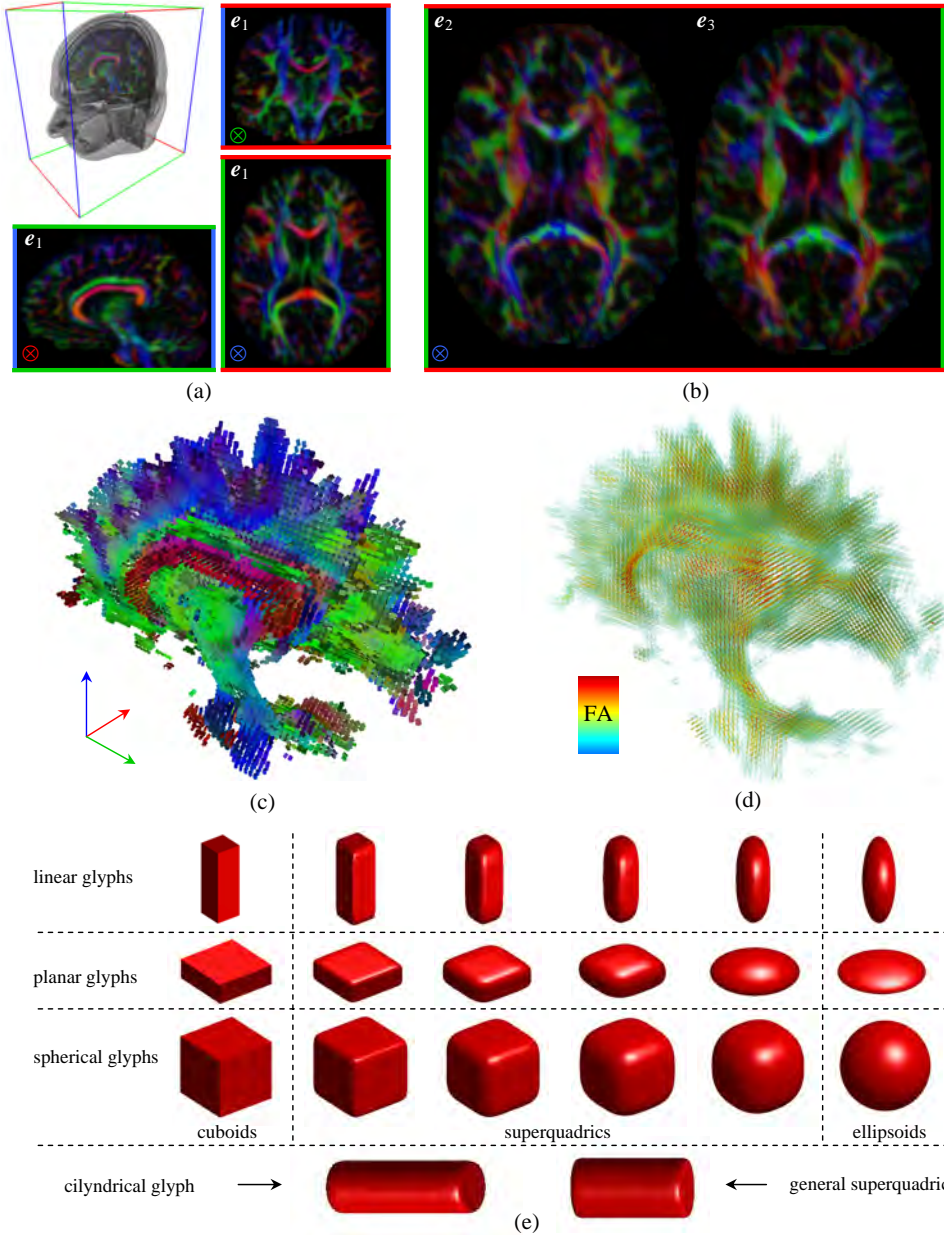


**Figure 1.7.** Color-encoded FA maps according to the PDV [Eq. 1.22] (a) and the other eigenvectors  $e_2$  and  $e_3$  (b) [86]. PDV color-encoded cuboids (c) and FA pseudo-color-encoded ellipsoids with transparency rendering (d) for voxels with  $FA > 0.3$  in the right hemisphere of the human brain. In (e), a general overview of superquadrics is given.

between WM fiber structures (bright colors) and gray matter (dark colors)<sup>3</sup>.

### 1.4.3 Glyphs

In general, a glyph can be considered as a symbolic object that describes the data information by its color, shape, texture, transparency, position, etc. These symbols can be lines, i.e. arrows without arrowheads due to the inherently bi-directional diffusion symmetry (Fig. 1.5) [89], cuboids [Fig. 1.7 (c)] [90], cylinders [91, 92], octahedra [93], ellipsoids [Figs. 1.4 and 1.7 (d)] [9, 70], and other objects, such as superquadrics [Fig. 1.7 (e)] [94–96], which try to combine the optimal visibility features of both cuboids and ellipsoids (i.e., smooth directions with sharp edges). In the work of Laidlaw et al. and Kindlmann et al. [97, 98], highly specialized rendering strategies have been developed, such as volume texture maps, to further enhance the display of the diffusion properties.

As shown in Fig. 1.7, several aspects of diffusion can be emphasized by combining glyphs with different color-encodings. In addition, transparency and threshold settings can further improve the visibility of the relevant diffusion information.

A more detailed description of visualizing diffusion tensor fields can be found in the work of Masutani et al. [99] and in the more recent survey of Vilanova et al. [100].

## 1.5 DTI Artifacts

In this section, a brief overview of the main artifacts in DTI is presented.

### 1.5.1 Subject motion

In general, subject motion can be divided into physiological motion (e.g., eye movements and pulsation of CSF) and ‘repositioning’ of the subject during data acquisition (e.g., rotation of the head or a large twitch). This latter can cause ghost artifacts or a spatial redistribution of the DW signal intensities. The geometric distortions can be corrected for by applying a uniform phase transformation to the entire image [101, 102]. In Refs. [103, 104], motion artifacts in DW images have been corrected using navigator echoes. Physiological motion artifacts on the other hand, can be mitigated by applying the inherently fast EPI-acquisition techniques and using cardiac-gated approaches [105, 106].

---

<sup>3</sup>However, note that this is a general observation and that specific WM tract configurations could also result in low FA values, and thus dark colors.

### 1.5.2 Eddy current distortions

As described previously, for the acquisition of DTI data sets, gradient fields are applied during the DW measurements. These large and rapidly switched gradients induce ‘eddy currents’ in the electrically conductive framework of the MRI scanner. The eddy currents produce additional undesirable magnetic fields which, in turn, result in the following unwanted effects:

1. A difference between the prescribed and the actual  $b$ -value will occur, since it is dependent on several gradient field properties which are now being modified by the eddy currents.
2. A slowly decaying magnetic gradient field, induced by the eddy currents, will cause geometrical distortions during readout of the DW images. This can easily be observed by the presence of high-valued anisotropy ‘rims’ in the phase-encode direction.

Both artifacts could adversely affect DTI studies. Quantitative parameters that are calculated from the diffusion tensor depend on the assumption that several gradient field parameters are constant during acquisition. This assumption is invalid for uncompensated image distortions and can therefore lead to a significant systematic deviation (bias) in the estimated diffusion parameters.

To compensate for these eddy current artifacts, correction schemes during acquisition can be applied [107, 108]. At the post-processing level, coregistration techniques have been used [48, 50, 91, 109–111] for correcting geometrical distortions (see Fig. 1.8).

It is important to note that, in addition to the spatial correction, the intensity values of the DW images should be adjusted [111]. Moreover, it has been shown that the signal variance in the interpolated images (after coregistration) differs significantly from the signal variance of the original images and should be taken into account in parameter estimation analyses [112]. Other post-processing techniques that correct for eddy current induced artifacts are calibration via water phantom images and modeling of the geometric distortions [113–115].

### 1.5.3 Image noise

Noise in DW images can introduce a significant bias in the estimates of quantitative diffusion parameters. Especially for higher diffusion weightings and reduced acquisition times<sup>4</sup>, which reduce the Signal-to-Noise Ratio (SNR), it is difficult to obtain reliable quantitative results.

<sup>4</sup>To remain clinically feasible, the effective acquisition time per DW measurement is smaller for an higher number of diffusion directions.

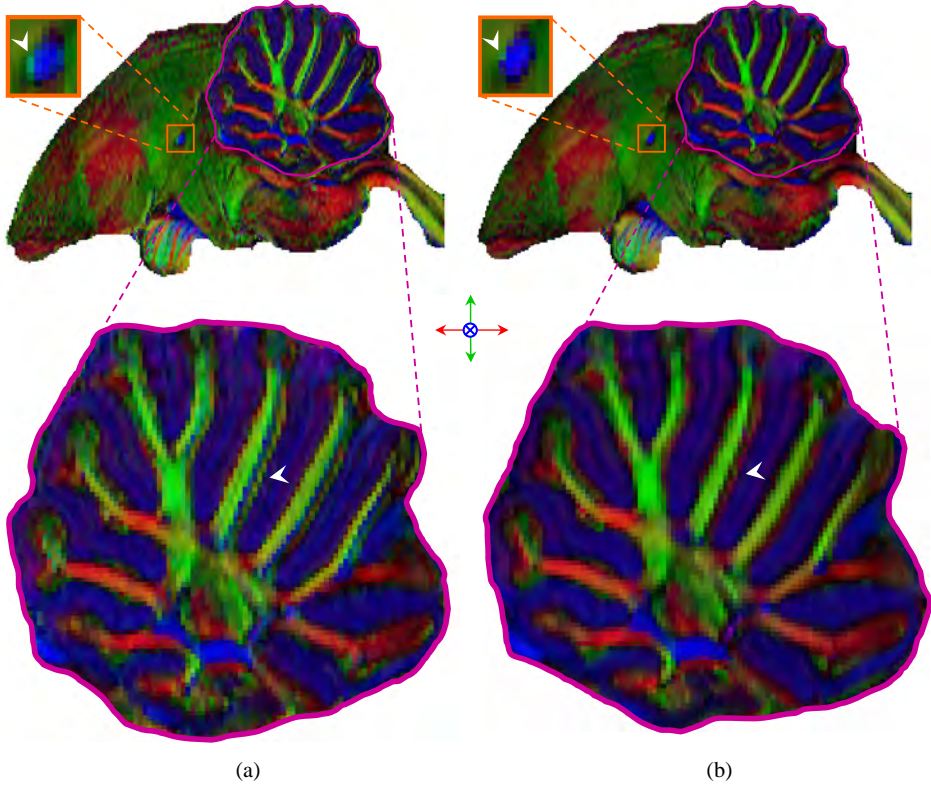


**Figure 1.8.** Sagittal PDV color-encoded FA maps of the starling brain, calculated from (a) the raw uncorrected and (b) the eddy current corrected DW data sets. In this example, the technique described in Ref. [111] was applied. As indicated by the arrowheads, the unwanted high FA ‘rims’ in (a) are no longer present in the corrected image (b).

It has been shown that noise in the DW images introduces errors in the estimation and sorting of the diffusion tensor eigenvalues and the derived anisotropy measures [116–122]. In addition, it has been described in the work of Pierpaoli et al. that image noise overestimates the anisotropy of both isotropic and anisotropic diffusion environments [70].

The simplest way to reduce the image noise is by employing more acquisition averages, diffusion gradient directions, or a combination of these. Regardless of the strategy, the scan time is always proportionally lengthened with an increased SNR.

A potential alternative for acquiring additional images is to apply post-processing noise-removal filtering and regularization techniques [91, 119, 123–134]. However, due to the low-pass nature of most smoothing filters, the SNR enhancement is often accompanied by spatial blurring, which may cause loss of fine structures and

exacerbate the PVE at tissue borders. Moreover, it has been shown in the work of Jones et al., that in voxel based morphometry analyses, the choice of filter size (within a commonly applied range) significantly affects the outcome of statistical inferences [135]. Therefore, depending on the application, noise-removal filtering should be performed with great care.

#### 1.5.4 Susceptibility artifacts

At tissue-air interfaces like regions adjacent to the sinuses, large discontinuities in magnetic susceptibility can occur, producing additional local magnetic field gradients [136, 137]. These field gradients cause geometrical distortions in the DW images and, in addition, make the  $b$ -values spatially dependent. Note that on higher field strength magnets (3 Tesla and above), susceptibility artifacts become more severe. The sensitivity encoding (SENSE) approach, developed by Bammer et al., appears to mitigate these artifacts [138]. In the work of Andersson et al., the distortions are minimized by acquiring two images for each diffusion gradient, which can provide information of the underlying displacement field [139].

A general survey discussing the aforementioned DTI artifacts in further detail can be found in an excellent review of Basser et al. [5].

## 1.6 Limitations

It is known that ambiguous results are obtained when DTI is used to study regions in which WM fibers cross or multiple fibers merge (e.g., Refs. [140, 141]). In such regions, it can be shown that the second-rank diffusion tensor model is incapable of describing multiple fiber orientations within an individual voxel [142]. The acquired signal of a single voxel can be considered as the powder-averaging of the differently oriented fiber structures. This effect, known as the Partial Volume Effect (PVE), is more apparent for small structures (in the order of a single voxel) or when using a coarse resolution, i.e. a large voxel size. Therefore, it is important to keep in mind that DTI is only valid for unidirectional fiber bundles that are large with respect to the voxel size.

To resolve the issue of multiple fiber orientations, a number of High-Angular-Resolution Diffusion (HARD) techniques have been proposed, such as multiple-component DTI [143], High-Angular-Resolution Diffusion-Weighted Imaging (HARDI) [144, 145], Q-Ball Imaging (QBI) [146–148], Diffusion Spectrum Imaging (DSI) [149, 150], Persistent Angular Structure (PAS) reconstruction [151], Generalized Diffusion Tensor Imaging (GDTI) [152–155], spherical deconvolution using HARDI [156], and a framework that combines hindered and restricted models of water diffusion [157–159]. Although these recently developed techniques might



provide more accurate and unambiguous results, long acquisition times or strong demands on the magnetic field gradient hardware still impede practical application in a clinical setting.

## 1.7 Applications

It is important to note that DTI is a truly quantitative imaging technique that can provide physical characteristics of biological tissue. Therefore, these characteristics can be objectively compared between different research centers and hospitals, which is indispensable for the further development of numerous DTI findings. In addition, DTI appeals to one's imagination: e.g., in the work of Schmithorst et al., differences in WM architecture between musicians and non-musicians were observed [160]. Findings like these demonstrate the sensitivity of DTI for differentiating populations with specific features. The objective of the following sections is to briefly summarize the different fields of DTI research and clinical applications. Excellent reviews describing several of these research fields in detail can be found in Refs. [12, 13, 65, 161–165].

### 1.7.1 Animal studies

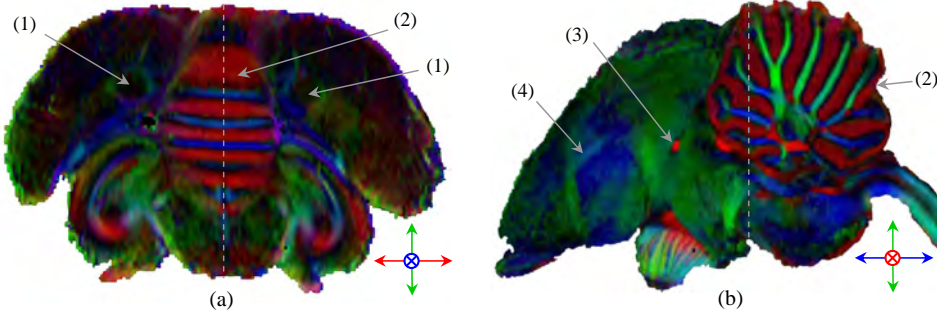
A large number of DTI animal studies have been performed providing exciting new insights in the fiber architecture of the bovine tongue [93], the spinal cord and the brain of both the mouse and the rat [84, 98, 166–179], the cat visual cortex [180], the primate brain (macaque, baboon) [181, 182], the myocardial architecture in the heart of the sheep and the swine [183, 184], and the songbird brain [185].

In the work of De Groof et al., the potentials of in vivo DTI were explored to visualize the major connections of the song control system in the brain of the starling (*sturnus vulgaris*) [185]. Several brain subdivisions and tract connections between important song control nuclei were observed, demonstrating the potential of DTI to investigate in vivo and non-invasively the neuroanatomy of the songbird brain (Fig. 1.9). It is expected that DTI will play an important role in the investigation of brain plasticity such as the seasonal changes in the structure and connections of these song control nuclei [186]. In addition, DTI can be considered as a complementary tool to Manganese Enhanced MRI (MEMRI) and functional MRI (fMRI) for studying the songbird brain [187–189].

### 1.7.2 Human studies

The amount of human research studies dealing with DTI has been soaring during the last decade, taking an important place within the burgeoning field of neuroimaging.





(1) robust nucleus of the arcopallium; (2) cerebellum; (3) commissura anterior; (4) lamina pallio-subpallialis

**Figure 1.9.** Coronal (a) and sagittal (b) FA map (with PDV color-encoding as indicated) of the starling brain. The dashed lines in (a) and (b) indicate the position of the cross-sectional maps in (b) and (a), respectively. In addition, several brain structures are depicted.

Although the exact mechanism for diffusion anisotropy is not well understood, it is clear that this anisotropy directly reflects the presence of spatially oriented structures in tissue. In addition, the degree of anisotropy, as measured with the various anisotropy indices which have been proposed in the literature, can somewhat be linked to the quality and the density of oriented structures in tissue. Therefore, it is assumed that a change in tissue orientation patterns inside a voxel would probably result in a change in the degree of anisotropy. This assumption has been supported by many clinical studies carried out on patients with WM diseases, in which DTI has shown to detect abnormalities at an early stage or to characterize them in terms of WM fiber integrity [12]. In the following paragraphs, several promising DTI applications are briefly summarized.

**The normal brain** DTI has already proven to be useful in the study of aging, [162, 165, 190–198], lateralization [87, 199–203], cognitive performance and reading ability [204–207], structure-function relation [208–210], and brain development in premature infants, ‘normal’ infants, children, adolescents, and adults [163, 211–220]. In addition, several WM fiber structures have been investigated in detail, such as the gyri [221, 222], the pyramidal tracts [223], the cranial nerves [224], and the thalamic nuclei [225].

**Brain pathology** DTI has been used to demonstrate subtle abnormalities in a variety of diseases and is currently becoming part of many routine clinical protocols. Several types of brain disorders have recently been investigated with DTI, such as schizophrenia [161, 200, 226–240], multiple sclerosis and amyotrophic lateral sclerosis [241–251], epilepsy [252–258], cognitive impairment and Alzheimer’s dis-

ease [259–264], COACH syndrome [265], Attention-Deficit Hyperactivity Disorder (ADHD) [266], fragile X syndrome [81], autism [267], velocardiofacial syndrome [268, 269], bipolar spectrum illnesses [270], Leber’s hereditary optic neuropathy [271], acute disseminated encephalomyelitis [272], Niemann-Pick Type C disease [273], Rett syndrome [274], Cerebral Autosomal Dominant Arteriopathy with Subcortical Infarcts and Leukoencephalopathy (CADASIL) [275, 276], Parkinson [277], pre-symptomatic Huntingtons disease [278], Wallerian degeneration [279, 280], optic neuritis [281], hemiparesis [282], and focal cortical dysplasia [283].

The application of DTI to infer WM characteristics has been reported in several other studies as well, such as presurgical planning for brain tumors [284–294], stroke and ischemic lesions [164, 295–301], Human Immunodeficiency Virus (HIV) [302–304], chronic alcoholism [194, 305, 306], hypertension [307], irradiation and chemotherapy [308, 309], marijuana smoking and cocaine dependence [310, 311], chronic head injury [312], blindness [313], postmortem formalin-fixed brain [314], cell density and proliferation activity of glioblastomas [315]. In addition, DTI may provide additional findings of central nervous system anomalies beyond those seen with conventional MRI [316]. An example of such a structural anomaly, i.e. callosal agenesis, is shown in Fig 1.10 (a). Note the difference with a normal brain [Fig. 1.10(b)] in the midsagittal region.

**Body** Although respiratory motion further complicates the DW data acquisitions, the potential of DTI to characterize tissue outside the brain has been shown as well, such as the heart [90, 317–320], the spinal cord [321, 322], peripheral nervous system [323–325], muscle tissue [326], the trabecular bone network [327, 328], and the eye lens [329].

## Bibliography

- [1] P.T. Callaghan. *Principles of nuclear magnetic resonance microscopy*. Clarendon Press, Oxford, 2nd edition, 1995.
- [2] C.P. Slichter. *Principles of magnetic resonance*. Springer, New York, 3rd edition, 1996.
- [3] R.H. Hashemi et al. *MRI: the basics*. Lippincott Williams and Wilkins, Philadelphia, 2nd edition, 2004.
- [4] P.J. Basser. Inferring microstructural features and the physiological state of tissues from diffusion-weighted images. *NMR Biomed*, 8(7–8):333–344, 1995.
- [5] P.J. Basser and D.K. Jones. Diffusion-tensor MRI: theory, experimental design and data analysis - a technical review. *NMR Biomed*, 15(7–8):456–467, 2002.
- [6] P.J. Basser et al. Estimation of the effective self-diffusion tensor from the NMR spin echo. *J Magn Reson B*, 103(3):247–254, 1994.
- [7] P.J. Basser et al. MR diffusion tensor spectroscopy and imaging. *Biophys J*, 66(1):259–267, 1994.
- [8] P.J. Basser et al. Diffusion tensor echo-planar imaging of human brain. In *SMRM*, page 584, New York, USA, 1993.

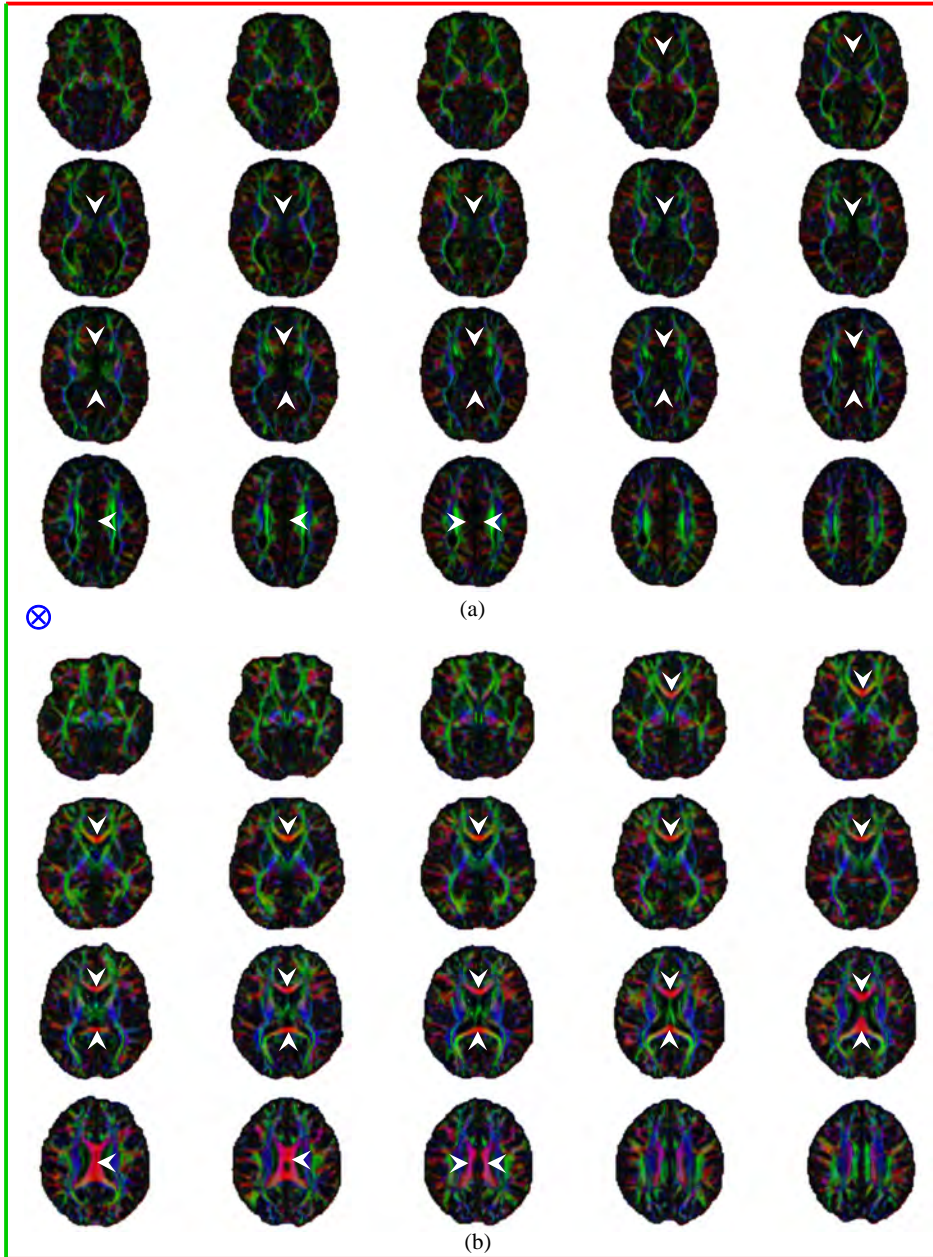


**Figure 1.10.** Axial FA maps (with PDV color-encoding as indicated) of the human brain. In (a) callosal agenesis can be observed, i.e. the missing of the corpus callosum (data provided by courtesy of Prof. Dr. P. Parizel). As indicated by the white arrowheads, a large difference in the midsagittal area can be observed between this rare structural anomaly (a) and the normal brain (b).

- [9] P.J. Basser and C. Pierpaoli. Microstructural and physiological features of tissues elucidated by quantitative-diffusion-tensor MRI. *J Magn Reson B*, 111(3):209–219, 1996.
- [10] P.J. Basser and C. Pierpaoli. A symplified method to measure the diffusion tensor from seven MR images. *Magn Reson Med*, 39(6):928–934, 1998.
- [11] C. Beaulieu. The basis of anisotropic water diffusion in the nervous system - a technical review. *NMR Biomed*, 15(7–8):435–455, 2002.
- [12] M.A. Horsfield and D.K. Jones. Applications of diffusion-weighted and diffusion tensor MRI to white matter diseases - a review. *NMR Biomed*, 15(7–8):570–577, 2002.
- [13] K.O. Lim and J.A. Helpert. Neuropsychiatric applications of DTI - a review. *NMR Biomed*, 15(7–8):587–593, 2002.
- [14] R. Brown. A brief account of microscopical observations made in the months of june, july, and august 1827 on the particles contained in the pollen of plants; and on the general existence of active molecules in organic and inorganic bodies. *Philosoph Mag*, 4:161–173, 1828.
- [15] A. Einstein. Über die von der molekularkinetischen Theorie der Wärme geforderte Bewegung von in ruhenden Flüssigkeiten suspendierten Teilchen. *Annal Phys*, 4:549–560, 1905.
- [16] D. Le Bihan. *Diffusion and perfusion magnetic resonance imaging. Applications to functional MRI*. Raven Press, New York, 1995.
- [17] L.D. Landau and E.M. Lifschitz. *Statistical physics*. Butterworth-Heinemann, 1999.
- [18] L. Onsager. Electric moments of molecules in liquids. *J Am Chem Soc*, 58:1486–1493, 1936.
- [19] H.C. Berg. *Random walks in biology*. Princeton University Press, Princeton, NJ, 1983.
- [20] A. Despopoulos and S. Silbernagl. *Taschenatlas der Physiologie*. Thieme Verlag, Stuttgart, Germany, 13 edition, 2001. ISBN 9055743038.
- [21] T.H. Williams et al. The human brain: dissections of the real brain. *Virtual Hospital, University of Iowa*, 1997. URL <http://www.vh.org/Providers/Textbooks/BrainAnatomy>.
- [22] H.Y. Carr and E.M. Purcell. Effects of diffusion on free precession in nuclear magnetic resonance experiments. *Phys Rev*, 94:630–638, 1954.
- [23] E.O. Stejskal and J.E. Tanner. Spin diffusion measurements: spin echoes in the presence of a time dependent field gradient. *J Chem Phys*, 42:288–292, 1965.
- [24] E.O. Stejskal and J.E. Tanner. Restricted self-diffusion of protons in colloidal systems by the pulsed-gradient, spin-echo method. *J Chem Phys*, 49:1768–1777, 1968.
- [25] H.C. Torrey. Bloch equations with diffusion terms. *Phys Rev*, 104:563–565, 1956.
- [26] D. Le Bihan. Molecular diffusion nuclear magnetic resonance imaging. *Magn Reson Q*, 7(1):1–30, 1991.
- [27] D.L. Thomas et al. The measurement of diffusion and perfusion in biological systems using magnetic resonance imaging. *Phys Med Biol*, 45(8):97–138, 2000.
- [28] R. Bammer. Basic principles of diffusion-weighted imaging. *Eur J Radiol*, 45(3):169–184, 2003.
- [29] M. Cercignani and M.A. Horsfield. The physical basis of diffusion-weighted MRI. *J Neurol*, 186(1):S11–S14, 2001.
- [30] R. Luytbaert et al. Diffusion and perfusion MRI: basic physics. *Eur J Radiol*, 38(1):19–27, 2001.
- [31] D. Le Bihan et al. MR imaging of intravoxel incoherent motions: application to diffusion and perfusion in neurologic disorders. *Radiology*, 161(2):401–407, 1986.
- [32] P. Mansfield. Multi-planar image formation using NMR spin echoes. *J Phys C*, 10:55–58, 1977.
- [33] P. Mansfield. Real-time echo-planar imaging by NMR. *Br Med Bull*, 40(2):187–190, 1984.
- [34] G.G. Cleveland et al. Nuclear magnetic resonance measurements of skeletal muscle: anisotropy of the diffusion coefficient of the intracellular water. *Biophys J*, 16(9):1043–

- 1053, 1976.
- [35] M.E. Moseley et al. Diffusion-weighted MR imaging of anisotropic water diffusion in cat central nervous system. *Radiology*, 176(2):439–445, 1990.
  - [36] T.L. Chenevert et al. Anisotropic diffusion within human white matter: demonstration with NMR techniques in vivo. *Radiology*, 177(2):401–405, 1990.
  - [37] G.J. Barker. Diffusion-weighted imaging of the spinal cord and optic nerve. *J Neurol Sci*, 186(1):S45–S49, 2001.
  - [38] J.V. Hajnal et al. MR imaging of anisotropically restricted diffusion of water in the nervous system: technical, anatomic, and pathologic considerations. *J Comput Assist Tomogr*, 15(1):1–18, 1991.
  - [39] F.A. Howe et al. Magnetic resonance neurography. *Magn Reson Med*, 28(2):328–338, 1992.
  - [40] M.D. King et al. Diffusion-weighted imaging of kainic acid lesions in the rat brain. *Magn Reson Med*, 20(1):158–164, 1991.
  - [41] M.E. Moseley et al. Anisotropy in diffusion-weighted MRI. *Magn Reson Med*, 19(2):321–326, 1991.
  - [42] M.E. Moseley et al. Early detection of regional cerebral ischemia in cats: comparison of diffusion- and T2-weighted MRI and spectroscopy. *Magn Reson Med*, 14(2):330–346, 1990.
  - [43] M.E. Moseley et al. Diffusion-weighted MR imaging of acute stroke: correlation with T2-weighted and magnetic susceptibility-enhanced MR imaging in cats. *AJNR Am J Neuroradiol*, 11(3):423–429, 1990.
  - [44] S. Warach et al. Fast magnetic resonance diffusion-weighted imaging of acute human stroke. *Neurology*, 42(9):1717–1723, 1992.
  - [45] P. Douek et al. MR color mapping of myelin fiber orientation. *J Comput Assist Tomogr*, 15(6):923–929, 1991.
  - [46] M.A. Rutherford et al. MR imaging of anisotropically restricted diffusion in the brain of neonates and infants. *J Comput Assist Tomogr*, 15(2):188–198, 1991.
  - [47] H. Sakuma et al. Adult and neonatal human brain: diffusional anisotropy and myelination with diffusion-weighted MR imaging. *Radiology*, 180(1):229–233, 1991.
  - [48] D.K. Jones et al. Optimal strategies for measuring diffusion in anisotropic systems by magnetic resonance imaging. *Magn Reson Med*, 42(3):515–525, 1999.
  - [49] L.-C. Chang et al. RESTORE: robust estimation of tensors by outlier rejection. *Magn Reson Med*, 53(5):1088–1095, 2005.
  - [50] J.-F. Mangin et al. Distortion correction and robust tensor estimation for MR diffusion imaging. *Med Image Anal*, 6(3):191–198, 2002.
  - [51] K.M. Hasan et al. Comparison of gradient encoding schemes for diffusion-tensor MRI. *J Magn Reson Imaging*, 13(5):769–780, 2001.
  - [52] K.M. Hasan et al. Magnetic resonance water self-diffusion tensor encoding optimization methods for full brain acquisition. *Image Anal & Stereol*, 21(2):87–96, 2002.
  - [53] N.G. Papadakis et al. Minimal gradient encoding for robust estimation of diffusion anisotropy. *Magn Reson Imaging*, 18(6):671–679, 2000.
  - [54] N.G. Papadakis et al. A comparative study of acquisition schemes for diffusion tensor imaging using MRI. *J Magn Reson*, 137(1):67–82, 1999.
  - [55] D.K. Jones. The effect of gradient sampling schemes on measures derived from diffusion tensor MRI: a Monte Carlo study. *Magn Reson Med*, 51(4):4607–4621, 2004.
  - [56] K.M. Hasan et al. Analytical computation of the eigenvalues and eigenvectors in DT-MRI. *J Magn Reson*, 152(1):41–47, 2001.
  - [57] K.M. Martin et al. The reduction of the sorting bias in the eigenvalues of the diffusion tensor. *Magn Reson Imaging*, 17(6):893–901, 1999.
  - [58] S. Pajevic and C. Pierpaoli. Color schemes to represent the orientation of anisotropic tissues



- from diffusion tensor data: application to white matter fiber tract mapping in the human brain. *Magn Reson Med*, 42(3):526–540, 1999.
- [59] C.-F. Westin et al. Image processing for diffusion tensor magnetic resonance imaging. In *MICCAI*, pages 441–452, 1999.
  - [60] C.-F. Westin et al. Processing and visualization for diffusion tensor MRI. *Med Image Anal*, 6(2):93–108, 2002.
  - [61] M.M. Bohn. Comparison of scalar measures used in magnetic resonance diffusion tensor imaging. *J Magn Reson*, 139(1):1–7, 1999.
  - [62] M.M. Bohn. Invariant and orthonormal scalar measures derived from magnetic resonance diffusion tensor imaging. *J Magn Reson*, 141(1):68–77, 1999.
  - [63] D. Le Bihan et al. Diffusion tensor imaging: concepts and applications. *J Magn Reson Imaging*, 13(4):534–546, 2001.
  - [64] D. Le Bihan and P. van Zijl. From the diffusion coefficient to the diffusion tensor. *NMR Biomed*, 15(7–8):431–434, 2002.
  - [65] W.D. Taylor et al. Diffusion tensor imaging: background, potential, and utility in psychiatric research. *Biol Psychiatry*, 55(3):201–207, 2004.
  - [66] R. Watts et al. Fiber tracking using magnetic resonance diffusion tensor imaging and its applications to human brain development. *Ment Retard Dev Disabil Res Rev*, 9(3):168–177, 2003.
  - [67] P.B. Kingsley and W.G. Monahan. Contrast-to-noise ratios of diffusion anisotropy indices. *Magn Reson Med*, 53(4):911–918, 2005.
  - [68] N.G. Papadakis et al. A study of rotationally invariant and symmetric indices of diffusion anisotropy. *Magn Reson Imaging*, 17(6):881–892, 1999.
  - [69] T.E. Conturo et al. Encoding of anisotropic diffusion with tetrahedral gradients: a general mathematical diffusion formalism and experimental results. *Magn Reson Med*, 35(3):399–412, 1996.
  - [70] C. Pierpaoli and P.J. Basser. Toward a quantitative assessment of diffusion anisotropy. *Magn Reson Med*, 36(6):893–906, 1996.
  - [71] A.M. Uluğ and P.C.M. van Zijl. Orientation-independent diffusion imaging without tensor diagonalization: anisotropy definitions based on physical attributes of the diffusion ellipsoid. *J Magn Reson Imaging*, 9(6):804–813, 1999.
  - [72] A.L. Alexander et al. A geometric analysis of diffusion tensor measurements of the human brain. *Magn Reson Med*, 44(2):283–291, 2000.
  - [73] H. Mamata et al. Characterization of central nervous system structures by magnetic resonance diffusion anisotropy. *Neurochem Int*, 45(4):553–560, 2004.
  - [74] J.S. Shimony et al. Quantitative diffusion-tensor anisotropy brain MR imaging: normative human data and anatomic analysis. *Radiology*, 212(3):770–784, 1999.
  - [75] S. Pajevic and P.J. Basser. Parametric and non-parametric statistical analysis of DT-MRI data. *J Magn Reson*, 161(1):1–14, 2003.
  - [76] T. Delmarcelle. *The visualization of second-order tensor fields*. PhD thesis, Stanford University, Stanford, CA, USA, 1994.
  - [77] H. Hagen et al. *Scientific visualization - overview, methodologies and techniques*, chapter Visualization of deformation tensor fields, pages 357–371. IEEE Computer Society Press, 1997. ISBN 0-818-67777-5.
  - [78] L. Hesselink et al. Research issues in vector and tensor field visualization. *IEEE CG&A*, 14(2):76–79, 1994.
  - [79] O. Abea et al. Normal aging in the central nervous system: quantitative MR diffusion-tensor analysis. *Neurobiol Aging*, 23(3):433–441, 2002.
  - [80] I. Agartz et al. Abnormal brain white matter in schizophrenia: a diffusion tensor imaging

- study. *NeuroReport*, 12(10):2251–2254, 2001.
- [81] N. Barnea-Goraly et al. White matter tract alterations in fragile X syndrome: preliminary evidence from diffusion tensor imaging. *Am J Med Genet*, 118(1):81–88, 2003.
  - [82] P. van Gelderen et al. Water diffusion and acute stroke. *Magn Reson Med*, 31(2):154–163, 1994.
  - [83] J. Coremans et al. A method for myelin fiber orientation mapping using diffusion-weighted MR images. *Magn Reson Imaging*, 12(3):443–454, 1994.
  - [84] B.A. Inglis et al. Diffusion anisotropy in excised normal rat spinal cord measured by NMR microscopy. *Magn Reson Imaging*, 15(4):441–450, 1997.
  - [85] D. Jones et al. Full representation of white-matter fibre direction on one map via diffusion tensor analysis. In *ISMRM*, page 1743, 1997.
  - [86] M. Lazar et al. Axial asymmetry of water diffusion in brain white matter. *Magn Reson Med*, 54(4):860–867, 2005.
  - [87] S. Peled et al. Magnetic resonance imaging shows orientation and asymmetry of white matter fiber tracts. *Brain Res*, 780(1):27–33, 1998.
  - [88] C. Pierpaoli. Oh no! one more method for color mapping of fiber tract direction using diffusion MR imaging data. In *ISMRM*, page 1741, 1997.
  - [89] H. Mamata et al. High-resolution line scan diffusion tensor MR imaging of white matter fiber tract anatomy. *AJNR Am J Neuroradiol*, 23(1):67–75, 2002.
  - [90] L. Zhukov and A.H. Barr. Heart-muscle fiber reconstruction from diffusion tensor MRI. In *IEEE Vis*, 2003.
  - [91] C. Poupon et al. Regularization of MR diffusion tensor maps for tracking brain white matter bundles. *Lect Notes Comp Sci*, 1496:489–498, 1998.
  - [92] M.R. Wiegell et al. Fiber crossing in human brain depicted with diffusion tensor MR imaging. *Radiology*, 217(3):897–903, 2000.
  - [93] V.J. Wedeen et al. Demonstration of primary and secondary muscle fiber architecture of the bovine tongue by diffusion tensor magnetic resonance imaging. *Biophys J*, 80(2):1024–1028, 2001.
  - [94] A. Barr. Superquadrics and angle-preserving transformations. *IEEE CG&A*, 18:11–23, 1981.
  - [95] D.B. Ennis et al. Visualization of tensor fields using superquadric glyphs. *Magn Reson Med*, 53(1):169–176, 2005.
  - [96] G. Kindlmann et al. Strategies for direct volume rendering of diffusion tensor fields. *IEEE T Vis Comput Gr*, 6(2):124–138, 2000.
  - [97] G. Kindlmann and D. Weinstein. Hue-balls and lit-tensors for direct volume rendering of diffusion tensor fields. In *IEEE Vis*, pages 183–189, 1999.
  - [98] D.H. Laidlaw et al. Visualizing diffusion tensor images of the mouse spinal cord. In *IEEE Vis*, pages 127–134, Los Alamitos, CA, USA, 1998. IEEE Computer Society Press.
  - [99] Y. Masutani et al. MR diffusion tensor imaging: recent advance and new techniques for diffusion tensor visualization. *Eur J Radiol*, 46(1):53–66, 2003.
  - [100] A. Vilanova et al. *Visualization and image processing of tensor fields*, chapter An introduction to visualization of diffusion tensor imaging and its applications, pages 121–153. Springer Verlag series Mathematics and Visualization, 2006. ISBN 3-540-25032-8.
  - [101] A.W. Anderson and C.J. Gore. Analysis and correction of motion artifacts in diffusion weighted imaging. *Magn Reson Med*, 32(3):379–387, 1994.
  - [102] K.L. Miller and J.M. Pauly. Nonlinear phase correction for navigated diffusion imaging. *Magn Reson Med*, 50(2):343–353, 2003.
  - [103] R.J. Ordidge et al. Correction of motional artifacts in diffusion-weighted MR images using navigator echoes. *J Am Chem Soc*, 12(3):455–460, 1994.

- [104] J.-J. Wang et al. Selective averaging for the diffusion tensor measurement. *Magn Reson Imaging*, 23(4):585–590, 2005.
- [105] C. Pierpaoli et al. Analyzing the contribution of cardiac pulsation to the variability of quantities derived from the diffusion tensor. In *ISMRM*, page 70, 2003.
- [106] S. Skare and J.L.R. andersson. On the effects of gating in diffusion imaging of the brain using single shot EPI. *Magn Reson Imaging*, 19(8):1125–1128, 2001.
- [107] A.L. Alexander et al. Elimination of eddy current artifacts in diffusion-weighted echo-planar images: the use of bipolar gradients. *Magn Reson Med*, 38(6):1016–1021, 1997.
- [108] N.G. Papadakis et al. Gradient pre-emphasis calibration in diffusion weighted echo-planar imaging. *Magn Reson Med*, 44(4):616–624, 2000.
- [109] M.E. Bastin. Correction of eddy current-induced artefacts in diffusion tensor imaging using iterative cross-correlation. *Magn Reson Imaging*, 17(7):1011–1024, 1999.
- [110] J.F. Nielsen et al. Affine and polynomial mutual information coregistration for artifact elimination in diffusion tensor imaging of newborns. *Magn Reson Imaging*, 22(9):1319–1323, 2004.
- [111] G.K. Rohde et al. Comprehensive approach for correction of motion and distortion in diffusion-weighted MRI. *Magn Reson Med*, 51(1):103–114, 2004.
- [112] G.K. Rohde et al. Estimating intensity variance due to noise in registered images: applications to diffusion tensor MRI. *NeuroImage*, 26(3):673–684, 2005.
- [113] M.E. Bastin. On the use of the FLAIR technique to improve the correction of eddy current induced artefacts in MR diffusion tensor imaging. *Magn Reson Imaging*, 19(7):937–950, 2001.
- [114] M.E. Bastin and P.A. Armitage. On the use of water phantom images to calibrate and correct eddy current induced artefacts in MR diffusion tensor imaging. *Magn Reson Imaging*, 18(6):681–687, 2000.
- [115] P. Jezzard et al. Characterization of and correction for eddy current artifacts in echo planar diffusion imaging. *Magn Reson Med*, 39(5):801–812, 1998.
- [116] A.W. Anderson. Theoretical analysis of the effects of noise on diffusion tensor imaging. *Magn Reson Med*, 46(6):1174–1188, 2001.
- [117] P.J. Basser and S. Pajevic. Statistical artifacts in diffusion tensor MRI (DT-MRI) caused by background noise. *Magn Reson Med*, 44(1):41–50, 2000.
- [118] M.E. Bastin et al. A theoretical study of the effect of experimental noise on the measurement of anisotropy in diffusion imaging. *Magn Reson Imaging*, 16(7):773–785, 1998.
- [119] B. Chen and E.W. Hsu. Noise removal in magnetic resonance diffusion tensor imaging. *Magn Reson Med*, 54(2):393–407, 2005.
- [120] D.K. Jones and P.J. Basser. “squashing peanuts and smashing pumpkins”: how noise distorts diffusion-weighted MR data. *Magn Reson Med*, 52(5):979–993, 2004.
- [121] S. Skare et al. Condition number as a measure of noise performance of diffusion tensor data acquisition schemes with MRI. *J Magn Reson*, 147(2):340–352, 2000.
- [122] S. Skare et al. Noise considerations in the determination of diffusion tensor anisotropy. *Magn Reson Imaging*, 18(6):659–669, 2000.
- [123] A. Aldroubi and P. Basser. Reconstruction of vector and tensor field from sampled discrete data. *Contemp Math*, 247:1–15, 1999.
- [124] J.-M. Bonny and J.-P. Renou. Euclidian distance-weighted smoothing for quantitative MRI: application to intervoxel anisotropy index mapping with DTI. *J Magn Reson*, 159(2):183–189, 2002.
- [125] O. Coulon et al. A regularization scheme for diffusion tensor magnetic resonance images. *Lect Notes Comp Sci*, 2082:92–105, 2001.
- [126] O. Coulon et al. Diffusion tensor magnetic resonance image regularization. *Med Image*



- Anal*, 8(1):47–67, 2004.
- [127] J. Frandsen et al. Regularization of diffusion tensor fields in axonal fibre tracking. In *ISMRM*, page 1221, 2004.
  - [128] W. Li et al. Tensor field regularization for diffusion tensor MR images using nonlinear smoothing. In *ISMRM*, page 1222, 2004.
  - [129] T. McGraw et al. DT-MRI denoising and neuronal fiber tracking. *Med Image Anal*, 8(2): 95–111, 2004.
  - [130] S. Pajevic et al. A continuous tensor field approximation of discrete DT-MRI data for extracting microstructural and architectural features of tissue. *J Magn Reson*, 154(1): 85–100, 2002.
  - [131] G.J.M. Parker et al. Nonlinear smoothing for reduction of systematic and random errors in diffusion tensor imaging. *J Magn Reson Imaging*, 11(6):702–710, 2000.
  - [132] C. Poupon et al. Regularization of diffusion-based direction maps for the tracking of brain white matter fascicles. *NeuroImage*, 12(2):184–195, 2000.
  - [133] B.C. Vemuri et al. Fiber tract mapping from diffusion tensor MRI. In *IEEE VLSM*, 2001.
  - [134] Z. Wang et al. A constrained variational principle for direct estimation and smoothing of the diffusion tensor field from complex DWI. *IEEE Trans Med Imaging*, 23(8):930–939, 2004.
  - [135] D.K. Jones et al. The effect of filter size on VBM analyses of DT-MRI data. *NeuroImage*, 26(2):546–554, 2005.
  - [136] C.A. Clark et al. An in vivo evaluation of the effects of local magnetic susceptibility-induced gradients on water diffusion measurements in human brain. *J Magn Reson*, 141(1):52–61, 1999.
  - [137] F. Farzaneh et al. Analysis of T2 limitations and off-resonance effects on spatial resolution and artifacts in echo-planar imaging. *Magn Reson Med*, 14(1):123–139, 1990.
  - [138] R. Bammer et al. Improved diffusion-weighted single-shot echo-planar imaging (EPI) in stroke using sensitivity encoding (SENSE). *Magn Reson Med*, 46(3):548–554, 2001.
  - [139] J.L.R. Andersson et al. How to correct susceptibility distortions in spin-echo echo-planar images: application to diffusion tensor imaging. *NeuroImage*, 20(2):870–888, 2003.
  - [140] A.L. Alexander et al. Analysis of partial volume effects in diffusion-tensor MRI. *Magn Reson Med*, 45(5):770–780, 2001.
  - [141] R. Bammer et al. In vivo MR tractography using diffusion imaging. *Eur J Radiol*, 45(3): 223–234, 2003.
  - [142] D.C. Alexander et al. Detection and modeling of non-Gaussian apparent diffusion coefficient profiles in human brain data. *Magn Reson Med*, 48(2):331–340, 2002.
  - [143] E.L. Bossart et al. Multiple component diffusion tensor imaging in excised fixed CNS tissue. In *ISMRM*, page 328, 1999.
  - [144] L.R. Frank. Anisotropy in high angular resolution diffusion-weighted MRI. *Magn Reson Med*, 45(6):935–939, 2001.
  - [145] D.S. Tuch et al. High angular resolution diffusion imaging of the human brain. In *ISMRM*, page 321, 1999.
  - [146] D.S. Tuch. Q-ball imaging. *Magn Reson Med*, 52(6):1358–1372, 2004.
  - [147] D.S. Tuch et al. Diffusion MRI of complex neural architecture. *Neuron*, 40(5):885–895, 2003.
  - [148] D.S. Tuch et al. Q-ball imaging of macaque white matter architecture. *Philos Trans R Soc Lond B Biol Sci*, 360(1457):869–879, 2005.
  - [149] D.S. Tuch et al. Measuring cortico-cortical connectivity matrices with diffusion spectrum imaging. In *ISMRM*, page 502, 2001.
  - [150] V.J. Wedeen et al. Mapping fibre orientation spectra in cerebral white matter with fourier-

- transform diffusion MRI. In *ISMRM*, page 82, 2000.
- [151] K.M. Jansons and D.C. Alexander. Persistent angular structure: new insights from diffusion magnetic resonance imaging data. *Inverse Probl*, 19:1031–1046, 2003.
  - [152] C. Liu et al. Generalized diffusion tensor imaging (GDTI) using higher-order tensor (HOT) statistics. In *ISMRM*, page 242, 2003.
  - [153] C. Liu et al. Characterizing non-Gaussian diffusion by using generalized diffusion tensors. *Magn Reson Med*, 51(5):924–937, 2004.
  - [154] E. Özarslan and T.H. Mareci. Generalized diffusion tensor imaging and analytical relationships between diffusion tensor imaging and high angular resolution diffusion imaging. *Magn Reson Med*, 50(5):955–965, 2003.
  - [155] E. Özarslan et al. Generalized scalar measures for diffusion MRI using trace, variance, and entropy. *Magn Reson Med*, 53(4):866–876, 2005.
  - [156] J.-D. Tournier et al. Direct estimation of the fiber orientation density function from diffusion-weighted MRI data using spherical deconvolution. *NeuroImage*, 23(3):1176–1185, 2004.
  - [157] Y. Assaf and P.J. Basser. Composite hindered and restricted model of diffusion (CHARMED) MR imaging of the human brain. *NeuroImage*, 27(1):48–58, 2005.
  - [158] Y. Assaf et al. New modeling and experimental framework to characterize hindered and restricted water diffusion in brain white matter. *Magn Reson Med*, 52(5):965–978, 2004.
  - [159] P.N. Sen and P.J. Basser. Modeling diffusion in white matter in the brain: A composite porous medium. *Magn Reson Imaging*, 23(2):215–220, 2005.
  - [160] V.J. Schmithorst and M. Wilke. Differences in white matter architecture between musicians and non-musicians: a diffusion tensor imaging study. *Neurosci Lett*, 321(1–2):57–60, 2002.
  - [161] M. Kubicki et al. A review of diffusion tensor imaging studies in schizophrenia. *J Psychiatr Res*, (in press) 2005.
  - [162] M. Moseley. Diffusion tensor imaging and aging - a review. *NMR Biomed*, 15(7–8):553–560, 2002.
  - [163] J. Neil et al. Diffusion tensor imaging of normal and injured developing human brain - a technical review. *NMR Biomed*, 15(7–8):543–552, 2002.
  - [164] C.H. Sotak. The role of diffusion tensor imaging in the evolution of ischemic brain injury - a review. *NMR Biomed*, 15(7–8):561–569, 2002.
  - [165] E.V. Sullivan and A. Pfefferbaum. Diffusion tensor imaging in normal aging and neuropsychiatric disorders. *Eur J Radiol*, 45(3):244–255, 2003.
  - [166] I. Elshafiey et al. In vivo diffusion tensor imaging of rat spinal cord at 7 T. *Magn Reson Imaging*, 20(3):243–247, 2002.
  - [167] B.A. Inglis et al. Diffusion tensor MR imaging and comparative histology of glioma engrafted in the rat spinal cord. *AJNR Am J Neuroradiol*, 20(4):713–716, 1999.
  - [168] J.H. Kim et al. Detecting axon damage in spinal cord from a mouse model of multiple sclerosis. *Neurobiol Dis*, 21(3):626–632, 2006.
  - [169] W.-T. Lee and C. Chang. Magnetic resonance imaging and spectroscopy in assessing 3-nitropropionic acid-induced brain lesions: an animal model of Huntington’s disease. *Prog Neurobiol*, 72(2):87–110, 2004.
  - [170] C.-Y. Lin et al. Unsupervised identification of white matter tracts in a mouse brain using a directional correlation-based region growing (DCRG) algorithm. *NeuroImage*, 28(2):380–388, 2005.
  - [171] G. Nair et al. Myelination and long diffusion times alter diffusion-tensor-imaging contrast in myelin-deficient shiverer mice. *NeuroImage*, 28(1):165–174, 2005.
  - [172] T. Numano et al. In vivo isotropic 3D diffusion tensor mapping of the rat brain using diffusion-weighted 3D MP-RAGE MRI. *Magn Reson Imaging*, (in press) 2006.

- [173] S.-K. Song et al. Dysmyelination revealed through MRI as increased radial (but unchanged axial) diffusion of water. *NeuroImage*, 17(3):1429–1436, 2002.
- [174] S.-K. Song et al. Diffusion tensor imaging detects age-dependent white matter changes in a transgenic mouse model with amyloid deposition. *Neurobiol Dis*, 15(3):640–647, 2004.
- [175] S.-K. Song et al. Diffusion tensor imaging detects and differentiates axon and myelin degeneration in mouse optic nerve after retinal ischemia. *NeuroImage*, 20(3):1714–1722, 2003.
- [176] S.-K. Song et al. Demyelination increases radial diffusivity in corpus callosum of mouse brain. *NeuroImage*, 26(1):132–140, 2005.
- [177] S.-W. Sun et al. Detection of age-dependent brain injury in a mouse model of brain amyloidosis associated with Alzheimer’s disease using magnetic resonance diffusion tensor imaging. *Exp Neurol*, 191(1):77–85, 2005.
- [178] J. Zhang et al. Three-dimensional anatomical characterization of the developing mouse brain by diffusion tensor microimaging. *NeuroImage*, 20(3):1639–1648, 2003.
- [179] J. Zhang et al. Three-dimensional diffusion tensor magnetic resonance microimaging of adult mouse brain and hippocampus. *NeuroImage*, 15(4):892–901, 2002.
- [180] D.-S. Kim et al. In vivo mapping of functional domains and axonal connectivity in cat visual cortex using magnetic resonance imaging. *Magn Reson Imaging*, 21(10):1131–1140, 2003.
- [181] C.D. Kroenke et al. Diffusion MR imaging characteristics of the developing primate brain. *NeuroImage*, 26(8):2137–2143, 2005.
- [182] G.J.M. Parker et al. Initial demonstration of in vivo tracing of axonal projections in the macaque brain and comparison with the human brain using diffusion tensor imaging and fast marching tractography. *NeuroImage*, 15(4):779–809, 2002.
- [183] Walker J.C. et al. Helical myofiber orientation after myocardial infarction and left ventricular surgical restoration in sheep. *J Thorac Cardiovasc Surg*, 129(2):243–245, 2005.
- [184] P. Schmid et al. Ventricular myocardial architecture as visualised in postmortem swine hearts using magnetic resonance diffusion tensor imaging. *Eur J Cardiothoracic Surg*, 27(3):468–474, 2005.
- [185] G. De Groof et al. In vivo diffusion tensor imaging (DTI) of brain subdivisions and vocal pathways in songbirds. *NeuroImage*, 29(3):754–763, 2006.
- [186] G. De Groof et al. Seasonal changes in neuronal connectivity in the songbird brain discerned by repeated in vivo DTI. In *ISMRM*, page 715, 2005.
- [187] A. Van der Linden et al. Applications of manganese-enhanced magnetic resonance imaging (MEMRI) to image brain plasticity in song birds. *NMR Biomed*, 17(8):602–612, 2004.
- [188] V. Van Meir et al. Spatiotemporal properties of the BOLD response in the songbirds’ auditory circuit during a variety of listening tasks. *NeuroImage*, 25(4):1242–1255, 2005.
- [189] V. Van Meir et al. Differential effects of testosterone on neuronal populations and their connections in a sensorimotor brain nucleus controlling song production in songbirds: a manganese enhanced magnetic resonance imaging study. *NeuroImage*, 21(3):914–923, 2004.
- [190] J. Krejza and E.R. Melhem. Quantitative diffusion tensor imaging of the brain in young adults shows age-related structural changes in gray and white matter. *Acad Radiol*, 12(3):265–267, 2005.
- [191] D.J. Madden et al. Diffusion tensor imaging of adult age differences in cerebral white matter: relation to response time. *NeuroImage*, 21(3):1174–1181, 2004.
- [192] A.O. Nusbaum et al. Regional and global changes in cerebral diffusion with normal aging. *AJNR Am J Neuroradiol*, 22(1):136–142, 2001.
- [193] A. Pfefferbaum et al. Frontal circuitry degradation marks healthy adult aging: evidence from diffusion tensor imaging. *NeuroImage*, 26(3):891–899, 2005.

- [194] A. Pfefferbaum et al. Dymorphology and microstructural degradation of the corpus callosum: Interaction of age and alcoholism. *Neurobiol Aging*, (in press) 2005.
- [195] A. Pfefferbaum et al. Age-related decline in brain white matter anisotropy measured with spatially corrected echo-planar diffusion tensor imaging. *Magn Reson Med*, 44(2):259–268, 2000.
- [196] D.H. Salat et al. Age-related alterations in white matter microstructure measured by diffusion tensor imaging. *Neurobiol Aging*, 26(8):1215–1227, 2005.
- [197] V.J. Schmithorst et al. Correlation of white matter diffusivity and anisotropy with age during childhood and adolescence: a cross-sectional diffusion-tensor MR imaging study. *Radiology*, 222(1):212–218, 2002.
- [198] T. Yoshiura et al. Age-related structural changes in the young adult brain shown by magnetic resonance diffusion tensor imaging. *Acad Radiol*, 12(3):268–275, 2005.
- [199] C. Büchel et al. White matter asymmetry in the human brain: a diffusion tensor MRI study. *Cereb Cortex*, 14(9):945–951, 2004.
- [200] H.-J. Park et al. White matter hemisphere asymmetries in healthy subjects and in schizophrenia: a diffusion tensor MRI study. *NeuroImage*, 23(1):213–223, 2004.
- [201] G.J.M. Parker et al. Lateralization of ventral and dorsal auditory-language pathways in the human brain. *NeuroImage*, 24(3):656–666, 2005.
- [202] R. Westerhausen et al. Effects of handedness and gender on macro- and microstructure of the corpus callosum and its subregions: a combined high-resolution and diffusion-tensor MRI study. *Brain Res Cogn Brain Res*, 21(3):418–426, 2004.
- [203] R. Westerhausen et al. The influence of handedness and gender on the microstructure of the human corpus callosum: a diffusion-tensor magnetic resonance imaging study. *Neurosci Lett*, 351(2):99–102, 2003.
- [204] C. Beaulieu et al. Imaging brain connectivity in children with diverse reading ability. *NeuroImage*, 25(4):1266–1271, 2005.
- [205] T. Klingberg et al. Microstructure of temporo-parietal white matter as a basis for reading ability: evidence from diffusion tensor magnetic resonance imaging. *Neuron*, 25(2):493–500, 2000.
- [206] M. Moseley et al. Diffusion-tensor imaging of cognitive performance. *Brain Cogn*, 50(3):396–413, 2002.
- [207] S.D. Shenkin et al. Childhood and current cognitive function in healthy 80 - year- olds: a DT-MRI study. *NeuroReport*, 14(3):1–5, 2003.
- [208] M.A. Koch et al. An investigation of functional and anatomical connectivity using magnetic resonance imaging. *NeuroImage*, 16(1):241–250, 2002.
- [209] A.T. Toosy et al. Characterizing functionstructure relationships in the human visual system with functional MRI and diffusion tensor imaging. *NeuroImage*, 21(4):1452–1463, 2004.
- [210] D.J. Werring et al. A direct demonstration of both structure and function in the visual system: combining diffusion tensor imaging with functional magnetic resonance imaging. *NeuroImage*, 9(3):352–361, 1999.
- [211] J.I. Berman et al. Quantitative diffusion tensor MRI fiber tractography of sensorimotor white matter development in premature infants. *NeuroImage*, 27(4):862–871, 2005.
- [212] L.C. Maas et al. Early laminar organization of the human cerebrum demonstrated with diffusion tensor imaging in extremely premature infants. *NeuroImage*, 22(3):1134–1140, 2004.
- [213] B.P. Murphy et al. Line scan diffusion tensor MRI of the cervical spinal cord in preterm infants. *J Magn Reson Imaging*, 13(6):949–953, 2001.
- [214] S.C. Partridge et al. Diffusion tensor imaging: serial quantitation of white matter tract maturity in premature newborns. *NeuroImage*, 22(3):1302–1314, 2004.

- [215] S. Boujrafa et al. Study of pediatric brain development using magnetic resonance imaging of anisotropic diffusion. *Magn Reson Imaging*, 20(4):327–336, 2002.
- [216] J. Dubois et al. Assessment of the early organization and maturation of infants’ cerebral white matter fiber bundles: a feasibility study using quantitative diffusion tensor imaging and tractography. *NeuroImage*, (in press) 2006.
- [217] L. Hermoye et al. Pediatric diffusion tensor imaging: normal database and observation of the white matter maturation in early childhood. *NeuroImage*, 29(2):493–504, 2006.
- [218] T.-Q. Li and M.D. Noseworthy. Mapping the development of white matter tracts with diffusion tensor imaging. *Dev Sci*, 5(3):293–300, 2002.
- [219] L. Snook et al. Diffusion tensor imaging of neurodevelopment in children and young adults. *NeuroImage*, 26(4):1164–1173, 2005.
- [220] A.M. Ulug. Monitoring brain development with quantitative diffusion tensor imaging. *Dev Sci*, 5(3):286–292, 2002.
- [221] A. Hiwatashi et al. Fractional anisotropy is higher in Heschl’s gyrus than in superior temporal gyrus in normal subjects. *Acad Radiol*, 13(1):73–76, 2006.
- [222] H.W.R. Powell et al. Noninvasive in vivo demonstration of the connections of the human parahippocampal gyrus. *NeuroImage*, 22(2):740–747, 2004.
- [223] A. Virta et al. Visualizing and characterizing white matter fiber structure and architecture in the human pyramidal tract using diffusion tensor MRI. *Magn Reson Imaging*, 17(8):1121–1133, 1999.
- [224] M.A. Koch et al. Distortion-free diffusion tensor imaging of cranial nerves and of inferior temporal and orbitofrontal white matter. *NeuroImage*, 17(1):497–506, 2002.
- [225] M.R. Wiegell et al. Automatic segmentation of thalamic nuclei from diffusion tensor magnetic resonance imaging. *NeuroImage*, 19(2):391–401, 2003.
- [226] J. Burns et al. Structural disconnectivity in schizophrenia: a diffusion tensor magnetic resonance imaging study. *Br J Psychiatry*, 182:439–443, 2003.
- [227] M.J. Hoptman et al. Frontal white matter microstructure, aggression, and impulsivity in men with schizophrenia: a preliminary study. *Biol Psychiatry*, 52(1):9–14, 2002.
- [228] D.K. Jones et al. A diffusion tensor magnetic resonance imaging study of frontal cortex connections in very-late-onset schizophrenia-like psychosis. *Am J Geriatr Psychiatry*, 13(12):1092–1099, 2005.
- [229] P. Kalus et al. New evidence for involvement of the entorhinal region in schizophrenia: a combined MRI volumetric and DTI study. *NeuroImage*, 24(4):1122–1129, 2005.
- [230] P. Kalus et al. The amygdala in schizophrenia: a trimodal magnetic resonance imaging study. *Neurosci Lett*, 375(3):151–156, 2005.
- [231] R.A.A. Kanaan et al. Diffusion tensor imaging in schizophrenia. *Biol Psychiatry*, 58(12):921–929, 2005.
- [232] M. Kubicki et al. DTI and MTR abnormalities in schizophrenia: analysis of white matter integrity. *NeuroImage*, 26(4):1109–1118, 2005.
- [233] M. Kubicki et al. Uncinate fasciculus findings in schizophrenia: a magnetic resonance diffusion tensor imaging study. *Am J Psychiatry*, 159(5):813–820, 2002.
- [234] M. Kubicki et al. Cingulate fasciculus integrity disruption in schizophrenia: a magnetic resonance diffusion tensor imaging study. *Biol Psychiatry*, 54(11):1171–1180, 2003.
- [235] S. Kumra et al. Reduced frontal white matter integrity in early-onset schizophrenia: a preliminary study. *Biol Psychiatry*, 55(12):1138–1145, 2004.
- [236] N. Kuroki et al. Fornix integrity and hippocampal volume in male schizophrenic patients. *Biol Psychiatry*, (in press) 2006.
- [237] M. Nakamura et al. Frontotemporal disconnectivity in schizotypal personality disorder: a diffusion tensor imaging study. *Biol Psychiatry*, 58(6):468–478, 2005.

- [238] Y.W. Shin et al. Increased water diffusivity in the frontal and temporal cortices of schizophrenic patients. *NeuroImage*, (in press) 2006.
- [239] R.M. Steel et al. Diffusion tensor imaging (DTI) and proton magnetic resonance spectroscopy ( $^1\text{H}$  MRS) in schizophrenic subjects and normal controls. *Psychiat Res - Neuroim*, 106(3):161–170, 2001.
- [240] F. Wang et al. A diffusion tensor imaging study of middle and superior cerebellar peduncle in male patients with schizophrenia. *IEEE Trans Med Imaging*, 23(8):930–939, 2004.
- [241] M. Codella et al. Cerebral grey matter pathology and fatigue in patients with multiple sclerosis: a preliminary study. *J Neurol Sci*, 194(1):71–74, 2002.
- [242] C.M. Ellis et al. Diffusion tensor MRI assesses corticospinal tract damage in ALS. *Neurology*, 53(5):1051–1058, 1999.
- [243] M. Filippi. MRclinical correlations in the primary progressive course of MS: new insights into the disease pathophysiology from the application of magnetization transfer, diffusion tensor, and functional MRI. *J Neurol Sci*, 206(2):157–164, 2003.
- [244] M. Filippi et al. Magnetization transfer and diffusion tensor MR imaging of basal ganglia from patients with multiple sclerosis. *J Neurol Sci*, 183(1):69–72, 2001.
- [245] M. Filippi and M. Inglese. Overview of diffusion-weighted magnetic resonance studies in multiple sclerosis. *J Neurol Sci*, 186(1):S37–S43, 2001.
- [246] M. Filippi et al. Correlations between structural CNS damage and functional MRI changes in primary progressive MS. *NeuroImage*, 15(3):537–546, 2002.
- [247] Y.-H. Hong et al. Diffusion tensor MRI as a diagnostic tool of upper motor neuron involvement in amyotrophic lateral sclerosis. *J Neurol Sci*, 227(1):73–78, 2004.
- [248] M. Rovaris and M. Filippi. MR-based technology for in vivo detection, characterization, and quantification of pathology of relapsing-remitting multiple sclerosis. *J Rehabil Res Dev*, 39(2):243–260, 2002.
- [249] M. Rovaris et al. Short-term accrual of gray matter pathology in patients with progressive multiple sclerosis: an in vivo study using diffusion tensor MRI. *NeuroImage*, 24(4):1139–1146, 2005.
- [250] M. Rovaris et al. Cognitive dysfunction in patients with mildly disabling relapsingremitting multiple sclerosis: an exploratory study with diffusion tensor MR imaging. *J Neurol Sci*, 195(2):103–109, 2002.
- [251] P. Valsasina et al. Mean diffusivity and fractional anisotropy histogram analysis of the cervical cord in MS patients. *NeuroImage*, 26(3):822–828, 2005.
- [252] K. Arfanakis et al. Diffusion tensor MRI in temporal lobe epilepsy. *Magn Reson Imaging*, 20(7):511–519, 2002.
- [253] X. Cao et al. Quantitative effectiveness analysis of radiation therapy in temporal lobe epilepsy using diffusion tensor imaging techniques. *Int Congr Ser*, 1256:1292, 2003.
- [254] B. Diehl et al. Postictal diffusion tensor imaging. *Epilepsy Res*, 65(3):137–146, 2005.
- [255] A. Okumura et al. Diffusion tensor imaging in frontal lobe epilepsy. *Pediatr Neurol*, 31(3):203–206, 2004.
- [256] F.J. Rugg-Gunn et al. Diffusion tensor imaging of cryptogenic and acquired partial epilepsies. *Brain*, 124(3):627–36, 2001.
- [257] F.J. Rugg-Gunn et al. Diffusion tensor imaging in refractory epilepsy. *The Lancet*, 359(9319):1748–1751, 2002.
- [258] L. Thivard et al. Diffusion tensor imaging in medial temporal lobe epilepsy with hippocampal sclerosis. *NeuroImage*, 28(3):682–690, 2005.
- [259] A. Fellgiebel et al. Color-coded diffusion-tensor-imaging of posterior cingulate fiber tracts in mild cognitive impairment. *Neurobiol Aging*, 26(8):1193–1198, 2005.
- [260] P. Kalus et al. Examining the gateway to the limbic system with diffusion tensor imaging:

- The perforant pathway in dementia. *NeuroImage*, (in press) 2006.
- [261] D. Medina et al. White matter changes in mild cognitive impairment and AD: A diffusion tensor imaging study. *Neurobiol Aging*, (in press) 2005.
  - [262] M. O'Sullivan et al. Normal-appearing white matter in ischemic leukoaraiosis: a diffusion tensor MRI study. *Neurology*, 57(12):2301–2310, 2001.
  - [263] S.E. Rose et al. Loss of connectivity in Alzheimer's disease: an evaluation of white matter tract integrity with colour coded MR diffusion tensor imaging. *J Neurol Neurosurg Psychiatry*, 69(4):528–530, 2000.
  - [264] S. Takahashi et al. Selective reduction of diffusion anisotropy in white matter of Alzheimer disease brains measured by 3.0 Tesla magnetic resonance imaging. *Neurosci Lett*, 332(1):45–48, 2002.
  - [265] K. Ando et al. Diffusion tensor imaging of the brainstem whitematter tract anomaly in a case of COACH syndrome. *Eur J Radiol Extra*, 51:1–4, 2004.
  - [266] M. Ashtari et al. Attention-deficit/hyperactivity disorder: a preliminary diffusion tensor imaging study. *Biol Psychiatry*, 57(5):448–455, 2005.
  - [267] N. Barnea-Goraly et al. White matter structure in autism: preliminary evidence from diffusion tensor imaging. *Biol Psychiatry*, 55(3):323–326, 2004.
  - [268] N. Barnea-Goraly et al. Arithmetic ability and parietal alterations: a diffusion tensor imaging study in velocardiofacial syndrome. *Brain Res Cogn Brain Res*, 25(3):735–740, 2005.
  - [269] A. Pantelyat. White matter changes in children with velocardiofacial syndrome. *PennScience*, 1(2):8–12, 2003.
  - [270] M.M. Haznedar et al. Fronto-thalamo-striatal gray and white matter volumes and anisotropy of their connections in bipolar spectrum illnesses. *Biol Psychiatry*, 57(7):733–742, 2005.
  - [271] M. Inglese et al. Magnetization transfer and diffusion tensor MR imaging of the optic radiations and calcarine cortex from patients with Leber's hereditary optic neuropathy. *J Neurol Sci*, 188(1–2):33–36, 2001.
  - [272] M. Holtmannspötter et al. A diffusion tensor MRI study of basal ganglia from patients with ADEM. *J Neurol Sci*, 206(1):27–30, 2003.
  - [273] T.P. Trouard et al. Diffusion tensor imaging in Niemann-Pick type C disease. *Pediatr Neurol*, 33(5):325–330, 2005.
  - [274] S. Naidu et al. Neuroimaging studies in Rett syndrome. *Brain Dev*, 23(1):S62–S71, 2001.
  - [275] N. Molko et al. Monitoring disease progression in CADASIL with diffusion magnetic resonance imaging: a study with whole brain histogram analysis. *Stroke*, 33(12):2902–2908, 2002.
  - [276] N. Molko et al. Diffusion tensor imaging study of subcortical gray matter in CADASIL. *Stroke*, 32(9):2049–2054, 2001.
  - [277] M.F.H Schocke et al. Trace of diffusion tensor differentiates the parkinson variant of multiple system atrophy and Parkinson's disease. *Neuroimage*, 21(4):1443–1451, 2004.
  - [278] S.A.J. Reading et al. Regional white matter change in pre-symptomatic Huntington's disease: a diffusion tensor imaging study. *Psychiat Res - Neuroim*, 140(1):55–62, 2005.
  - [279] C. Pierpaoli et al. Water diffusion changes in Wallerian degeneration and their dependence on white matter architecture. *NeuroImage*, 13(6):1174–1185, 2001.
  - [280] G. Thomalla et al. Diffusion tensor imaging detects early Wallerian degeneration of the pyramidal tract after ischemic stroke. *NeuroImage*, 22(4):1767–1774, 2004.
  - [281] S.A. Trip et al. Optic nerve diffusion tensor imaging in optic neuritis. *NeuroImage*, (in press) 2005.
  - [282] U.C. Wieshmann et al. Anisotropy of water diffusion in corona radiata and cerebral peduncle



- in patients with hemiparesis. *NeuroImage*, 10(2):225–230, 1999.
- [283] S.-K. Lee et al. Diffusion tensor MRI visualizes decreased subcortical fiber connectivity in focal cortical dysplasia. *NeuroImage*, 22(4):1826–1829, 2004.
  - [284] D.P. Auer et al. Visualization of major fiber tracts and cortical functions in patients with cerebral gliomas. *Int Congr Ser*, 1247:153–163, 2002.
  - [285] C.A. Clark et al. White matter fiber tracking in patients with space-occupying lesions of the brain: a new technique for neurosurgical planning? *NeuroImage*, 20(3):1601–1608, 2003.
  - [286] T. Inoue et al. Diffusion tensor imaging for preoperative evaluation of tumor grade in gliomas. *Clin Neurol Neurosurg*, 107(3):174–180, 2005.
  - [287] R. Jena et al. Diffusion tensor imaging: possible implications for radiotherapy treatment planning of patients with high-grade glioma. *Clin Oncol*, 17(8):581–590, 2005.
  - [288] R.W. Koot et al. Epidermoid of the lateral ventricle: evaluation with diffusion-weighted and diffusion tensor imaging. *Clin Neurol Neurosurg*, 105(4):270–273, 2003.
  - [289] S.J. Price et al. Diffusion tensor imaging of brain tumours at 3T: a potential tool for assessing white matter tract invasion? *Clin Radiol*, 58(6):455–462, 2003.
  - [290] M.H.T. Reinges et al. Imaging of postthalamal visual fiber tracts by anisotropic diffusion weighted MRI and diffusion tensor imaging: principles and applications. *Eur J Radiol*, 49(2):91–104, 2004.
  - [291] T. Schonberg et al. Characterization of displaced white matter by brain tumors using combined DTI and fMRI. *Neuroimage*, (in press) 2006.
  - [292] U.C. Wieshmann et al. Diffusion tensor imaging demonstrates deviation of fibres in normal appearing white matter adjacent to a brain tumour. *J Neurol Neurosurg Psychiatry*, 68(4):501–503, 2000.
  - [293] B.P. Witwer et al. Diffusion-tensor imaging of white matter tracts in patients with cerebral neoplasm. *J Neurosurg*, 97(3):568–575, 2002.
  - [294] C.S. Yu et al. Diffusion tensor tractography in patients with cerebral tumors: A helpful technique for neurosurgical planning and postoperative assessment. *Eur J Radiol*, 56(2):197–204, 2005.
  - [295] J.R. Carhuapoma et al. Diffusion-weighted MRI and proton MR spectroscopic imaging in the study of secondary neuronal injury after intracerebral hemorrhage. *Stroke*, 31(3):726–732, 2000.
  - [296] W. Li et al. Robust unsupervised segmentation of infarct lesion from diffusion tensor MR images using multiscale statistical classification and partial volume voxel reclassification. *NeuroImage*, 23(4):1507–1518, 2004.
  - [297] Y. Ozsunar et al. MRI measurements of water diffusion: impact of region of interest selection on ischemic quantification. *Eur J Radiol*, 51(3):195–201, 2004.
  - [298] M.L. Seghier et al. Functional magnetic resonance imaging and diffusion tensor imaging in a case of central poststroke pain. *J Pain*, 6(3):208–212, 2005.
  - [299] M.L. Seghier et al. Combination of event-related fMRI and diffusion tensor imaging in an infant with perinatal stroke. *NeuroImage*, 21(1):463–472, 2004.
  - [300] C. Wang et al. Longitudinal changes in white matter following ischemic stroke: a three-year follow-up study. *Neurobiol Aging*, (in press) 2005.
  - [301] F. Zelaya et al. An evaluation of the time dependence of the anisotropy of the water diffusion tensor in acute human ischemia. *Magn Reson Imaging*, 17(3):331–348, 1999.
  - [302] C.G. Filippi et al. Diffusion tensor imaging of patients with HIV and normal-appearing white matter on MR images of the brain. *AJNR Am J Neuroradiol*, 22(2):277–283, 2001.
  - [303] N. Pomara et al. White matter abnormalities in HIV-1 infection: a diffusion tensor imaging study. *Psychiat Res - Neuroim*, 106(1):15–24, 2001.
  - [304] K.A. Tucker et al. Neuroimaging in human immunodeficiency virus infection. *J Neuroim-*



- munol*, 157(1–2):153–162, 2004.
- [305] A. Pfefferbaum et al. Supratentorial profile of white matter microstructural integrity in recovering alcoholic men and women. *Biol Psychiatry*, 59(4):364–372, 2006.
  - [306] A. Pfefferbaum and E.V. Sullivan. Microstructural but not macrostructural disruption of white matter in women with chronic alcoholism. *NeuroImage*, 15(3):708–718, 2002.
  - [307] Y. Assaf et al. Hypertension and neuronal degeneration in excised rat spinal cord studied by high- $b$  value  $q$ -space diffusion magnetic resonance imaging. *Exp Neurol*, 184(2):726–736, 2003.
  - [308] L.H.T Leung et al. White-matter diffusion anisotropy after chemo-irradiation: a statistical parametric mapping study and histogram analysis. *NeuroImage*, 21(1):261–268, 2004.
  - [309] D. Qiu et al. Mapping radiation dose distribution on the fractional anisotropy map: applications in the assessment of treatment-induced white matter injury. *NeuroImage*, (in press) 2006.
  - [310] S.A. Gruber and D.A. Yurgelun-Todd. Neuroimaging of marijuana smokers during inhibitory processing: a pilot investigation. *Brain Res Cogn Brain Res*, 23(1):107–118, 2005.
  - [311] K.O. Lim et al. Reduced frontal white matter integrity in cocaine dependence: a controlled diffusion tensor imaging study. *Biol Psychiatry*, 51(11):890–895, 2002.
  - [312] C.H. Salmond et al. Diffusion tensor imaging in chronic head injury survivors: Correlations with learning and memory indices. *NeuroImage*, 29(1):117–124, 2006.
  - [313] F. Schoth et al. Diffusion tensor imaging in acquired blind humans. *Neurosci Lett*, (in press) 2006.
  - [314] A. Pfefferbaum et al. Postmortem MR imaging of formalin-fixed human brain. *NeuroImage*, 21(4):1585–1595, 2004.
  - [315] T. Beppu et al. Fractional anisotropy value by diffusion tensor magnetic resonance imaging as a predictor of cell density and proliferation activity of glioblastomas. *Surg Neurol*, 63(1):56–61, 2005.
  - [316] S.-K. Lee et al. Diffusion-tensor MR imaging and fiber tractography: a new method of describing aberrant fiber connections in developmental CNS anomalies. *Radiographics*, 25(1):53–65, 2005.
  - [317] G.D. Buckberg. Imaging, models, and reality: a basis for anatomicphysiologic planning. *J Thorac Cardiovasc Surg*, 129(2):243–245, 2005.
  - [318] F.B. Sachse et al. Modeling of fiber orientation in the ventricular myocardium with MR diffusion imaging. In *CinC*, volume 28, pages 617–620, 2001.
  - [319] G.I. Sanchez-Ortiz et al. Knowledge-based tensor anisotropic diffusion of cardiac magnetic resonance images. *Med Image Anal*, 3(1):77–101, 1999.
  - [320] D.F. Scollan et al. Histological validation of myocardial microstructure obtained from diffusion tensor magnetic resonance imaging. *Am J Physiol*, 275(6):2308–2318, 1998.
  - [321] H. Mamata et al. Collateral nerve fibers in human spinal cord: visualization with magnetic resonance diffusion tensor imaging. *NeuroImage*, (in press) 2006.
  - [322] C.A.M. Wheeler-Kingshott et al. Investigating cervical spinal cord structure using axial diffusion tensor imaging. *NeuroImage*, 16(1):93–102, 2002.
  - [323] J. Hiltunen et al. Diffusion tensor imaging and tractography of distal peripheral nerves at 3 T. *Clin Neurophysiol*, 116(10):2315–2323, 2005.
  - [324] M.F. Meek et al. In vivo three-dimensional reconstruction of human median nerves by diffusion tensor imaging. *Exp Neurol*, (in press) 2006.
  - [325] M. Skorpila et al. Peripheral nerve diffusion tensor imaging. *Magn Reson Imaging*, 22(5):743–745, 2004.
  - [326] J.-M. Bonny and J.-P. Renou. Water diffusion features as indicators of muscle structure ex vivo. *Magn Reson Imaging*, 20(5):395–400, 2002.

- [327] S. Capuana et al. Diffusion tensor imaging to study anisotropy in a particular porous system: the trabecular bone network. *Solid State Nucl Magn Reson*, 28(2–4):266–272, 2005.
- [328] C. Rossi et al. DTI of trabecular bone marrow. *Magn Reson Imaging*, 23(2):245–248, 2005.
- [329] B.A. Moffat and J.M. Pope. Anisotropic water transport in the human eye lens studied by diffusion tensor NMR micro-imaging. *Exp Eye Res*, 74(6):677–687, 2002.



## Chapter 2

# MR fiber tractography

Parts of the work in this chapter have been published in

*G. De Groof, M. Verhoye, V. Van Meir, I. Tindemans, A. Leemans, and A. Van der Linden, “In vivo diffusion tensor imaging (DTI) of brain subdivisions and vocal pathways in songbirds”, NeuroImage, Vol. 29, Nr. 3, p. 754–763, 2006.*

## 2.1 Abstract

MR Fiber Tractography (FT), also referred to as fiber tracking or tract tracing, can be defined as the virtual reconstruction of the 3D fiber architecture. This technique is based on the assumption that it can retrieve the spatial information of the underlying fiber network, using the available information of the corresponding MR diffusion data. FT provides exciting new opportunities to study several architectural characteristics of fibrous tissue in vivo and non-invasively, and has generated much enthusiasm, resulting in the development of a large number of FT algorithms. In this chapter, the basic principles of tractography are reviewed. Different tracking methods with varying degrees of complexity are described and their potential strengths and weaknesses are discussed. Finally, several examples are presented to demonstrate the importance of FT in a clinical and biomedical setting.

## 2.2 Introduction

As described in the previous chapter, it is generally assumed that the measured diffusion anisotropy reflects the presence of spatially oriented micro-structures (e.g., myocardial tissue or neural fibers in the CNS), for here, the mobility of the diffusion particles is mainly determined by the fiber pathway [1]. Therefore, by traversing continuous pathways that follow this anisotropic diffusion, both spatial and orien-

tational information of these fiber pathways and subsequently the anatomical brain connectivity can be reconstructed [2]. This in vivo virtual 3D reconstruction of the fibrous architecture in biological tissue using MR diffusion data is called MR FT<sup>1</sup>, and was mainly pioneered by Basser, Mori, and Jones [4–15].

With the advent of DTI, a rigorous formulation of the full 3D Gaussian diffusion process was established providing not only a quantitative measure for diffusion anisotropy, but also the corresponding predominant directions of water diffusion [16, 17]. This framework has led to a proliferation of FT algorithms with varying degrees of complexity and emphasizing different aspects to extricate the structural connectivity [4–15, 18–110]. Although the diversity of approaches in this burgeoning field restrains from self-evidently categorizing the state-of-the-art FT techniques, a general classification has been presented previously in Refs. [111–113].

## 2.3 Principals of MR fiber tractography

### 2.3.1 Basic concept

Conceptually, MR FT can be compared to the reconstruction of fluid streamlines from discretely sampled velocity field data [114]. But instead of following fluid pathways from vector data, FT reconstructs fiber tracts from diffusion MR data. In DTI, these data sets are discretely sampled diffusion tensor fields  $\mathbf{D}(\mathbf{r})$ , i.e. each voxel at position  $\mathbf{r}$  is characterized by the second-rank diffusion tensor  $\mathbf{D}$  which represents the local 3D anisotropic Gaussian diffusion process. When applied specifically to DTI data sets, FT is referred to as Diffusion Tensor Tractography (DTT) [115].

Assuming that the PDV field  $\mathbf{e}_1(\mathbf{r})$  corresponding to  $\mathbf{D}(\mathbf{r})$  is aligned with the direction of the WM fiber bundle at position  $\mathbf{r}$ , DTT can be performed based on this PDV field [Fig. 2.1 (a)]. Note that in this approach, the diffusion tensor field is approximated by a vector field, omitting information that is contained in the remaining DOF of the diffusion tensor field. Moreover, notice in Fig. 2.1 (a) that only the orientation and not the direction of  $\mathbf{e}_1(\mathbf{r})$  is defined, for diffusion is inherently a center-symmetric phenomenon, i.e. both  $\mathbf{e}_1(\mathbf{r})$  and  $-\mathbf{e}_1(\mathbf{r})$  represent the predominant diffusion direction. Therefore, each individual fiber pathway can be computed by propagating a line both anterograde, i.e.  $\mathbf{e}_1(\mathbf{r})$ , and retrograde, i.e.  $-\mathbf{e}_1(\mathbf{r})$ , from an initial seed point  $\mathbf{r}_0$  [Fig. 2.1 (b)] [9–11].

The process of connecting consecutive voxels is iterated many times until certain stopping criteria are met. For example, to ensure that the tracts would not erroneously pass into areas of very low anisotropy, such as CSF or gray matter, the

<sup>1</sup>Note that within this context, the terminology ‘MR tractography’ was already described in the work of Kinosada et al. before the DTI framework was developed [3].

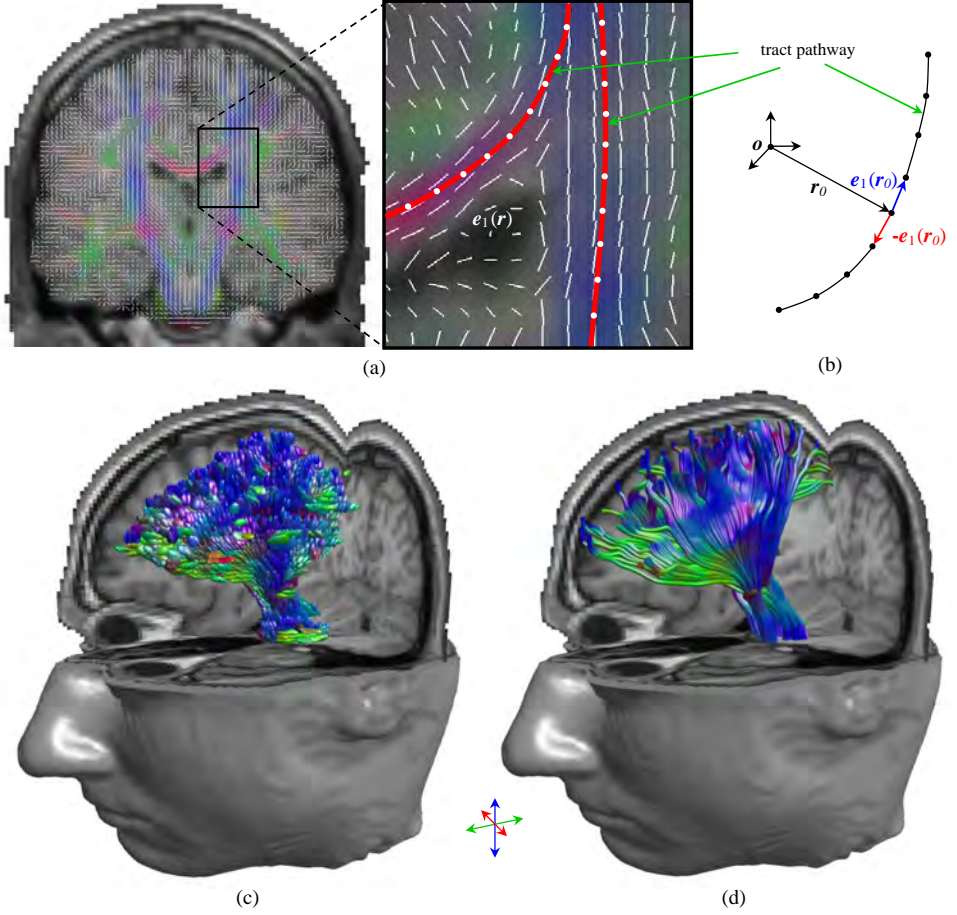


**Figure 2.1.** Basically, FT can be obtained by connecting each voxel to the adjacent one according to its corresponding predominant diffusion direction field  $\mathbf{e}_1(\mathbf{r})$ . This concept is indicated by the white dots on the red lines in (a). The voxel at position  $\mathbf{r}_0$  that initiates the FT procedure (bidirectionally) is called the seed point (b). By applying FT, the diffusion tensor field in the brain can be represented more clearly using lines (or tubes, iso-surfaces, etc.) that ‘connect’ different brain regions. The diffusion tensor field of the corticospinal pathways and the corresponding FT result are shown in (c) and (d), respectively, with PDV color-encoding as indicated by the arrows. Note that the width of the cylindrical tubes in (d) does not represent any physical width, but is only used to enhance the 3D visibility.

tracking process is stopped when a diffusion anisotropy measure falls below a fixed threshold (e.g.,  $FA \lesssim 0.15$ ) [9, 15]. In addition, it has been proposed that only a limited amount of curvature and/or torsion between consecutive segments should be tolerated, further reducing the number of spurious tracts<sup>2</sup> [6, 15]. In general, the FT procedure is performed for a large number of seed points  $\{\mathbf{r}_0\}$  that define a specific Region Of Interest (ROI) [Fig. 2.1 (c,d)].

### 2.3.2 Regularized and continuous DTI data

Due to the MR acquisition process, the diffusion tensor field is only available at discrete points, i.e. the voxel positions. Although initially performed on these discretely sampled diffusion tensor data (e.g., Refs. [9–11, 14, 15, 19, 20, 28–30, 36]), it became apparent that the tracking procedure often deviated from the true fiber orientation, for here, the choice of direction is limited to the 26 neighboring voxels [9]. This problem can be avoided when tracking a continuous rather than a discrete diffusion tensor field and can be accomplished, for instance, by applying (linear) interpolation techniques and the fitting of Lagrange polynomials or B-splines [4, 6, 39, 116, 117]. In addition, a large number of methods have been developed to further regularize and smooth the diffusion tensor field which could improve the FT procedure [24–27, 69, 118–124] (see Fig. 2.2).

## 2.4 Fiber connectivity reconstruction methods

As mentioned previously, a large number of papers have been published on the development of new FT methodologies. In this section, FT techniques are categorized into streamline-based, front propagation, and (pseudo-)probabilistic approaches. Several of these FT methods are described and their potential strengths and weaknesses are discussed.

### 2.4.1 Streamline DTT

The first mathematically founded FT framework was proposed by Basser et al., in which he proposed that a WM fiber tract can be represented as a 3D space curve parameterized by the arc length  $s$  of the trajectory [4–7]. In this context, the tract pathway  $\mathbf{r}(s) = [x(s) \ y(s) \ z(s)]^T$  can be characterized by the Frénet equation, i.e.

$$\frac{d\mathbf{r}(s)}{ds} = \mathbf{t}(s) \ , \quad (2.1)$$

---

<sup>2</sup>Note, however, that this consideration is based on a priori information of the WM fiber tract geometry.

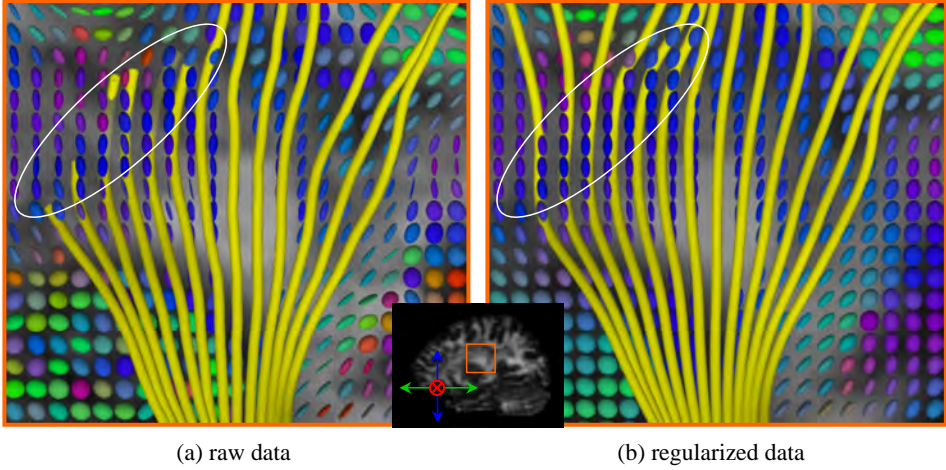


**Figure 2.2.** A sagittal FA map with ellipsoids and pyramidal fiber tracts using (a) the raw DTI data and (b) the regularized data, which was calculated using a modified version of the adaptive anisotropic noise filtering technique described in Ref. [125]. As indicated by the encircled region, FT is ameliorated in the regularized data. However, if too much regularization or smoothing is applied, the likelihood of creating ‘phantom’ tracts is very high.

where  $\mathbf{t}(s)$  represents the unit vector tangential to  $\mathbf{r}(s)$  at arc length  $s$ . Assuming that the PDV field  $\mathbf{e}_1(\mathbf{r})$  corresponding to  $\mathbf{D}(\mathbf{r})$  is aligned with the tangential direction of the WM fiber bundle, Eq. (2.1) can be rewritten as

$$\frac{d\mathbf{r}(s)}{ds} = \mathbf{e}_1[\mathbf{r}(s)] \quad (2.2)$$

or

$$\mathbf{r}(s) = \int_{s_0}^s \mathbf{e}_1[\mathbf{r}(s)] ds, \quad (2.3)$$

where  $\mathbf{r}(s = s_0) = \mathbf{r}_0$  represents the seed point.

#### 2.4.1.1 Euler’s method

The most trivial way to perform the numerical integration of Eq. (2.3) is by starting the DTT procedure at the seed point  $\mathbf{r}_0$ , which is assumed to be located on the putative fiber tract, calculating the corresponding PDV, i.e.  $\mathbf{e}_1(\mathbf{r}_0)$ , and following that direction for a short predefined distance  $\Delta$  (i.e., the ‘step size’) to obtain the next point  $\mathbf{r}_1 = \mathbf{r}_0 + \mathbf{e}_1(\mathbf{r}_0)\Delta$  on the fiber pathway. With this procedure, known as Euler’s method, the fiber pathway can be reconstructed by iteratively performing the aforementioned steps, i.e.

$$\mathbf{r}_{i+1} = \mathbf{r}_i + \mathbf{e}_1(\mathbf{r}_i)\Delta. \quad (2.4)$$



This scheme has an associated error of order  $\mathcal{O}\{\Delta^2\}$  and is somewhat heuristically implemented in Refs. [22, 31, 32, 37, 42, 43, 46, 47, 49, 115, 126]. Note that with this streamline procedure (and the streamline methods discussed below), a single fiber tract pathway can be described by a sampled space curve  $\alpha$ , i.e. an  $N \times 3$ -matrix where each row denotes a coordinate  $\mathbf{r}_i$ . Consequently, a fiber tractography result obtained from a set of seed points can then be represented by the set  $\{\alpha\}$ . As previously mentioned, there is the problem of eigenvector ambiguity, i.e. both  $\mathbf{e}_1$  and  $-\mathbf{e}_1$  represent the first eigenvector of  $\mathbf{D}$ . This can be resolved by assuming that the integral curve does not turn more than  $90^\circ$  between consecutive integration steps. This can be checked by determining the sign of the dot product between each intermediate tangent vector  $\mathbf{r}_i - \mathbf{r}_{i-1}$  and eigenvector  $\mathbf{e}_1(\mathbf{r}_i)$ , i.e.

$$\text{if } (\mathbf{r}_i - \mathbf{r}_{i-1}) \cdot \mathbf{e}_1(\mathbf{r}_i) < 0 \quad \text{then} \quad \mathbf{e}_1(\mathbf{r}_i) \rightarrow -\mathbf{e}_1(\mathbf{r}_i) . \quad (2.5)$$

Note, however, that from each seed point, a tract must propagate in both forward and backward directions [Fig. 2.1 (b)].

#### 2.4.1.2 Runge-Kutta integration

It is important to note that Euler's method can suffer substantially from a large accumulating error propagation, especially for larger step sizes  $\Delta$  (Fig. 2.3). Therefore, higher-order numerical integration schemes are preferred, such as the

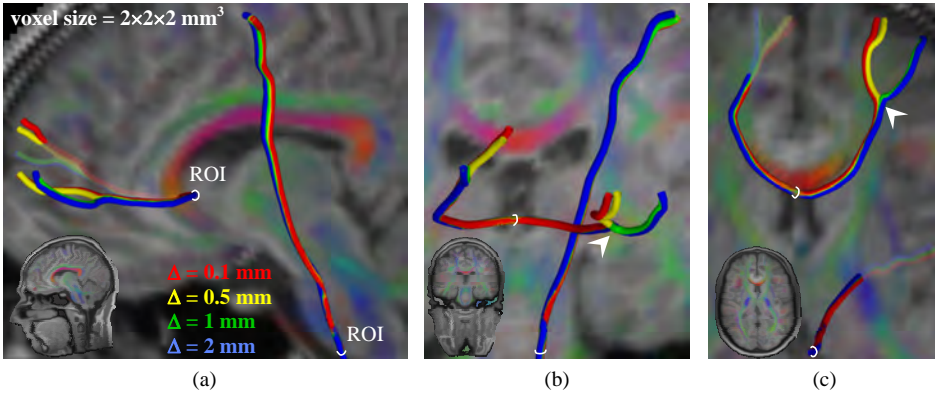


**Figure 2.3.** In these (a) sagittal, (b) coronal, and (c) axial views ( $T_1$ -weighted maps fused with PDV color-encoded FA maps), the sensitivity of the fiber trajectory in Euler's method with respect to the choice of the step size  $\Delta$  is clearly visible. Additionally, in (b) and (c), the arrowhead indicates a tract bifurcation. Note that in such regions, the PDV is not unambiguously determined, further affecting the difference in spatial organization of the fiber trajectory.

second-order Runge-Kutta (RK2) integration scheme [127], i.e.

$$\mathbf{r}_{i+1} = \mathbf{r}_i + \mathbf{e}_1 \left( \mathbf{r}_i + \frac{\Delta}{2} \mathbf{e}_1(\mathbf{r}_i) \right) \Delta, \quad (2.6)$$

which has error propagation on the order of  $\mathcal{O}\{\Delta^3\}$ , or the fourth-order Runge-Kutta (RK4) scheme [127], i.e.

$$\mathbf{r}_{i+1} = \mathbf{r}_i + \frac{\mathbf{k}_1}{6} + \frac{\mathbf{k}_2}{3} + \frac{\mathbf{k}_3}{3} + \frac{\mathbf{k}_4}{6}, \quad (2.7)$$

with

$$\begin{aligned} \mathbf{k}_1 &= \mathbf{e}_1(\mathbf{r}_i) \Delta \\ \mathbf{k}_2 &= \mathbf{e}_1 \left( \mathbf{r}_i + \frac{\mathbf{k}_1}{2} \right) \Delta \\ \mathbf{k}_3 &= \mathbf{e}_1 \left( \mathbf{r}_i + \frac{\mathbf{k}_2}{2} \right) \Delta \\ \mathbf{k}_4 &= \mathbf{e}_1(\mathbf{r}_i + \mathbf{k}_3) \Delta. \end{aligned} \quad (2.8)$$

The RK4 scheme has an associated error of order  $\mathcal{O}\{\Delta^5\}$  and is known to be a good candidate for the numerical solution of Eq. (2.3). In addition, it is possible to employ adaptive step sizing to further control the amount of error introduced in each integration step. The robust RK4 integration method is implemented in several streamline FT algorithms (with or without additional heuristic modifications) and is capable of accurately integrating tract streamlines with large step size  $\Delta$  [6, 18, 21, 23, 39, 50, 102, 128–131]. Note, however, that for equal step size, the RK4 approach is approximately a factor 4 slower than Euler’s method.

The aforementioned integration schemes can be further regularized using a variational framework for global energy minimization, as described in Refs. [27, 68–71, 74, 123].

#### 2.4.1.3 Tensor deflection

An alternative approach for determining the local tract direction is to use the entire diffusion tensor  $\mathbf{D}$  to estimate the propagation direction of the trajectory [33], i.e.

$$\mathbf{r}_{i+1} = \mathbf{r}_i + \Delta \frac{\mathbf{D}(\mathbf{r}_i) \cdot (\mathbf{r}_i - \mathbf{r}_{i-1})}{\|\mathbf{D}(\mathbf{r}_i) \cdot (\mathbf{r}_i - \mathbf{r}_{i-1})\|}. \quad (2.9)$$

This specific streamline algorithm is referred to as tensorline propagation [33] or tensor deflection (TEND) [34, 35, 95, 131]. In Eq. (2.9), the dot product with  $\mathbf{D}$  deflects the propagation direction towards the major eigenvector direction, but

limits the curvature of the deflection, resulting in a smoother tract reconstruction. For instance, when the diffusion distribution within a voxel of interest is planar, suggesting a high Intra-Voxel Orientational Heterogeneity (IVOH), the propagation direction is determined by the superposition of the first and second eigenvector. In the highly linear situation, the TEND approach and the ‘regular’ streamline method result in a similar tract propagation direction (Fig. 2.4).

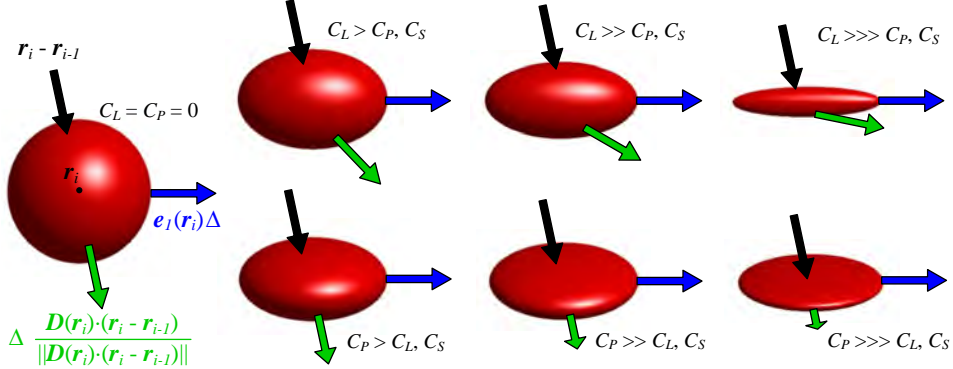


**Figure 2.4.** Comparison between the propagation directions of TEND and ‘regular’ streamline FT. Notice that the propagation direction for streamline FT (blue arrows) is independent of the diffusion profile. For the TEND approach (green arrows), increasing the linearity of the diffusion tensor profile, increases the deflection of the previous propagation direction  $\mathbf{r}_i - \mathbf{r}_{i-1}$  (black arrows) towards the direction of  $\mathbf{e}_1(\mathbf{r}_i)$  (top row). In the case of an increase of the diffusion planarity, this propagation direction is deflected more towards the plane spanned by the first two eigenvectors (bottom row). In the spherical situation, the propagation direction is not deflected (left).

A similar approach uses the diffusion measures based on the diffusion ellipsoid’s shape, differentiating between prolate, oblate and spherical fiber distributions [40, 41, 98]. Depending on these geometric measures, the propagation direction is calculated as a user-defined weighted sum of all three diffusion eigenvectors, i.e. the diffusion tensor  $\mathbf{D} = \mathbf{D}(\mathbf{r}_i)$  in Eq. (2.9) is then generally defined as

$$\mathbf{D} = \sum_{i=1}^3 f_i(\lambda_i) \mathbf{e}_i \cdot \mathbf{e}_i^T, \quad (2.10)$$

where the functions  $f_j$  can, for example, serve as threshold operators, i.e.

$$\mathbf{D} = \begin{cases} C_L \mathbf{D}_L & \text{if } C_L > C_P, C_S \\ C_P \mathbf{D}_P & \text{if } C_P > C_L, C_S \\ C_S \mathbf{D}_S & \text{if } C_S > C_L, C_P \end{cases}. \quad (2.11)$$

In Eq. (2.11), the coefficients  $C_L, C_P, C_S$  and tensor basis elements  $\mathbf{D}_L, \mathbf{D}_P, \mathbf{D}_S$  are calculated according to Eq. (1.33). This propagation approach has been further regularized by minimizing a tract cost model, as described in Ref. [73].

#### 2.4.1.4 Tractography termination thresholds

During the last decade, a large number of FT termination thresholds have been proposed, characterizing different aspects of the underlying fiber tissue (see e.g., Ref. [111]). The two most important threshold criteria are described next.

**Curvature threshold** Assuming that WM tracts do not bend sharply within the order of the voxel size, the integration procedure is terminated if the angle  $\theta$  between consecutive segments exceeds a specific threshold  $\theta_t$ , i.e. for a point  $\mathbf{r}_N$ , tracking is stopped if

$$\theta = \left| \arccos[(\mathbf{r}_N - \mathbf{r}_{N-1}) \cdot (\mathbf{r}_{N-1} - \mathbf{r}_{N-2})] \right| > \theta_t . \quad (2.12)$$

In literature, a widely accepted range of values for human brain data is in the neighborhood of  $\theta_t \simeq 10^\circ - 45^\circ$  for a step size  $\Delta \simeq 0.5\text{mm} - 2\text{mm}$ .

It is important to note that changing the step size affects the constraint of the local physical tract curvature  $\kappa$ . Therefore, it is preferred to apply an explicit curvature threshold  $\kappa_t$  instead of  $\theta_t$  [6]. Consequently, the tracking procedure is terminated if

$$\kappa = \frac{\sin \theta}{\Delta \sin\left(\frac{\pi - \theta}{2}\right)} > \kappa_t , \quad (2.13)$$

Similarly, torsion can be incorporated as well to further refine the constraints imposed on the geometrical properties of fiber trajectories.

**Anisotropy threshold** A second stopping criterium to terminate the propagation of a streamline tract is insufficient diffusion anisotropy. In regions of homogeneous, highly anisotropic linear diffusion, the PDV followed by the streamline method is considered to be a good approximation of the local tract structure. On the other hand, the local tract orientational homogeneity for regions that exhibit low non-linear (or highly planar) diffusion anisotropy precludes a reliable assessment of the PDV. Therefore, the validity of the orientational information, as described by the diffusion tensor model, can be inferred through the corresponding linear diffusion anisotropy. For the FA measure, the tracking process is generally terminated for values of FA  $\lesssim 0.15$ . Note that high FA values can also stem from highly planar configurations, in which the PDV is not unambiguously determined. Therefore, the linear anisotropy coefficient  $c_l$ , as defined in Eq. (1.27), is often used instead [41].

#### 2.4.1.5 Limitations

It is essential to understand the limitations of the streamline DTT procedure. It has been shown that each calculated PDV is associated with an uncertainty due to, e.g. the PVE and image noise [96, 110, 131–134]. With a typical resolution in human DTI data of approximately  $2 \times 2 \times 2 \text{ mm}^3$ , which is several orders of magnitude larger than the diameter of a single axon, it is important to realize that the PDV is a voxel-averaged quantity. Therefore, the PDV does not necessarily correspond to the main fiber direction, particularly when bundles intersect, branch or merge [135] [see Fig. 2.3 (b) and (c)].

In regions that exhibit a high IVOH, tensor field singularities occur resulting in an indistinct and unreliable PDV, as described in Refs. [96, 136, 137]. Consequently, spurious fiber trajectories may be reconstructed if the tracking algorithm incorporates only the PDV for determining the propagation direction and has been previously proclaimed as one of the main problems for fiber tracking based on DTI data [6, 9, 20, 138]. Moreover, it is known that DTI cannot differentiate between specific tract configurations, such as fiber kissing and oblique fiber crossing. Therefore, without additional prior knowledge, no tracking algorithm is able to resolve these situations correctly.

Several DTT approaches have been proposed to overcome some of the aforementioned limitations that were encountered using streamline FT and are described next.

### 2.4.2 Front evolution approaches

Another way to perform tractography is the use of so-called Fast Marching (FM) methods derived from level set theory [139–141]. In contrast to line propagation algorithms, these techniques model the evolution of an advancing 3D front through the WM tracts by following the local directionality provided by the diffusion tensor field.

#### 2.4.2.1 Fast marching tractography

A FT technique based on the FM algorithm of Tsitsiklis was first developed by Parker et al. [51, 52, 54, 142]. In this FT approach, referred to as Fast Marching Tractography (FMT), a 3D front was evolved with a speed function proportional to the projection of the front normal to the PDV (Fig. 2.5). A discrete approximation of the front direction was used to drive the evolution through the PDV field, since the original FM method does not correctly handle propagation in oriented domains. The major benefit of the FMT technique is the access to a voxel-based connectivity metric which allows one to rank the resulting connections of the voxels to the seed area. In addition, this connectivity metric can be used to color-code the

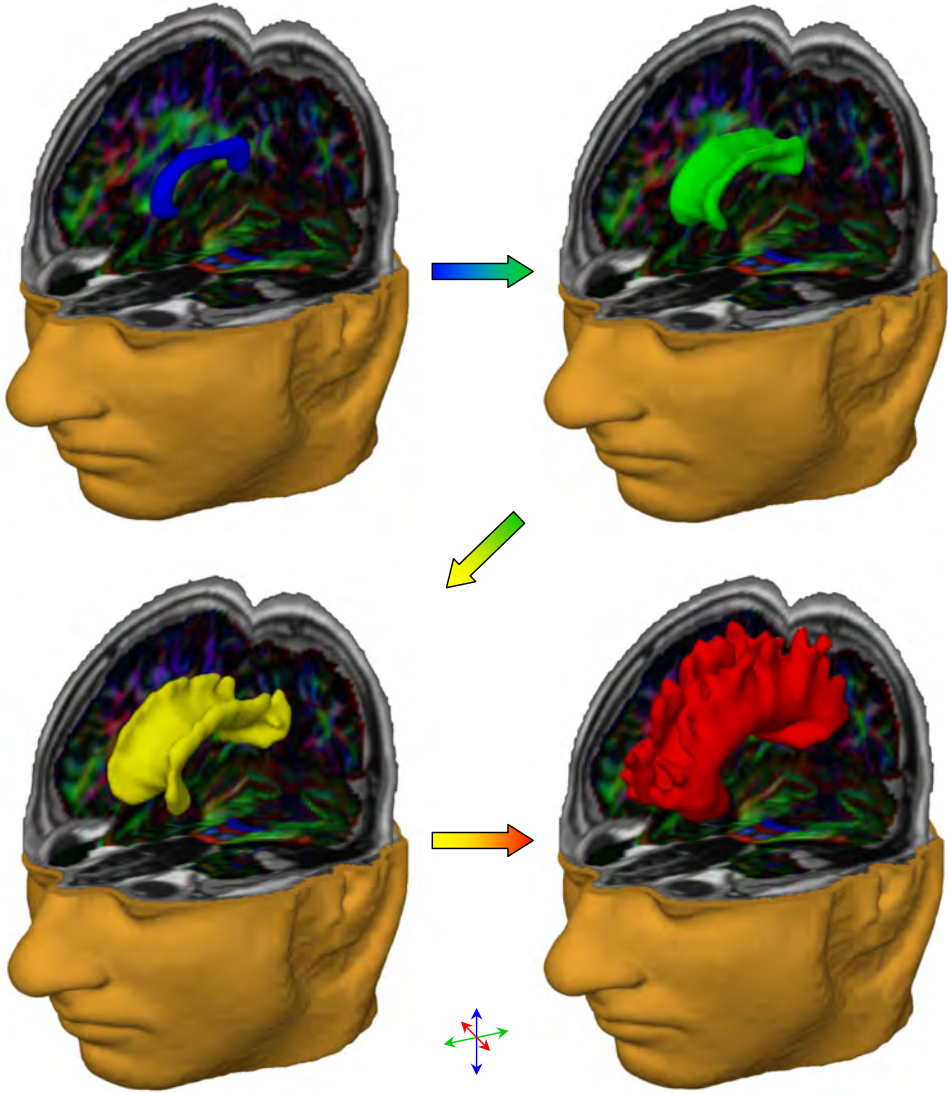


**Figure 2.5.** The 3D front evolution of the callosal fibers using a FM front propagation technique, which is based on the work of Parker et al. [54]. The images represent snapshots of the front propagation in time with increasing time as indicated by the block arrows. In this example, the seed points were placed in the midsagittal area of the corpus callosum. The background maps represent the PDV color-encoded FA maps, embedded in a  $T_1$  context.

reconstructed fiber bundle corresponding to its likelihood or can serve as a threshold criterium to abort fiber reconstruction.

The reliability of the FMT approach was initially verified in the macaque brain and human spinal cord [53, 55]. The accuracy of the FMT algorithm was also investigated in human DTI data, where anterior callosal fibers, the optic radiation, the pyramidal tracts, and the parahippocampal gyrus were reconstructed [56, 58]. Additionally, a reproducibility study, investigating the same three pathways, was performed in the work of Ciccarelli et al. [57].

#### 2.4.2.2 Further developments

An intrinsic property of the FM method is its discrete front evolution, i.e. the possible propagation directions are limited by the number of neighboring voxels, and causes discretization errors. In the work of Tournier et al., an adaptive evolution grid is proposed to overcome this obstacle [66].

In the work of O'Donnell et al., two new approaches were proposed [72]. The first approach models the tractography problem as a heat diffusion equation and is based on the previous work of Batchelor et al. and Gembris et al. [75, 76, 88]. The second approach casts the problem in a Riemannian framework, considering each tensor as a local warping of space, and finding geodesic paths in this space.

Campbell et al. proposed a new speed function to improve the propagation of the 3D front, based on the Root-Mean-Square (RMS) of the diffusion distance along the normal of the front [59, 60]. This speed function is indicative of the likelihood that a tract exists along the direction of propagation and allows for propagation through voxels where tracts cross or branch. Additionally, Campbell et al. developed a level set approach for determining connectivity using both tensor and HARD acquisitions [61, 62, 143]. There, a wavefront was propagated using the fiber Orientation Distribution Function (ODF) derived from the spin displacement probability function.

Another approach is proposed in the work of Kang et al. [105]. This technique is based on successive anisotropic diffusion simulations, which are utilized to construct three dimensional diffusion fronts. There, the fiber pathways are determined by evaluating the distance and orientation from the fronts to their corresponding diffusion seeds.

Other developments in front-evolution based FT approaches are the description of the 3D front propagation speed function in terms of the similarity of adjacent voxels within a tract [64], the incorporation of an anisotropic distance function for front evolution in which the discrete approximation of front normal is not required [63, 99, 103, 104], the integration of prior knowledge and a global optimization criteria [65], and the application of segmentation-based and directional correlation-based region growing techniques [106–108, 144–147].



### 2.4.3 Probabilistic approaches

With some abuse of terminology, a large number of ‘probabilistic’, ‘stochastic’, and ‘statistical’ FT methods have been proposed in both a streamline and a front-propagation based setting. Several heuristic measures have been defined that provide a pseudo-probabilistic index or likelihood for assessing fiber connectivity (e.g., Refs. [67, 83–87, 97]). Nevertheless, these techniques provide a certain relative likelihood which is important to indicate the reliability of different pathways within a tractography result (Fig. 2.6). In this context, several other approaches have

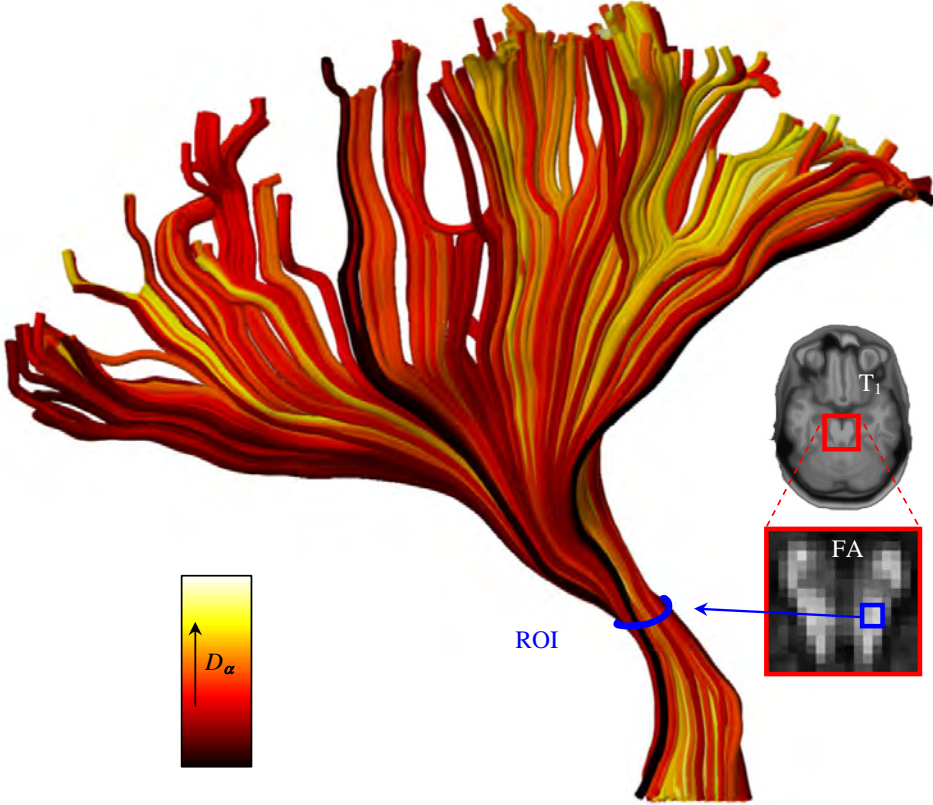


**Figure 2.6.** An example of a pseudo-probabilistic fiber tractography result. For each of the four seed points (as indicated by the ROI) a group of 100 tracts were generated using the ‘random vector’ (RAVE) approach [83]. A pseudo-probabilistic measure  $D_{\alpha}$  is calculated for each tract  $\alpha$  describing the degree of fiber trajectory significance. More specifically, for each tract  $\alpha$ ,  $D_{\alpha}$  represents the median number of times an image voxel is intersected by all tracts  $\{\alpha\}$ , where the median is calculated over only those voxels that are intersected by  $\alpha$ .



been proposed to reconstruct fiber pathways or infer brain connectivity, such as random walk [89, 90, 109], stochastic labeling [38], linear state space models [48], and sequential importance sampling and resampling [93, 94].

In the work of Behrens et al., a probabilistic framework is proposed for estimating the global connectivity, i.e. the probability of the existence of a connection between two points in the brain [79–82]. The Probability Density Functions (PDFs) that describe this global connectivity are estimated using Markov Chain Monte Carlo (MCMC) sampling techniques. The benefit of this Bayesian approach is that it allows one to determine the uncertainty of parameters that define the local fiber direction. A similar statistical framework is proposed in Refs. [77, 78]. There, a path integral approach is used for finding the optimal pathway that connects two points in the brain.

In the work of Jones et al. [91, 92, 100, 101, 110] and Lazar et al. [95, 96], a bootstrap analysis of the fiber trajectories is proposed. This non-parametric statistical approach enables one to determine the uncertainty of specific tract parameters without the need of prior knowledge of the corresponding PDFs. In addition, this bootstrap approach allows one to use any deterministic tractography algorithm in a probabilistic fashion. Furthermore, all sources of variability (including those that cannot be modeled, such as physiologic noise and hardware instabilities) are inherently taken into account.

## 2.5 FT visualization techniques

The objective of any visualization technique is to provide a clear and representative user-friendly view of the data information of interest. For DTI, this task is highly challenging due to its multivariate and 3D spatial nature. With the advent of FT techniques, additional visualization tools are required to provide further aspects of the underlying DTI data, such as the brain connectivity and its corresponding statistical significance. Several FT visualization techniques are discussed in the following sections.

### 2.5.1 Streamlines, streamtubes and hyperstreamlines

The most straightforward way to visualize fiber tracts is the streamline representation. This visualization approach, in which sampled space curves are drawn, has a low computational complexity, which makes it ideal for a fast and interactive exploration of the spatial organization of fiber pathways. For each sample point, a specific local tract characteristic can be assigned using color-encoding schemes providing additional information of the underlying tissue [Fig. 2.7 (a,c) and Fig. 2.8 (a,c)] [148–150].

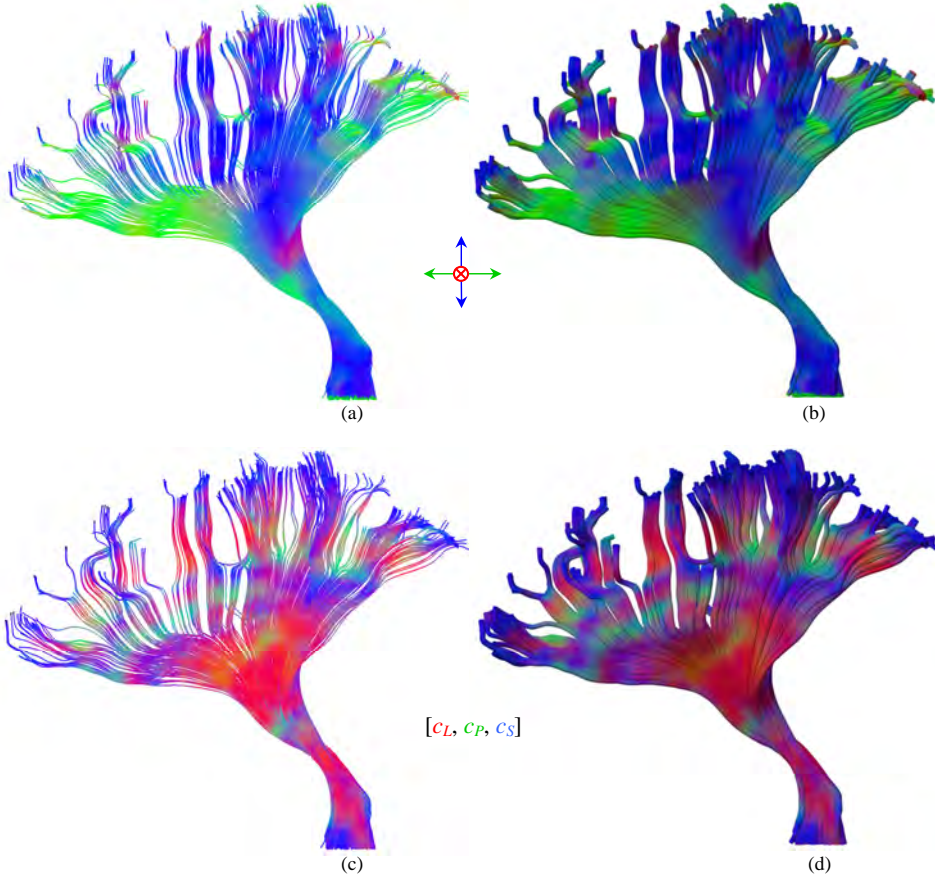


**Figure 2.7.** Streamlines (a,c) and streamtubes (b,d) with color-encoding according to the PDV (a,b) and the geometrical shape measures (c,d).

An alternative to streamlines are streamtubes, i.e. cylindrical 3D tubes which are generated by sweeping a circle along the corresponding streamline. By rendering the streamtube as a lit surface using shading, better directional information may be conveyed to the viewer than with streamlines (e.g., Ref. [21]). Important to note is that the streamtube width does not represent a real physical fiber tract width and is only used to provide a better display quality [Fig. 2.7 (b,d) and Fig. 2.8 (b,d)].

An extension to the streamtube is the hyperstreamline, which in general can be considered as a 3D tube-like structure with its main axis as defined by the corresponding streamline, but with a variable tube width and shape [e.g., see Fig. 2.9 (a)] [151]. Zang et al. first used these hyperstreamlines for DTI data, in which they defined the local cross-sectional shape perpendicular to the axis as an ellipse

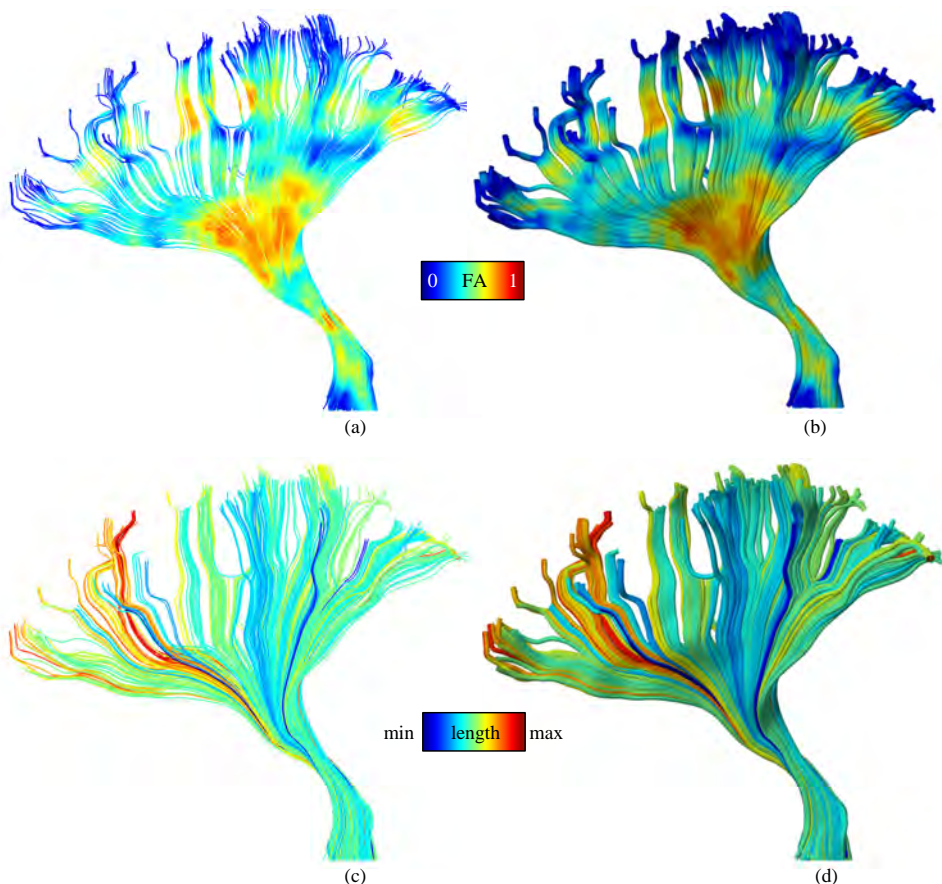


**Figure 2.8.** Streamlines (a,c) and streamtubes (b,d) with color-encoding according to the FA (a,b) and the tract length (c,d).

with axes proportional to  $\lambda_2 \mathbf{e}_2$  and  $\lambda_3 \mathbf{e}_3$  [45, 152]. In other approaches, the local tract shape is related to the fiber density or the degree of statistical confidence of, for instance, the predominant diffusion direction [92, 100–102, 110, 153].

### 2.5.2 Streamsurfaces and volume rendering

In regions with a high IVOH, such as fiber crossing, kissing, and branching configurations, planar diffusion anisotropy is often observed, i.e. a relatively high anisotropy in combination with a non-univocally determined PDV. As proposed by Zhang et al., these configurations can be visualized more clearly using streamsurfaces [45, 152]. In the work of Vilanova et al., a hybrid FT visualization approach is developed combining both streamline and streamsurface methods in a more general

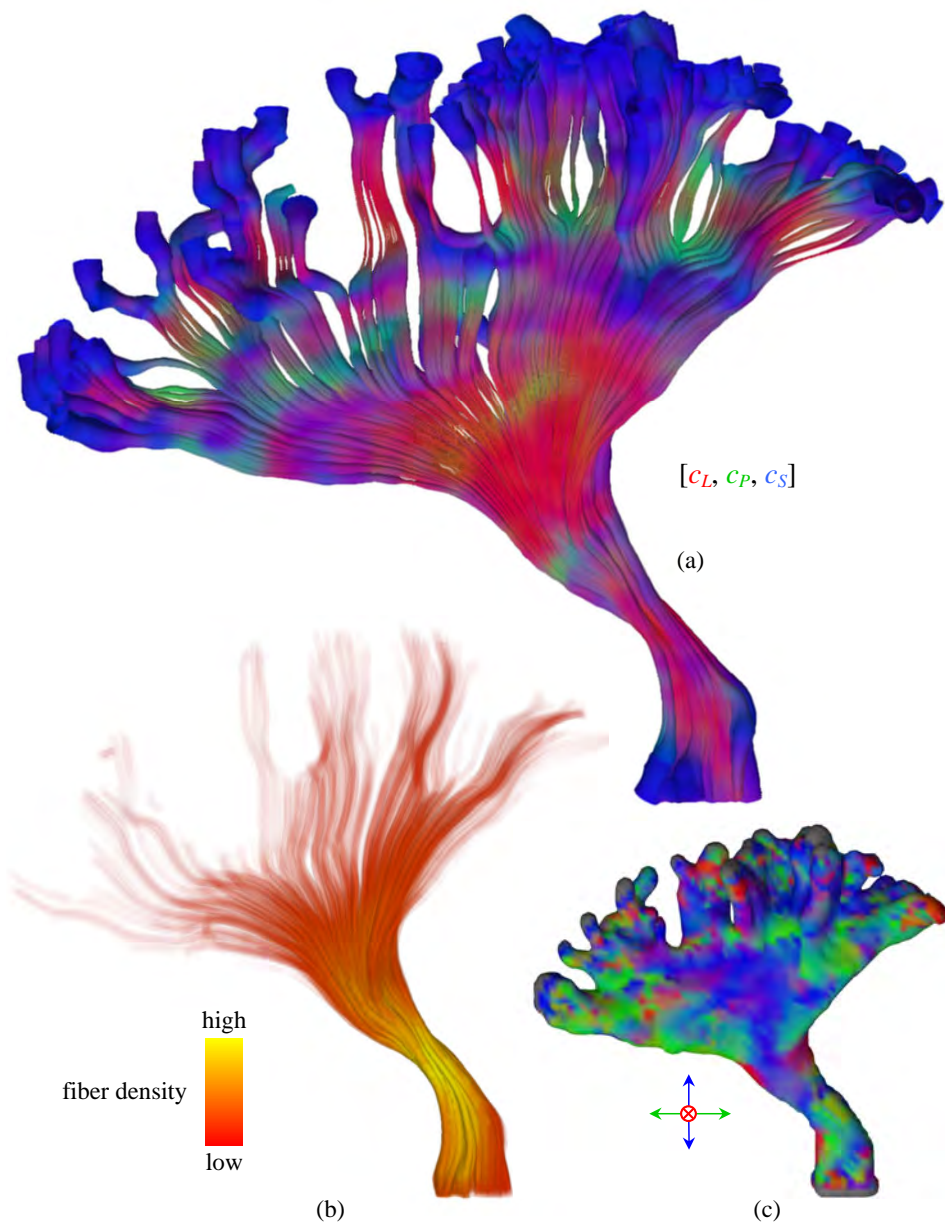


**Figure 2.9.** (a) An example of hyperstreamlines with tube width proportional to  $1 - FA$ . Application of (b) transparency rendering according to the local fiber density and (c) tract iso-surface rendering.

framework [44].

As mentioned in the previous chapter, advanced volume rendering techniques can be applied to visualize several properties of diffusion tensor data (e.g., Ref. [154]). For FT visualization, these techniques can be further modified to represent specific tract characteristics of interest. In Fig. 2.9 (b), for instance, transparency rendering has been applied according to the local fiber tract density [102]. This representation, however, has a high computational cost. Fig. 2.9 (c) shows another visualization approach in which iso-surface rendering is used to represent the fiber structure. This approach has a low computational complexity (comparable to streamlines) and additionally provides a clearer view of the fiber structure's volume.

### 2.5.3 Fiber clustering

It is often more interesting to visualize bundles of fiber tracts, which make up a specific anatomical structure, rather than the local characteristics along a single tract pathway (e.g., see Fig. 2.10). In this context, several fiber tract clustering techniques have been proposed [155–166]. Furthermore, a general framework has been developed to objectively evaluate and validate several of these cluster approaches [167].

A general survey discussing the aforementioned FT visualization techniques in more detail can be found in the work of Vilanova et al. [168].

## 2.6 Applications

The ability to reconstruct axonal fiber bundles in neuronal networks *in vivo* can be important for the understanding of normal and pathological processes affecting brain functions [138, 169, 170]. For example, complex cognitive and motor-oriented processes that involve different functional areas of the brain are mediated by such neural networks [171, 172]. The study of neural association networks is therefore essential for understanding how different functionally active areas interact and, in addition, how the brain reacts to trauma or pathology [87, 173–177].

In combination with fMRI, the availability of a non-invasive technique that outlines fascicles could enhance the understanding of the spatio-temporal interaction of normal brain function and adaptive processes such as brain plasticity [50, 130, 178–182]. Several other studies have been reported such as inter-subject variability and reproducibility FT analyses [37, 56, 57, 183] and FT in several fiber structures of the CNS and the heart [6, 28, 31, 43, 184–187]. As an example, the FT results of a patient with agenesis of the corpus callosum and a normal subject are compared in Fig. 2.11 (see also Fig. 1.10).



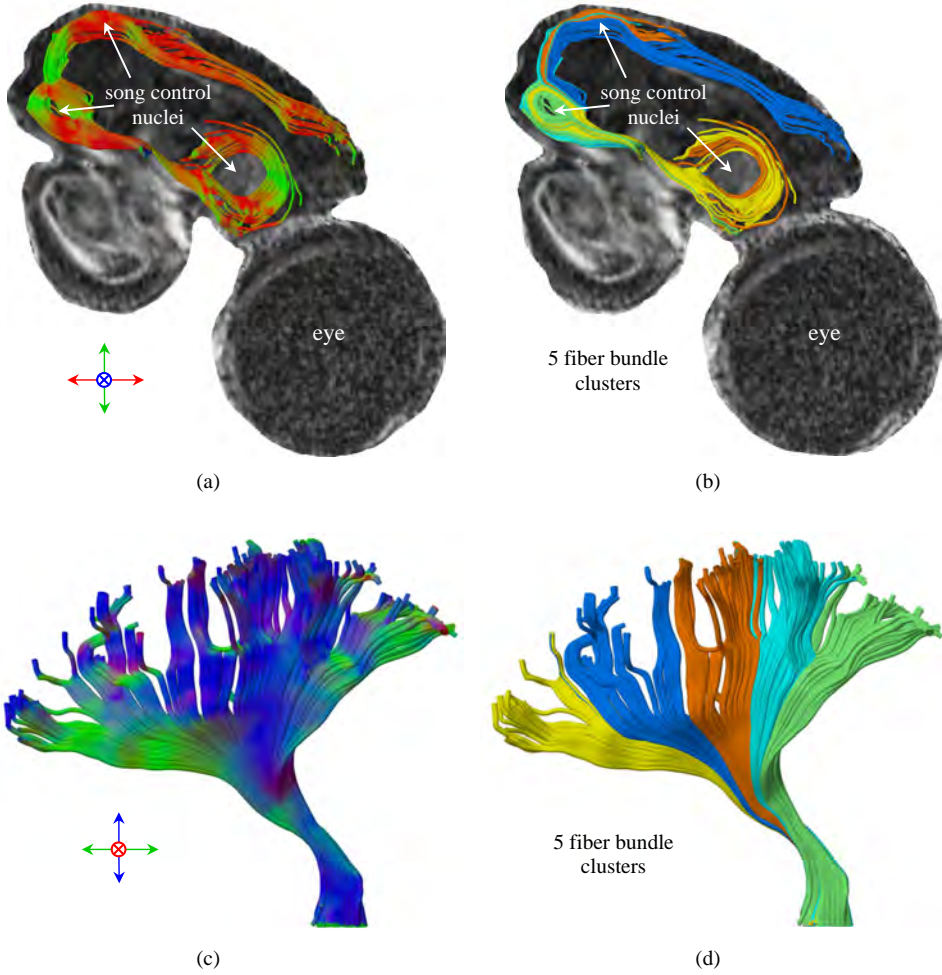


**Figure 2.10.** (a) and (c) represent PDV color-encoded fiber tracts in the starling and human brain, respectively. Using the technique developed in Ref. [155], these fiber tracts are clustered into groups of fiber bundles to enhance visibility (b,d). In this approach, the begin and end point coordinates of the WM fiber tracts are used for creating the 6D feature space for clustering. Then, *k*-means clustering is applied to reconstruct the different fiber bundles. Notice, for instance, that the tract organization in (b) is depicted more clearly than in (a). Additionally, note that fiber tract clustering can be applied to further automate the selection of fiber tract bundles of interest.

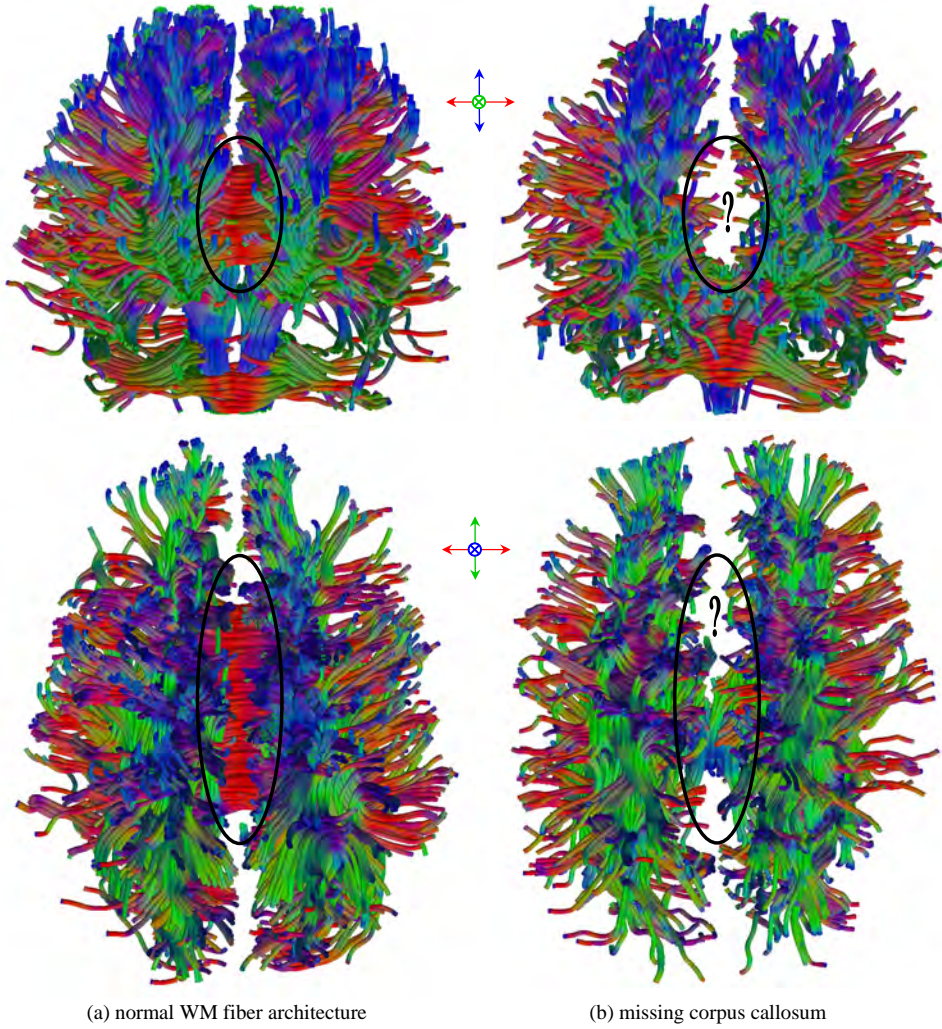


**Figure 2.11.** Coronal (top row) and axial (bottom row) view of (a) the normal and (b) an abnormal (callosal agenesis) WM fiber tract configuration of the human brain. As indicated by the black ellipses, the tracts that connect the cerebral hemispheres, which are visible in (a), are clearly missing in (b).

Finally, FT may play an important role in treatment planning of neurosurgery and dose sculpting in radiation therapy [188–192], morphology of WM fiber bundles [193], and localization of lacunar infarctions [194].

Although this survey is somewhat limited, the growing diversity of reported applications shows great promise for FT to become a well-established research tool in a both clinical and biomedical settings. Moreover, it has the potential to expand our understanding of fiber organization and structural connectivity in the central and peripheral nervous system and in other structured tissues without the need of invasive procedures (Fig. 2.12).

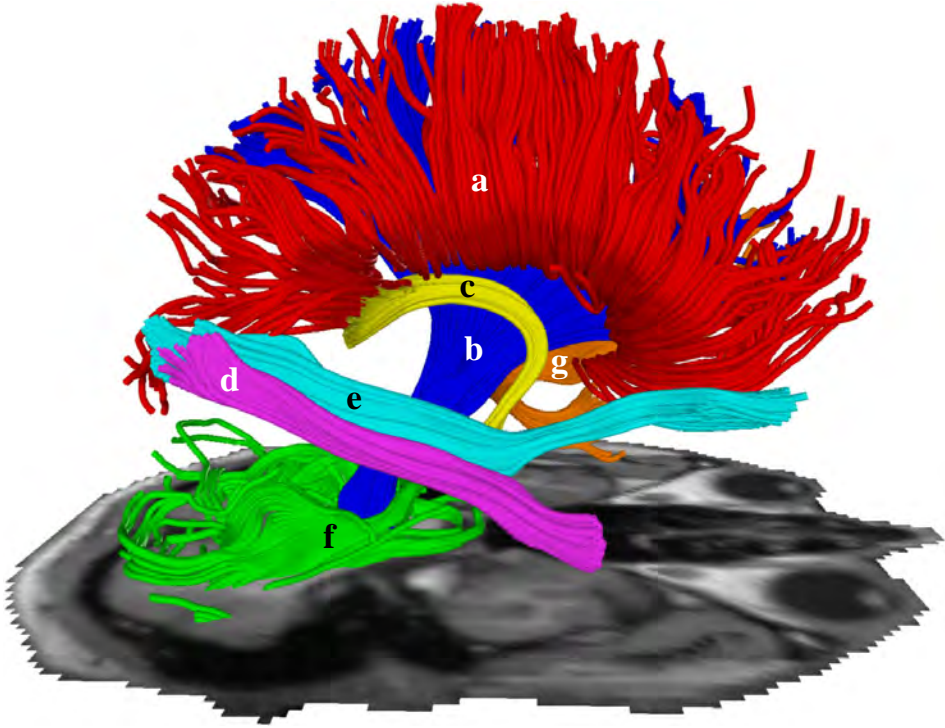


**Figure 2.12.** To illustrate the potential of FT, several WM fiber structures of the human brain are reconstructed: (a) corpus callosum; (b) pyramidal tracts; (c) fornix; (d) inferior longitudinal fasciculus; (e) superior longitudinal fasciculus; (f) ponto-cerebellar tracts; (g) uncinate fasciculus.



## Bibliography

- [1] C. Beaulieu. The basis of anisotropic water diffusion in the nervous system - a technical review. *NMR Biomed*, 15(7-8):435-455, 2002.
- [2] B. Horwitz. The elusive concept of brain connectivity. *NeuroImage*, 19(2):466-470, 2003.
- [3] Y. Kinosada et al. MR tractography: visualization of structure of nerve fiber system from diffusion weighted images with maximum intensity projection method. *Nippon Igaku Hoshasen Gakkai Zasshi*, 53(2):171-179, 1993.
- [4] P.J. Basser. Fiber-tractography via diffusion tensor MRI (DT-MRI). In *ISMRM*, page 1226, 1998.
- [5] P.J. Basser et al. Fiber-tractography in human brain using diffusion tensor MRI (DT-MRI). In *ISMRM*, page 784, 2000.
- [6] P.J. Basser et al. In vivo fiber tractography using DT-MRI data. *Magn Reson Med*, 44(4): 625-632, 2000.
- [7] P.J. Basser et al. Fiber tract following in the human brain using DT-MRI data. *IEICE T Inf Syst*, E85-D:15-21, 2002.
- [8] S. Mori et al. 3D brain fiber reconstruction from diffusion MRI. In *Intl Conf on Func Mapping (HBM)*, 1998.
- [9] S. Mori et al. Three-dimensional tracking of axonal projections in the brain by magnetic resonance imaging. *Ann Neurol*, 45(2):265-269, 1999.
- [10] S. Mori and P.B. Barker. Diffusion magnetic resonance imaging: its principles and applications. *Anat Rec B New Anat*, 257(3):102-109, 1999.
- [11] S. Mori et al. 3D reconstruction of axonal fibers from diffusion tensor imaging using Fiber Assignment by Continuous Tracking (FACT). In *ISMRM*, page 320, 1999.
- [12] S. Mori et al. In vivo visualization of human neural pathways by magnetic resonance imaging. *Ann Neurol*, 47(3):412-414, 2000.
- [13] D. Jones et al. Full representation of white-matter fibre direction on one map via diffusion tensor analysis. In *ISMRM*, page 1743, 1997.
- [14] D.K. Jones et al. Noninvasive assessment of structural connectivity in white matter by diffusion tensor MRI. In *ISMRM*, 1998.
- [15] D.K. Jones et al. Non-invasive assessment of axonal fiber connectivity in the human brain via diffusion tensor MRI. *Magn Reson Med*, 42(1):37-41, 1999.
- [16] P.J. Basser et al. MR diffusion tensor spectroscopy and imaging. *Biophys J*, 66(1):259-267, 1994.
- [17] P.J. Basser and C. Pierpaoli. Microstructural and physiological features of tissues elucidated by quantitative-diffusion-tensor MRI. *J Magn Reson B*, 111(3):209-219, 1996.
- [18] A. Leemans et al. TRACT: Tissue Relative Anisotropy based Curvature Thresholding for deterministic MR diffusion tensor tractography. In *ESMRMB*, page 289, Basle, Switzerland, 2005.
- [19] R. Xue et al. In vivo 3D fiber reconstruction in the rat brain using rapid diffusion tensor imaging. In *ISMRM*, page 323, 1999.
- [20] R. Xue et al. In vivo three-dimensional reconstruction of rat brain axonal projections by diffusion tensor imaging. *Magn Reson Med*, 42(6):1123-1127, 1999.
- [21] M. Catani et al. Virtual in vivo interactive dissection of white matter fasciculi in the human brain. *NeuroImage*, 17(1):77-94, 2002.
- [22] K.H. Kim et al. A novel fiber-tracking method using vector criterion and predictive directivity in diffusion tensor imaging. In *ISMRM*, page 546, 2002.
- [23] D.-S. Kim et al. In vivo mapping of functional domains and axonal connectivity in cat visual cortex using magnetic resonance imaging. *Magn Reson Imaging*, 21(10):1131-1140,

- 2003.
- [24] C. Poupon et al. Regularization of MR diffusion tensor maps for tracking brain white matter bundles. *Lect Notes Comp Sci*, 1496:489–498, 1998.
  - [25] C. Poupon et al. Tracking white matter fascicles with diffusion tensor imaging. In *ISMRM*, page 325, 1999.
  - [26] C. Poupon et al. Regularization of diffusion-based direction maps for the tracking of brain white matter fascicles. *NeuroImage*, 12(2):184–195, 2000.
  - [27] C. Poupon et al. Towards inference of human brain connectivity from MR diffusion tensor data. *Med Image Anal*, 5(1):1–15, 2001.
  - [28] B. Stieltjes et al. Diffusion tensor imaging and axonal tracking in the human brainstem. *NeuroImage*, 14(3):723–735, 2001.
  - [29] W. Li et al. Unsupervised fiber reconstruction of distinct anatomical structure using diffusion tensor MRI. In *ISMRM*, page 1282, 2004.
  - [30] S. Wakana et al. Fiber tract-based atlas of human white matter anatomy. *Radiology*, 230(1):77–87, 2004.
  - [31] T.E. Conturo et al. Tracking neuronal fiber pathways in the living human brain. In *Proc Natl Acad Sci USA*, volume 96, pages 10422–10427, 1999.
  - [32] N.F. Lori et al. Tracking neuronal fibers in the living human brain with diffusion MRI. In *ISMRM*, page 324, 1999.
  - [33] D. Weinstein et al. Tensorlines: advection-diffusion based propagation through diffusion tensor fields. In *IEEE Vis*, pages 249–254, 1999.
  - [34] M. Lazar et al. Axon tractography with tensorlines. In *ISMRM*, page 482, 2000.
  - [35] M. Lazar et al. White matter tractography using diffusion tensor deflection. *Hum Brain Mapp*, 18(4):306–321, 2003.
  - [36] S. Mori et al. A probabilistic map approach for the analysis of DTI-based fiber tracking and its application to white matter injuries. In *ISMRM*, page 1522, 2001.
  - [37] D. Xu et al. A framework for callosal fiber distribution analysis. *NeuroImage*, 17(3):1131–1143, 2002.
  - [38] C.R. Tench et al. Improved white matter fiber tracking using stochastic labeling. *Magn Reson Med*, 48(4):677–683, 2002.
  - [39] C.R. Tench et al. White matter mapping using diffusion tensor MRI. *Magn Reson Med*, 47(5):967–972, 2002.
  - [40] C.-F. Westin et al. Image processing for diffusion tensor magnetic resonance imaging. In *MICCAI*, pages 441–452, 1999.
  - [41] C.-F. Westin et al. Processing and visualization for diffusion tensor MRI. *Med Image Anal*, 6(2):93–108, 2002.
  - [42] L. Zhukov and A.H. Barr. Oriented tensor reconstruction: tracing neural pathways from diffusion tensor MRI. In *IEEE Vis*, pages 387–394, 2002.
  - [43] L. Zhukov and A.H. Barr. Heart-muscle fiber reconstruction from diffusion tensor MRI. In *IEEE Vis*, 2003.
  - [44] A. Vilanova et al. DTI visualization with streamsurfaces and evenly-spaced volume seeding. In *VisSym '04 Joint EG IEEE TCVG Symposium on Visualization*, pages 173–182, 2004.
  - [45] S. Zhang and D. Laidlaw. Elucidating neural structure in diffusion tensor MRI volumes using streamtubes and streamsurfaces. In *ISMRM*, page 505, 2001.
  - [46] R. Blyth et al. Tractography with multiple fibre directions. In *ISMRM*, page 240, 2003.
  - [47] Y. Masutani et al. Rbf-based reconstruction of fiber orientation vector field for the white matter fiber tract modeling. In *ISMRM*, page 1281, 2004.
  - [48] C. Gössl et al. Fiber tracking from DTI using linear state space models: detectability of the pyramidal tract. *NeuroImage*, 16(2):378–388, 2002.

- [49] K. Terajima and T. Nakada. EZ-tracing: a new ready-to-use algorithm for magnetic resonance tractography. *J Nucl Med*, 116(2):147–155, 2002.
- [50] L.-W. Kuo et al. Mapping white matter connectivity with BOLD activated regions using diffusion spectrum imaging and fMRI. In *ISMRM*, page 1286, 2004.
- [51] G.J.M. Parker. Tracing fiber tracts using fast marching. In *ISMRM*, page 85, 2000.
- [52] G.J.M. Parker et al. Distributed anatomical brain connectivity derived from diffusion tensor imaging. In *Inf Process Med Imaging*, pages 106–120, 2001.
- [53] G.J.M. Parker et al. Initial demonstration of in vivo tracing of axonal projections in the macaque brain and comparison with the human brain using diffusion tensor imaging and fast marching tractography. *NeuroImage*, 15(4):779–809, 2002.
- [54] G.J.M. Parker et al. Estimating distributed anatomical connectivity using fast marching methods and diffusion tensor imaging. *IEEE Trans Med Imaging*, 21(5):505–512, 2002.
- [55] C.A.M. Wheeler-Kingshott et al. Investigating cervical spinal cord structure using axial diffusion tensor imaging. *NeuroImage*, 16(1):93–102, 2002.
- [56] O. Ciccarelli et al. Diffusion tractography based group mapping of major white-matter pathways in the human brain. *NeuroImage*, 19(4):1545–1555, 2003.
- [57] O. Ciccarelli et al. From diffusion tractography to quantitative white matter tract measures: a reproducibility study. *NeuroImage*, 18(2):348–359, 2003.
- [58] H.W.R. Powell et al. Noninvasive in vivo demonstration of the connections of the human parahippocampal gyrus. *NeuroImage*, 22(2):740–747, 2004.
- [59] J.S.W. Campbell et al. A geometric flow for white matter fibre tract reconstruction. In *ISBI*, pages 505–508, 2002.
- [60] J.S.W. Campbell et al. White matter fibre tract likelihood evaluated using normalized RMS diffusion distance. In *ISMRM*, page 1130, 2002.
- [61] J.S.W. Campbell et al. White matter fibre tractography and scalar connectivity assessment using fibre orientation likelihood distribution. In *Comp Vision and Patt Recog*, 2004.
- [62] J.S.W. Campbell et al. Comparison of flow- and streamline-based fibre tracking algorithms using an anisotropic diffusion phantom. In *ISMRM*, page 1277, 2004.
- [63] J.S. Duncan et al. Geometric strategies for neuroanatomic analysis from MRI. *NeuroImage*, 23(1):S34–S45, 2004.
- [64] L. Jonasson et al. White matter fiber tract segmentation in DT-MRI using geometric flows. *Med Image Anal*, 9(3):223–236, 2005.
- [65] S. Jbabdi et al. A level set method for building anatomical connectivity paths between brain areas using DTI. In *ISBI*, pages 1024–1027, 2004.
- [66] J.-D. Tournier et al. Diffusion-weighted magnetic resonance imaging fibre tracking using a front evolution algorithm. *NeuroImage*, 20(1):276–288, 2003.
- [67] G. Sela et al. Brain white matter tractography from DT images using global coverings and maximal likelihood connectivity. In *ISMRM*, page 1284, 2004.
- [68] B.C. Vemuri et al. Automatic fiber tractography from DTI and its validation. In *ISBI*, pages 501–504, 2002.
- [69] B.C. Vemuri et al. Fiber tract mapping from diffusion tensor MRI. In *IEEE VLISM*, 2001.
- [70] Y. Cointepas et al. A spin glass based framework to reconstruct brain fiber bundles from images of the water diffusion process. *Information Processes*, 2(1):30–36, 2002.
- [71] J.-F. Mangin et al. A framework based on spin glass models for the inference of anatomical connectivity from diffusion-weighted MR data - a technical review. *NMR Biomed*, 15(7–8): 481–492, 2002.
- [72] L. O’Donnell et al. New approaches to estimation of white matter connectivity in diffusion tensor MRI: elliptic PDEs and geodesics in a tensor-warped space. In *MICCAI*, volume 2489, pages 459–466, 2002.

- [73] W. Li et al. White matter tractography based on minimizing the tracking cost model from diffusion tensor MRI. In *SPIE MI*, volume 5370, pages 1795–1803, 2004.
- [74] J.-C. Weng et al. A global approach for non-invasive axonal fiber tracking on diffusion tensor magnetic resonance image. In *ISMRM*, page 1133, 2002.
- [75] P.G. Batchelor et al. Fibre-tracking by solving the diffusion-convection equation. In *ISMRM*, page 1135, 2002.
- [76] D. Gembris et al. Solving the diffusion equation for fiber tracking in the living human brain. In *ISMRM*, page 1529, 2001.
- [77] D.S. Tuch et al. A path integral approach to white matter tractography. In *ISMRM*, page 791, 2000.
- [78] D.S. Tuch. Mapping cortical connectivity with diffusion MRI. In *ISBI*, pages 392–394, 2002.
- [79] T.E.J. Behrens et al. A probabilistic framework for estimating neural connectivity from diffusion weighted MRI. In *ISMRM*, page 1142, 2002.
- [80] T.E.J. Behrens et al. Bayesian parameter estimation in diffusion weighted MRI. In *ISMRM*, page 1160, 2002.
- [81] T.E.J. Behrens et al. Characterization and propagation of uncertainty in diffusion-weighted MR imaging. *Magn Reson Med*, 50(5):1077–1088, 2003.
- [82] T.E.J. Behrens et al. Delineation of functional subunits in the human cortex from diffusion based connectivity matrices. In *ISMRM*, page 621, 2004.
- [83] M. Lazar and A.L. Alexander. White matter tractography using random vector (RAVE) perturbation. In *ISMRM*, page 539, 2002.
- [84] G.J.M. Parker et al. A framework for a streamline-based Probabilistic Index of Connectivity (PICO) using a structural interpretation of anisotropic diffusion. In *ISMRM*, page 1165, 2002.
- [85] G.J.M. Parker and D.C. Alexander. Probabilistic Monte Carlo based mapping of cerebral connections utilising whole-brain crossing fibre information. In *Inf Process Med Imaging*, volume 2737, pages 684–695, 2003.
- [86] G.J.M. Parker and C.A.M. Haroon, H.A. Wheeler-Kingshott. A framework for a streamline-based Probabilistic Index of Connectivity (pico) using a structural interpretation of MRI diffusion measurements. *J Magn Reson Imaging*, 18(2):242–254, 2003.
- [87] A.T. Toosy et al. Characterizing functionstructure relationships in the human visual system with functional MRI and diffusion tensor imaging. *NeuroImage*, 21(4):1452–1463, 2004.
- [88] P.G. Batchelor et al. Study of connectivity in the brain using the full diffusion tensor from MRI. In *Inf Process Med Imaging*, pages 121–133, 2001.
- [89] P. Hagmann et al. DTI mapping of human brain connectivity: statistical fibre tracking and virtual dissection. *NeuroImage*, 19(3):545–554, 2003.
- [90] B.W. Kreher et al. Potential of fiber tracking and connectivity mapping with multi diffusion tensor. In *ISMRM*, page 1280, 2004.
- [91] D.K. Jones and C. Pierpaoli. Towards a marriage of deterministic and probabilistic tractography methods: bootstrap analysis of fiber trajectories in the human brain. In *ISMRM*, page 1276, 2004.
- [92] D.K. Jones et al. Artifact or architecture? An integrated approach to visualizing uncertainty and partial volume effects in DT-MRI tractography. In *ISMRM*, page 618, 2004.
- [93] M. Björnemo et al. Regularized stochastic white matter tractography using diffusion tensor MRI. In *MICCAI*, pages 435–442, 2002.
- [94] A. Brun et al. White matter tractography using sequential importance sampling. In *ISMRM*, page 1131, 2002.
- [95] M. Lazar et al. Bootstrap analysis of DT-MRI tractography techniques: streamlines and

- tensorlines. In *ISMRM*, page 1527, 2001.
- [96] M. Lazar and A.L. Alexander. Bootstrap white matter tractography (BOOT-TRAC). *NeuroImage*, 24(2):524–532, 2005.
  - [97] Y. Lu et al. Adaptive Bayesian tracking of neuronal fiber pathways from diffusion tensor images. In *ISMRM*, page 1275, 2004.
  - [98] S. Zhang et al. Visualization and analysis of white matter structural asymmetry in diffusion tensor MRI data. *Magn Reson Med*, 51(1):140–147, 2004.
  - [99] P. Staempfli et al. Resolving fiber crossing using advanced fast marching tractography based on diffusion tensor imaging. *NeuroImage*, 30(1):110–120, 2006.
  - [100] D.K. Jones and C. Pierpaoli. Confidence mapping in diffusion tensor magnetic resonance imaging tractography using a bootstrap approach. *Magn Reson Med*, 53(5):1143–1149, 2005.
  - [101] D.K. Jones et al. PASTA: pointwise assessment of streamline tractography attributes. *Magn Reson Med*, 53(6):1462–1467, 2005.
  - [102] S. Delputte et al. Density regularized fiber tractography of the brain white matter using diffusion tensor MRI. In *ISMRM*, page 1309, 2005.
  - [103] M. Jackowski et al. Estimation of anatomical connectivity by anisotropic front propagation and diffusion tensor imaging. *Lect Notes Comp Sci*, 3217:663–671, 2004.
  - [104] M. Jackowski et al. White matter tractography by anisotropic wavefront evolution and diffusion tensor imaging. *Med Image Anal*, 9(5):427–440, 2005.
  - [105] N. Kang et al. White matter fiber tractography via anisotropic diffusion simulation in the human brain. *IEEE Trans Med Imaging*, 24(9):1127–1137, 2005.
  - [106] C.Y. Lin et al. Identify 3-dimensional white matter tracts by directional correlation based regional growing (DCRG) method. In *ISMRM*, page 2163, 2003.
  - [107] S.W. Sun et al. Improving relative anisotropy measurement using directional correlation of diffusion tensors. *Magn Reson Med*, 46(6):1088–1092, 2001.
  - [108] S.W. Sun et al. Directional correlation characterization and classification of white matter tracts. *Magn Reson Med*, 49(2):271–275, 2003.
  - [109] M.A. Koch et al. An investigation of functional and anatomical connectivity using magnetic resonance imaging. *NeuroImage*, 16(1):241–250, 2002.
  - [110] D.K. Jones. Determining and visualizing uncertainty in estimates of fiber orientation from diffusion tensor MRI. *Magn Reson Med*, 49(1):7–12, 2003.
  - [111] S. Mori and P.C.M. van Zijl. Fiber tracking: principles and strategies - a technical review. *NMR Biomed*, 15(7–8):468–480, 2002.
  - [112] R. Bammer et al. In vivo MR tractography using diffusion imaging. *Eur J Radiol*, 45(3):223–234, 2003.
  - [113] E.R. Melhem et al. Diffusion tensor MR imaging of the brain and white matter tractography. *Am J Roentgenol*, 178(1):3–16, 2002.
  - [114] P. Yeung and S. Pope. An algorithm for tracking fluid particles in numerical simulations of homogeneous turbulence. *J Comput Phys*, 79:373–416, 1988.
  - [115] N.F. Lori et al. Diffusion tensor tracking of human neuronal fiber bundles: Simulation of effects of noise, voxel size and data interpolation. In *ISMRM*, page 775, 2000.
  - [116] S. Pajevic et al. A continuous tensor field approximation of discrete DT-MRI data for extracting microstructural and architectural features of tissue. *J Magn Reson*, 154(1):85–100, 2002.
  - [117] A. Aldroubi and P. Basser. Reconstruction of vector and tensor field from sampled discrete data. *Contemp Math*, 247:1–15, 1999.
  - [118] J. Frandsen et al. Regularization of diffusion tensor fields in axonal fibre tracking. In *ISMRM*, page 1221, 2004.

- [119] W. Li et al. Tensor field regularization for diffusion tensor MR images using nonlinear smoothing. In *ISMRM*, page 1222, 2004.
- [120] O. Coulon et al. A regularization scheme for diffusion tensor magnetic resonance images. *Lect Notes Comp Sci*, 2082:92–105, 2001.
- [121] O. Coulon et al. Diffusion tensor magnetic resonance image regularization. *Med Image Anal*, 8(1):47–67, 2004.
- [122] G.J.M. Parker et al. Nonlinear smoothing for reduction of systematic and random errors in diffusion tensor imaging. *J Magn Reson Imaging*, 11(6):702–710, 2000.
- [123] T. McGraw et al. DT-MRI denoising and neuronal fiber tracking. *Med Image Anal*, 8(2):95–111, 2004.
- [124] Z. Wang et al. A constrained variational principle for direct estimation and smoothing of the diffusion tensor field from complex DWI. *IEEE Trans Med Imaging*, 23(8):930–939, 2004.
- [125] J. Sijbers et al. Adaptive anisotropic noise filtering for magnitude MR data. *Magn Reson Imaging*, 17(10):1533–1539, 1999.
- [126] N.F. Lori et al. Diffusion tensor fiber tracking of human brain connectivity: acquisition methods, reliability analysis and biological results. *NMR Biomed*, 15(7–8):493–515, 2002.
- [127] W.H. Press et al. *Numerical recipes in C: the art of scientific computing*. Cambridge University Press, New York, NY, USA, 1992.
- [128] B. Wünsche et al. DTI volume rendering techniques for visualising the brain anatomy. *Int Congr Ser*, 1281:80–85, 2005.
- [129] E. Pagani et al. A method for obtaining tract-specific diffusion tensor MRI measurements in the presence of disease: application to patients with clinically isolated syndromes suggestive of multiple sclerosis. *NeuroImage*, 26(1):258–265, 2005.
- [130] P. Thottakara et al. Application of Brodmann’s area templates for ROI selection in white matter tractography studies. *NeuroImage*, 29(3):868–878, 2006.
- [131] M. Lazar and A.L. Alexander. White matter tractography algorithms error analysis. *NeuroImage*, 20(2):1140–1153, 2003.
- [132] J.-D. Tournier et al. Limitations and requirements of diffusion tensor fiber tracking: an assessment using simulations. *Magn Reson Med*, 47(4):701–708, 2002.
- [133] M. Lazar et al. Axial asymmetry of water diffusion in brain white matter. *Magn Reson Med*, 54(4):860–867, 2005.
- [134] A.W. Anderson. Theoretical analysis of the effects of noise on diffusion tensor imaging. *Magn Reson Med*, 46(6):1174–1188, 2001.
- [135] A.L. Alexander et al. Analysis of partial volume effects in diffusion-tensor MRI. *Magn Reson Med*, 45(5):770–780, 2001.
- [136] T.R. Barrick and C.A. Clark. Singularities in diffusion tensor fields and their relevance in white matter fiber tractography. *NeuroImage*, 22(2):481–491, 2004.
- [137] D.S. Tuch et al. High angular resolution diffusion imaging reveals intravoxel white matter fiber heterogeneity. *Magn Reson Med*, 48(4):577–582, 2002.
- [138] R. Watts et al. Fiber tracking using magnetic resonance diffusion tensor imaging and its applications to human brain development. *Ment Retard Dev Disabil Res Rev*, 9(3):168–177, 2003.
- [139] J.A. Sethian. A fast marching level set method for monotonically advancing fronts. In *Proc Natl Acad Sci USA*, pages 1591–1595, 1996.
- [140] S. Osher and J.A. Sethian. Fronts propagating with curvature-dependent speed: algorithms based on HamiltonJacobi formulations. *J Comput Phys*, 79(1):12–49, 1988.
- [141] J.A. Sethian. *Level set methods: evolving interfaces in geometry, fluid mechanics, computer vision, and materials science*. Cambridge monographs on applied and computational

- mathematics. Cambridge University Press, Cambridge, U.K., 1996.
- [142] J.N. Tsitsiklis. Efficient algorithms for globally optimal trajectories. *IEEE T Automat Contr*, 40:1528–1538, 1995.
  - [143] J.S.W. Campbell et al. Flow-based fiber tracking with diffusion tensor and Q-ball data: validation and comparison to principal diffusion direction techniques. *NeuroImage*, 27(4):725–736, 2005.
  - [144] C.-Y. Lin et al. Unsupervised identification of white matter tracts in a mouse brain using a directional correlation-based region growing (DCRG) algorithm. *NeuroImage*, 28(2):380–388, 2005.
  - [145] Z. Wang and B.C. Vemuri. Tensor field segmentation using region based active contour model. *Lect Notes Comp Sci*, 3024:304–315, 2004.
  - [146] M. Rousson et al. Level set and region based surface propagation for diffusion tensor MRI segmentation. *Lect Notes Comp Sci*, 3117:123–134, 2004.
  - [147] C. Feddern et al. Level-set methods for tensor valued images. In *IEEE VLSM*, pages 65–72, 2003.
  - [148] A. Leemans et al. A geometric color scheme for visualizing diffusion tensor magnetic resonance fiber pathways. In *BHPA*, Brussels, Belgium, 2004.
  - [149] C. Pierpaoli. Oh no! one more method for color mapping of fiber tract direction using diffusion MR imaging data. In *ISMRM*, page 1741, 1997.
  - [150] S. Pajevic and C. Pierpaoli. Color schemes to represent the orientation of anisotropic tissues from diffusion tensor data: application to white matter fiber tract mapping in the human brain. *Magn Reson Med*, 42(3):526–540, 1999.
  - [151] T. Delmarcelle and L. Hesselink. Visualizing second order-tensor fields with hyperstreamlines. *IEEE CG&A*, 13(4):25–33, 1993.
  - [152] S. Zhang et al. Visualizing diffusion tensor MR images using streamtubes and streamsurfaces. *IEEE T Vis Comput Gr*, 9(4):454–462, 2003.
  - [153] H.-H. Ehrlicke et al. Visualizing MR diffusion tensor fields by dynamic fiber tracking and uncertainty mapping. *Comput Graph*, (in press) 2006.
  - [154] G. Kindlmann et al. Strategies for direct volume rendering of diffusion tensor fields. *IEEE T Vis Comput Gr*, 6(2):124–138, 2000.
  - [155] A. Leemans et al. End point clustering for diffusion tensor white matter fiber bundle tractography. In *ESMRMB*, pages 129–130, Basle, Switzerland, 2005.
  - [156] Z. Ding et al. Classification and quantification of neuronal fiber pathways using diffusion tensor MRI. *Magn Reson Med*, 49(4):716–721, 2003.
  - [157] I. Corouge et al. A statistical shape model of individual fiber tracts extracted from diffusion tensor MRI. In *MICCAI*, pages 671–679, 2004.
  - [158] I. Corouge et al. Towards a shape model of white matter fiber bundles using diffusion tensor MRI. In *ISBI*, pages 344–347, 2004.
  - [159] A. Brun et al. Clustering fiber traces using normalized cuts. In *MICCAI*, pages 368–375, 2004.
  - [160] A. Brun et al. Coloring of DT-MRI fiber traces using Laplacian eigenmaps. *Lect Notes Comp Sci*, 2809:564–572, 2003.
  - [161] L. Jonasson et al. Fiber tracts of high angular resolution diffusion MRI are easily segmented with spectral clustering. In *ISMRM*, page 1310, 2005.
  - [162] L. O’Donnell and C.-F. Westin. White matter tract clustering and correspondence in populations. In *Lect Notes Comp Sci*, volume 3749, pages 140–147, 2005.
  - [163] S. Zhang and D.H. Laidlaw. DTI fiber clustering and cross-subject cluster analysis. In *ISMRM*, page 2727, 2005.
  - [164] S. Zhang and D.H. Laidlaw. Hierarchical clustering of streamtubes. Technical Report



- CS-02-18, Brown University Computer Science Department, August 2002.
- [165] J.S. Shimony et al. Automated fuzzy clustering of neuronal pathways in diffusion tensor tracking. In *ISMRM*, page 540, 2002.
  - [166] P.G. Batchelor et al. Classification of bundles of white matter tract from DTI without registration. In *ESMRMB*, page 101, 2003.
  - [167] B. Moberts et al. DTI visualization with streamsurfaces and evenly-spaced volume seeding. In *IEEE Vis*, pages 65–72, 2005.
  - [168] A. Vilanova et al. *Visualization and image processing of tensor fields*, chapter An introduction to visualization of diffusion tensor imaging and its applications, pages 121–153. Springer Verlag series Mathematics and Visualization, 2006. ISBN 3-540-25032-8.
  - [169] W.D. Taylor et al. Diffusion tensor imaging: background, potential, and utility in psychiatric research. *Biol Psychiatry*, 55(3):201–207, 2004.
  - [170] D.K. Jones et al. Age effects on diffusion tensor magnetic resonance imaging tractography measures of frontal cortex connections in schizophrenia. *Hum Brain Mapp*, 27(3):230–238, 2005.
  - [171] R.G. Henry et al. Subcortical pathways serving cortical language sites: initial experience with diffusion tensor imaging fiber tracking combined with intraoperative language mapping. *NeuroImage*, 21(2):616–622, 2004.
  - [172] N. Shinoura et al. Fibers connecting the primary motor and sensory areas play a role in grasp stability of the hand. *NeuroImage*, 25(3):936–941, 2005.
  - [173] N.K. Iwata et al. Corticospinal tract and corticobulbar tract dysfunction in ALS: combined study using transcranial magnetic stimulation and diffusion tensor tractography. *Int Congr Ser*, 1278:181–184, 2005.
  - [174] X. Lin et al. Importance sampling in MS: Use of diffusion tensor tractography to quantify pathology related to specific impairment. *J Neurol Sci*, 237(1–2):13–19, 2005.
  - [175] D.K. Jones et al. A diffusion tensor magnetic resonance imaging study of frontal cortex connections in very-late-onset schizophrenia-like psychosis. *Am J Geriatr Psychiatry*, 13(12):1092–1099, 2005.
  - [176] M. Catani et al. Occipito-temporal connections in the human brain. *Brain*, 126(9):2093–2107, 2003.
  - [177] C. van Pul et al. Fiber tracking in newborns with perinatal hypoxic-ischemia at birth and at 3 months. *Radiology*, (in press) 2005.
  - [178] M. Guye et al. Combined functional MRI and tractography to demonstrate the connectivity of the human primary motor cortex in vivo. *NeuroImage*, 19(4):1349–1360, 2003.
  - [179] S.L. Heller et al. Evidence of cerebral reorganization following perinatal stroke demonstrated with fMRI and DTI tractography. *J Clin Imaging*, 29(4):283–287, 2005.
  - [180] A.W. Song et al. Functional activation using apparent diffusion coefficient-dependent contrast allows better spatial localization to the neuronal activity: evidence using diffusion tensor imaging and fiber tracking. *NeuroImage*, 20(2):955–961, 2003.
  - [181] G. De Groof et al. Seasonal changes in neuronal connectivity in the songbird brain discerned by repeated in vivo DTI. In *ISMRM*, page 715, 2005.
  - [182] G. De Groof et al. In vivo diffusion tensor imaging (DTI) of brain subdivisions and vocal pathways in songbirds. *NeuroImage*, 29(3):754–763, 2006.
  - [183] U. Bürgel et al. White matter fiber tracts of the human brain: three-dimensional mapping at microscopic resolution, topography and intersubject variability. *NeuroImage*, 29(4):1092–1105, 2006.
  - [184] L. Concha et al. Diffusion tensor tractography of the limbic system. *AJNR Am J Neuroradiol*, 26(9):2267–2274, 2005.
  - [185] H.U. Voss et al. Fiber tracking in the cervical spine and inferior brain regions with reversed



- gradient diffusion tensor imaging. *Magn Reson Imaging*, (in press) 2006.
- [186] S. Mori et al. Imaging cortical association tracts in the human brain using diffusion-tensor-based axonal tracking. *Magn Reson Med*, 47(2):215–223, 2002.
  - [187] D.K. Jones et al. Isotropic resolution diffusion tensor imaging with whole brain acquisition in a clinically acceptable time. *Hum Brain Mapp*, 15(4):216–230, 2002.
  - [188] M. Kinoshita et al. Fiber-tracking does not accurately estimate size of fiber bundle in pathological condition: initial neurosurgical experience using neuronavigation and subcortical white matter stimulation. *NeuroImage*, 25(2):424–429, 2005.
  - [189] C. Nimsy et al. Three-dimensional visualization of major white matter tracts by diffusion tensor imaging-based fiber tracking. *Int Congr Ser*, 1268:703–706, 2004.
  - [190] C. Nimsy et al. Visualization strategies for major white matter tracts identified by diffusion tensor imaging for intraoperative use. *Int Congr Ser*, 1281:793–797, 2005.
  - [191] C. Nimsy et al. Intraoperative visualization of the pyramidal tract by diffusion-tensor-imaging-based fiber tracking. *NeuroImage*, (in press) 2005.
  - [192] I.-F. Talos et al. Diffusion tensor and functional MRI fusion with anatomical MRI for image-guided neurosurgery. *Lect Notes Comp Sci*, 2878:407–415, 2003.
  - [193] H. Huang et al. DTI tractography based parcellation of white matter: application to the mid-sagittal morphology of corpus callosum. *NeuroImage*, 26(1):195–205, 2005.
  - [194] J.S. Lee et al. Fiber tracking by diffusion tensor imaging in corticospinal tract stroke: topographical correlation with clinical symptoms. *NeuroImage*, 26(3):771–776, 2005.

Part II

Diffusion Tensor Image  
Processing



## Chapter 3

# Simulated diffusion tensor phantom

The work in this chapter has been published in

*A. Leemans, J. Sijbers, M. Verhoye, A. Van der Linden, and D. Van Dyck, “Mathematical framework for simulating diffusion tensor MR neural fiber bundles”, Magnetic Resonance in Medicine, Vol. 53, Nr. 4, p. 944–953, 2005.*

### 3.1 Abstract

WM FT is known to be an important application of DTI. For the quantitative evaluation of several FT properties, such as accuracy, noise sensitivity, and robustness, synthetic ground-truth DTI data are required. Moreover, an accurate simulated phantom is also required for optimization of the user-defined tractography parameters, and objective comparisons between FT algorithms. Therefore, in this chapter, a mathematical framework for simulating DTI data, based on the physical properties of WM fiber bundles, is developed. A model of a WM fiber bundle is obtained by parameterizing the various features that characterize this bundle. Three different synthetic DTI models were evaluated using experimental data in order to test the developed methodology, and to determine the optimum model and parameter settings for constructing a realistic simulated DTI phantom. Several examples of how the mathematical framework can be applied to compare FT algorithms are presented.

## 3.2 Introduction

An important application of DTI is the reconstruction of the 3D WM fiber network using DTT and is based on the assumption that it can accurately retrieve the spatial information of the underlying fiber network, using the available diffusion information of the corresponding tensor field. As described in the previous chapter, DTT provides exciting new opportunities to study the CNS anatomy, and has generated much enthusiasm, resulting in the development of a large number of FT algorithms. Although qualitative results may be very valuable, the lack of a gold standard still precludes an objective quantitative evaluation of these FT algorithms with respect to precision, accuracy, reproducibility, etc. Although histology has been used to identify major WM fiber bundles, and can provide complementary anatomical information for DTI [1–5], technical difficulties related to tissue preparation impede a quantitative validation of the 3D WM fiber tract reconstruction. In the work of Lin et al., a comparison study between DTI and MEMRI has demonstrated good correspondence between the PDV and the tangential vector of the optic tract in rats, as seen in the  $T_1$ -weighted image [6]. However, the  $Mn^{2+}$  enhancement in large fiber bundles is often diffuse, making the fiber orientation indistinct. In addition, long fibers are difficult to study due to a considerable decay of the  $Mn^{2+}$  enhancement within the time frame to transport the  $Mn^{2+}$  ions over the full length of these fibers.

To address this lack of a gold standard, an accurate simulated DTI phantom is necessary to evaluate the numerous criteria that characterize a FT algorithm. Only with such a phantom can a comparison between different FT algorithms yield decisive answers regarding accuracy, precision, robustness, reproducibility, etc. In addition, with such a phantom one could study the effect of DTI data processing prior to diffusion tensor and fiber tract computing (e.g., image coregistration, noise filtering, and correction of motion artifacts) quantitatively. For example, fiber tracking requires geometrically coregistered DW images. With the use of a simulated DTI phantom, the sensitivity of FT algorithms with respect to the misaligned DW images can be studied.

Although the need for an accurate simulated DTI phantom has been emphasized in the literature (e.g., Refs. [7–9]), only a few tractography-related articles have described a technique for computing a simulated DTI phantom. In Ref. [10], a continuous diffusion vector field is used to describe the tracts, omitting information that is contained in the remaining DOF of the diffusion tensor field. Other methods use the two-dimensional (2D) continuous diffusion tensor field, where the tracts are represented by rings with a fixed width [11, 12]. More advanced techniques employ a cylindrical tube in a 3D continuous diffusion tensor field that has a curved trajectory given by, for instance, a circular helix (e.g., Refs. [8, 13, 14]). Within this tube, the diffusion anisotropy measure that characterizes the WM fiber pathway is

set to a predefined threshold. However, none of these DTI tract phantoms simulate a smooth transition between the actual WM pathway and the surrounding tissue, although the diffusion tensor field itself, which is used as ‘background tissue’, is continuous. Also, as suggested by Basser, nonconstant curvature and torsion within a single tract, possibly derived from experimental data, should be employed to give a more realistic representation of the WM fiber pathway [15].

In the following sections, a mathematical framework is developed for simulating a DTI phantom that represents the physical properties of a WM fiber pathway within its surrounding tissue and models the cross-sectional dependency of the fiber density, based on the corresponding FA and MD. The objective of this mathematical framework is to simulate ground-truth DTI data of a corresponding WM fiber system in order to 1) quantitatively evaluate the numerous criteria that characterize a FT algorithm, 2) optimize the user-defined tractography parameters, and 3) objectively compare different FT algorithms. The analytical form of the tract allows the simulation of more complex configurations in an elegant way (e.g., branching and crossing of WM fiber bundles). Finally, different synthetic DTI models are evaluated using experimental DTI data, and several applications to WM fiber tracking are described.

### 3.3 Theory

This section presents the development of the mathematical framework for simulating DTI data based on the physical properties of WM fiber bundles. These properties can be summarized as follows. A realistic fiber trajectory should exhibit a nonconstant curvature and torsion, and have a certain extent. Also, a smooth transition between the diffusion tensor field of the WM fiber bundle and the diffusion tensor field of the surrounding tissue should be incorporated.

The first step in the modeling process is to generate a set of points that define the position and curvature of the WM fiber pathway. A piecewise continuous 3D space curve can be associated with these points, which represents the skeleton of the fiber bundle trajectory. This space curve is then convolved with a model kernel to obtain the physical extent that defines the cross-sectional dependency of the fiber density. The PDV field is assessed by a weighted sum of the vector lines that define the backbone of the WM fiber bundle. Finally, the diffusion tensor field is calculated using the PDV field and the eigenvalues obtained from the model. Throughout this section, the dimensions of the synthetic DTI data are considered to be in units of voxel size.

### 3.3.1 Backbone of the fiber bundle

The first step in the modeling process is the parameterization of a WM fiber. The fiber backbone is constructed from a set of spatial coordinates  $\{\mathbf{r}_i\}$  (with  $i = 1, \dots, N$ ), where the direction of the vector line  $\mathbf{\Delta}_i = \mathbf{r}_{i+1} - \mathbf{r}_i$  smoothly varies for consecutive points  $\mathbf{r}_i$ . The vector lines  $\mathbf{\Delta}_i$  describe a piecewise differential 3D space curve, which can be represented by

$$t(\mathbf{r}) = \sum_{i=1}^{N-1} \int_0^1 \delta[\mathbf{r} - (\mathbf{r}_i + \alpha \mathbf{\Delta}_i)] d\alpha, \quad (3.1)$$

where  $\delta$  denotes the Dirac-delta distribution and  $\alpha$  is a parameterization variable. Basically,  $t(\mathbf{r}) = 1$  for the positions  $\mathbf{r}$  that define the backbone and  $t(\mathbf{r}) = 0$  elsewhere. In the following text, and without loss of generality, it will be assumed that the length of the vectors  $\mathbf{\Delta}_i$  is constant, i.e.  $\forall i : \|\mathbf{\Delta}_i\| = \Delta$ .

### 3.3.2 Physical thickness of the fiber bundle

After the coordinates that represent the center of the WM fiber bundle have been defined, a parameter that models the physical thickness should be incorporated to refine the physical properties of the fiber tract. This thickness represents the cross-sectional dependency of the fiber density, which is assumed here to be nonconstant. It can be introduced in a natural way by convolving the fiber trajectory  $t(\mathbf{r})$ , defined in Eq. (3.1), with a proper kernel  $k(\mathbf{r})$ . The resulting convolution function  $T(\mathbf{r})$  is calculated as:

$$T(\mathbf{r}) = t(\mathbf{r}) * k(\mathbf{r}) = \sum_{i=1}^{N-1} \underbrace{\int_0^1 k[\mathbf{r} - (\mathbf{r}_i + \alpha \mathbf{\Delta}_i)] d\alpha}_{\equiv T^i(\mathbf{r})}. \quad (3.2)$$

Consequently, the continuously varying quantitative measures FA and MD can be associated with every point within the WM fiber bundle, as follows:

$$FA(\mathbf{r}) = \frac{FA_M T(\mathbf{r})}{T_M} \quad ; \quad MD(\mathbf{r}) = \frac{MD_M T(\mathbf{r})}{T_M}, \quad (3.3)$$

where  $FA_M$  and  $MD_M$  are predefined values that control the maximum FA and maximum MD, respectively, and  $T_M = \max_{\mathbf{r}} T(\mathbf{r})$ . In Eq. (3.3),  $T(\mathbf{r})/T_M$  can be considered as the normalized cross-sectional dependency of the fiber density, confining  $FA(\mathbf{r})$  and  $MD(\mathbf{r})$  to their predefined value range. Depending on the kernel  $k(\mathbf{r})$ , different diffusion characteristics within the fiber can be generated by defining another model to describe the physical thickness, which is equivalent to choosing a different model kernel. Since FA and MD are independent, different model kernels  $k(\mathbf{r})$  can be associated with these diffusion measures. To illustrate this concept, three specific models (solid, Gaussian, and saturated) are elaborated.

### 3.3.2.1 Solid model

The techniques that are currently used to simulate a 3D WM fiber phantom (e.g., Ref. [13]) can be obtained by using a rectangle function  $\Pi$ , which is defined as:

$$k_r(\mathbf{r}) = \Pi\left(\frac{\|\mathbf{r}\|}{w}\right) = \begin{cases} 0 & \Leftrightarrow \|\mathbf{r}\| > w \\ 1 & \Leftrightarrow \|\mathbf{r}\| \leq w \end{cases}, \quad (3.4)$$

where  $w$  is the parameter that describes the width of the fiber bundle [Figs. 3.1 (a) and 3.1 (d)]. After some calculations, the convolution of the fiber tract  $t(\mathbf{r})$  from Eq. (3.1) with  $k_r(\mathbf{r})$  is given by:

$$T_r(\mathbf{r}) = \sum_{i=1}^{N-1} \left| \alpha_i^+ \Pi\left(\alpha_i^+ - \frac{1}{2}\right) - \alpha_i^- \Pi\left(\alpha_i^- - \frac{1}{2}\right) + H(1 - \alpha_i^-) - H(1 - \alpha_i^+) \right|, \quad (3.5)$$

where  $H$  represents the Heaviside step function and

$$\alpha_i^\pm \equiv \alpha_i^\pm(\mathbf{r}) = \Re \left\{ \frac{\hat{\Delta}_i \cdot (\mathbf{r} - \mathbf{r}_i) \pm \sqrt{\frac{w^2}{4} - \|\mathbf{d}_i(\mathbf{r})\|^2}}{\Delta} \right\} \quad (3.6)$$

with

$$\begin{cases} \hat{\Delta}_i = \Delta_i / \Delta \\ \mathbf{d}_i(\mathbf{r}) = \hat{\Delta}_i \times (\mathbf{r} - \mathbf{r}_i) \end{cases}. \quad (3.7)$$

Here,  $\Re\{\cdot\}$  denotes the real part. Also note that  $\|\mathbf{d}_i(\mathbf{r})\|$  indicates the distance between the position  $\mathbf{r}$  and the line defined by  $\hat{\Delta}_i$ , and that  $T_r(\mathbf{r}) = 0$  for  $\|\mathbf{d}_i(\mathbf{r})\| \geq w/2$ . Therefore,  $T_r(\mathbf{r}) = FA_M$  is finally taken for  $\|\mathbf{d}_i(\mathbf{r})\| < w/2$ . This model assumes no continuous cross-sectional dependency of the microstructural fiber organization, resulting in a cylindrical tube with constant FA and MD.

### 3.3.2.2 Gaussian model

A second, more realistic model to characterize the physical extent of a WM fiber bundle is obtained by convolving the fiber backbone with a 3D Gaussian kernel:

$$k_g(\mathbf{r}) = e^{-\frac{\|\mathbf{r}\|^2}{2\sigma^2}}, \quad (3.8)$$

where the standard deviation  $\sigma$  controls the extent of the fiber bundle [Figs. 3.1 (b) and 3.1 (e)]. The convolution of the fiber tract  $t(\mathbf{r})$  with  $k_g(\mathbf{r})$ , denoted as  $T_g(\mathbf{r})$ , is given by (see Appendix B):

$$T_g(\mathbf{r}) = \frac{\sigma}{\Delta} \sqrt{\frac{\pi}{2}} \sum_{i=1}^{N-1} e^{-\frac{\|\mathbf{d}_i(\mathbf{r})\|^2}{2\sigma^2}} \left\{ \operatorname{erf} \left[ \frac{\hat{\Delta}_i \cdot (\mathbf{r} - \mathbf{r}_i)}{\sqrt{2}\sigma} \right] + \operatorname{erf} \left[ \frac{\hat{\Delta}_i \cdot (\mathbf{r}_{i+1} - \mathbf{r})}{\sqrt{2}\sigma} \right] \right\}. \quad (3.9)$$



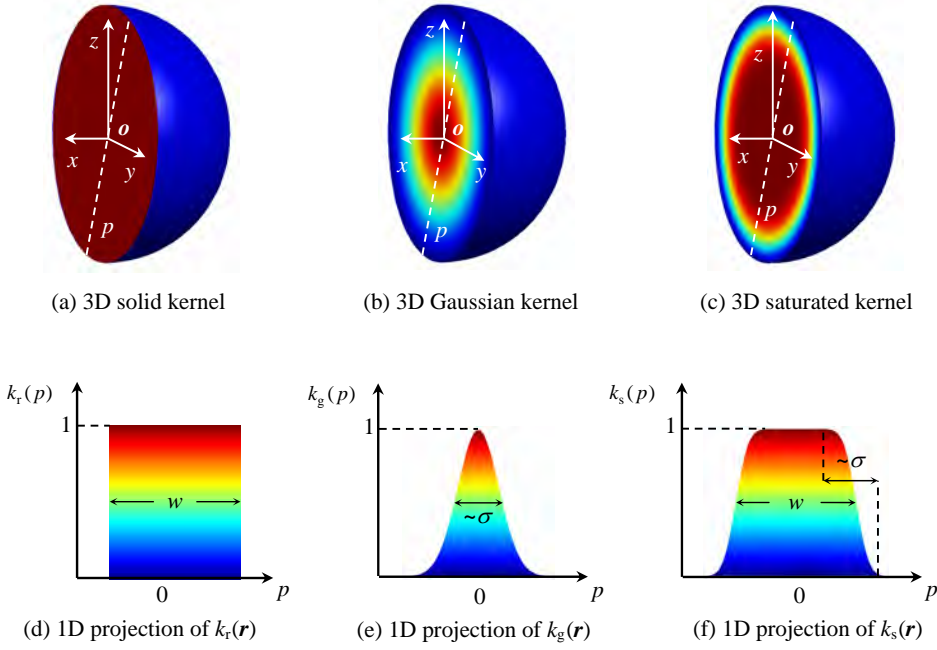


**Figure 3.1.** Different model kernels that describe the physical extent of a WM fiber bundle. Figures (a)  $\rightarrow$  (c) are 3D color-encoded representations of these kernels. The 1D projection (dashed line, with  $p$  as parameterization variable) is depicted in (d)  $\rightarrow$  (f).

### 3.3.2.3 Saturated model

Finally, a general model can be obtained by combining the Gaussian and solid models. Basically, the resulting kernel is defined as the sum of two error functions:

$$k_s(\mathbf{r}) = \frac{\operatorname{erf}\left(\frac{w+2\|\mathbf{r}\|}{2\sqrt{2}\sigma}\right) + \operatorname{erf}\left(\frac{w-2\|\mathbf{r}\|}{2\sqrt{2}\sigma}\right)}{2 \operatorname{erf}\left(\frac{w}{2\sqrt{2}\sigma}\right)}, \quad (3.10)$$

where  $w$  controls the width of the fiber bundle and  $\sigma$  determines the edge steepness [Figs. 3.1 (c) and 3.1 (f)]. Note that the previous kernels  $k_r(\mathbf{r})$  and  $k_g(\mathbf{r})$  are special cases of this saturation model (see Fig. 3.2), i.e.

$$k_g(\mathbf{r}) = \lim_{w \rightarrow 0} k_s(\mathbf{r}) \quad \text{and} \quad k_r(\mathbf{r}) = \lim_{\sigma \rightarrow 0} k_s(\mathbf{r}). \quad (3.11)$$

### 3.3.3 Principal diffusion direction and eigenvalue fields

The PDV field of a WM fiber bundle is characterized by the first eigenvector field  $\mathbf{e}_1(\mathbf{r})$ . To reflect the width and continuity of the WM fiber bundle,  $\mathbf{e}_1(\mathbf{r})$  is

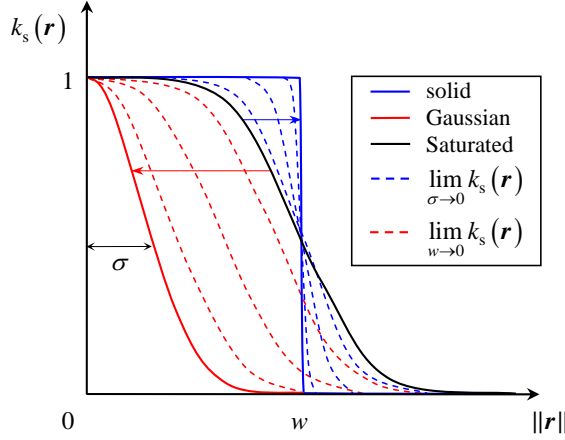


**Figure 3.2.** Illustration of the saturated model  $k_s(\mathbf{r})$ . The solid and the Gaussian model are special cases of  $k_s(\mathbf{r})$ , taking the limits  $w \rightarrow 0$  and  $\sigma \rightarrow 0$  respectively.

calculated as a weighted sum of the vector lines  $\Delta_i$ :

$$\mathbf{e}_1(\mathbf{r}) = \frac{\sum_{i=1}^{N-1} T^i(\mathbf{r}) \Delta_i}{\left\| \sum_{i=1}^{N-1} T^i(\mathbf{r}) \Delta_i \right\|}, \quad (3.12)$$

where the weighting coefficients  $T^i(\mathbf{r})$  are derived from the model kernel, as described in Eq. (3.2). The other eigenvector fields  $\mathbf{e}_2(\mathbf{r})$  and  $\mathbf{e}_3(\mathbf{r})$  can easily be found by solving the equations  $\mathbf{e}_1(\mathbf{r}) \cdot \mathbf{e}_2(\mathbf{r}) = 0$  and  $\mathbf{e}_1(\mathbf{r}) \times \mathbf{e}_2(\mathbf{r}) = \mathbf{e}_3(\mathbf{r})$ .

To calculate the eigenvalue fields  $\lambda_i(\mathbf{r})$ , several aspects of the WM fiber bundle with respect to FA and MD should be considered. The diffusion of a single ideal WM fiber bundle is mainly along the PDV and has an axial symmetric diffusion tensor field, i.e.  $\lambda_1(\mathbf{r}) > \lambda_2(\mathbf{r}) = \lambda_3(\mathbf{r})$ . Therefore,  $FA(\mathbf{r})$  and  $MD(\mathbf{r})$  are calculated as:

$$FA(\mathbf{r}) = \frac{\sqrt{3}[\lambda_1(\mathbf{r}) - \lambda_2(\mathbf{r})]}{\sqrt{\lambda_1^2(\mathbf{r}) + 2\lambda_2^2(\mathbf{r})}} \quad ; \quad MD(\mathbf{r}) = \frac{\lambda_1(\mathbf{r}) + 2\lambda_2(\mathbf{r})}{3}. \quad (3.13)$$

From this equation system, the eigenvalue fields  $\lambda_1(\mathbf{r})$  and  $\lambda_2(\mathbf{r}) = \lambda_3(\mathbf{r})$  are calculated as:

$$\lambda_1(\mathbf{r}) = \frac{3 MD(\mathbf{r}) \left[ 3 + FA(\mathbf{r}) \sqrt{9 - 2 FA^2(\mathbf{r})} \right]}{9 - 2 FA^2(\mathbf{r}) + FA(\mathbf{r}) \sqrt{9 - 2 FA^2(\mathbf{r})}} \quad (3.14)$$

and

$$\lambda_2(\mathbf{r}) = \frac{3 MD(\mathbf{r}) [3 - FA^2(\mathbf{r})]}{9 - 2 FA^2(\mathbf{r}) + FA(\mathbf{r})\sqrt{9 - 2 FA^2(\mathbf{r})}} , \quad (3.15)$$

where  $FA(\mathbf{r})$  and  $MD(\mathbf{r})$  are now given by Eq. (3.3).

### 3.3.4 Total diffusion tensor field

After the eigenvalues and eigenvectors that describe the WM fiber bundle have been defined, the corresponding diffusion tensor field  $\mathbf{T}(\mathbf{r})$  is calculated as  $\mathbf{T}(\mathbf{r}) = \mathbf{E}(\mathbf{r}) \mathbf{\Lambda}(\mathbf{r}) \mathbf{E}(\mathbf{r})^{-1}$ , where the columns of the matrix  $\mathbf{E}(\mathbf{r})$  define the orthonormal eigenvectors  $\mathbf{e}_i(\mathbf{r})$  and the diagonal matrix  $\mathbf{\Lambda}(\mathbf{r})$  represents the eigenvalues  $\lambda_i(\mathbf{r})$ . Analogously, the diffusion tensor field of a background tissue with particular anisotropic properties, denoted as  $\mathbf{D}_b(\mathbf{r})$ , can be computed. Finally, the total diffusion tensor field  $\mathbf{D}_{\text{tot}}(\mathbf{r})$  of  $J$  WM fiber bundles  $\mathbf{T}_{\{j\}}(\mathbf{r})$  with  $j = 1, \dots, J$  is determined as follows:

$$\mathbf{D}_{\text{tot}}(\mathbf{r}) = \frac{MD^M(\mathbf{r}) \sum_{j=1}^J \mathbf{T}_j(\mathbf{r})}{\sum_{j=1}^J MD_j(\mathbf{r})} + \frac{MD_M^M - MD^M(\mathbf{r})}{MD_M^M} \mathbf{D}_b(\mathbf{r}) , \quad (3.16)$$

where  $MD_j(\mathbf{r})$  represents the mean diffusivity of the  $j$ th WM fiber bundle and

$$MD^M(\mathbf{r}) = \max_j MD_j(\mathbf{r}) \quad ; \quad MD_M^M = \max_{\mathbf{r}} MD^M(\mathbf{r}) . \quad (3.17)$$

This weighted sum allows one to model more complex configurations, such as the crossing, merging, kissing and branching of WM fiber bundles. The first term in Eq. (3.16) ensures that if multiple fibers with their unique corresponding diffusion properties coincide, their global combined mean diffusion is normalized. The second term in Eq. (3.16) enables the continuous transition of the diffusion properties of each fiber separately to the diffusion properties of the surrounding background tissue.

## 3.4 Methods

In vivo DTI of a starling brain was performed on an 7 Tesla MR system. A total of 24 sagittal slices (0.6 mm thick), covering the whole brain, were obtained. Spin echo images, incorporating symmetric trapezoidal diffusion gradients were sequentially applied in seven noncollinear directions. The components of the  $b$ -matrices were calculated using analytical expressions, as described in Ref. [16], incorporating

both the diffusion gradients (0 or 70 mTesla  $\text{m}^{-1}$  with  $\delta = 12$  ms and  $\Delta = 20$  ms) and the image gradients. Additional acquisition parameters were as follows: BW = 25 kHz, FOV = 22 mm, TE = 43 ms, TR = 2400 ms, ramp time = 0.1 ms, acquisition matrix = (256 x 128), and number of averages = 14. The six DW images were coregistered to the non-DW image by maximization of mutual information [17]. The effective diffusion tensor and the derived FA and MD maps were calculated in each voxel according to Ref. [18].

## 3.5 Results

### 3.5.1 Theoretical model

#### 3.5.1.1 Single WM fiber bundles

The first step in constructing the simulated phantom is to define a set of points  $\{\mathbf{r}_i\}$  that represent the fiber backbone  $t(\mathbf{r})$  [see Eq. (3.1)]. These points may describe a model of a particular anatomical structure or they may be obtained from the FT results of experimental data. The width of a WM fiber bundle is obtained by convolving the fiber skeleton with a predefined model kernel. This physical thickness reflects the natural continuous dependence of FA and MD values across the fiber pathway, and is elucidated in Fig. 3.3 (a).

The PDV [i.e., the first eigenvector  $\mathbf{e}_1(\mathbf{r})$ ] is constructed using a weighted sum of the vector line segments that define the WM fiber skeleton [see Eq. (3.12)]. In this way, the PDV field is continuous and aligned along the fiber backbone. Fig. 3.3 (b) illustrates the first eigenvector field after the real eigenvalue decomposition is calculated. Note that only the orientation and not the direction of  $\mathbf{e}_1(\mathbf{r})$  is defined, for diffusion is inherently a center-symmetric phenomenon, i.e. both  $\mathbf{e}_1(\mathbf{r})$  and  $-\mathbf{e}_1(\mathbf{r})$  represent the main diffusion direction.

As described in Eqs. (3.14) and (3.15), the eigenvalues  $\lambda_1(\mathbf{r})$  and  $\lambda_2(\mathbf{r}) = \lambda_3(\mathbf{r})$  are defined using the modeled diffusion maps. Thus,  $FA(\mathbf{r})$  and  $MD(\mathbf{r})$  can be chosen independently and with high flexibility [see Fig. 3.4 (a)]. Analogously, the diffusion tensor field of the background tissue can be constructed. Figure 3.4 (b) gives an example of the WM fiber bundle embedded in its surrounding tissue. Notice the continuous transition of the diffusion properties between the WM fiber bundle and the surrounding tissue.

#### 3.5.1.2 Complex WM configurations

In DTI tractography, fiber crossing is an important issue in determining the PDV [19]. Lower anisotropy values are observed, and eigenvector directions do not correspond with the direction of both fiber tracts at the crossing. In a previous study

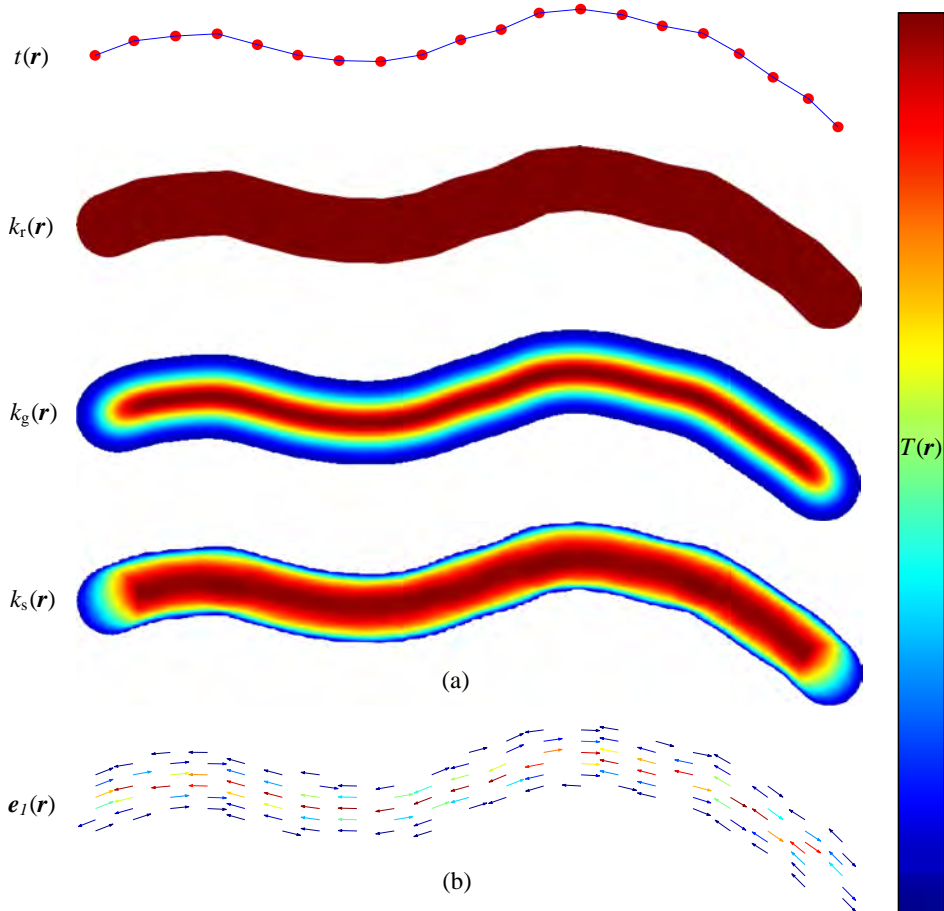


**Figure 3.3.** A single WM fiber skeleton  $t(\mathbf{r})$  is completely defined by the set of points  $\{\mathbf{r}_i\}$ . (a) Several examples of the convolution function  $T(\mathbf{r})$ , according to the different model kernels  $k(\mathbf{r})$ . (b) Principal diffusion direction of the WM fiber bundle, using the color-encoding of  $T(\mathbf{r})$  to reflect the corresponding model kernel [in this case  $k_g(\mathbf{r})$ ].

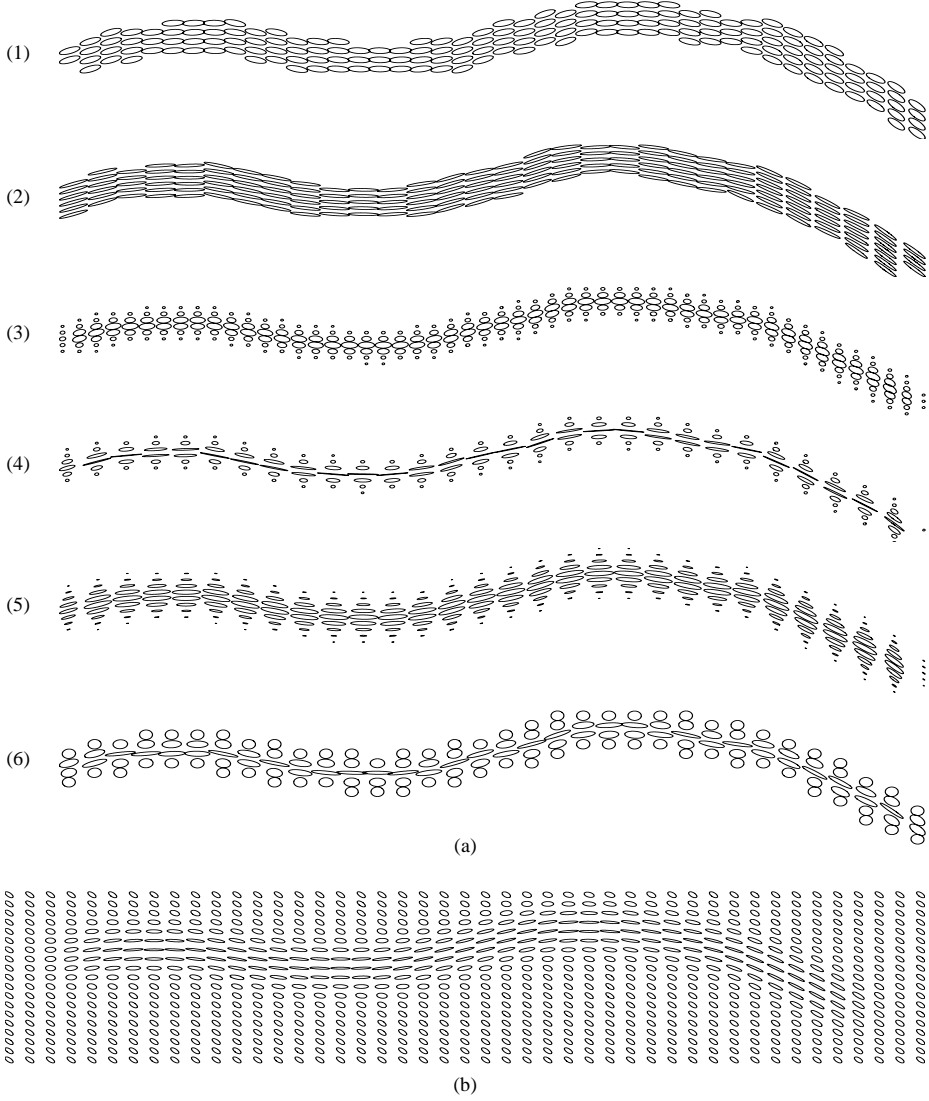


**Figure 3.4.** Elliptical representations of a WM fiber bundle. (a) Without background tissue: (1) and (2) are calculated using the solid model  $k_r(\mathbf{r})$ , both with equal  $MD(\mathbf{r}) = MD_M$ , but different  $FA(\mathbf{r}) = FA_M$ ; (3) and (4) are calculated using the Gaussian model  $k_g(\mathbf{r})$ , also both with equal  $MD_M$ , but different  $FA_M$ ; (5) and (6) are combinations of the models  $k_r(\mathbf{r})$  and  $k_g(\mathbf{r})$ : in (5)  $FA(\mathbf{r}) = FA_M$  and in (6)  $MD(\mathbf{r}) = MD_M$ . (b) With background tissue: in this example, a uniform field is given, i.e.  $FA(\mathbf{r}) = FA$ ,  $MD(\mathbf{r}) = MD$  and  $\mathbf{e}_1(\mathbf{r}) = \mathbf{e}_1$ .

using a geometric analysis of the diffusion tensor [20], the predominance of the planar component was observed at fiber crossings.

It is generally known that the rank of the diffusion tensor increases when lower-rank, noncollinear tensors are summed [21]. Therefore, calculating the weighted sum of the fiber bundle diffusion tensor fields [see Eq. (3.16)] yields a natural representation of WM fiber crossing, which is consistent with the experimental observations. An example of two crossing fiber bundles is given in Fig. 3.5. Also, other config-

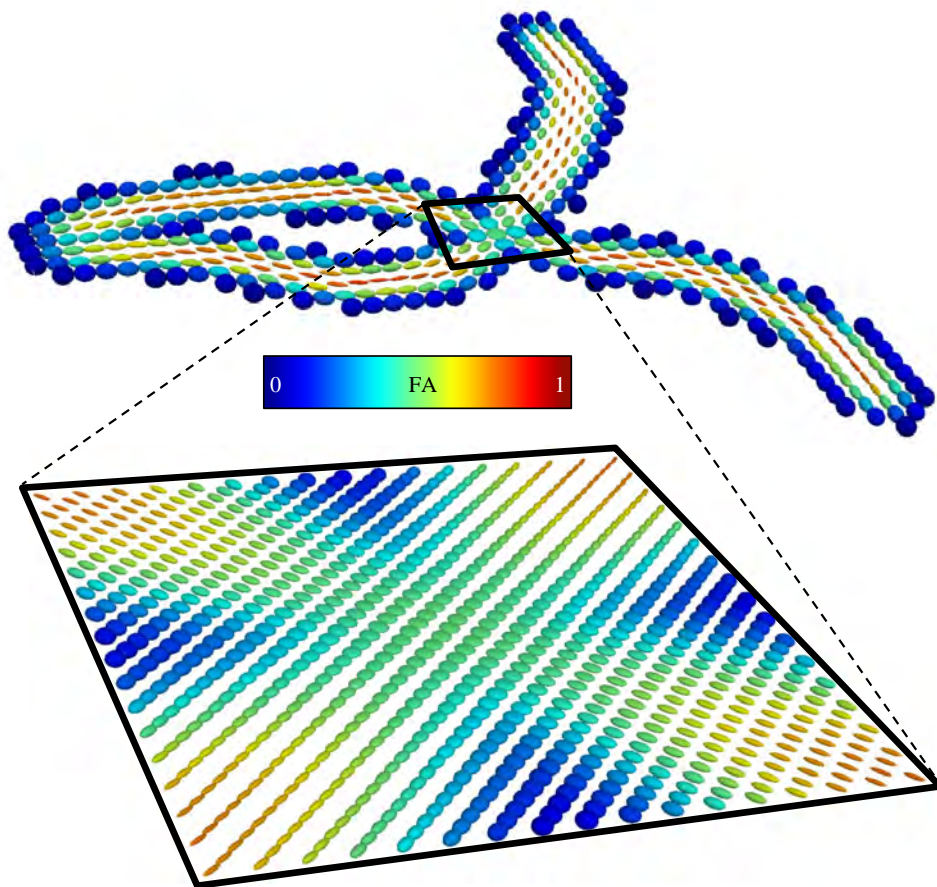


**Figure 3.5.** Ellipsoidal diffusion tensor field representation of fiber crossing using the Gaussian model. The ellipsoids are color-encoded according to their FA to facilitate differentiating the planar from the spherical diffusion. Note the decreasing FA at the crossing area of the fiber bundles, for there, the planar component is much larger than the linear component.



urations like fiber merging, branching, and kissing can easily be constructed with the use of this mathematical framework.

### 3.5.2 Experimental evaluation of the mathematical framework

In this section, our method is evaluated with real characteristics of existing fibers, which are derived from experimentally measured DTI data of the starling brain. More specifically, a particular part of the cerebellum where WM fiber bundles are clearly visible [see Fig. 3.6 (a,b,c)] was synthesized. A comparison of the different

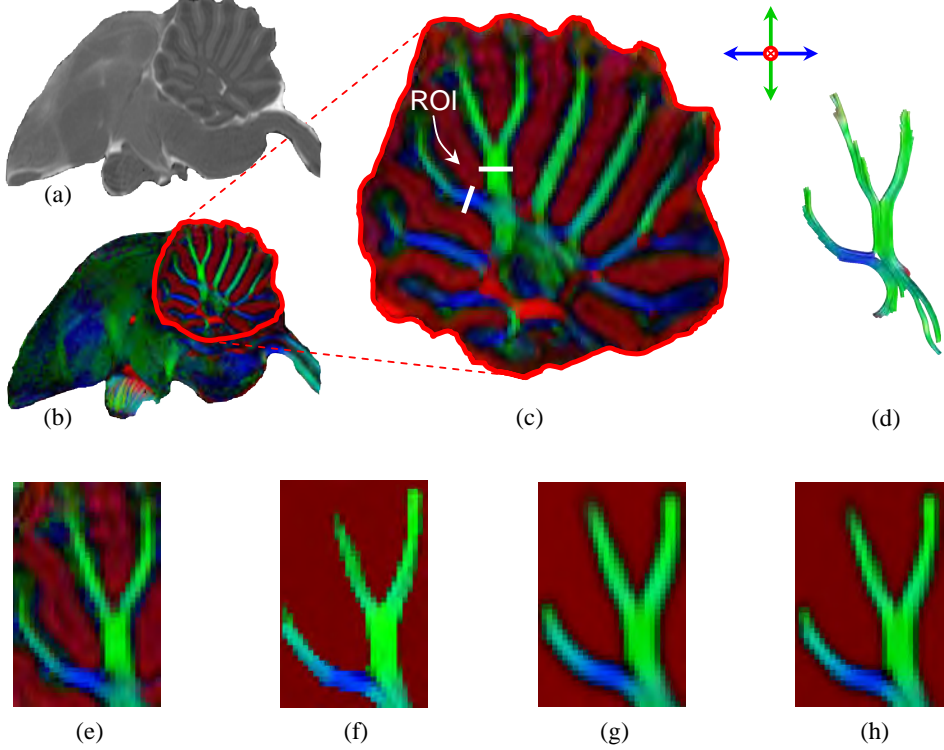


**Figure 3.6.** (a) MD and (b) FA sagittal map of the starling brain; (c) FA map of the cerebellum. The color-encoding of the FA maps provides directional information of the local fiber orientation [22]. The white lines indicate the ROI to start the fiber tracking from; (d) reconstructed fiber pathways of a particular part of the cerebellum; (e) the experimental FA map of these specified WM fiber bundles; the corresponding (f) solid, (g) Gaussian and (h) saturated modeled synthetic FA map.

synthetic DTI data sets with the corresponding experimental data allows one to



determine the optimum model and parameter settings. The evaluation procedure is performed as follows:

- The WM fiber backbone trajectories at a specific ROI are defined by the corresponding FT results, which in this case are obtained by the Fiber Assignment by Continuous Tracking (FACT) approach [23].
- $FA_M$  and  $MD_M$  of the WM fibers, and the characteristics of the background tissue (global MD, FA, and PDV) are experimentally measured.
- Different model kernels are applied and the corresponding model parameters are optimized (in a least-squares sense) to fit the experimental DTI data.

To account for the PVE, the total diffusion tensor field was integrated over its local neighborhood, as specified by the experimental voxel dimensions. The resulting simulated DTI data sets according to the solid, Gaussian, and saturated models are depicted in Fig. 3.6 (f,g,h). The highest similarity (i.e., the lowest mean squared difference (MSD) between the diffusion tensor components of the experimental and the synthetic data) was obtained from the Gaussian and saturated models.

### 3.5.3 Example of a simulated phantom from experimental data

Fig. 3.7 (a) shows the WM fiber network of the starling cerebellum, which is computed with the FACT algorithm [23]. These fiber pathways are then synthesized according to their experimentally derived diffusion properties to define the ground-truth DTI data set. As shown in Figs. 3.7 (b) and (c), different fiber tracking algorithms can now be compared using the simulated DTI data set. This conceptual illustration already demonstrates the feasibility of evaluating DTT algorithms.

### 3.5.4 Application to WM FT

The main application of the simulated DTI phantom is to quantitatively test and objectively compare different fiber tracking algorithms. Such a study consists of evaluating the numerous criteria that characterize a tractography algorithm, as elaborately described in Ref. [13]. Here we present only a few examples to demonstrate how our methodology can be applied to evaluate and compare FT algorithms.

#### 3.5.4.1 Synthetic data

The simulated DTI data ( $100 \times 100 \times 100$  matrix size) is constructed by randomly generating  $2^9$  WM fiber pathways with step size  $\Delta = 0.5$ , varying cross-sectional widths ( $\{\sigma, w\} \in [0.5, 1.5]$ ), FA values ( $FA_M \in [\sqrt{3}/10, \sqrt{3}]$ ), MD values

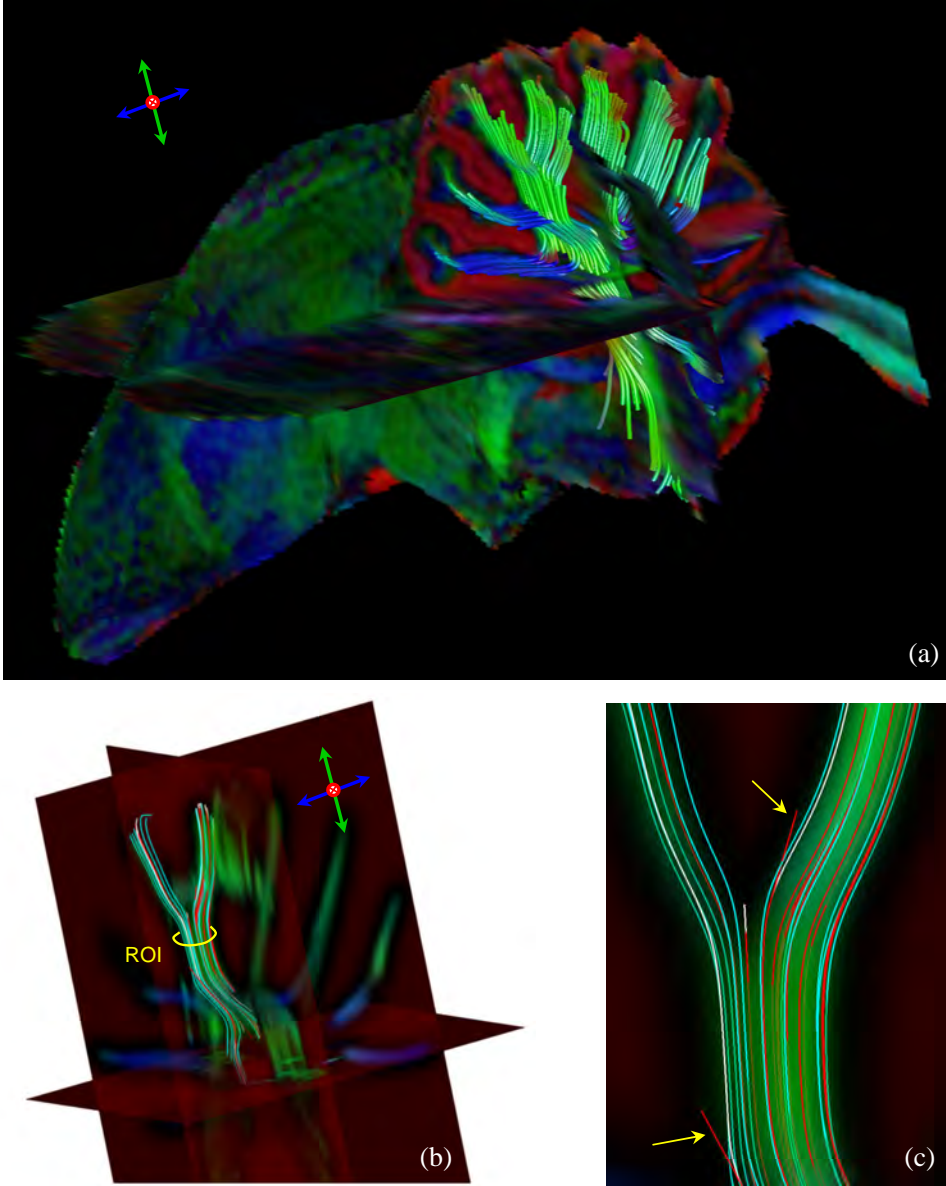


**Figure 3.7.** (a) A 3D representation of the starling cerebellum with three orthogonal FA maps (again color-encoded to provide directional information). (b) After synthesizing this fiber network, fiber tracking results of the FACT approach (colored in cyan) and the approach developed in [21] (colored in red), are compared with the ground-truth fiber pathways (colored in white). In (c), subtle differences between these approaches can be observed (e.g. indicated by the arrows), indicating a high sensitivity of the synthetic data.

( $MD_M \in [0.5, 1.5]$ ), and local curvatures  $\kappa$  ( $\kappa \in [0, 1]$ ) in an isotropic background with MD equal to one [see Fig. 3.8 (a)]. Note that the MD values are normalized (dimensionless units), since actual experimental measurements were not performed.

### 3.5.4.2 Fiber similarity

The similarity measure  $S$  between a pair of fiber pathways (i.e., the simulated tract  $t_s$  and the experimentally reconstructed tract  $t_e$ ) is here defined as [24]:

$$S(t_s, t_e) = R_{cs} e^{-\frac{E(t_s, t_e)}{C}} \quad \text{with} \quad R_{cs} = \frac{L_{cs}}{L_s + L_e - L_{cs}} \quad , \quad (3.18)$$

where  $L_s$  and  $L_e$  are the lengths of  $t_s$  and  $t_e$ , respectively, and  $L_{cs}$  represents the length of the corresponding fiber segment (i.e., the overlapping part of both fiber tracts).  $E(t_s, t_e)$  is defined as the mean point-by-point Euclidean distance between the corresponding segments of  $t_s$  and  $t_e$ , and the coefficient  $C$  regulates the trade-off between  $E(t_s, t_e)$  and the corresponding segment ratio  $R_{cs}$ . In this study,  $C$  is chosen to be one voxel width.

### 3.5.4.3 Optimal curvature threshold

Most DTT algorithms require multiple user-defined FT termination thresholds, such as the maximum fiber curvature  $\kappa_M$ , minimum FA ( $FA_m$ ), etc. As shown in Fig. 3.8 (b), the optimal curvature threshold  $\tilde{\kappa}_M$  can now be determined via the similarity measure  $S$ , averaged over all fiber pathways ( $S_{av}$ ), i.e.  $\tilde{\kappa}_M = \arg \max_{\kappa_M} S_{av}(\kappa_M)$ . Here  $\tilde{\kappa}_M$  is observed to be independent of the predefined  $FA_m$  and  $\Delta$ .

### 3.5.4.4 Sensitivity to noise

By adding different levels of Rician distributed noise to the DW images of the corresponding ground-truth DTI data set [see Fig. 3.8 (c)→(f)], the sensitivity to noise of DTT algorithms can now be studied. As shown in Fig. 3.8 (g), the FACT approach is more sensitive to noise than the technique developed in Ref. [21].

## 3.6 Discussion

DTT has become a specialized application of DTI, resulting in the development of a wide variety of algorithms. Basic DTT techniques reconstruct WM fiber pathways by consecutively following the local first eigenvector of the corresponding diffusion tensor, which is similar to calculating fluid streamlines in hydrodynamics (e.g., Refs. [11, 23, 25, 26]). To evaluate these approaches, simulated vector fields and

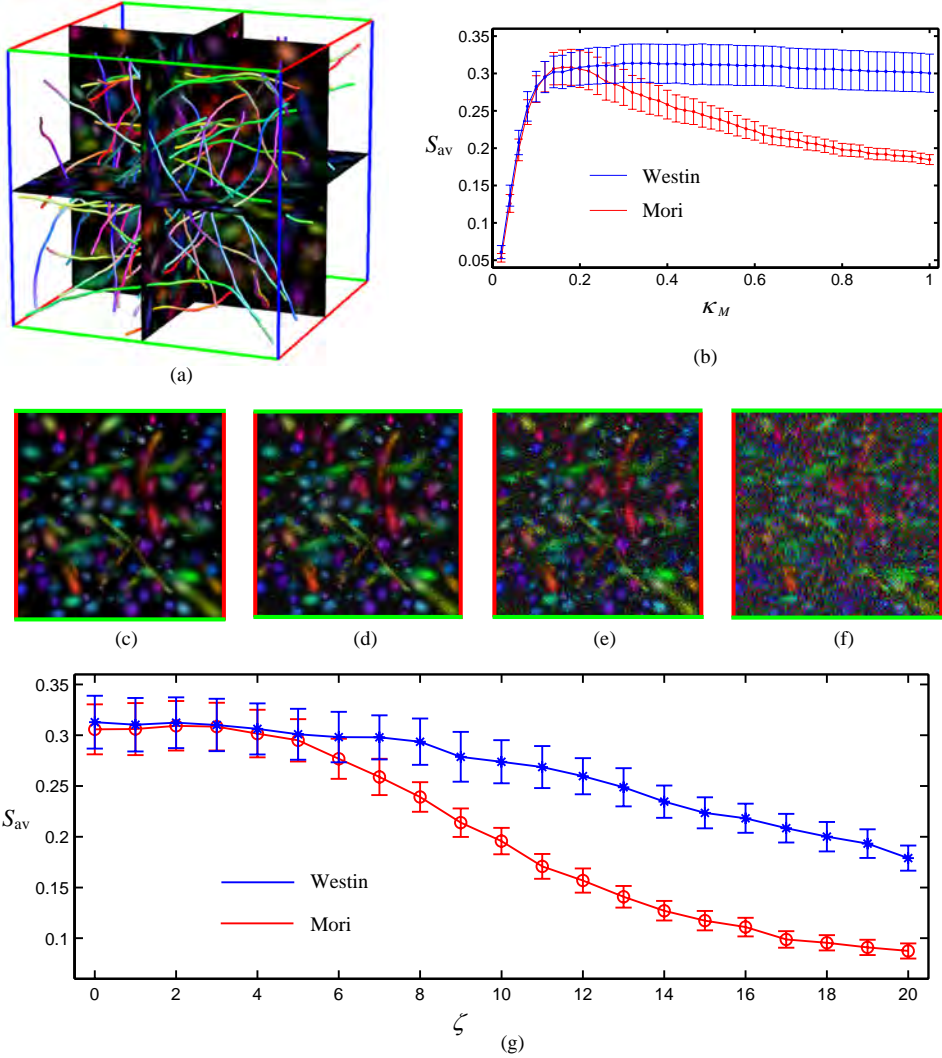


**Figure 3.8.** (a) 3D representation of a simulated WM fiber system (for clarity, only fibers longer than  $50\Delta$  are shown). (b) The averaged fiber similarity  $S_{av}$  as a function of  $\kappa_M$  with  $FA_m = \sqrt{3}/10$  and  $\Delta = 0.5$ , compared between the FT approaches of Mori et al. [23] and Westin et al. [21]. (c)→(f) represent a slice of the synthetic DTI data set with noise levels  $\zeta = \{0, 5, 10, 20\}$  respectively, where  $\zeta$  represents the standard deviation of the Gaussian distribution that underlies the Rician distribution of the noise. (g) The averaged fiber similarity  $S_{av}$  as a function of  $\zeta$ .

elementary diffusion tensor phantoms suffice, because it is not necessary to incorporate all diffusion tensor characteristics to compute the fiber pathways. Although these basic DTT methods can offer qualitative and diagnostic information about the global anatomical connectivity of the brain, it is difficult to obtain reliable quantitative results [7].

More advanced DTT algorithms take into account the entire diffusion tensor information, and use statistical approaches to explore many potential connections and select appropriate tracts. These FT techniques are less sensitive to noise and make it possible to study fiber crossing and diverging in a quantitative way. To objectively evaluate the DTT algorithms that accomplish these improvements, a mathematical framework has been developed to simulate more advanced and realistic DTI phantoms, which are useful for studying specific architectural configurations (e.g., fiber crossing and merging) or single WM fiber bundles with varying cross-sectional diffusion properties. DTT techniques that utilize all DOF of the diffusion tensor to compute WM fiber tracts require synthetic DTI data that also exhibit these DOF of the diffusion tensor. Otherwise, an evaluation of these DTT techniques could yield biased and incomplete results. Therefore, these synthetic DTI phantoms will also play an important role in testing more advanced FT algorithms.

The evaluation of the proposed methodology for simulating DTI data of WM fiber bundles indicates that a simple FA threshold within the modeled fiber structure (i.e., the solid model) does not provide the most realistic synthetic data (see Fig. 3.6). An improved similarity between the experimental and synthetic data has been obtained by defining the WM fiber bundle diffusion properties that vary cross-sectionally, and incorporating a smooth transition between the WM fiber bundle and its surrounding tissue (Gaussian and saturated models). These results suggest that the PVE alone do not provide the optimum way to model WM fiber structures.

An important aspect of evaluating and comparing different FT algorithms is uniformity, i.e. equal conditions for testing different DTT algorithms. Therefore, a library of simulated DTI phantoms, each with specific configurations and diffusion properties, should be developed and disseminated. Such a library can easily be constructed with this framework, since it allows one to model specific anatomical configurations that are obtained from actual experimental results. In addition, the diffusion properties can be chosen independently and with high flexibility, or they can be determined experimentally to attain a maximal accuracy.

The applications of this mathematical framework are not limited to the evaluation, optimization, and comparison of DTT algorithms. Several DTI preprocessing techniques, such as noise filtering, image coregistration, and regularization, also require ground-truth data for testing and evaluation, and therefore can make use of this framework to simulate DTI phantoms.

## 3.7 Conclusions

A general mathematical framework for simulating DTI data sets of WM fiber bundles is developed based on the corresponding physical diffusion properties. This framework allows one to model a smooth transition between the WM fiber system and its surrounding tissue. In addition, complex configurations of multiple fiber bundles, such as crossing, merging, and kissing of fiber pathways, can also be constructed.

Several models were quantitatively evaluated using experimental DTI data, and the results indicate that a higher correspondence between experimental and synthetic DTI data exists when the cross-sectional dependency of the WM fiber density is modeled as nonconstant. Furthermore, these results suggest that modeling of the PVE alone is not the optimum way to model WM fiber structures.

It has been demonstrated that the developed mathematical framework can provide the necessary ground-truth DTI data for the quantitative evaluation and optimization of user-defined tractography termination parameters. Moreover, the synthetic ground-truth data allows one to objectively compare different FT algorithms. Finally, an example of how this framework can be applied to study FT sensitivity with respect to different noise levels was presented.

## Bibliography

- [1] E.W. Hsu et al. Magnetic resonance myocardial fiber-orientation mapping with direct histological correlation. *Am J Physiol*, 274(5):1627–1634, 1998.
- [2] D.F. Scollan et al. Histological validation of myocardial microstructure obtained from diffusion tensor magnetic resonance imaging. *Am J Physiol*, 275(6):2308–2318, 1998.
- [3] B.A. Inglis et al. Diffusion tensor MR imaging and comparative histology of glioma engrafted in the rat spinal cord. *AJNR Am J Neuroradiol*, 20(4):713–716, 1999.
- [4] J. Zhang et al. Three-dimensional diffusion tensor magnetic resonance microimaging of adult mouse brain and hippocampus. *NeuroImage*, 15(4):892–901, 2002.
- [5] M.R. Wiegell et al. Automatic segmentation of thalamic nuclei from diffusion tensor magnetic resonance imaging. *NeuroImage*, 19(2):391–401, 2003.
- [6] C.-P. Lin et al. Validation of diffusion tensor magnetic resonance axonal fiber imaging with registered manganese-enhanced optic tracts. *NeuroImage*, 14(5):1035–1047, 2001.
- [7] P.J. Basser et al. Fiber tract following in the human brain using DT-MRI data. *IEICE T Inf Syst*, E85–D:15–21, 2002.
- [8] C. Gössel et al. Fiber tracking from DTI using linear state space models: detectability of the pyramidal tract. *NeuroImage*, 16(2):378–388, 2002.
- [9] S. Mori et al. Brain white matter anatomy of tumor patients evaluated with diffusion tensor imaging. *Ann Neurol*, 51(3):377–380, 2002.
- [10] C.R. Tench et al. Improved white matter fiber tracking using stochastic labeling. *Magn Reson Med*, 48(4):677–683, 2002.
- [11] P.J. Basser et al. In vivo fiber tractography using DT-MRI data. *Magn Reson Med*, 44(4):625–632, 2000.

- [12] S. Pajevic et al. A continuous tensor field approximation of discrete DT-MRI data for extracting microstructural and architectural features of tissue. *J Magn Reson*, 154(1):85–100, 2002.
- [13] N.F. Lori et al. Diffusion tensor fiber tracking of human brain connectivity: acquisition methods, reliability analysis and biological results. *NMR Biomed*, 15(7–8):493–515, 2002.
- [14] J.-D. Tournier et al. Limitations and requirements of diffusion tensor fiber tracking: an assessment using simulations. *Magn Reson Med*, 47(4):701–708, 2002.
- [15] P.J. Basser. Fiber-tractography via diffusion tensor MRI (DT-MRI). In *ISMRM*, page 1226, 1998.
- [16] J. Mattiello et al. *Diffusion and perfusion magnetic resonance imaging*, chapter Analytical calculation of the  $b$  matrix in diffusion imaging, pages 77–90. New York: Raven Press, 1995.
- [17] F. Maes et al. Multimodality image registration by maximization of mutual information. *IEEE Trans Med Imaging*, 16(2):187–198, 1997.
- [18] P.J. Basser et al. MR diffusion tensor spectroscopy and imaging. *Biophys J*, 66(1):259–267, 1994.
- [19] M.R. Wiegell et al. Fiber crossing in human brain depicted with diffusion tensor MR imaging. *Radiology*, 217(3):897–903, 2000.
- [20] A.L. Alexander et al. A geometric analysis of diffusion tensor measurements of the human brain. *Magn Reson Med*, 44(2):283–291, 2000.
- [21] C.-F. Westin et al. Processing and visualization for diffusion tensor MRI. *Med Image Anal*, 6(2):93–108, 2002.
- [22] S. Pajevic and C. Pierpaoli. Color schemes to represent the orientation of anisotropic tissues from diffusion tensor data: application to white matter fiber tract mapping in the human brain. *Magn Reson Med*, 42(3):526–540, 1999.
- [23] S. Mori et al. Three-dimensional tracking of axonal projections in the brain by magnetic resonance imaging. *Ann Neurol*, 45(2):265–269, 1999.
- [24] Z. Ding et al. Classification and quantification of neuronal fiber pathways using diffusion tensor MRI. *Magn Reson Med*, 49(4):716–721, 2003.
- [25] T.E. Conturo et al. Tracking neuronal fiber pathways in the living human brain. In *Proc Natl Acad Sci USA*, volume 96, pages 10422–10427, 1999.
- [26] C.R. Tench et al. White matter mapping using diffusion tensor MRI. *Magn Reson Med*, 47(5):967–972, 2002.

## Chapter 4

# Voxel based DTI coregistration

The work in this chapter has been published in

*A. Leemans, J. Sijbers, S. De Backer, E. Vandervliet, and P. M. Parizel, “Affine coregistration of diffusion tensor magnetic resonance images using mutual information”, Lecture Notes in Computer Science, Vol. 3708, p. 523–530, 2005.*

### 4.1 Abstract

In this chapter, an affine image coregistration technique for DTI data sets is developed based on mutual information. The technique is based on a multi-channel approach where the DW images are aligned according to the corresponding acquisition gradient directions. Also, in addition to the coregistration of the DTI data sets, an appropriate reorientation of the diffusion tensor is developed in order to remain consistent with the corresponding underlying anatomical structures. This reorientation strategy is determined from the spatial transformation while preserving the diffusion tensor shape. The method is fully automatic and has the advantage to be independent of the applied diffusion framework.

### 4.2 Introduction

Image coregistration, also referred to as matching or warping, is the process of aligning images in order to relate corresponding features. The objective of any coregistration technique is therefore finding the transformation that maps these images into a common reference frame in which direct comparison is possible.



Only then, abnormalities can be quantified based on a statistical analysis of these multiple data sets.

Image coregistration has become an important application in many fields of image analysis (e.g., multispectral classification in remote sensing, coregistration of computer tomography (CT), Positron Emission Tomography (PET), and MRI data in medicine, cartography, image fusion, etc.) due to the rapid development of many image acquisition devices and the growing diversity of imaging modalities during the last decades. This diversity of images to be registered makes it impossible to design a universal method applicable to all coregistration tasks, resulting in an ever-increasing number of publications on the topic each year. Excellent surveys of recent and classic image coregistration techniques can be found in [1–3].

Specifically for DTI, a multiresolution elastic coregistration technique has been developed using similarity measures of the tensor data instead of scalar data [4]. In the work of Jones et al., the FA images were used for coregistration [5]. Other techniques have been proposed using tensor similarity, extending the general concept of intensity-based similarity for matching to the tensor case [6, 7]. In Refs. [6] and [7], an interpolation method is developed by means of the Kriging estimator and spatial alignment is established via a locally optimized similarity function. Also, coregistration techniques based on multiple channel information of several diffusion tensor properties have been proposed [8, 9]. Xu et al. applied the ‘Hierarchical Attribute Matching Mechanism for Elastic Registration’ (HAMMER) approach, a high dimensional elastic transformation procedure, to DTI data sets [10]. For all these DTI coregistration techniques, an additional step in the alignment procedure is required to adjust the orientation of the underlying diffusion tensor according to the transformation. To incorporate this task, a technique has been developed by Alexander et al., in which the rotational component of the linear transformation, or the locally derived rotational component of a non-linear transformation, is determined to reorient the tensors in the entire diffusion tensor field [4].

In the following sections, a 3D affine (rotation, translation, scale, and skew) DTI coregistration technique is presented, based on the work of Maes et al. [11] using mutual information as a similarity measure. To preserve the orientational information of the diffusion tensor after affine transformation, an appropriate tensor reorientation must be applied in order to remain consistent with the alignment of the underlying anatomical structures. Current reorientation strategies (RS) for such an affine transformation, such as the preservation of principal direction (PPD) method, require calculating several rotation matrices to reorient the diffusion tensor [12]. Here, a direct diffusion tensor reconstruction approach is developed without the need to calculate these rotation matrices, resulting in a lower computational cost.

## 4.3 Theory

### 4.3.1 Spatial normalization

Mutual Information (MI) has already proven to be of high value for multimodality image registration since its development in the mid nineties and could be considered as the current ‘gold standard’ [11, 13, 14]. For scalar images, the registration solution, i.e. the final transformation  $\Phi$ , is determined by maximizing the MI between the reference image  $R$  and the source image  $S$ :

$$\Phi = \arg \max_{\phi} \text{MI}[\phi(S), R] \quad , \quad (4.1)$$

where  $\phi$  represents the affine transformation which is parameterized using a transformation matrix. In Eq. (4.1), the MI measure is defined as follows [15]:

$$\text{MI}[G \equiv \phi(S), R] = \sum_{g,r} p_{GR}(g,r) \log_2 \frac{p_{GR}(g,r)}{p_G(g)p_R(r)} \quad , \quad (4.2)$$

where  $G$  is the transformed source image,  $g$  and  $r$  are the image intensity values,  $p_G$  and  $p_R$  denote the marginal probability distribution functions, and  $p_{GR}(g,r)$  represents the joint probability distribution.

Specifically for DTI, we apply a  $k$ -channel MI registration approach, where  $k = 0, \dots, K$  represents the number of DW images<sup>1</sup>:

$$\Phi_k = \arg \max_{\phi} \text{MI}[\phi(S_k), R_k] \quad , \quad (4.3)$$

where  $R_k$  and  $S_k$  denote the reference and source DW images, respectively. It is important to note that the assumption is made that the DW images, derived from a single acquisition, are already mutually aligned with the non-DW image, i.e.

$$\begin{aligned} \forall k = 1, \dots, K : \arg \max_{\phi} \text{MI}[\phi(R_k), R_0] &= \mathbf{1} \\ \forall k = 1, \dots, K : \arg \max_{\phi} \text{MI}[\phi(S_k), S_0] &= \mathbf{1} \quad , \end{aligned} \quad (4.4)$$

where  $\mathbf{1}$  represents the unity transformation.

From Eq. (4.3), the final transformation  $\Phi$  can be calculated as a weighted function of the transformations  $\Phi_k$  with the corresponding MI values as weighting factors, i.e.

$$\hat{\Phi} = \frac{1}{\Omega} \sum_{k=0}^K \omega_k \hat{\Phi}_k \quad \text{with} \quad \omega_k = \text{MI}[\Phi_k(S_k), R_k] \quad \text{and} \quad \Omega = \sum_{k=0}^K \omega_k \quad , \quad (4.5)$$

where  $\hat{\Phi}$  and  $\hat{\Phi}_k$  represent the transformation parameters of  $\Phi$  and  $\Phi_k$ , respectively. Using Eq. (4.5) to calculate the final parameters  $\hat{\Phi}$ , one can also obtain the

<sup>1</sup>In our experiments,  $K = 60$ , where  $k = 0$  represents the non-DW image.

corresponding registration precisions  $S_{\hat{\Phi}}$  of these transformation parameters:

$$S_{\hat{\Phi}} = \sqrt{\frac{1}{\Omega K} \sum_{k=0}^K (\hat{\Phi} - \hat{\Phi}_k)^2} , \quad (4.6)$$

which are valuable measures to evaluate the quality of the registration technique.

### 4.3.2 Diffusion tensor reorientation

It is obvious that there are no difficulties in transforming scalar images. The image value from a specific voxel is transferred, via the spatial transformation, to the reference image, where a posteriori an interpolation method must be applied to reconstruct the reference grid. For rank one (and higher) tensors, a specific reorientation should be applied in order to keep the orientational information intact. For diffusion tensors (rank two), an extra condition is required, i.e. the shape should also be preserved [12].

Consider the real-valued symmetric diffusion tensor  $\mathbf{D}$ . After eigenvalue decomposition,  $\mathbf{D}$  can be written as  $\mathbf{D} = \mathbf{E} \cdot \mathbf{\Lambda} \cdot \mathbf{E}^T$ , where the matrix  $\mathbf{E}$  defines the orthonormal eigenvectors  $\mathbf{e}_i$  and the diagonal matrix  $\mathbf{\Lambda}$  represents the eigenvalues  $\lambda_i$  of  $\mathbf{D}$ . Extracting the linear transformation matrix  $\Phi_L$  of  $\Phi$ , the new eigenvectors  $\mathbf{n}_i$  are calculated as follows:

$$\mathbf{n}_1 = \frac{\Phi_L \mathbf{e}_1}{\|\Phi_L \mathbf{e}_1\|} , \mathbf{n}_2 = \frac{\Phi_L \mathbf{e}_2 - (\mathbf{n}_1^T \Phi_L \mathbf{e}_2) \mathbf{n}_1}{\|\Phi_L \mathbf{e}_2 - (\mathbf{n}_1^T \Phi_L \mathbf{e}_2) \mathbf{n}_1\|} , \mathbf{n}_3 = \mathbf{n}_1 \times \mathbf{n}_2 \quad (4.7)$$

The reoriented diffusion tensor  $\mathbf{D}_{\Phi}$  can now be reconstructed as  $\mathbf{D}_{\Phi} = \mathbf{N} \cdot \mathbf{\Lambda} \cdot \mathbf{N}^T$ , where the matrix  $\mathbf{N}$  defines the transformed eigenvectors  $\mathbf{n}_i$ . Notice that the diffusion tensor shape is fully defined by the eigenvalue matrix  $\mathbf{\Lambda}$  and is equal for  $\mathbf{D}_{\Phi}$  and  $\mathbf{D}$ .

## 4.4 Methods

### 4.4.1 Simulated DTI data

The mathematical framework, as described in the previous chapter, is used to simulate DTI data sets of WM neural fiber bundles, based on the corresponding diffusion related physical properties [16]. In summary, several synthetic DTI data sets are constructed by first defining the fiber pathway, its corresponding width, FA, MD, and cross-sectional dependency of the fiber density. Subsequently, these properties are translated in the eigenvalues and eigenvectors that define the diffusion tensor.

### 4.4.2 Experimental DTI data

Two in vivo DTI data sets of the (healthy) human brain (male, 25y) were acquired on a 1.5 Tesla MR system (Fig. 4.1). Thereby, 60 axial slices with thickness

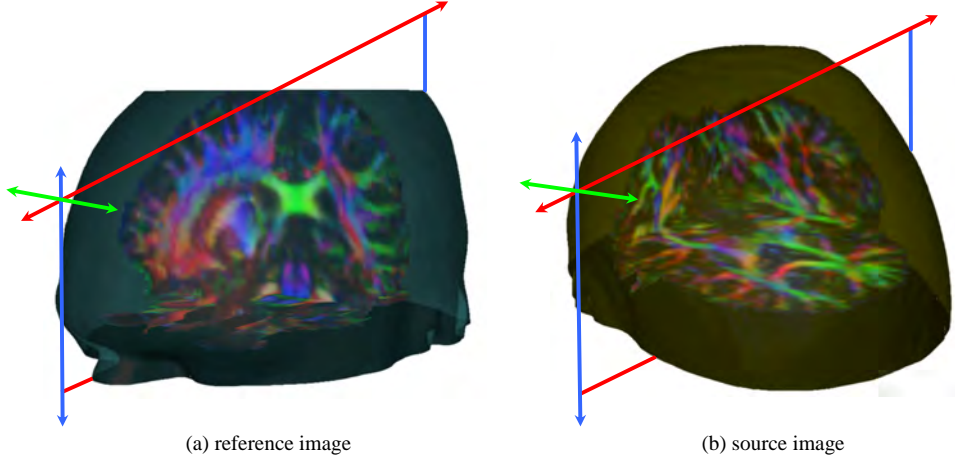


**Figure 4.1.** Two DTI data acquisitions of the (same) brain under different orientations: (a) the reference image  $R$  and (b) the source image  $S$ . The color-encoding in both images provides directional information, as indicated by the axes, of the underlying fiber orientation, which is assumed to be tangential to the local diffusion tensor.

of 2 mm were obtained covering the whole brain (voxel size of  $2 \times 2 \times 2 \text{ mm}^3$ ). A gradient configuration with 60 directions was used and additional acquisition parameters were as follows:  $b$ -factor =  $700 \text{ s/mm}^2$ , repetition time = 8.3 s, echo time = 108 ms, and number of  $b_0$  (no diffusion weighting) averages = 10. Further image processing of the DTI data sets, i.e. calculation of the diffusion tensor and the direction color-encoded maps, was performed with ‘ExploreDTI’, a graphical toolbox for exploratory DTI [17].

## 4.5 Results

### 4.5.1 Coregistration of simulated DTI data sets

As shown in Fig. 4.2 (a→c), rotating a DTI data set 90 degrees clockwise, as if considered to be scalar data, results in a loss of directional information of the underlying fiber tissue. Applying the RS corrects for both the shape and the predominant diffusion direction.

A second, less trivial example, is elucidated in Fig. 4.2 (d→g): a skew has been

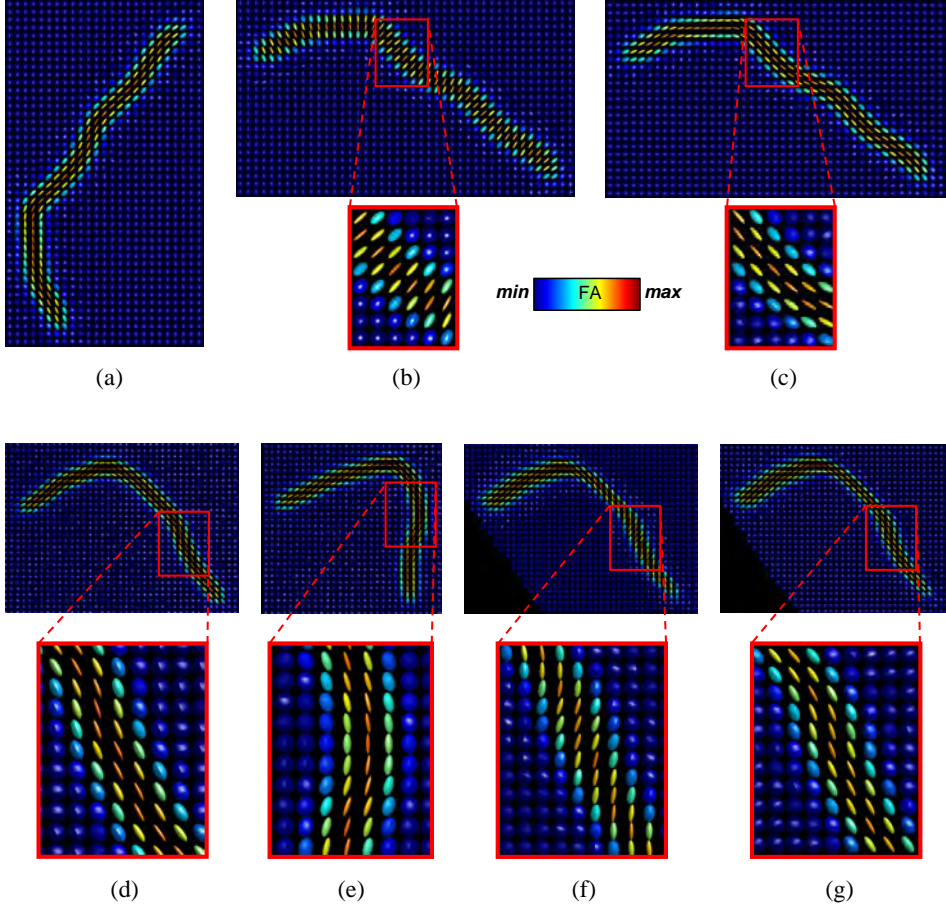


**Figure 4.2.** Ellipsoidal representations of synthetic DTI data sets using FA color-encoding. Example 1: (a) source image; (b) 90 degrees rotated (source) image without RS and (c) with RS. Example 2: the ground-truth data sets (d) reference image and (e) source image (=skewed reference image); the registered images without RS (f) and with RS (g).

applied to the horizontal direction. After coregistration, a significant difference exists between the reoriented and non-reoriented diffusion tensor field.

Both qualitative results indicate that the proposed RS effectively reorients the diffusion tensor field, preserving the directional information of the underlying fiber direction.

### 4.5.2 Coregistration of experimental DTI data sets

Figure 4.3 shows the results when applying the registration method to experimental DTI data. A specific part of the brain, i.e. the CC, is zoomed in to properly visualize the (bidirectional) first eigenvector of both the reference (red), the registered *without* RS (blue), and the registered *with* RS (orange) images. Although these results are qualitatively, they strongly indicate feasibility of the proposed coregistration technique to align experimental data.

## 4.6 Conclusions

A new 3D affine voxel based DTI coregistration technique has been developed using a direct diffusion tensor reconstruction approach to preserve the underlying orientational information. This multi-channel matching method applies mutual information as a similarity measure for the multi-valued DTI data sets. Simulations have been performed, demonstrating the applicability of the diffusion tensor shape preserving reorientation strategy. Also, an in-vivo coregistration example has been worked out, indicating feasibility of the proposed technique to coregister experimental data.

## Bibliography

- [1] L.G. Brown. A survey of image registration techniques. *ACM Comput Surv*, 24:326–376, 1992.
- [2] J.B. Maintz and M.A. Viergever. A survey of medical image registration. *Med Image Anal*, 2(1):1–36, 1998.
- [3] B. Zitová and J. Flusser. Image registration methods: a survey. *Image and Vision Computing*, 21:977–1000, 2003.
- [4] D.C. Alexander and J.C. Gee. Elastic matching of diffusion tensor images. *Comp Vision and Image Understanding*, 77(2):233–250, 2000.
- [5] D.K. Jones et al. Spatial normalization and averaging of diffusion tensor MRI data sets. *NeuroImage*, 17(2):592–617, 2002.
- [6] J. Ruiz-Alzola et al. Nonrigid registration of 3D scalar, vector and tensor medical data. In *MICCAI*, volume 1935, pages 541–550, 2000.
- [7] J. Ruiz-Alzola et al. Nonrigid registration of 3D tensor medical data. *Med Image Anal*, 6(2):143–161, 2002.



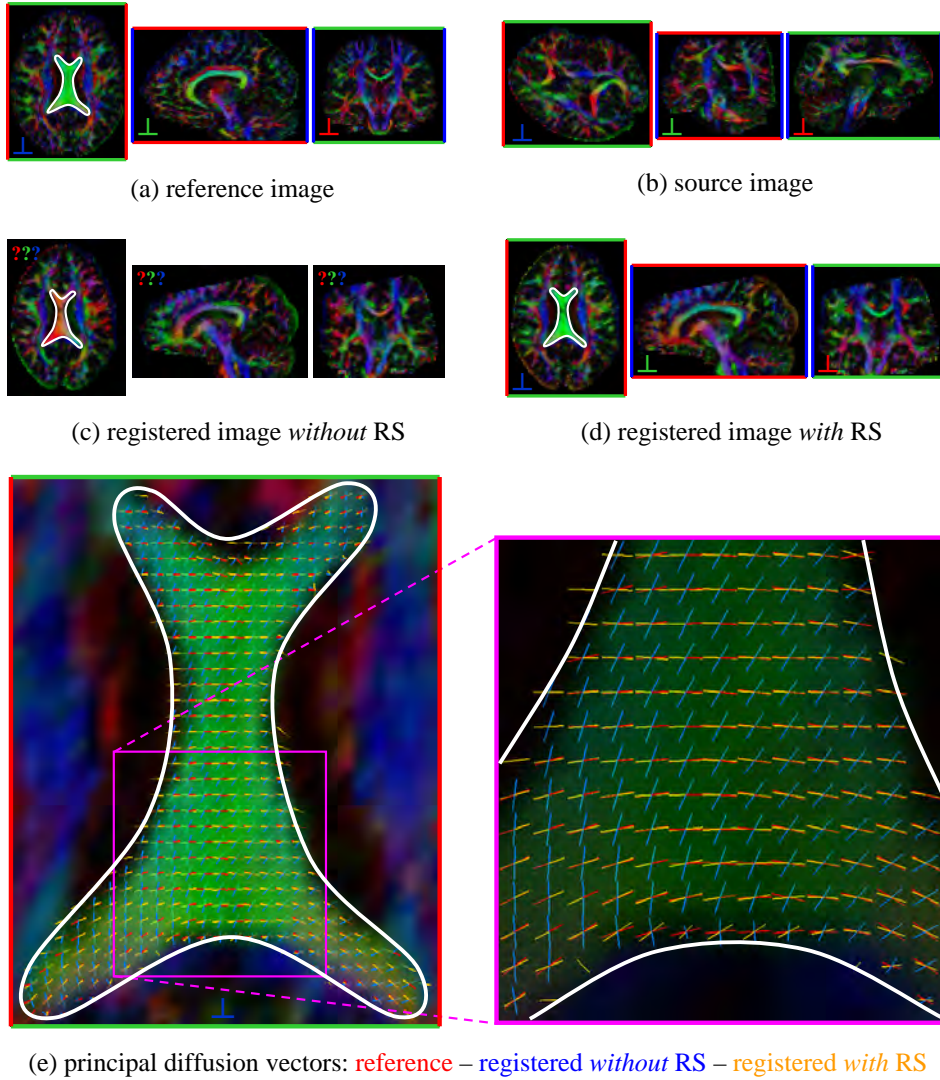


**Figure 4.3.** Human brain DTI images (three orthogonal slices of the volume data): color-encoding again provides directional information, which is reflected by the colored axes (notice the question marks in (c) due to the unknown directional information). Note that in (e), the principal diffusion vectors of the registered image with RS are better aligned with the reference image, than when the RS is omitted.

- [8] H.-J. Park et al. Spatial normalization of diffusion tensor MRI using multiple channels. *NeuroImage*, 20(4):1995–2009, 2003.
- [9] A. Guimond et al. Deformable registration of DT-MRI data based on transformation invariant tensor characteristics. In *ISBI*, 2002.
- [10] D. Xue et al. Spatial normalization of diffusion tensor fields. *Magn Reson Med*, 50(1): 175–182, 2003.
- [11] F. Maes et al. Multimodality image registration by maximization of mutual information. *IEEE Trans Med Imaging*, 16(2):187–198, 1997.
- [12] D.C. Alexander et al. Spatial transformations of diffusion tensor magnetic resonance images. *IEEE Trans Med Imaging*, 20(11):1131–1139, 2001.
- [13] P. Viola and W.M. Wells. Multi-modal volume registration by maximization of mutual information. *Med Image Anal*, 1(1):35–51, 1996.
- [14] A. Collingnon et al. Automated multimodality medical image registration using information theory. In *Inf Process Med Imaging*, volume 2082, pages 92–105, 2001.
- [15] T.M. Cover and J.A. Thomas. *Elements of information theory*. John Wiley and Sons, New York, 1991.
- [16] A. Leemans et al. Mathematical framework for simulating diffusion tensor MR neural fiber bundles. *Magn Reson Med*, 53(4):944–953, 2005.
- [17] A. Leemans et al. A graphical toolbox for exploratory diffusion tensor imaging and fiber tractography. In *SMRT*, Miami, USA, 2005.





## Chapter 5

# Feature based DTI coregistration

The work in this chapter has been published in

*A. Leemans, J. Sijbers, S. De Backer, E. Vandervliet, and P. M. Parizel, “Multi-scale white matter fiber tract coregistration: a new feature-based approach to align diffusion tensor data”, Magnetic Resonance in Medicine, (in press) 2006.*

### 5.1 Abstract

In this chapter, an automatic multiscale feature-based rigid-body coregistration technique for diffusion tensor imaging is developed based on the local curvature  $\kappa$  and torsion  $\tau$  of the white matter fiber pathways. As a similarity measure, the Mean Squared Difference (MSD) of corresponding fiber pathways in  $(\kappa, \tau)$ -space is chosen. After minimizing the MSD along the arc length of the curve, principal component analysis is applied to calculate the transformation parameters. In addition, a scale-space representation of the space curves is incorporated, resulting in a multiscale robust coregistration technique. This fully automatic technique inherently allows one to apply region of interest coregistration and is adequate to perform both global and local transformations. Simulations on synthetic diffusion tensor data are performed evaluating the coregistration accuracy and precision. Finally, an in-vivo coregistration example is presented and compared with a voxel based coregistration approach, demonstrating the feasibility and advantages of the proposed technique to align diffusion tensor data of the human brain.

## 5.2 Introduction

It is often desirable to combine the WM fiber tractography results from two or more studies on the same patient (follow up), or even to merge intersubject fiber tracking information (control versus pathology). Accurate alignment of different WM fiber bundle data in a common reference frame is then indispensable for quantitative analysis.

WM fiber pathways that are obtained from a tractography calculation can be considered as piecewise differentiable 3D space curves. Since these space curves represent the relevant information in several studies, it would be more efficient to coregister the space curves than to match the full voxel based DTI data. Here, only the data of the WM fiber tracts are used for the computation process which is considerably less than the full voxel based DTI data.

Only a few feature-based coregistration techniques have been developed for matching 3D curves: Kishon et al. address the problem of finding the longest matching subcurve appearing in two space curves, based on the rotationally and translationally invariant measures curvature  $\kappa$  and torsion  $\tau$  [1]. Each of these measures (or shape signatures) are stored in the form of a *hash table*, where the entries are associated with the values of  $(\kappa, \tau)$ -pairs. Improvements of this technique, introduced by the work of Guéziec et al., relate to the efficient one-dimensional *hash table* implementation, the spline approximation of the space curves, and the statistical analysis of different invariance measures for matching [2]. Comparison with other approaches to curve model matching, regarding the optimization and the transformation computation, have been described in [3, 4].

Within the field of DTI, the importance of the measures curvature and torsion for characterizing fiber tracking results has been mentioned previously [5, 6]. Moreover, in this context, Batchelor et al. and Corouge et al. employed these intrinsic measures to classify fiber tracts and quantify their local shape [7–11]. However, in their work, curvature and torsion were not used to coregister different data sets, i.e. no spatial transformations were explicitly calculated to map two (or more) data sets to a common coordinate frame.

In this chapter, a multiscale 3D rigid-body (rotation and translation) coregistration technique for DTI WM fiber tractography data sets is developed. The fiber tracts (which are space curves) are used to determine the optimal transformation instead of the voxels of the diffusion tensor data. From these space curves, local curvature  $\kappa$  and torsion  $\tau$  are calculated to establish direct labeling of corresponding space curves. For each pair of matched space curves a local transformation is calculated from which the final global transformation is estimated. A scale-space-based constant arc length parameterization at different scales is incorporated to obtain a robust multiscale coregistration algorithm.

To our knowledge, this methodology represents the first mathematical framework

for coregistering DTI data sets based on the corresponding fiber tracts. The proposed coregistration technique is fully automatic, allows one to apply ROI coregistration, and is adequate to perform both global and local transformations. Simulations are performed to evaluate the coregistration accuracy and precision for different noise levels and several user-defined parameters. In addition, an in vivo intra-subject coregistration example is given to demonstrate the feasibility of the proposed technique to align DTI data of the human brain. Finally, a comparison is made with a voxel based coregistration approach to evaluate the performance for the experimental results.

## 5.3 Theory

This section gives the mathematical framework of the coregistration technique. First, the concepts of curvature and torsion with respect to space curves, i.e. the WM fiber pathways<sup>1</sup>, are briefly described. Next, the new coregistration technique is expounded. Finally, the computation of the transformation parameters is described.

### 5.3.1 Curvature and torsion of space curves

#### 5.3.1.1 Definitions

For a regular space curve  $\alpha(s) = [x(s), y(s), z(s)]$ , where the spatial coordinates  $x$ ,  $y$  and  $z$  are parameterized by the arc length  $s$ , curvature  $\kappa(s)$  is defined as [12]:

$$\kappa(s) = |\alpha''(s)| \quad (5.1)$$

It is a measure for the rate at which the curve pulls away from the tangent vector  $\mathbf{t}(s) = \alpha'(s)$ . The direction in which  $\alpha(s)$  is pulled, is given by the normal vector  $\mathbf{n}(s)$ . If the normal to the plane spanned by  $\mathbf{t}(s)$  and  $\mathbf{n}(s)$  is given by  $\mathbf{b}(s) = \mathbf{n}(s) \times \mathbf{t}(s)$ , also called the binormal vector, then torsion  $\tau(s)$  is defined as [12]:

$$\mathbf{b}'(s) = \tau(s)\mathbf{n}(s) . \quad (5.2)$$

It measures how quickly the space curve pulls away from the plane spanned by  $\mathbf{n}(s)$  and  $\mathbf{t}(s)$ . Note that, in contrast to curvature, torsion may be either positive (for right-handed space curves) or negative (for left-handed space curves). An example of a space curve is displayed in Fig. 5.1 (a)→(c) to elucidate the meaning of  $\tau$  and  $\kappa$ .

In WM fiber tractography, only the sampled version of a space curve is available. Subsequently, the space curve  $\alpha$  can be represented by a  $(3 \times N)$ -matrix, where  $N$

---

<sup>1</sup>In this section, the mathematical term ‘space curve’ is used to denote WM fiber pathways.

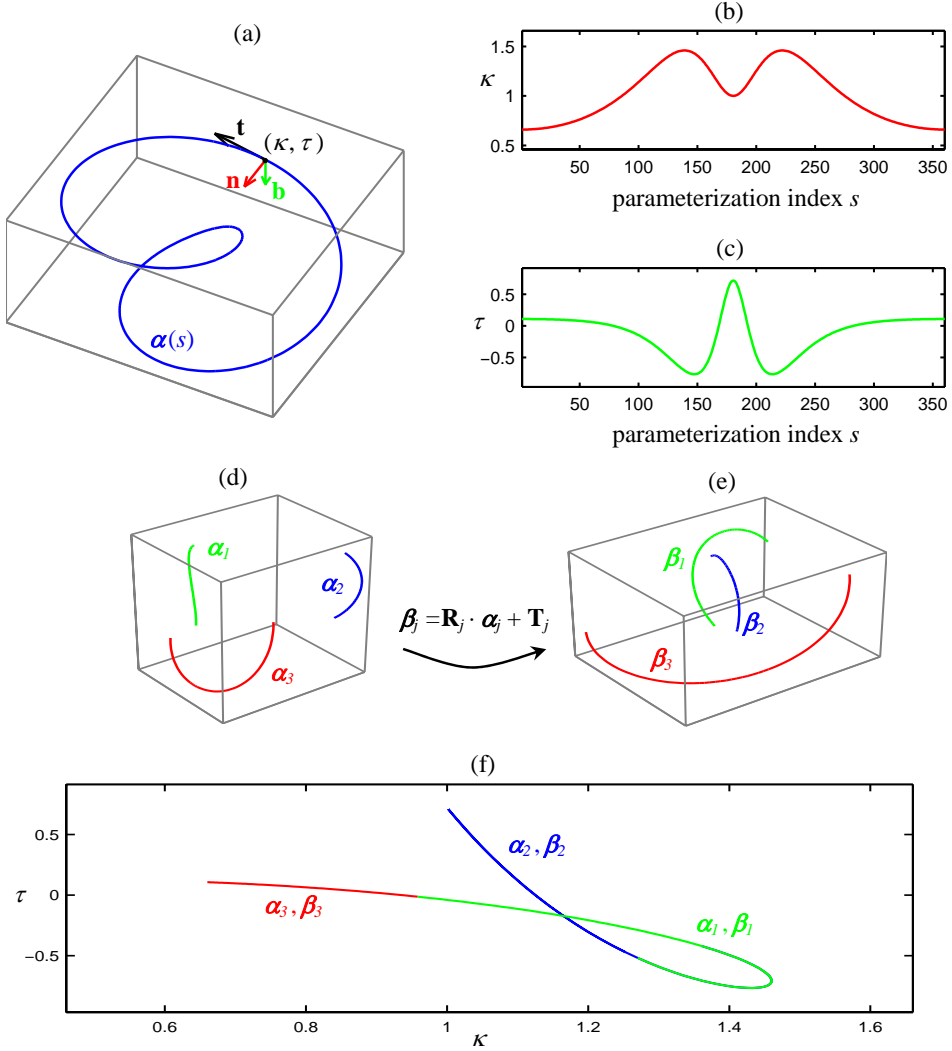


**Figure 5.1.** (a) With every point  $s$  of the space curve  $\alpha(s)$ , a Frénet frame, i.e. the vector triple  $(\mathbf{t}, \mathbf{n}, \mathbf{b})$ , can be associated describing the local geometrical properties  $\kappa$  and  $\tau$ . In (b) and (c),  $\kappa$  respectively  $\tau$  are shown as a function of the parameterization index  $s$ . In (d), three parts of the space curve of (a) are shown with random orientation and position. Rigid transformation of these space curves  $\alpha_j$  (with respective rotation  $\mathbf{R}_j$  and translation  $\mathbf{T}_j$ ) results in the corresponding curves  $\beta_j$ , displayed in (e). In (f), transforming the space curves  $\alpha_j$  and  $\beta_j$  to  $(\kappa, \tau)$ -space shows the invariance properties of  $\kappa$  and  $\tau$ .

is the number of positions  $\alpha(i) = (x_i, y_i, z_i)$ . A segment between consecutive space curve points is denoted as  $\Delta_i = \alpha(i+1) - \alpha(i)$ . For every sample point  $i$  of the space curve  $\alpha$  curvature and torsion can now explicitly be written as

$$\kappa_i = \frac{|\alpha'(i) \times \alpha''(i)|}{|\alpha'(i)|^3} \quad (5.3)$$

and

$$\tau_i = \frac{\alpha'(i) \cdot (\alpha''(i) \times \alpha'''(i))}{|\alpha'(i) \times \alpha''(i)|^2}, \quad (5.4)$$

where the derivatives  $\alpha'(i)$ ,  $\alpha''(i)$  and  $\alpha'''(i)$  are discretely calculated (e.g.,  $\alpha'(i) = \Delta_i / \|\Delta_i\|$ ). Note that in  $(\kappa, \tau)$ -space,  $\alpha$  can now be represented by a  $(2 \times N)$ -matrix, where each sample point is given by  $g_i(\alpha) \equiv (\kappa_i, \tau_i)$ . From a technical point of view, it is also important to note that when  $\kappa \approx 0$ ,  $\tau$  is undefined. Therefore, in this case (e.g.,  $\kappa < 10^{-6}$ ), the space curve  $\alpha$  was locally only characterized by  $\kappa$ .

### 5.3.1.2 Invariance properties

A fundamental theorem in differential geometry states that the intrinsic properties of a parameterized space curve  $\alpha$  are uniquely defined by the curvature  $\kappa$  and the torsion  $\tau$ , i.e. every other space curve  $\beta$  that differs from  $\alpha$  by a rigid motion (i.e.,  $\beta = \mathbf{R} \cdot \alpha + \mathbf{T}$  with  $\mathbf{R}$  a rotation matrix and  $\mathbf{T}$  a translation vector) will have identical  $\kappa$  and  $\tau$  assuming that a one-to-one correspondence between the parameterizations is feasible [see Fig. 5.1 (d)→(f)] [12]. With this theorem, immediate comparison of curves in  $(\kappa, \tau)$ -space independent of rotation and translation is feasible, forming the basis of our mathematical framework to coregister space curves.

## 5.3.2 Space curve coregistration

In this section, the different aspects of the proposed coregistration technique are expounded. Consider two sets of space curves (or stated equivalently, two fiber tracking results) that need to be registered: the source curves  $\{\alpha\} \equiv \{\alpha_j \mid j = 1, \dots, J_\alpha\}$  and the target curves  $\{\beta\} \equiv \{\beta_j \mid j = 1, \dots, J_\beta\}$ . Note that the tract pathways  $\{\alpha\}$  and  $\{\beta\}$  are not necessarily confined to a specific anatomical fiber structure. Subsequently, the proposed technique inherently allows one to coregister tractography data sets that have a different FOV, i.e. tracts that are not present in one data set will hardly influence the coregistration result.

In summary, the coregistration framework contains the following steps:

1. For each space curve  $\alpha_j$ , or a subcurve thereof, find the optimal matching space curve  $\beta_j$ , or a subcurve thereof, by minimizing the MSD between their corresponding local curvature and torsion. This local matching procedure,

dubbed ‘curve index correspondence’, is performed for each space curve separately.

2. For each set of matched space (sub)curves  $(\alpha_j, \beta_j)$  a local transformation  $\Phi_j$  is calculated by applying a fast point-to-point coregistration approach, which is equivalent to Schönemann’s solution of the ‘orthogonal Procrustes problem’ [13].
3. The global rigid-body transformation  $\Psi$  that maps the source curves  $\{\alpha\}$  to the target curves  $\{\beta\}$  is estimated from the set of local transformations  $\Phi_j$ .

The previous steps are repeated for different scale-space representations of the space curves. The optimal transformation is finally calculated by minimizing the global residue with respect to this scale parameter. By applying this multiscale approach, a more robust coregistration can be achieved.

### 5.3.2.1 Curve index correspondence

Before the transformations  $\Phi_j$  can be calculated, correspondence between the space curves  $\{\alpha\}$  and  $\{\beta\}$  must be established, i.e. for each curve  $\alpha_j$ , the optimal corresponding  $\beta_j$  must be found. For this purpose, we reparameterize each space curve along its arc length with a constant step size  $\Delta$ , i.e. for each space curve  $\alpha_j$  and  $\beta_j$  the distance between consecutive sample points is now given by  $\Delta$ . Here,  $\Delta$  can be taken equal to the step size parameter that was defined in the tractography procedure. This uniform arc length reparametrization is computed analytically by consecutively intersecting the space curve with a sphere of radius  $\Delta$ , where the center of each sphere is determined by the preceding intersection point.

The constant arc length reparametrization allows one to compare individual space curves in  $(\kappa, \tau)$ -space by minimizing the MSD of different space curves according to both the space curve index and the set of subcurves. A subcurve of  $\alpha_j$  or  $\beta_j$  containing  $L$  consecutive sample points is denoted as  $\alpha_j^L$  and  $\beta_j^L$ , respectively. For every source subcurve, the corresponding target subcurve is now determined by minimizing the MSD over all pairs of subcurves in all pairs of curves, i.e.  $\forall j \in \{1, \dots, J_\alpha\} \exists k \in \{1, \dots, J_\beta\}$  :

$$(\alpha_j^K, \beta_k^K) = \arg \min_{l,L} MSD(\alpha_j^L, \beta_l^L) \quad (5.5)$$

with

$$MSD(\alpha_j^L, \beta_l^L) = \frac{1}{L} \sum_{i=1}^L \|g_i(\alpha_j^L) - g_i(\beta_l^L)\|^2 \quad (5.6)$$

and

$$L \in \{L_{\min}, \dots, \min(N_{\alpha_j}, N_{\beta_l})\} \quad , \quad (5.7)$$

where  $N_{\alpha_j}$  and  $N_{\beta_j}$  represent the number of sample points of the space curves  $\alpha_j$  and  $\beta_j$ , respectively, and the predefined parameter  $L_{\min}$  denotes the minimum number of sample points that represent a subcurve.

Eq. (5.5) describes the matching process for finding the optimal curve (or subcurve) in the set  $\{\alpha\}$  for each of the curves (or subcurves) of the set  $\{\beta\}$ . The optimization with respect to the index  $L$  represents the search for the best match within the set of possible subcurves for a particular pair of curves  $\alpha_j$  and  $\beta_l$ . The index  $l$  simply denotes the space curve index of a particular curve in the set  $\{\beta\}$ . In Eq. (5.6), the MSD of  $\mathbf{g} \equiv (\kappa, \tau)$  is taken between the corresponding sample points  $i$  of  $\alpha_j^L$  and  $\beta_l^L$ . Finally, Eq. (5.7) states that the number of sample points of any subcurve of the space curves  $\alpha_j$  and  $\beta_j$  used in the matching procedure is confined between  $L_{\min}$  and the minimum of  $N_{\alpha_j}$  and  $N_{\beta_j}$ .

### 5.3.2.2 Local space curve transformation

After establishing the correspondence between the space curves [see Eq. (5.5)], the transformation  $\Phi_j$  associated with each pair of space curves ( $\alpha_j^K, \beta_j^K$ ) is determined by applying a fast point-to-point coregistration approach, which is equivalent to Schönemann's solution of the 'orthogonal Procrustes problem' [13], as follows (for clarity, the indices  $j$  and  $K$  are omitted in this section):

1. Calculate the auto-covariance matrices  $\mathbf{C}$  of the space curve traces:

$$\begin{aligned} \mathbf{C}_\alpha &= (\alpha - \langle \alpha \rangle \cdot \mathbf{1}) \cdot (\alpha - \langle \alpha \rangle \cdot \mathbf{1})^T \\ \mathbf{C}_\beta &= (\beta - \langle \beta \rangle \cdot \mathbf{1}) \cdot (\beta - \langle \beta \rangle \cdot \mathbf{1})^T. \end{aligned} \quad (5.8)$$

The centroids of  $\alpha$  and  $\beta$  are represented by the  $(3 \times 1)$ -matrices  $\langle \alpha \rangle$  and  $\langle \beta \rangle$ , respectively, and  $\mathbf{1}$  represents the  $(1 \times N)$ -column vector filled with 1.

2. After real eigenvalue decomposition of these covariance matrices, the rotation matrix  $\mathbf{R}$  and the translation matrix  $\mathbf{T}$  are computed as:

$$\mathbf{R} = \sum_{i=1}^3 \mathbf{e}_i^\beta \cdot (\mathbf{e}_i^\alpha)^t \quad (5.9)$$

and

$$\mathbf{T} = \langle \beta \rangle \cdot \mathbf{1} - \mathbf{R} \cdot \langle \alpha \rangle \cdot \mathbf{1} \quad (5.10)$$

with  $\mathbf{e}_i^\alpha$  and  $\mathbf{e}_i^\beta$  the eigenvectors of  $\mathbf{C}_\alpha$  and  $\mathbf{C}_\beta$ , respectively. The registered space curves  $\gamma \equiv \Phi(\alpha)$  can now be determined by  $\gamma = \mathbf{R} \cdot \alpha + \mathbf{T}$ . Note that only the orientation and not the direction of the eigenvectors is known. Therefore, the matrix  $\mathbf{R}$  that minimizes the MSD between  $\beta$  and  $\gamma$  in real space is finally taken, i.e.

$$\mathbf{R} = \arg \min_{\mathbf{S}} \text{MSD}(\beta, \gamma = \mathbf{S} \cdot \alpha + \mathbf{T}) \quad (5.11)$$



with the MSD now defined in real space, i.e.

$$MSD(\beta, \gamma) = \frac{1}{K} \sum_{i=1}^K \|\beta(i) - \gamma(i)\|^2, \quad (5.12)$$

where  $K$  denotes the number of sample points.

A schematic illustration is given in Fig. 5.2 to elucidate this Principal Component Analysis (PCA) based transformation.

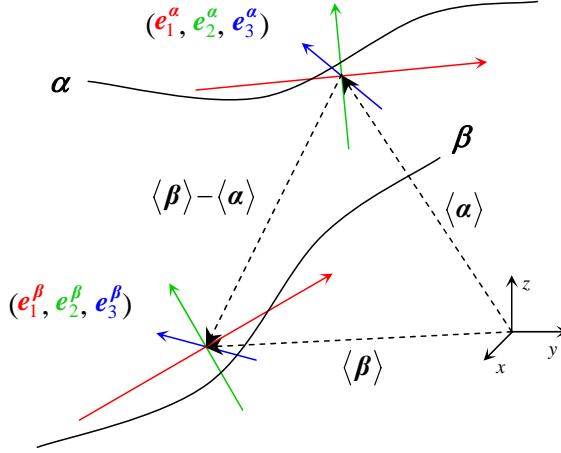


**Figure 5.2.** The principal components  $e_i^\alpha$  and  $e_i^\beta$  of  $\alpha$  respectively  $\beta$  determine the rotation matrix  $\mathbf{R}$ . The translation matrix  $\mathbf{T}$  is computed from the centroids  $\langle \alpha \rangle$  and  $\langle \beta \rangle$ .

### 5.3.2.3 Global space curve transformation

The following procedure is applied for finding the global transformation  $\Psi$  from the local transformations  $\Phi_j$ :

1. For each transformation  $\Phi_j$ , associated with a pair of corresponding space curves  $(\alpha_j, \beta_j)$ , a global coregistration residue  $\varepsilon_j$  is calculated after transforming all the source curves  $\{\alpha\}$  with  $\Phi_j$ , i.e.

$$\varepsilon_j = MSD[\{\beta\}, \{\gamma\} \equiv \Phi_j(\{\alpha\})], \quad (5.13)$$

where the MSD over all pairs of curves (hence the curly brackets) and all points of each curve is calculated in real space as in Eq. (5.12).

2. For the  $p$  percent smallest residues  $\varepsilon_j$ , the transformation parameters  $\mu^j = [\theta_x^j, \theta_y^j, \theta_z^j, t_x^j, t_y^j, t_z^j]$  are calculated.

3. From the sets of transformation parameters  $\mu^j$ , a final global transformation  $\Psi$  can now be estimated with a corresponding coregistration residue  $\varepsilon$ , calculated as:

$$\varepsilon = MSD [\{\beta\}, \{\gamma\} \equiv \Psi(\{\alpha\})] . \quad (5.14)$$

Calculation of the median and the interquartile range of the transformation parameters  $\mu^j$  is preferred due to the potential non-normality of the  $\mu^j$  distribution.

From a technical point of view, it is important to note that two (or more) source curves theoretically could match the same target curve. In this situation however, the corresponding residues  $\varepsilon_j$  will be ranked differently, providing a natural way to estimate the final global transformation.

### 5.3.2.4 Multiscale coregistration

In order to construct a space curve  $\alpha$  at different levels of detail  $\sigma$ , a scale-space method is applied [14]. In this approach,  $\alpha(s)$  is convolved with a Gaussian kernel  $g(s, \sigma)$  with mean 0 and standard deviation  $\sigma$  to compute the varying levels of detail, i.e.

$$\alpha_\sigma(s) = \alpha(s) * g(s, \sigma) . \quad (5.15)$$

The process of constructing the curves  $\alpha_\sigma$  as  $\sigma$  varies from 0 to  $\infty$ , is referred to as the *evolution* of  $\alpha$ . Notice that with this scale-space approach curvature and torsion of the evolved versions of a space curve can efficiently be computed: taking the  $i$ th derivative in both sides of Eq. (5.15), it is known that

$$\alpha_\sigma^{(i)}(s) = \alpha(s) * g^{(i)}(s, \sigma) , \quad (5.16)$$

which eliminates the necessity to directly calculate the derivatives of the space curve coordinates [14]. As a consequence, the discrete calculation of the derivatives, as previously described, can now be replaced by Eq. (5.16) for  $\sigma > 0$ . The final transformation  $\Psi$  can now be found as follows:

$$\Psi = \arg \min_{\tilde{\Psi}} MSD(\{\beta\}, \tilde{\Psi}(\{\alpha_\sigma\})) , \quad (5.17)$$

where the MSD is computed in real space as in Eq. (5.12).

An alternative to this scale-space approach is fitting of 3D splines to the space curve coordinates at multiple scales [15]. From those splines, curvature and torsion could then be computed. The drawbacks of this method are the high computational cost and the variability of the results due to the arbitrary choice of knot points.

### 5.3.2.5 Computational complexity

The general computational complexity of coregistering  $J_\alpha$  source curves  $\{\alpha\}$  with  $J_\beta$  target curves  $\{\beta\}$  for  $\sigma$  different levels of detail is proportional to  $\langle S \rangle \sigma J_\alpha J_\beta$ , where  $\langle S \rangle$  represents the average number of comparisons necessary for finding sub-curve correspondence. It can be shown that this number of comparisons  $S$  for finding subcurve correspondence between a source curve  $\alpha$  and a target curve  $\beta$  with  $N_\alpha$  respectively  $N_\beta$  sample points (take  $N_\alpha < N_\beta$ ) is given by:

$$S = \frac{(N_\alpha - L_{\min} + 2)(N_\alpha - L_{\min} + 1)(3N_\beta - N_\alpha - 2L_{\min} + 3)}{3}. \quad (5.18)$$

The factor  $S$  is mainly determined by  $L_{\min}$ , which in this work is defined as the minimum length (expressed in number of sample points) of  $\alpha_j$  and  $\beta_j$  [see Eqs. (5.5) and (5.7)]. This definition implicitly assumes that source curves should exist which can be considered as subcurves of the target curves or vice versa. For WM fiber tractography this assumption appears to be valid, resulting in a total number of comparisons, which is approximately proportional to  $\langle N_\beta - N_\alpha \rangle \sigma J_\alpha J_\beta$ .

A reduction of the computational complexity can be achieved by introducing a space curve sampling factor  $\xi$ . This user-defined parameter uniformly samples the space curve data sets, reducing computation times by a factor of  $\xi^{-2}$ , and can be applied for densely seeded fiber tracking results.

## 5.4 Methods

### 5.4.1 Simulated DTI data

The mathematical framework described in chapter 3 is used to simulate DTI data of WM neural fiber bundles, based on the corresponding diffusion related physical properties [16]. In order to evaluate the accuracy of the proposed coregistration technique, two synthetic DTI phantoms of WM fiber bundles were generated under different orientations. Without loss of generality, the misalignment between the fiber tracts was predefined by one parameter  $\theta_z = \pi/6$ , i.e. the rotation angle associated to the  $z$ -axis [Fig. 5.3 (a) and (b)].

It is important to note that for simulating a ground-truth DTI data set of the same fiber tracts, but with a different orientation, the fiber tracts should be transformed first and then the synthetic DTI data set should be generated, for then, the smoothing effect caused by interpolation (which influences the fiber tractography results) can be avoided.

Both DTI data sets had a  $(50 \times 50 \times 50)$ -matrix size with isotropic voxel dimensions  $(2 \times 2 \times 2 \text{ mm}^3)$ . Other image parameters were equal to the experimental data acquisition parameters, which are described in the next section. Different levels of Rician distributed noise were added to the DW images of the corresponding

ground-truth DTI data sets in order to study the noise sensitivity of the proposed coregistration technique.

### 5.4.2 Brain DTI data

Two in vivo DTI data sets of the healthy human brain (male, 25 year) were acquired on a 1.5 Tesla MR. After the first ‘normal’ acquisition, the volunteer was asked to reposition his head randomly for the second acquisition, mainly resulting in an axial rotation [Fig. 5.3 (c) and (d)]. Thereby, 60 axial slices with thickness of 2 mm were obtained covering the whole brain (voxel size of  $2 \times 2 \times 2 \text{ mm}^3$ ). A gradient configuration with 60 directions (evenly distributed on a sphere and identical for both acquisitions) was used and additional acquisition parameters were:  $b$ -factor =  $700 \text{ s/mm}^2$ ,  $\text{TR} = 8300 \text{ ms}$ ,  $\text{TE} = 108 \text{ ms}$ , and number of averages of the  $T_2$ -weighted image = 10. The mean SNR values of the  $T_2$ -weighted images and the DW images were 21 and 10, respectively. The DW images were coregistered to the  $T_2$ -weighted image by maximization of mutual information to correct for motion artifacts and residual eddy current distortions (typically less than 1-2 voxels) using MIRIT (Multimodality Image Registration using Information Theory) [17]. Trilinear interpolation was performed to resample the transformed images. It is important to note that an appropriate intensity correction of the DW images should be incorporated within this procedure if motion artifacts or eddy current distortions would not be negligible (i.e., higher than  $\sim 2$  voxels) [18].

The effective diffusion tensor, the corresponding eigensystem, and the subsequently derived FA and MD values were calculated in each voxel according to [19]. Further image processing of the DTI data sets, i.e. calculation of the direction color-encoded maps, was performed with ‘ExploreDTI’ [20].

### 5.4.3 Fiber tractography

A standard deterministic streamline fiber tracking approach was applied to both the synthetic and the brain diffusion tensor data sets, as described previously in [5]. For the synthetic data, fiber tracking was initiated from predefined positions on each WM fiber pathway, ensuring identical seed points in both data sets. The step size  $\Delta$  was set to 1 mm, fiber tracking was terminated when entering locations where  $\text{FA} < 0.1$  or the angle between consecutive tract segments  $\theta_t$  was larger than  $\pi/4$ . For the DTI data of the brain, fiber tracts were initiated from each voxel with  $\text{FA} > 0.5$ . To minimize the cluttering of short fiber tracts, all tracts with length smaller than 50 mm were omitted.

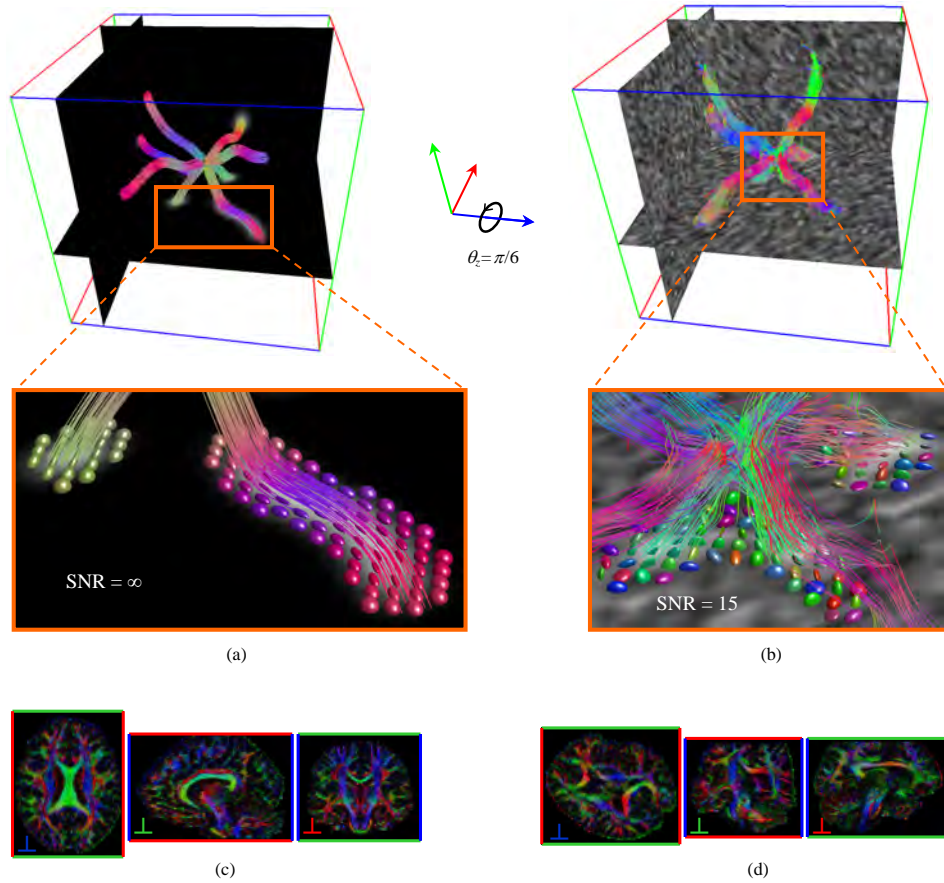


**Figure 5.3.** (a) and (b) represent the tractography results of, respectively, a (noiseless) target and a (noisy) source synthetic DTI phantom. The ellipsoids depict the local diffusion properties and the background gray scaling reflects the corresponding FA value. Two DTI data acquisitions of the (same) brain under different orientations are shown in (c), i.e. the ‘normal’ image, and in (d), i.e. the ‘rotated’ image. As indicated by the axes, the color-encoding in the images provides directional information of the underlying fiber orientation, which is assumed to be tangential to the local PDV.

## 5.5 Results

### 5.5.1 Quantitative analysis of the white matter fiber coregistration technique

#### 5.5.1.1 Noise sensitivity

In order to study the noise sensitivity of the proposed coregistration technique, different levels of Rician distributed noise were added to the DW images and the  $T_2$  images of the corresponding synthetic DTI data sets. This procedure was repeated for a large number of trials ( $10$ ,  $10^2$ , and  $10^3$ ) and the resulting averaged SNR values ranged from 15 to 150. For each trial, both target curves  $\{\beta\}$  and source tracts  $\{\alpha\}$  were reconstructed first (with  $J_\alpha \simeq J_\beta \simeq 10^3$  and  $\langle N_\alpha \rangle \simeq \langle N_\beta \rangle \simeq 75$ ) using the fiber tractography approach as mentioned previously. Second, the coregistration technique was applied with the following parameters: residue cut-off value  $p = 10\%$ , i.e. 10% of the calculated local registration transformations is used to estimate the final global transformation; multiscale values  $\sigma = 0, 1, 2, \dots, 20$  in unit size  $\Delta$ ; space curve sampling factor  $\xi = 1$ . As shown by the simulation results in Fig. 5.4 (a), no indications of a bias, i.e. a systematic deviation of the coregistration result with respect to the ground-truth solution, were obtained. Note that the error bars represent the inter-quartile range instead of the 95% confidence interval due to the non-normality of the  $\theta_z$  distribution of the coregistration results.

#### 5.5.1.2 Multiscale coregistration

To demonstrate the benefit of the proposed multiscale approach, the coregistration technique was applied (SNR = 21;  $\xi = 1$ ;  $p = 10\%$ ; single trial<sup>2</sup>) for each level of detail  $\sigma = 0, 1, 2, \dots, 20$  independently [see Fig. 5.4 (b)]. As indicated by the minimal corresponding coregistration residue  $\varepsilon$ , the most accurate result is obtained at a higher (non-zero) scale. Also, it has been observed that a decrease in SNR results in an increase of the optimal scale  $\sigma$ .

#### 5.5.1.3 Global transformation estimation

In Fig. 5.4 (c), the effect of the residue cut-off value  $p$  on the coregistration precision and accuracy is shown (SNR = 21;  $\xi = 1$ ;  $\sigma = 0, 1, 2, \dots, 20$ ; single trial). Here, it was observed that the choice of the  $p$  percent residue cut-off influenced the trade-off between the coregistration precision and accuracy, i.e. increasing the  $p$  value increased the accuracy, but decreased the precision and vice versa.

<sup>2</sup>The error bars (inter-quartile range), associated with the registration solution of a single trial, stem from the final estimation of the global transformation  $\Psi$ , as previously described in the section ‘global space curve transformation’.

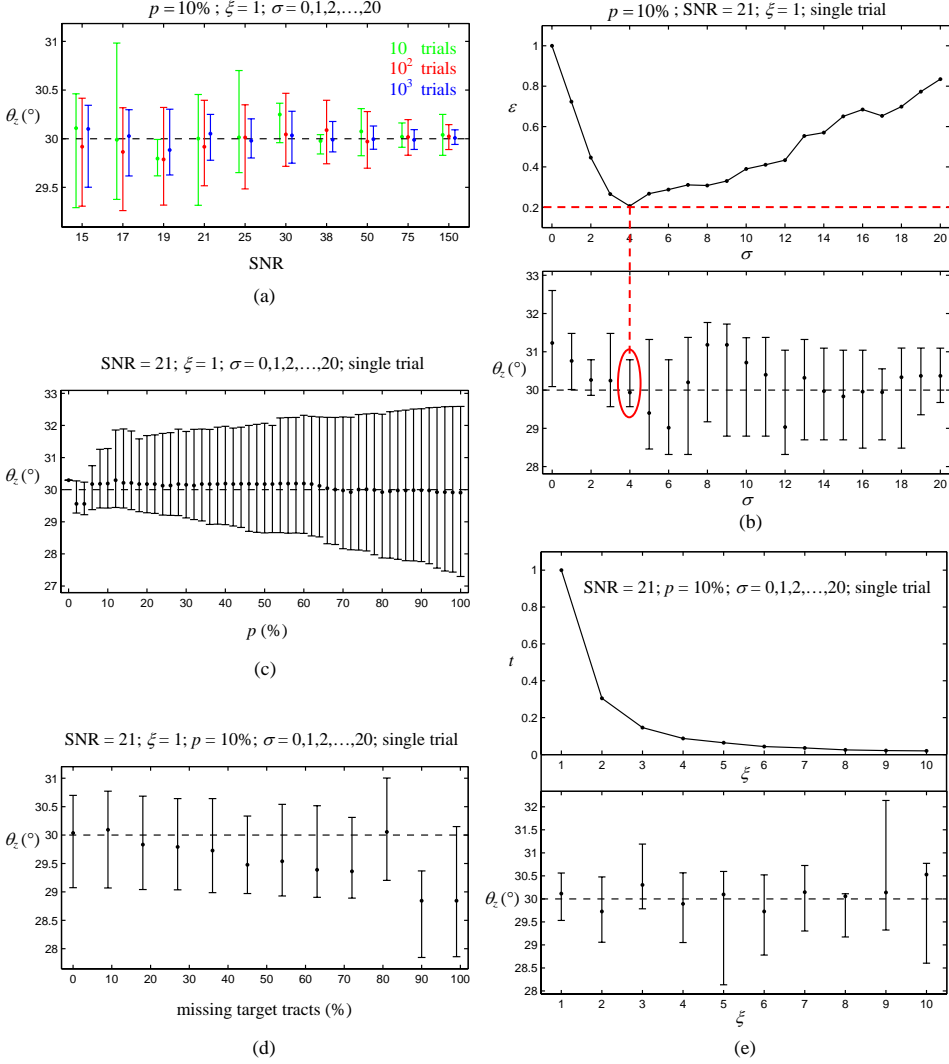


**Figure 5.4.** (a) The coregistration accuracy and precision as a function of the SNR. (b) The coregistration solution and the corresponding residue  $\varepsilon$  as a function of the evolution scale  $\sigma$ . As indicated in red, the final transformation is determined according to Eq. (5.17). (c) The coregistration accuracy and precision as a function of the residue cut-off  $p$ . (d) The effect of excluding target tracts on the coregistration result. (e) The effect of the space curve sampling factor  $\xi$  on the coregistration result and the corresponding normalized time complexity  $t$ .

#### 5.5.1.4 ROI based coregistration

As shown in Fig. 5.4 (d), the precision is not decreased by systematically omitting a predefined percentage of target space curves with consecutive curve indices (or equivalently source space curves) in the coregistration procedure. The accuracy on the other hand is decreased for an increasing amount of missing tracts, but remains acceptable up to 80%.

#### 5.5.1.5 Space curve sampling and time complexity

To reduce the computation time for densely seeded fiber tracking results, a user-defined space curve sampling factor  $\xi$  can be defined which uniformly subsamples the set of space curves. In the performed simulation [see Fig. 5.4 (e)], no significant decrease in coregistration accuracy or precision is observed for uniform space curve subsampling (i.e., only every  $\xi$ th space curve is used in the computation of the coregistration result) up to 10% of the total set of space curves.

Effective computation times<sup>3</sup> (with parameters  $J_\alpha \approx J_\beta \approx 10^3$ ;  $\sigma = 0, 1, \dots, 20$ ;  $\langle N_\alpha \rangle \approx \langle N_\beta \rangle \approx 75$ ) ranged from  $\sim 15$  min (for  $\xi = 1$ ) to  $\sim 10$  sec (for  $\xi = 10$ ). The corresponding general time complexity  $t$  (normalized to one) as function of the space curve sampling factor  $\xi$  is also shown in Fig. 5.4 (e).

### 5.5.2 Coregistration of brain DTI data sets

First, fiber tractography was performed on both DTI data sets resulting in  $J_\alpha \simeq J_\beta \simeq 2 \times 10^3$  fiber pathways with  $\langle N_\alpha \rangle \simeq \langle N_\beta \rangle \simeq 100$  [see Fig. 5.5 (a) and (b)]. Second, the coregistration technique is applied with the following parameters:  $p = 10\%$ ,  $\xi = 5$ , and  $\sigma = 0, 1, 2, \dots, 20$  (total computation time was  $\sim 5$  min). As shown in Fig. 5.5 (c), (d), and (e), the coregistered space curves  $\{\gamma\} \equiv \Psi(\{\alpha\})$  are correctly aligned with the target curves  $\beta$ . An additional example is presented in Fig. 5.5 (f, g, and h) to visually evaluate the same coregistration result. Here, only the tracts of the entire body of the corpus callosum have been segmented (with separate midsagittal ROI selection on both the target and the registered data set) and transparency rendering has been applied to further facilitate the inspection of the coregistration accuracy. This qualitative example also demonstrates that the coregistration method inherently allows one to apply ROI coregistration, for in Fig. 5.5 (c, d, f, and g), the difference in FOV is clearly visible.

The obtained transformation parameters  $\mu = [\theta_x, \theta_y, \theta_z, t_x, t_y, t_z]$  that define the spatial transformation  $\Psi$  are given in Fig. 5.6 (a). In addition, pseudo-color-encoded maps are shown that approximately represent the FA map of the target data (red), the transformed source data (green), and the mutually overlapping

<sup>3</sup>All computations were performed with not optimized Matlab code on a 3.4 GHz CPU computer.



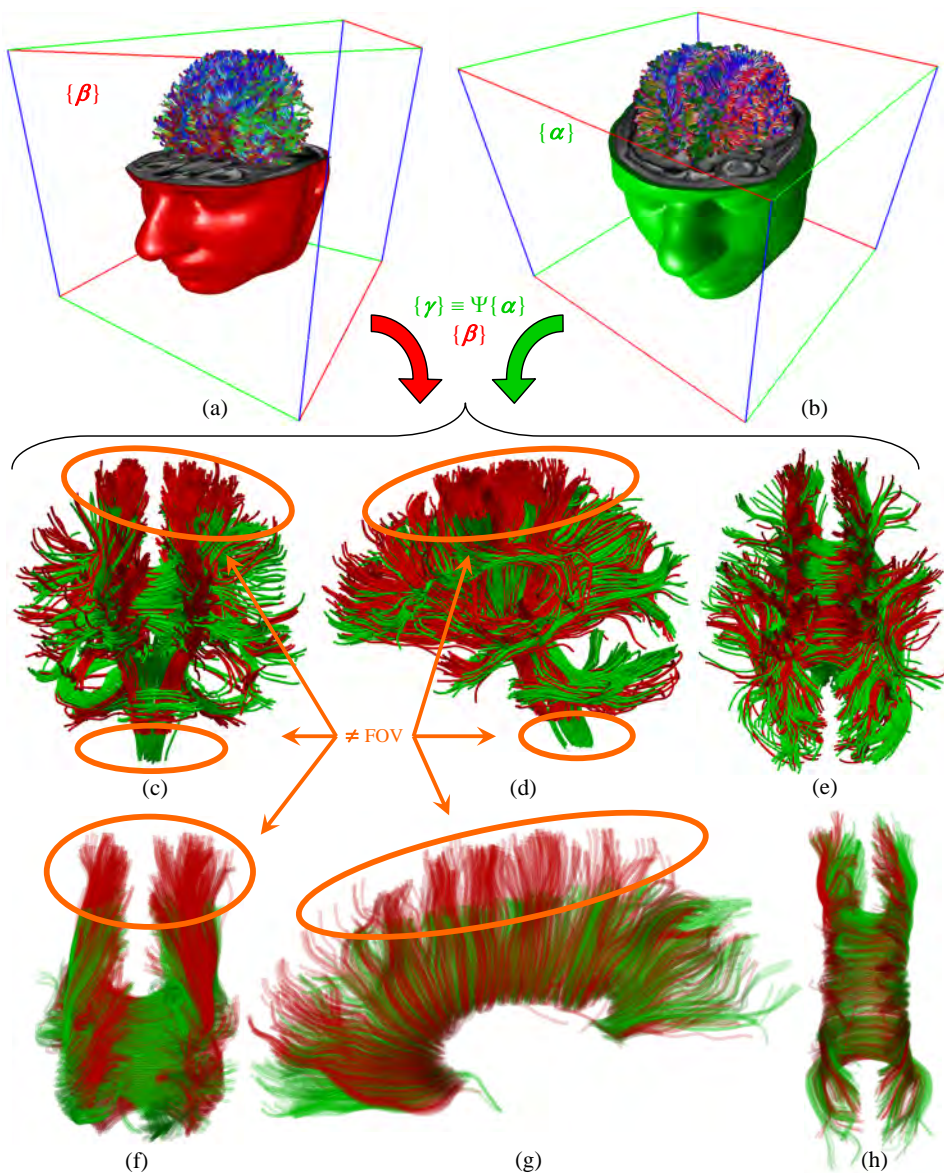
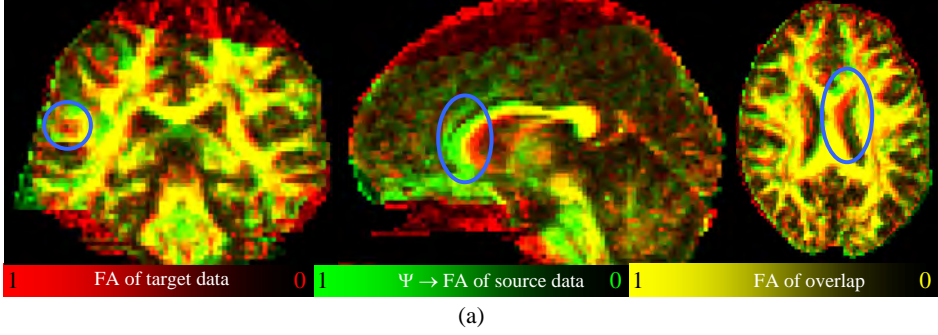


**Figure 5.5.** (a) The target curves  $\beta$  and (b) the source curves  $\alpha$ , both color-encoded according to the local direction (see axes). (c), (d), and (e) represent the coregistered curves  $\{\gamma\} \equiv \Psi\{\alpha\}$  (green) combined with the target curves (red) in the common reference frame along the coronal (c), sagittal (d), and axial (e) view. In (f), (g), and (h) only the corresponding body of the corpus callosum is shown to further facilitate the qualitative evaluation of the coregistration result. Note that there is a different FOV between the data sets, as indicated in (c, d, f, and g).

$$\theta_x = (-10 \pm 2)^\circ; \theta_y = (-1 \pm 3)^\circ; \theta_z = (65 \pm 3)^\circ; t_x = (-20 \pm 4) \text{ mm}; t_y = (11 \pm 3) \text{ mm}; t_z = (21 \pm 3) \text{ mm}; p = 10\%; \sigma = 0 \rightarrow 20; \xi = 5$$



$$\theta_x = -9^\circ; \theta_y = -2^\circ; \theta_z = 66^\circ; t_x = -19 \text{ mm}; t_y = 8 \text{ mm}; t_z = 22 \text{ mm}; s_x = 0.99; s_y = 0.98; s_z = 1.01; g_x = 0.03; g_y = 0.06; g_z = 0.02$$

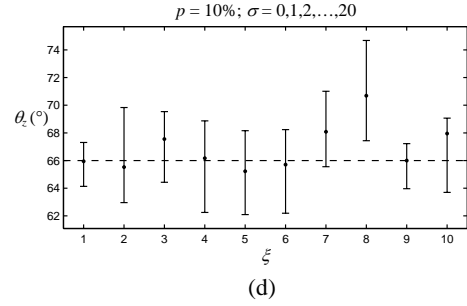
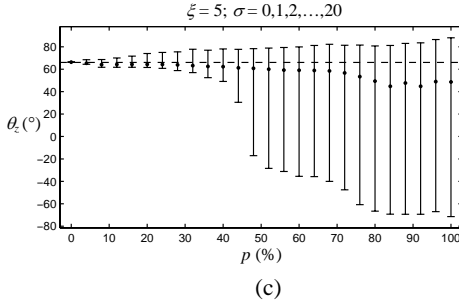
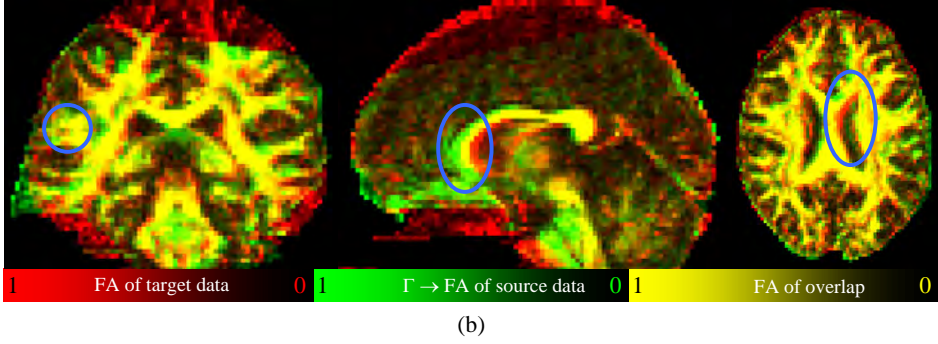


**Figure 5.6.** In (a) the transformation  $\Psi$  (obtained from the fiber tract coregistration), and in (b) the transformation  $\Gamma$  (obtained from the voxel based coregistration), are applied to the FA volume maps to qualitatively assess the coregistration result. Note that a higher correspondence (overlap) is established with  $\Gamma$  and that local non-linear geometric deformations are present (encircled in blue). (c) The coregistration ( $\Psi$ ) accuracy and precision of  $\theta_z$  as a function of the residue cut-off  $p$ . (d) The effect of the space curve sampling factor  $\xi$  on the coregistration result of  $\theta_z$ .

part (yellow). Basically, regions that are strongly red have high anisotropy but do not correspond with the same high anisotropy regions in the other image (and vice versa with green for the other image) and regions with strong yellow indicate high FA of corresponding structures in both data sets. This qualitative map is constructed by defining a pseudo-true-color map with ‘red’, ‘green’, and ‘blue’ components corresponding with the FA map of the target data, the FA map of the transformed source data, and a map filled with zero, respectively. In this way, a gradual difference in overlap between adjacent structures can be observed, as opposed to direct pseudo-color labeling.

A quantitative measure of this overlapping part can heuristically be defined as  $O = 2N_o/(N_t + N_{tr})$ , where  $N_t$ ,  $N_{tr}$ , and  $N_o$  denote the number of voxels with  $FA > 0.5$  of the target data, the transformed data, and the overlapping part, respectively. Here,  $O(\Psi) \simeq 93\%$ . As shown by the encircled regions in Fig. 5.6 (a), it is also important to note that the data suffered significantly from susceptibility artifacts, resulting in local geometric distortions.

To evaluate the performance of the coregistration technique experimentally, a voxel based coregistration approach is applied as described previously [21]. The assumption is made that the *rotation* and *translation* parameters obtained by the *affine* model of this voxel based coregistration method are more appropriate to represent the ground-truth, which is necessary for the quantitative comparison, than those obtained by the *rigid* model. Therefore, an affine transformation  $\Gamma$  (with non-rigid parameters: scale  $s_i$  and skew  $g_i$ ;  $i = x, y, z$ ) is determined to align the images. As shown in Fig. 5.6 (b), the affine voxel based coregistration results in a better local alignment. Also, the overlap percentage in this case was higher:  $O(\Gamma) \simeq 95\%$  ( $O(\Gamma)$  was always higher than  $O(\Psi)$ , independent of the choice of the FA threshold). However, it is important to note that here, the coregistration did not converge to the optimal result without defining the initial transformation close to the final transformation. For example,  $\theta_z$  was initialized in a range of  $20^\circ$  around the coregistration result, i.e.  $66^\circ$ , in order to achieve convergence.

In Fig. 5.6 (c), the effect of the residue cut-off value  $p$  on the accuracy and precision of the proposed coregistration technique is evaluated for  $\theta_z$  with respect to the corresponding result of the voxel based coregistration (with  $\xi = 5$  and  $\sigma = 0 \rightarrow 20$ ). Here, the dashed line represents  $\theta_z = 66^\circ$ , as obtained by  $\Gamma$ . Notice that with an increasing  $p$  value both accuracy and precision rapidly decrease. Finally, Fig. 5.6 (d) demonstrates that the coregistration result is quasi-independent of the space curve sampling factor  $\xi$ , again relative to  $\theta_z = 66^\circ$ , as obtained by  $\Gamma$ .

## 5.6 Discussion

It is known that the second-rank diffusion tensor model of DTI is incapable of describing multiple fiber orientations within an individual voxel, resulting in ambiguous tractography calculations [22]. Although HARD techniques can provide more accurate tractography results, for simplicity, the focus in this framework was confined to classic DTI, where a deterministic streamline fiber tracking technique was used to reconstruct the white matter fiber pathways. Note, however, that this coregistration framework is based on the fiber tracts and not the underlying diffusion data.

Although it is known that deterministic DTT techniques are very sensitive to noise and do not provide the most reliable results, applying a streamline tractography approach already demonstrates feasibility and robustness of the coregistration technique under these nontrivial conditions. It is obvious that a higher coregistration accuracy can be obtained if the WM fiber pathways are calculated by more advanced tractography algorithms and if more advanced diffusion imaging approaches are used. Furthermore, although local non-rigid geometric distortions were present in the brain DTI data, which complicated the coregistration even more, a correct coregistration result could still be obtained. However, as shown in Fig. 5.6 (c), a significant bias is introduced for  $p$  cut-off values higher than 10%.

Since every voxel of the data set is included in the coregistration optimization process for voxel based DTI coregistration techniques, these methods are inefficient, i.e. the majority of these voxels contains no information and does not contribute to the optimization process. In addition, most of these voxel based approaches are iteratively calculating the spatial transformation and therefore may suffer from local optima. Another drawback is the high computational cost, which is unavoidable due to the complex multi-valued nature of the diffusion tensor images.

The computation time for the voxel based approach, which was written in highly optimized C++ code, was in the order of 30 min (for the purpose of objective comparison, only the rigid model was applied). On the other hand, our proposed fiber tract registration technique could already obtain acceptable results in the order of 5 min using not-optimized Matlab code.

The proposed coregistration method is theoretically only applicable to data sets that differ by a rigid motion, although the example elaborated here demonstrates that acceptable results can also be obtained when small local distortions are present. Therefore, the main application of this technique is to study intra-subject follow-up studies. The coregistration result of this method can also be applied as the initialization input parameters for affine or non-affine coregistration techniques, for in the proposed fiber tract coregistration method, initialization of the transformation parameters is not required.

Although the main limitation of the described fiber tract coregistration technique is

its confinement to rigid deformations, which makes it inapplicable for inter-subject studies, a generalization of this approach in future research using affine-invariant shape similarity measures, such as affine curvature, could circumvent this issue [23, 24].

## 5.7 Conclusions

Based on a fundamental theorem of space curves, a non-iterative multiscale 3D rigid-body coregistration technique for WM fiber tractography data was developed. Simulations were performed demonstrating a high coregistration accuracy and precision as a function of different noise levels and several user-defined parameters. The coregistration method is fully automatic and has shown to be robust under non-trivial experimental conditions, like local geometric distortions and a different FOV between the data sets. Finally, a comparison with a voxel based coregistration approach was performed to evaluate the experimental coregistration results. Here, it was shown that both techniques were in agreement with each other confirming the feasibility of the proposed coregistration technique to align brain DTI data.

## Bibliography

- [1] E. Kishon et al. 3-D curve matching using splines. In *ECCV*, pages 589–591, 1990.
- [2] A. Guéziec and N. Ayache. Smoothing and matching of 3-D space curves. *Int J Comput Vision*, 12(1):79–107, 1994.
- [3] A.P. Guéziec et al. Medical image registration using geometric hashing. *IEEE Comput Sci Eng*, 4:29–41, 1997.
- [4] M.A. Audette et al. An algorithmic overview of surface registration techniques for medical imaging. *Med Image Anal*, 4(3):201–217, 2000.
- [5] P.J. Basser et al. In vivo fiber tractography using DT-MRI data. *Magn Reson Med*, 44(4):625–632, 2000.
- [6] P.J. Basser. New histological and physiological stains derived from diffusion-tensor MR images. *Ann NY Acad Sci*, 820:123–138, 1997.
- [7] P.G. Batchelor et al. Classification of bundles of white matter tract from DTI without registration. In *ESMRMB*, page 101, 2003.
- [8] P.G. Batchelor et al. Classification of fibre tracts using differential geometry. In *ISMRM*, page 1278, 2004.
- [9] P.G. Batchelor et al. Quantification of the shape of fiber tracts. *Magn Reson Med*, 55(4):894–903, 2006.
- [10] I. Corouge et al. A statistical shape model of individual fiber tracts extracted from diffusion tensor MRI. In *MICCAI*, pages 671–679, 2004.
- [11] I. Corouge et al. Towards a shape model of white matter fiber bundles using diffusion tensor MRI. In *ISBI*, pages 344–347, 2004.
- [12] M.P. do Carmo. *Differential geometry of curves and surfaces*, page 19. Prentice-Hall, inc., 1976.

- [13] P.H. Schönemann. A generalized solution of the orthogonal Procrustes problem. *Psychometrika*, 31:1–10, 1966.
- [14] F. Mokhtarian. A theory of multiscale, torsion-based shape representation for space curves. *Comp Vision and Image Understanding*, 68(1):1–17, 1997.
- [15] D.H. Ballard and C.M. Brown. *Computer vision*. Prentice-Hall, Inc. Englewood Cliffs, New Jersey, 1982.
- [16] A. Leemans et al. Mathematical framework for simulating diffusion tensor MR neural fiber bundles. *Magn Reson Med*, 53(4):944–953, 2005.
- [17] F. Maes et al. Multimodality image registration by maximization of mutual information. *IEEE Trans Med Imaging*, 16(2):187–198, 1997.
- [18] G.K. Rohde et al. Comprehensive approach for correction of motion and distortion in diffusion-weighted MRI. *Magn Reson Med*, 51(1):103–114, 2004.
- [19] P.J. Basser et al. Estimation of the effective self-diffusion tensor from the NMR spin echo. *J Magn Reson B*, 103(3):247–254, 1994.
- [20] A. Leemans et al. A graphical toolbox for exploratory diffusion tensor imaging and fiber tractography. In *SMRT*, Miami, USA, 2005.
- [21] A. Leemans et al. Affine coregistration of diffusion tensor magnetic resonance images using mutual information. *Lect Notes Comp Sci*, 3708:523–530, 2005.
- [22] R. Bammer et al. In vivo MR tractography using diffusion imaging. *Eur J Radiol*, 45(3): 223–234, 2003.
- [23] F. Mokhtarian and S. Abbasi. Affine curvature scale space with affine length parametrisation. *Pattern Anal Appl*, 4:1–8, 2001.
- [24] F. Mokhtarian and S. Abbasi. Shape similarity retrieval under affine transforms. *Pattern Recogn*, 35:31–41, 2002.



## Chapter 6

# Conclusions

### 6.1 Overview

As elucidated in the first part of this thesis, Diffusion Tensor Imaging (DTI) provides an excellent means to study the brain connectivity in vivo and non-invasively. In the second part, DTI processing techniques have been developed to further improve the reliability of quantitative analyses.

Based on the physical diffusion properties of White Matter (WM) fiber bundles, a mathematical framework has been developed for simulating DTI data sets. This framework allows one to model a smooth transition between the WM fiber system and its surrounding tissue. In addition, complex configurations of multiple fiber bundles, such as crossing, merging, and kissing of fiber pathways, can be constructed. Several models have been evaluated quantitatively using experimental DTI data. This evaluation indicates that a higher correspondence between experimental and synthetic DTI data exists when the cross-sectional dependency of the WM fiber density is modeled as nonconstant. Furthermore, these results suggest that modeling of partial-volume effects alone is not the optimum way to model WM fiber structures. It has been demonstrated that the proposed mathematical framework can provide the necessary ground-truth DTI data for the quantitative evaluation and optimization of user-defined tractography termination parameters. Moreover, the synthetic ground-truth data allows one to objectively compare different Fiber Tractography (FT) algorithms. Several examples of how the mathematical framework can be applied to compare FT algorithms have been presented.

A 3D affine voxel based DTI coregistration technique has been developed using a direct diffusion tensor reconstruction approach to preserve the underlying orientational information. This multi-channel matching method applies mutual infor-



mation as a similarity measure for the multi-valued DTI data sets. Simulations have been performed, demonstrating the applicability of the diffusion tensor shape preserving reorientation strategy. In addition, an in-vivo coregistration example has been worked out, indicating feasibility of the proposed technique to coregister experimental data.

Based on the local geometric invariance properties of space curves, a non-iterative multiscale 3D rigid-body coregistration technique for WM fiber tractography data was developed. Simulations were performed demonstrating a high coregistration accuracy and precision as a function of different noise levels and several user-defined parameters. The coregistration method is fully automatic and has shown to be robust under non-trivial experimental conditions, like local geometric distortions and a different field of view between the data sets. Finally, a comparison with a voxel based coregistration approach was performed to evaluate the experimental coregistration results. Here, it was shown that both techniques were in agreement with each other confirming the feasibility of the proposed coregistration technique to align brain DTI data.

## 6.2 Future work

The DTI processing tools that have been developed in this thesis could be applied in both medical and biomedical settings. For example, studies of brain plasticity in songbirds using voxel based morphometry require DTI coregistration. Within this context, a framework for constructing DTI atlases could be investigated additionally. Furthermore, the simulated DTI phantom data sets can be used to quantitatively evaluate, optimize, and compare FT algorithms.

Although it is important to understand the limitations of DTI, there are, fortunately and deplorably, still several interesting aspects within this burgeoning field that would require further investigation, such as super-resolution, non-affine DTI coregistration, and the development of adequate statistical analysis tools for DTI and FT. In addition, it would be interesting to explore new processing techniques for more advanced diffusion Magnetic Resonance Imaging (MRI) techniques, possibly in combination with other imaging modalities, such as functional MRI.

# Appendices

## Appendix A

Using Eqs. (3.1) and (3.4), the resulting convolution  $T_r(\mathbf{r})$  is calculated as follows:

$$\begin{aligned}
 T_r(\mathbf{r}) &= t(\mathbf{r}) * k_r(\mathbf{r}) \\
 &= \sum_{i=1}^{N-1} \int_0^1 \Pi\left(\frac{\|\mathbf{r} - \mathbf{r}_i - \alpha \Delta_i\|}{w}\right) d\alpha \\
 &= \sum_{i=1}^{N-1} \int_0^1 H\left(\frac{1}{4} - \frac{\|\mathbf{r} - \mathbf{r}_i - \alpha \Delta_i\|^2}{w^2}\right) d\alpha \\
 &= \sum_{i=1}^{N-1} \int_0^1 H[a_i(\mathbf{r}) + b_i(\mathbf{r})\alpha + c\alpha^2] d\alpha, \tag{A-1}
 \end{aligned}$$

where  $H$  represents the Heaviside step function and the coefficients of the second order polynomial form  $f_{\mathbf{r}}^i(\alpha) = a_i(\mathbf{r}) + b_i(\mathbf{r})\alpha + c\alpha^2$  are given by:

$$a_i(\mathbf{r}) = \frac{1}{4} - \frac{\|\mathbf{r} - \mathbf{r}_i\|^2}{w^2} \quad ; \quad b_i(\mathbf{r}) = \frac{2\Delta_i \cdot (\mathbf{r} - \mathbf{r}_i)}{w^2} \quad ; \quad c = -\frac{\Delta^2}{w^2}. \tag{A-2}$$

Note that  $f_{\mathbf{r}}^i(\alpha)$  is a concave function, i.e.

$$\forall \mathbf{r} : \frac{\partial^2 f_{\mathbf{r}}^i(\alpha)}{\partial \alpha^2} = -\frac{2\Delta^2}{w^2} < 0. \tag{A-3}$$

Hence, it is clear that:

$$\begin{cases} H[f_{\mathbf{r}}^i(\alpha)] = 1 & \text{for } \alpha_i^- < \alpha < \alpha_i^+ \\ H[f_{\mathbf{r}}^i(\alpha)] = 0 & \text{for } \alpha_i^+ < \alpha \quad ; \quad \alpha < \alpha_i^- \end{cases}, \tag{A-4}$$

where  $\alpha_i^+$  and  $\alpha_i^-$  are the real roots of  $f_{\mathbf{r}}^i(\alpha)$ , which are written out in Eq. (3.6). From the schematic representation of  $f_{\mathbf{r}}^i(\alpha)$ , which is depicted in Fig. A.1, and using Eqs. (A-3) and (A-4), one can easily see that the convolution  $T_r(\mathbf{r})$  can be calculated as given in Eq. (3.5).

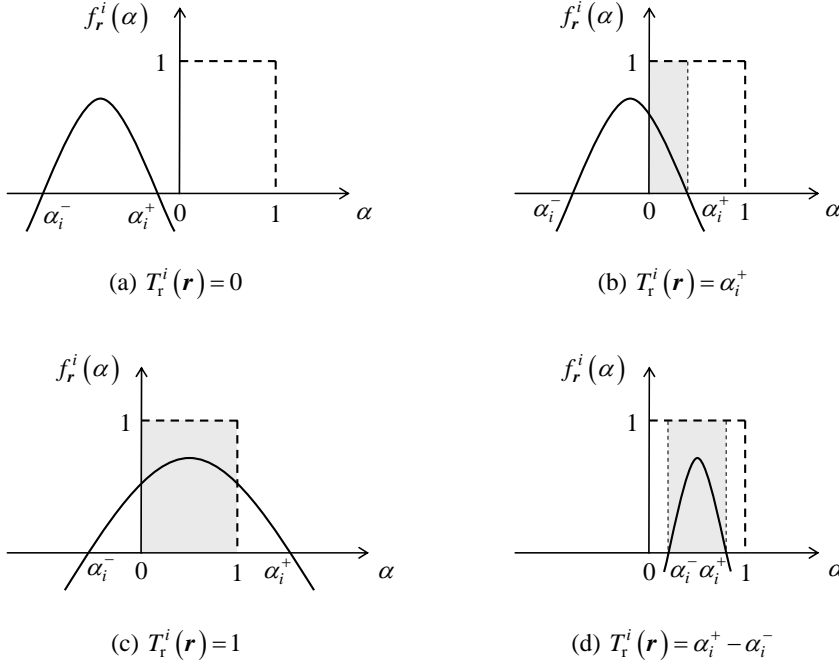


**Figure A.1.** Schematic illustration of  $T_r^i(\mathbf{r}) = \int_0^1 H[f_r^i(\alpha)] d\alpha$  (gray area) to elucidate the calculation of Eq. [3.5]. Figures (a)→(d) represent the four main configurations of  $f_r^i(\alpha)$  with respect to the integration interval  $[0, 1]$ . The analogous configurations of (a), i.e.  $1 < \alpha_i^- < \alpha_i^+$ , and (b), i.e.  $0 < \alpha_i^- < 1 < \alpha_i^+$ , are given by  $T_r^i(\mathbf{r}) = 0$  and  $T_r^i(\mathbf{r}) = 1 - \alpha_i^-$ , respectively. Combining all these possible values results in Eq. [3.5].

## Appendix B

Using Eqs. (3.1) and (3.8), the convolution of the fiber tract  $t(\mathbf{r})$  with  $k_g(\mathbf{r})$ , denoted as  $T_g(\mathbf{r})$ , is calculated as follows:

$$\begin{aligned}
 T_g(\mathbf{r}) &= \sum_{i=1}^{N-1} \iiint_{-\infty}^{\infty} \int_0^1 \delta[\mathbf{u} - (\mathbf{r}_i + \alpha \mathbf{\Delta}_i)] e^{-\frac{\|\mathbf{r} - \mathbf{u}\|^2}{2\sigma^2}} d\alpha d\mathbf{u} \\
 &= \sum_{i=1}^{N-1} \int_0^1 e^{-\frac{\|\mathbf{r} - (\mathbf{r}_i + \alpha \mathbf{\Delta}_i)\|^2}{2\sigma^2}} d\alpha \\
 &= \frac{\sigma}{\Delta} \sqrt{\frac{\pi}{2}} \sum_{i=1}^{N-1} e^{\frac{[\hat{\mathbf{\Delta}}_i \cdot (\mathbf{r} - \mathbf{r}_i)]^2 - \|\mathbf{r} - \mathbf{r}_i\|^2}{2\sigma^2}} \left\{ \operatorname{erf}\left[\frac{\hat{\mathbf{\Delta}}_i \cdot (\mathbf{r} - \mathbf{r}_i)}{\sqrt{2}\sigma}\right] + \operatorname{erf}\left[\frac{\hat{\mathbf{\Delta}}_i \cdot (\mathbf{r}_{i+1} - \mathbf{r})}{\sqrt{2}\sigma}\right] \right\},
 \end{aligned} \tag{B-1}$$

where  $\hat{\Delta}_i = \Delta_i/\Delta$ . The numerator of the exponential in Eq. (B-1) is further simplified using the identity

$$\left\| \hat{\Delta}_i \times (\mathbf{r} - \mathbf{r}_i) \right\|^2 = \|\mathbf{r} - \mathbf{r}_i\|^2 - \left[ \hat{\Delta}_i \cdot (\mathbf{r} - \mathbf{r}_i) \right]^2 . \quad (\text{B-2})$$



# List of abbreviations

1D	one-dimensional
2D	two-dimensional
3D	three-dimensional
ADC	Apparent Diffusion Coefficient
ADHD	Attention-Deficit Hyperactivity Disorder
B	Blue
BW	Band Width
CC	Corpus Callosum
CNS	Central Nervous System
CR	Corona Radiate
CSF	Cerebrospinal Fluid
CT	Computed Tomography
DOF	Degrees Of Freedom
DT	Diffusion Tensor
DSI	Diffusion Spectrum Imaging
DTI	Diffusion Tensor Imaging
DTT	Diffusion Tensor Tractography
DT-MRI	Diffusion Tensor Magnetic Resonance Imaging
DW	Diffusion-Weighted
DWI	Diffusion-Weighted Imaging
EPI	Echo-Planar Imaging
FA	Fractional Anisotropy
fMRI	functional Magnetic Resonance Imaging
FM	Fast Marching
FMT	Fast Marching Tractography
FT	Fiber Tractography
FACT	Fiber Assignment by Continuous Tracking
FOV	Field Of View
G	Green
GDTI	Generalized Diffusion Tensor Imaging

HARD	High-Angular-Resolution Diffusion
HARDI	High-Angular-Resolution Diffusion-weighted Imaging
HIV	Human Immunodeficiency Virus
IC	Internal Capsule
IVOH	Intra-Voxel Orientational Heterogeneity
LS	Least Square
MCMC	Markov Chain Monte Carlo
MD	Mean Diffusivity
MEMRI	Manganese Enhanced Magnetic Resonance Imaging
MI	Mutual Information
MIRIT	Multimodality Image Registration using Information Theory
MR	Magnetic Resonance
MRI	Magnetic Resonance Imaging
MSD	Mean Squared Distance
NMR	Nuclear Magnetic Resonance
ODF	Orientation Distribution Function
PAS	Persistent Angular Structure
PCA	Principal Component Analysis
PD	Principal Diffusivity
PDF	Probability Density Function
PDV	Principal Diffusion Vector
PET	Positron Emission Tomography
PPD	Preservation of Principal Direction
PVE	Partial Volume Effect
R	Red
RA	Relative Anisotropy
RAVE	Random Vector
RF	Radio Frequency
RK2	Second-order Runge-Kutta
RK4	Fourth-order Runge-Kutta
RMS	Root-Mean-Square
ROI	Region Of Interest
RS	Reorientation Strategy
SENSE	Sensitivity Encoding
SNR	Signal-to-Noise Ratio
TE	Echo Time
TEND	Tensor Deflection
TR	Repetition Time
QBI	Q-Ball Imaging
VF	Volume Fraction
VR	Volume Ratio

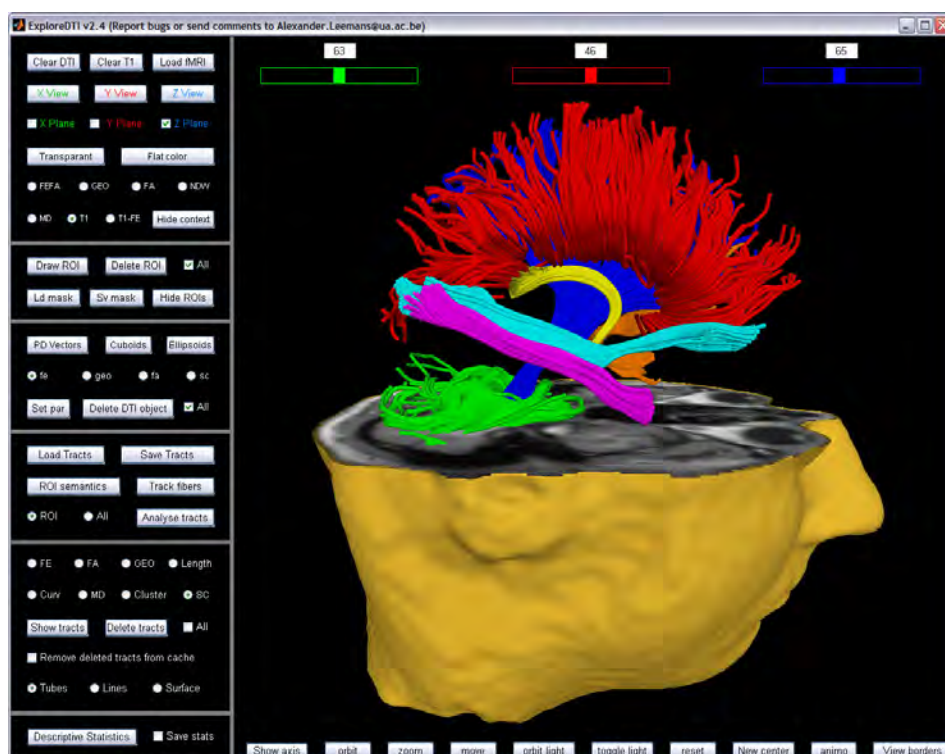
WM	White Matter
----	--------------





# ‘ExploreDTI’: toolbox for exploratory DTI and FT

During this PhD research, we developed a graphical toolbox to explore diffusion tensor magnetic resonance data sets and perform fiber tractography (see image below). This award-winning (open-source) software toolbox, dubbed ‘ExploreDTI’, is made available to other researchers at <http://www.dti.ua.ac.be/>.





# Curriculum vitae

Alexander Leemans was born in Antwerp (Belgium) on the 25<sup>th</sup> of June 1979. He received his high school diploma from the Xaverius College (Borgerhout – Belgium) in June 1997. Two months later, he started the study of Physics at the University of Antwerp. He received his licentiate diploma (M.Sc. degree) in June 2002 with great distinction. In September 2002, he started the research of which the results are described in this PhD dissertation.



# List of publications

## Journal articles

1. A. Leemans, J. Sijbers, M. Verhoye, A. Van der Linden, and D. Van Dyck, *Mathematical framework for simulating diffusion tensor MR neural fiber bundles*, Magnetic Resonance in Medicine, Vol. 53, Nr. 4, p. 944–953, **2005** (SCI IF: 3.468)
2. A. Leemans, J. Sijbers, S. De Backer, E. Vandervliet, and P. M. Parizel, *Affine coregistration of diffusion tensor magnetic resonance images using mutual information*, Lecture Notes in Computer Science, Vol. 3708, p. 523–530, **2005** (SCI IF: 0.513)
3. P. M. Parizel, J. Van Goethem, L. van den Hauwe, R. Salgado, E. Vandervliet, and A. Leemans, *Characterization of brain tumors*, Neuroradiology, Vol. 47, Nr. 1, p. 80–83, **2005** (SCI IF: 1.515)
4. G. De Groof, M. Verhoye, V. Van Meir, I. Tindemans, A. Leemans, and A. Van der Linden, *In vivo diffusion tensor imaging (DTI) of brain subdivisions and vocal pathways in songbirds*, NeuroImage, Vol. 29, Nr. 3, p. 754–763, **2006** (SCI IF: 4.869)
5. A. Leemans, J. Sijbers, S. De Backer, E. Vandervliet, and P. M. Parizel, *Multiscale white matter fiber tract coregistration: a new feature-based approach to align diffusion tensor data*, Magnetic Resonance in Medicine, (in press) **2006** (SCI IF: 3.468)

## Conference proceedings

*First-author contributions: 12 international (8 oral presentations and 4 posters) and 2 national (2 oral presentations) conference proceedings.*

1. J. H. Waarsing, A. Leemans, J. Day, A. G. H. Ederveen, D. Van Dyck, E. Buelens, N. De Clerck, A. Sasov and H. Weinans, *Effects of growth and OVX in the tibia of individual rats: an in-vivo micro-CT study*, 49th Annual Meeting – Orthopaedic Research Society, New Orleans, LA, USA, **2003**
2. A. Leemans, J. Sijbers, M. Verhoye, A. Van der Linden, and D. Van Dyck, *A simulated phantom for diffusion tensor fiber tracking*, IEEE Advanced Concepts for Intelligent Vision Systems, p. 281–285, Ghent, Belgium, **2003** (oral presentation)
3. A. Leemans, J. Sijbers, M. Verhoye, A. Van der Linden, and D. Van Dyck, *Simulating neuronal fiber bundles for DT-MRI tractography*, 20th Annual Scientific Meeting – European Society for Magnetic Resonance in Medicine and Biology, p. 278, Rotterdam, The Netherlands, **2003** (poster)
4. A. Leemans, J. Sijbers, M. Verhoye, A. Van der Linden, and D. Van Dyck, *A geometric color scheme for visualizing diffusion tensor magnetic resonance fiber pathways*, 19th Annual Symposium – Belgian Hospital Physicists Association, Brussels, Belgium, **2004** (oral presentation)
5. A. Leemans, J. Sijbers, M. Verhoye, A. Van der Linden, and D. Van Dyck, *White matter fiber bundle coregistration for diffusion tensor magnetic resonance tractography*, 13th Annual Meeting – Section for Magnetic Resonance Technologists, Kyoto, Japan, **2004** (poster)
6. M. Verhoye, G. De Groof, V. Van Meir, I. Tindemans, A. Leemans, and A. Van der Linden, *In vivo neuroanatomy of the songbird brain, visualized through diffusion tensor imaging*, 21th Annual Scientific Meeting – European Society for Magnetic Resonance in Medicine and Biology, p. 161, Copenhagen, Denmark, **2004**
7. N. Van Camp, M. Verhoye, A. Leemans, A. Postnov, D. Beque, J. Van den Eynden, J. Nuyts, E. Lauwers, A. Verbruggen, Z. Debyzer, V. Baekelandt, N. De Clerck, J. Sijbers, K. Van Laere, and A. Van der Linden, *In vivo multimodal imaging of a rat model for Parkinson’s disease: high resolution micro-MRI, micro-SPECT and micro-CT*, 21th Annual Scientific Meeting – European Society for Magnetic Resonance in Medicine and Biology, p. 22–23, Copenhagen, Denmark, **2004**

8. A. Leemans, J. Sijbers, M. Verhoye, and A. Van der Linden, *A Library of 3D synthetic DT-MRI models for testing white matter fiber tractography algorithms*, 21th Annual Scientific Meeting – European Society for Magnetic Resonance in Medicine and Biology, p. 42, Copenhagen, Denmark, **2004** (oral presentation)
9. A. Leemans, J. Sijbers, M. Verhoye, and A. Van der Linden, *Experimental evaluation of synthetic DT-MRI models*, 21th Annual Scientific Meeting – European Society for Magnetic Resonance in Medicine and Biology, p. 40–41, Copenhagen, Denmark, **2004** (oral presentation)
10. A. Leemans, J. Sijbers, W. Van den Broek, and Z. Yang, *An interactive curvature based rigid-body image registration technique: an application to EFTEM*, 13th European Microscopy Congress, Antwerp, Belgium, **2004** (oral presentation)
11. J. Sijbers, N. Van Camp, A. Leemans, A. J. den Dekker, M. Verhoye and A. Van der Linden, *Coregistration of Micro-MRI, microCT and microPET*, Workshop on non Invasive 3D Microscopy, p. 16, Antwerp, Belgium, **2004**
12. A. Leemans and J. Sijbers, *Multiresolutional rigid-body registration for space curves*, IEEE Advanced Concepts for Intelligent Vision Systems, p. 215–221, Brussels, Belgium, **2004** (poster)
13. M. Verhoye, G. De Groof, V. Van Meir, I. Tindemans, A. Leemans, and A. Van der Linden. *In vivo visualization of the neuroanatomy and brain connectivity of starling brain through diffusion tensor imaging*, 34rd Annual Meeting of the Society for Neuroscience, San Diego, USA, **2004**
14. A. Leemans, J. Sijbers, M. Verhoye, and A. Van der Linden, *Optimized fiber tractography based on diffusion tensor magnetic resonance simulations*, 20th Annual Symposium – Belgian Hospital Physicists Association, Namur, Belgium, **2005** (oral presentation)
15. G. De Groof, M. Verhoye, A. Leemans, and A. Van der Linden, *Seasonal changes in neuronal connectivity in the songbird brain discerned by repeated in vivo DTI*, International Society for Magnetic Resonance in Medicine – 13th Scientific Meeting in Miami Beach, Florida, USA, **2005**
16. A. Leemans, J. Sijbers, M. Verhoye, and A. Van der Linden, *Entropy-based coregistration for DT-MR images using an efficient tensor shape preserving reorientation strategy*, International Society for Magnetic Resonance in Medicine – 13th Scientific Meeting in Miami Beach, p. 227, Florida, USA, **2005** (oral presentation)



17. S. Delputte, A. Leemans, E. Fieremans, Y. D'asseler, I. Lemahieu, R. Achten, J. Sijbers, and R. Van de Walle, *Density Regularized fiber tractography of the brain white matter using diffusion tensor MRI*, International Society for Magnetic Resonance in Medicine – 13th Scientific Meeting in Miami Beach, p. 1309, Florida, USA, **2005**
18. A. Leemans, J. Sijbers, and P. Parizel, *A graphical toolbox for exploratory diffusion tensor imaging and fiber tractography*, Section for Magnetic Resonance Technologists (SMRT) – 14th Annual Meeting in Miami Beach, Florida, USA, **2005** (poster)
19. G. De Groof, M. Verhoye, V. Van Meir, I. Tindemans, A. Leemans, and A. Van der Linden, *In vivo visualization of the neuroanatomy and brain connectivity of starling brain through diffusion tensor imaging*, 6th Bi-Annual Meeting – Belgian Society for Neuroscience, Brussels, Belgium, **2005**
20. A. Leemans, S. De Backer, J. Sijbers, E. Vandervliet, and P. Parizel, *End point clustering for diffusion tensor white matter fiber bundle tractography*, 22th Annual Scientific Meeting – European Society for Magnetic Resonance in Medicine and Biology, p. 129–130, Basle, Switzerland, **2005** (oral presentation)
21. G. De Groof, M. Verhoye, A. Leemans, and A. Van der Linden. *DTI parameters: fractional anisotropy, radial and axial diffusivity reveal seasonal neuroplasticity in the adult songbird brain*, 4th annual meeting of the Society of Molecular Imaging, Keulen, Germany, **2005**
22. A. Leemans, S. De Backer, J. Sijbers, E. Vandervliet, and P. Parizel, *TRACT: Tissue Relative Anisotropy based Curvature Thresholding for deterministic MR diffusion tensor tractography*, 22th Annual Scientific Meeting – European Society for Magnetic Resonance in Medicine and Biology, p. 289, Basle, Switzerland, **2005** (poster)
23. G. De Groof, M. Verhoye, A. Leemans, and A. Van der Linden, *Using diffusion tensor imaging (DTI) to assess the neuronal plasticity in the brain of a songbird*, 4th Annual Symposium – Young Belgian Magnetic Resonance Scientists, Brussels, Belgium, **2005**
24. W. Van Hecke, A. Leemans, P.M. Parizel, J.W.M. Van Goethem, J. Sijbers, *DTI of normal appearing spinal cord in elderly*, 21th Annual Symposium – Belgian Hospital Physicists Association, p. 61, Ghent, Belgium, **2006**
25. A. Leemans, J. Sijbers, S. De Backer, E. Vandervliet, and P. Parizel, *Multi-scale white matter fiber tract coregistration: a new feature-based approach to*

- align diffusion tensor data*, International Society for Magnetic Resonance in Medicine – 14th Scientific Meeting in Seattle, USA, **2006** (oral presentation)
26. W. Van Hecke, A. Leemans, P.M. Parizel, J.W.M. Van Goethem, J. Sijbers, *DTI of normal appearing spinal cord in elderly*, 44th Annual Meeting of the American Society of Neuroradiology, San Diego, USA, **2006**
  27. G. De Groof, M. Verhoye, A. Leemans, and A. Van der Linden, *Using diffusion tensor imaging (DTI) to assess the neuronal plasticity in the brain of a songbird*, XX<sup>ème</sup> Congrès du Groupement d’Etudes de Résonance Magnétique, Blankenberge, Belgium, **2006**

## Awards

1. *Young Investigator Award* (Belgian Hospital Physicist of the Year) for the presented work, entitled: “A Geometric Color Scheme for Visualizing Diffusion Tensor Magnetic Resonance Fiber Pathways” at the 20th Annual BHPA Symposium – Brussels, Belgium, **2004**
2. *Cum Laude Award* for the submitted work, entitled: “In vivo neuroanatomy of the songbird brain, visualized through diffusion tensor imaging” at the 21th Annual ESMRMB Meeting – Copenhagen, Denmark, **2004**
3. *Research Focus Poster Award* for the work, entitled: “A graphical toolbox for exploratory diffusion tensor imaging and fiber tractography” at the 14th Annual SMRT Meeting – Miami, USA, **2005**
4. *Educational Stipend Award* for the submitted work, entitled: “Multiscale white matter fiber tract coregistration: a new feature-based approach to align diffusion tensor data” at the 14th Annual ISMRM Meeting – Seattle, USA, **2006**



# Nederlandse samenvatting

## Overzicht

Dit proefschrift handelt over de modellering en de verwerking van Diffusietensor (DT) Magnetische Resonantie (MR) data. Hierbij wordt de nadruk gelegd op de ontwikkeling van nieuwe DT beeldverwerkingstechnieken met als doel een verbeterde kwantitatieve analyse van de hersenconnectiviteit (het complexe netwerk van verbindingen waarmee hersencellen communiceren). Het proefschrift bestaat uit twee delen. In Deel I wordt een grondig literatuuroverzicht gegeven over DT MR beeldvorming (DTI) (hoofdstuk 1) en tractografie van vezelbanen (FT) (hoofdstuk 2). Deel II bevat de voornaamste originele bijdragen, i.e. de ontwikkeling van een algemeen wiskundig model om synthetische DT data te simuleren (hoofdstuk 3) en de ontwikkeling van twee nieuwe DT coregistratietechnieken (hoofdstukken 4 en 5).

## Motivatie en doelstellingen

De hersenen vormen ongetwijfeld het meest complexe systeem in de biologische wereld. Ze voeren immers een veelheid van taken uit, zoals waarneming, interpretatie van informatie, reactie, planning en uitvoering van gedrag. DTI maakt het mogelijk om de verbindingen in dit complexe systeem (de hersenconnectiviteit) in vivo en niet-invasief te bestuderen. Hoofdstuk 1 behandelt de fysische en wiskundige grondbeginselen van deze unieke MR techniek, waarbij het begrip diffusie wordt geïntroduceerd in de context van MR beeldvorming (MRI). De principes en het belang van diffusie-gewogen MRI worden beschreven en nadien verder uitgebreid tot DTI. Verder behandelt dit hoofdstuk verschillende DT visualisatie technieken en geeft het een overzicht van de belangrijkste scalaire maten die gerelateerd zijn aan het DT model. Nadien worden de voornaamste artefacten in DT beelden besproken en worden de beperkingen van DTI toegelicht. Tenslotte benadrukt dit hoofdstuk het belang van DTI in het kader van de medische en biomedische wetenschappen aan de hand van enkele toepassingen.

Eén van de belangrijkste toepassingen van DTI is FT en vormt het onderwerp van hoofdstuk 2. Met FT kunnen de vezelbundels in de witte hersenmaterie (WM) in vivo en niet-invasief virtueel gereconstrueerd worden aan de hand van de DT data. Na een korte beschrijving van de basisprincipes worden verscheidene FT technieken bestudeerd waarbij hun voor- en nadelen worden toegelicht. Verder behandelt dit hoofdstuk de voornaamste visualisatie methodes voor FT, waarbij ook hier het belang van een duidelijke data representatie wordt benadrukt. Tot slot worden de belangrijkste toepassingen van FT vermeld.

Voor fundamenteel onderzoek in DT beeldverwerking zijn simulaties en testen op synthetische data onontbeerlijk. Met deze testen kan men immers de nauwkeurigheid, precisie, reproduceerbaarheid en gevoeligheid aan ruis van de ontwikkelde DT beeldverwerkingstechnieken kwantitatief bestuderen. Een hoge nauwkeurigheid en een realistische representatie van een dergelijk synthetisch fantoom zijn hierbij van groot belang bij het uitvoeren van een betrouwbare analyse met het oog op toepassingen met experimentele DT data. Hoofdstuk 3 behandelt de ontwikkeling van een algemeen wiskundig model om deze gesimuleerde DT data te construeren. De synthetische DT data worden in het bijzonder gemodelleerd aan de hand van een vereenvoudigde voorstelling van de WM vezelbanen waarbij verschillende fysische eigenschappen van deze vezelbundels worden geïncorporeerd. De ontwikkelde synthetische fantomen dienen enerzijds als een betrouwbare referentie bij het kwantitatief evalueren en objectief vergelijken van verscheidene DT beeldverwerkingstechnieken, zoals bijvoorbeeld coregistratie, ruisreductie en het corrigeren van bewegingsartefacten. Anderzijds zijn deze gesimuleerde DT data ook onmisbaar om de talrijke parameters die een FT algoritme karakteriseren te optimaliseren. Verscheidene voorbeelden worden in detail uitgewerkt om aan te duiden hoe dit wiskundig model kan worden toegepast bij het vergelijken van FT algoritmes.

Coregistratie is een belangrijke techniek binnen de beeldverwerking die het mogelijk maakt om beelden, of meer algemeen ‘digitale representaties van objecten’, in een gemeenschappelijk referentiekader te plaatsen. Enkel op deze manier kan men vergelijkende, kwantitatieve DTI studies realiseren, zoals bijvoorbeeld het aantonen van statistisch significante verschillen tussen gezonde en pathologische structuren van de WM. Door de snelle evolutie en groeiende diversiteit van beeldvormingstechnieken tijdens de laatste decennia is de ontwikkeling van een universeel coregistratie algoritme echter onmogelijk geworden. De kwaliteit, aard van informatie, grootte en toepassingsgebied van het beeldmateriaal zijn immers belangrijke aspecten die het karakter van de coregistratietechniek bepalen. In dit kader behandelt hoofdstuk 4 de ontwikkeling van een affine (rotatie, translatie, schaling en scheefheid) voxel-gebaseerde coregistratietechniek voor DT data. De voxels van de DT data representeren geen scalaire waarden, maar tensoren van rang twee die de

driedimensionale, Gaussisch verdeelde diffusie definiëren, waardoor conventionele coregistratietechnieken ontoereikend zijn. Verder beschrijft dit hoofdstuk de ontwikkeling van een efficiënte reoriëntatie strategie, die nodig is om de belangrijke oriëntationele informatie van de diffusietensor te behouden. Als vergelijkingscriterium, i.e. de maatstaf die bepaalt hoe de overeenkomst tussen de beelden wordt gedefinieerd, wordt mutuele informatie gehanteerd. De affine DT coregistratietechniek wordt in de eerste plaats geëvalueerd aan de hand van gesimuleerde DT fantomen en nadien toegepast op DT data van humane hersenen.

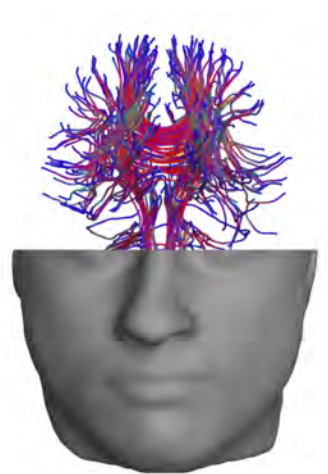
In hoofdstuk 5 wordt de ontwikkeling van een andere coregistratietechniek voorgesteld waarbij gebruik wordt gemaakt van de met FT gereconstrueerde hersenvezelbanen i.p.v. de voxel-gebaseerde data. Met deze aanpak wordt enkel de relevante informatie (nl., de hersenvezelbanen) in rekening gebracht hetgeen de coregistratie procedure efficiënter maakt. Veel voxels in DT data bevatten immers geen relevant signaal en leveren dus geen significante bijdrage in de optimalisatie procedure van voxel-gebaseerde DT coregistratietechnieken. De coregistratietechniek is volledig automatisch en is verder gebaseerd op de lokale invariantie eigenschappen van de hersenvezelbanen, die op hiërarchische wijze worden voorgesteld. In de eerste plaats worden simulaties uitgevoerd m.b.v. de ontwikkelde synthetische DT data om de nauwkeurigheid, de reproduceerbaarheid en het effect van ruis in de data te bestuderen. Verder behandelt dit hoofdstuk de optimalisatie van verscheidene parameters die de coregistratie procedure karakteriseren. Tenslotte wordt deze nieuwe techniek vergeleken met de coregistratiemethode uit hoofdstuk 4 en worden de voor- en nadelen toegelicht.











*White Matter Fiber Tractography of the Human Brain*